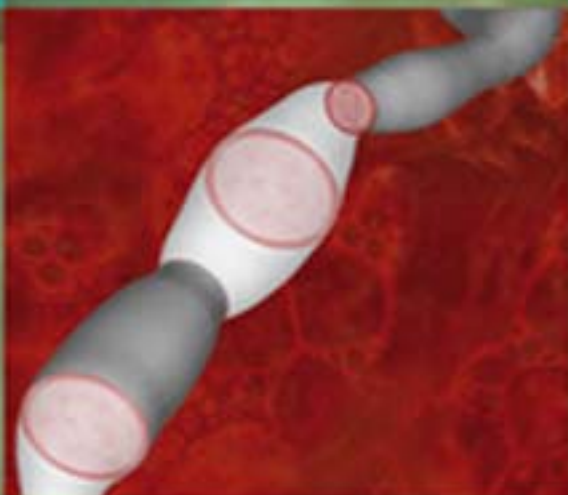
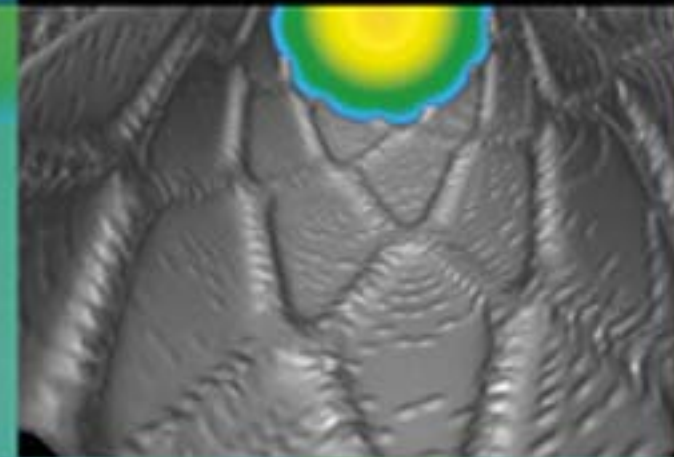
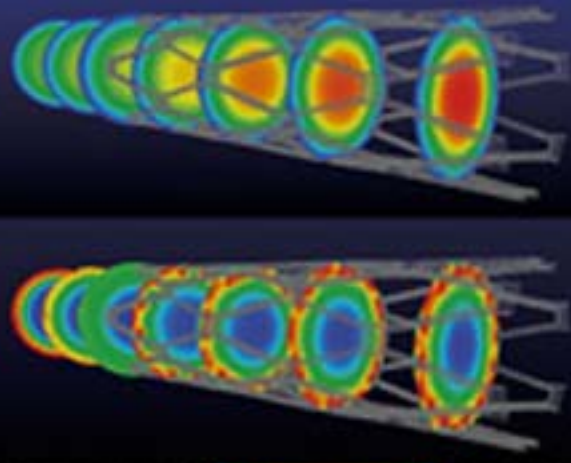


EDITOR  
C.A. Brebbia

# Modelling in Medicine and Biology



WITPRESS



# *Modelling in Medicine and Biology*

**WIT***PRESS*

WIT Press publishes leading books in Science and Technology.

Visit our website for the current list of titles.

[www.witpress.com](http://www.witpress.com)

**WIT***eLibrary*

Home of the Transactions of the Wessex Institute, the WIT electronic-library provides the international scientific community with immediate and permanent access to individual papers presented at WIT conferences. Visit the WIT eLibrary at <http://library.witpress.com>

*This page intentionally left blank*

# ***Modelling in Medicine and Biology***

*Editors:*

**C A Brebbia,**  
*Wessex Institute of Technology, UK*



**WIT***PRESS* Southampton, Boston

**C A Brebbia,**  
Wessex Institute of Technology, UK

Published by

WIT Press  
Ashurst Lodge, Ashurst, Southampton, SO40 7AA, UK  
Tel: 44 (0) 238 029 3223; Fax: 44 (0) 238 029 2853  
E-Mail: [witpress@witpress.com](mailto:witpress@witpress.com)  
<http://www.witpress.com>

For USA, Canada and Mexico  
WIT Press  
25 Bridge Street, Billerica, MA 01821, USA  
Tel: 978 667 5841; Fax: 978 667 7582  
E-Mail: [infousa@witpress.com](mailto:infousa@witpress.com)  
<http://www.witpress.com>

British Library Cataloguing-in-Publication Data  
A Catalogue record for this book is available  
from the British Library

ISBN: 978-1-84564-572-4

Library of Congress Catalog Card Number: 2011922774

The texts of the papers in this volume were set  
individually by the authors or under their supervision.

No responsibility is assumed by the Publisher, the Editors and Authors for any injury and/or damage to persons or property as a matter of products liability, negligence or otherwise, or from any use or operation of any methods, products, instructions or ideas contained in the material herein. The Publisher does not necessarily endorse the ideas held, or views expressed by the Editors or Authors of the material contained in its publications.

© WIT Press 2011.

Printed in Great Britain by Quay Digital, Bristol

The material contained herein is reprinted from a special edition of Design & Nature and Ecodynamics, Vol.4 No.3. published by WIT Press.

All rights reserved. No part of this publication may be reproduced, stored in a retrieval system, or transmitted in any form or by any means, electronic, mechanical, photocopying, recording, or otherwise, without the prior written permission of the Publisher.

# CONTENTS

Preface .....	1
Stress-strain distribution in the human stomach N.R. AKHMADEEV & R. MIFTAHOF .....	3
A computer-assisted internal examination training system using both anatomical and virtual models A. DOI, K. NOGUCHI, K. KATAMACHI, T. ISHII, H. UNO, Y. MEGA & K. MATSUI .....	21
A Numerical study of blood flow patterns in cerebral aneurysms and the causal relationship with platelet aggregation K. SHIMANO, T. KUDO, S. YOSHIMOTO, H. UJIIE & Y. ENOMOTO .....	35
Effects of different types of input waveforms in patient-specific right coronary atherosclerosis hemodynamics analysis S.I. BERNAD, E.S. BERNAD, T. BARBAT, V. ALBULESCU & R. SUSAN-RESIGA .....	55
The influence of heart stress on the brain: a preliminary study A.K. MACPHERSON, S. NETI, M. AVERBACH, P.A. MACPHERSON, C. CHUTAKOSITKANON & D. NATHANSON .....	73
Mathematical aspects of the mechanics of left ventricular contraction R.M. SHOUCRI .....	87
Universal features in the laws of growth P.P. DELSANTO, A. GLIOZZI, D. ALEXANDRU IORDACHE & C. GUIOT .....	103
Modeling stent expansion dynamics and blood flow patterns in a stenotic artery M.R. HYRE, R.M. PULLIAM & J.C. SQUIRE .....	115
Blood flow under external strains: phenomenological approach, theoretical development and numerical analysis R. PAULUS, S. ERPICUM, B.J. DEWALS, S. CESCOTTO & M. PIROTON .....	129
Investigation of pulsatile flow in the upper human airways G. EITEL, T. SOODT & W. SCHRÖDER .....	147
An innovative brace with pneumatic thrusts for scoliosis treatment M.G. ANTONELLI, P. BEOMONTE ZOBEL, P. RAIMONDI, T. RAPARELLI & G. COSTANZO .....	167
The human lumbar vertebral body as an intrinsic, functionally optimal structure D.N.GHISTA, S.C.FAN, K.RAMAKRISHNA & I.SRIDHAR .....	181
The optimal structural design of the human spinal intervertebral disc D.N.GHISTA, S.C.FAN, I.SRIDHAR & K.RAMAKRISHNA .....	195

*This page intentionally left blank*

## PREFACE

The idea of preparing this volume originated from the ever increasing importance of computational modelling of complex problems in medicine. Considerable advances have been made in this area as demonstrated by the continued success of the International Conference on Modelling in Medicine and Biology organised by the Wessex Institute of Technology, the first of which was held in Southampton (1991), followed by Bath (1993), Milan (1995), Acquasparta (1997), Ljubljana (2003), Bologna (2005), The New Forest (2007), Crete (2009), and Riga (2011).

The work reported at those meetings and the research carried out at our Institute indicated the increasing interaction and collaboration between medical and engineering scientists. The advances presented at some of our conferences are now being used in practice for a wide range of medical and surgical applications.

The considerable improvements and evolution of the field led me to invite some of the best scientists who have participated in our conferences to write an article on their most recent research. This has led to thirteen outstanding articles published in this volume which encompass important areas of biomedical modelling.

As the Editor of this book I am indebted to all authors for the quality of their contributions and I hope that the reader will find this volume useful.

Carlos A. Brebbia  
Director  
Wessex Institute of Technology  
The New Forest, 2011



*This page intentionally left blank*

# STRESS-STRAIN DISTRIBUTION IN THE HUMAN STOMACH

N.R. AKHMADEEV<sup>1</sup> & R. MIFTAHOV<sup>2</sup>

<sup>1</sup>Kazan Medical University, Kazan, Tatarstan, Russian Federation.

<sup>2</sup>Arabian Gulf University, Kingdom of Bahrain.

## ABSTRACT

A biomechanical model of the human stomach is proposed, that is based on detailed biological data of the structure and function of the organ. The process of electromechanical conjugation and the spread of the electro-mechanical wave along the stomach wall were analyzed numerically. Results revealed patterns of stress-strain distribution in the organ. Thus the fundus, the body and the antrum of the organ always experience biaxial stress-strain states, while the cardia and the pylorus undergo uniaxial loading. The circular smooth muscle layer produced greater total forces throughout in comparison to the outer longitudinal smooth muscle layer. The body of the organ along the *lesser* curvature and the cardia-fundus areas were overstressed compare to other regions. Although the theoretical results resemble qualitatively patterns of electrical and mechanical activity observed *in vivo* and *in vitro* there is currently no affirmative experimental evidence to provide a detailed quantitative comparison of the results.

*Keywords: mathematical model, human stomach, numerical simulations, electromechanical activity, peristalsis*

## 1 INTRODUCTION

High endurance and enormous functionality of abdominal viscera depend on biomechanical properties of the tissues they are made of and specific arrangements of internal constituents. Soft biological tissues, without exception, are regarded as anisotropic heterogeneous incompressible composites that possess nonlinear viscoelastic mechanical characteristics [1, 2]. The distinctive anatomical appearance of organs is strongly influenced by the force systems to which they are subjected and is correlated with their structural advantages. The stomach, the small and large intestines share these properties. For example, the stomach is the organ of the gastrointestinal tract that is located in the left upper quadrant of the abdomen immediately below the diaphragm. Its prime role is to accommodate and digest ingested food. Even at small thickness of the wall, which in normal subjects varies from 3 to 5 mm, and the characteristic radius of the curvature of the middle surface ranging within  $10 \leq R_i \leq 15$  (cm) it is capable of holding 2–5 l of mixed gastric content without significantly increasing intraluminal pressure [3].

Mathematical modeling allows one to gain the insight into hidden physiological mechanisms of function of experimentally inaccessible abdominal viscera [4–10]. However, most of the proposed models are based on a reductionist ‘mechanistic’ approach and, therefore, have a limited biological plausibility. Furthermore, these studies have been hampered by indiscrete and often inappropriate applications of ideas and methods borrowed from the mechanics of shells to describe their biomechanical behavior. It should be emphasized that biomechanics is not just the transformation of general laws and principles of mechanics to the study of biological phenomena, but rather the adequate development and extension of these laws and principles to the modeling and analysis of living things. Integrative models that incorporate multilevel data and serve as the basis for complex analysis of inter-related biological processes at the ion channel, cellular, tissue and organ levels are needed [11, 12]. Such models will have enormous implications for our understanding of the pathophysiology of various diseases and their pharmacological treatment.

The aims of this study are: (i) to formulate a biomechanical model of the human stomach as a thin soft biological shell, and (ii) to study the dynamics of the propagation of electromechanical waves within the organ under normal physiological conditions.

## 2 PHYSIOLOGY OF THE STOMACH

The configuration of the stomach is determined by: (i) the amount of the content, (ii) the stage of the digestive process, (iii) the degree of development of the gastric musculature, and (iv) the condition of the adjacent loops of the small and large intestines. Anatomically, the stomach is concave on its right side, convex on its left. The concave border is called the *lesser* curvature; the convex border, the *greater* curvature. The region that connects the lower esophagus with the upper part of the stomach is called the cardia. The uppermost adjacent part to it is the fundus. The fundus adapts to the varying volume of ingested food and it frequently contains a gas bubble, especially after a meal. The largest part of the stomach is known simply as the body. It functions as a reservoir for ingested food and liquids. The antrum, the lowermost part of the stomach, is usually funnel-shaped, with its narrow end connecting with the pyloric region. The latter empties into the duodenum – the upper division of the small intestine. The pyloric portion of the stomach tends to curve to the right and slightly upward and backward and thus gives the stomach its J-shaped appearance.

Physiological responses of the stomach to internal and external stimuli depend entirely on the inherent activity of histomorphological elements: smooth muscle cells, neurons, interstitial cells of Cajal, and their topographical organization in gastric tissue [13–16]. Longitudinal and circular smooth muscle layers, formed of smooth muscle cells, are embedded into a network of collagenous and elastin fibers and are coupled via gap junctions into three distinct syncytia (muscle layers). The external longitudinal muscle layer continues from the esophagus into the duodenum. The middle uniform circular layer is the strongest and completely covers the stomach. The circular fibers are best developed in the antrum and pylorus. At the pyloric end, the circular muscle layer greatly thickens to form the pyloric sphincter. The innermost oblique muscular layer is limited chiefly to the cardia-fundal regions and progressively weakens as it approaches the pylorus.

The smooth muscle syncytia react with a variety of rhythmical movements which are a result of an electrochemical coupling phenomenon. Electrophysiological and molecular cloning studies have shown that L- and T-type  $\text{Ca}^{2+}$  channels,  $\text{Ca}^{2+}$ -activated  $\text{K}^+$ , selective  $\text{K}^+$ ,  $\text{Na}^+$ , leak  $\text{Cl}^-$ , and nonselective cation channels are responsible for electrical activity of smooth muscle syncytia represented by slow waves and spikes [17–20]. Slow waves are low amplitude, 20–38 mV membrane potential fluctuations, and spikes are high amplitude, 35–45 mV, with action potentials occurring on the crests of slow waves. The role of pacemakers belongs to interstitial cells of Cajal, which are located within the myenteric nervous plexus and smooth muscle syncytia [21–23]. They are coupled to the syncytium via gap junctions. Contractions in the smooth muscle are initiated by myosin light chain phosphorylation via the activation of  $\text{Ca}^{2+}$  calmodulin-dependent myosin light chain-kinase. The key player in the process is free cytoplasmic  $\text{Ca}^{2+}$ . In the resting state, the concentration of intracellular  $\text{Ca}^{2+}$  is  $\approx 0.1 \mu\text{M}$  which upon stimulation rises to high levels as a result of influx through L- and T-type  $\text{Ca}^{2+}$  channels, and induced calcium release from the sarcoplasmic reticulum [24].

Connective tissue elastin and collagen fibers are built in a three dimensional loosely woven network. Elastin may be stretched to 250% of the unloaded configuration. Collagen is relatively inextensible stiff reinforcing structural component, and the main load carrying element. Collagen fibers are usually undulated and they become stiff when straightened under the action of applied loads. The strength of tissues is strongly correlated with the collagen content [1]. The uttermost tunica serosa coats the entire organ and provides its final shape.

The mucous membrane of the stomach consists of epithelial and glandular cells. Their main function is digestion, solute transport, protection and immune response and their role in load distribution is negligible.

Motility signals in the stomach originate in the upper part of the body of the organ. Three types of mechanical waves are observed: (i) small isolated contraction waves, (ii) peristaltic waves that

slowly move from the point of origin down toward the pyloric sphincter, and (iii) nonpropagating waves. Contractions produce slight or deep indentations in the wall and serve as mixing, crushing and pumping mechanisms for the gastric contents [25].

### 3 MECHANICAL PROPERTIES OF THE TISSUE

The soft tissue that makes the wall of the stomach is characterized as transversely anisotropic non-homogenous viscoelastic biocomposite that undergoes finite strains. This has been convincingly demonstrated in quasistatic uniaxial tests on specimens collected from different regions of the organ [26, 27]. The force-ratio of elongation ( $T$ - $\lambda$ ) data indicate that the tissue is initially compliant,  $1.0 < \lambda \leq 1.3$ – $1.4$ , and stiffens at higher loads. For  $1.4 < \lambda \leq 2.0$  the tissue behaves nearly elastically until it breaks at  $T_{\max} = 1.5$  N/cm. Stretching of specimens excised in the directions of the longitudinal, circumferential and oblique layers has shown properties of transverse anisotropy. The wall has lower extensibility along the orientation of longitudinal smooth muscle fibers and the highest along the circumferential layer. Experiments under biaxial tension have shown that the shear force applied to the tissue is significantly less,  $0.01T_{\max}$ , compared with the tangential force [28].

Microscopic analysis of the dynamics of crack nucleation and growth within the wall of the stomach has revealed that first small randomly oriented cracks appear in the submucosal and mucous layers at  $1.0 < \lambda \leq 1.1$  [29]. They align perpendicular to the axis of the stretch force as  $\lambda$  increases. The fracture of entire layers occurs at  $\lambda = 1.3$ – $1.4$  and  $T = 0.1$  N/cm. The most extensible and resistible to loads are the connective tissue network of elastin and collagen fibers, and smooth muscle syncytia. They elongate up to a maximum  $\lambda_{\max} = 2.2$ – $2.5$  and withstand the maximum force of  $T = 1.5$ – $2.0$  N/cm before the complete break.

The complex behavior of the stomach has also been studied under complex loading, i.e. a combined inflation with subsequent external local compression of the anterior surface of the organ [30]. Instantaneous intraluminal pressure, volume and stress-strain recordings indicate that in the low pressure domain  $0.1 \leq P \leq 3.0$  (kPa) the stomach experiences biaxial stress-strain states and smooth continuous deformations in all regions. In the higher pressure range  $3.0 < P \leq 25$  (kPa) creases appear in the cardia-fundal and antrum-pyloric areas.

### 4 MODEL ASSUMPTIONS

A biomechanical model of the stomach is based on the following anatomical, physiological and mechanical assumptions of its appearance and function:

1. The stomach is a closed thin soft shell of complex geometry; it satisfies the criterion of thin shells:  $\max(h/R_i) \leq 1/20$ , where  $h$  is the thickness and  $R_i$  are the radii of the curvature of the middle surface of the shell, and the conditions of softness: the wall of stomach does not resist compression and bending, the shear stresses are negligibly small, and creases may be formed during deformation.
2. The wall of the bioshell (stomach) is formed of two distinct longitudinal and circular smooth muscle layers embedded into a network of elastin and collagen fibers; the layers display an orthogonal type of weaving in the undeformed configuration.
3. The biocomposite is a nonlinear viscoelastic transversely anisotropic continuum undergoing finite strains; its 'passive' component depends on the mechanics of inactive smooth muscle syncytia, collagen and elastin fibers; the 'active' component – the generation of forces of contraction and relaxation, is the result of electromechanical conjugation at the level of intracellular contractile proteins; the key biochemical factor in the process of conjugation is free  $\text{Ca}^{2+}$  ions.
4. Muscle layers are electrically excitable biological media; the membrane potentials are due to the dynamics of  $\text{Ca}^{2+}$ ,  $\text{Na}^+$ ,  $\text{K}^+$  and  $\text{Cl}^-$  channels; the longitudinal smooth muscle layer possesses anisotropic cable electrical characteristics, while the circular layer is electrically isotropic.

5. The initial conditions assume that the stomach is in the resting unexcited state; a single pacemaker or multiple spatially distributed pacemakers are associated with interstitial cells of Cajal; their discharge rates and intensity are assumed to be known *a priori*; they provide excitatory signals to the system.
6. Clamped edge boundary conditions are realized at the cardiac and pyloric ends of the shell throughout simulations.

Let every point of the middle surface of the undeformed stomach be referred to the global Cartesian coordinate system  $x, y, z$ . Assume that the organ is inflated by intraluminal pressure  $p$  and subsequently excited by electrical discharges of the pacemaker cell of a given intensity and duration. As a result of depolarization the electrical waves are produced in the longitudinal and circular smooth muscle syncytia. They propagate along the surface of the organ and generate active forces of contraction-relaxation.

Mathematical formulation of the problem of the dynamics of electromechanical wave activity in the stomach comprises the equations of motion of the thin soft shell, constitutive relations for mechanical and cable electrical properties of the biocomposite, initial and boundary conditions. Thus, the equations of motion of the soft biological shell are given by

$$\begin{aligned}
 \rho_0 \frac{\partial v_x}{\partial t} &= \frac{\partial}{\partial \tilde{s}_1} \left[ \left( k \frac{\partial(\lambda_c - 1)}{\partial t} + T^a(\lambda_c) + T^p(\lambda_c, \lambda_l) \right) e_{1x} \sqrt{a_{22}} \right] \\
 &\quad + \frac{\partial}{\partial \tilde{s}_2} \left[ \left( k \frac{\partial(\lambda_l - 1)}{\partial t} + T^a(\lambda_l) + T^p(\lambda_c, \lambda_l) \right) e_{2x} \sqrt{a_{11}} \right] + p \sqrt{a} n_x, \\
 \rho_0 \frac{\partial v_y}{\partial t} &= \frac{\partial}{\partial \tilde{s}_1} \left[ \left( k \frac{\partial(\lambda_c - 1)}{\partial t} + T^a(\lambda_c) + T^p(\lambda_c, \lambda_l) \right) e_{1y} \sqrt{a_{22}} \right] \\
 &\quad + \frac{\partial}{\partial \tilde{s}_2} \left[ \left( k \frac{\partial(\lambda_l - 1)}{\partial t} + T^a(\lambda_l) + T^p(\lambda_c, \lambda_l) \right) e_{2y} \sqrt{a_{11}} \right] + p \sqrt{a} n_y, \\
 \rho_0 \frac{\partial v_z}{\partial t} &= \frac{\partial}{\partial \tilde{s}_1} \left[ \left( k \frac{\partial(\lambda_c - 1)}{\partial t} + T^a(\lambda_c) + T^p(\lambda_c, \lambda_l) \right) e_{1z} \sqrt{a_{22}} \right] \\
 &\quad + \frac{\partial}{\partial \tilde{s}_2} \left[ \left( k \frac{\partial(\lambda_l - 1)}{\partial t} + T^a(\lambda_l) + T^p(\lambda_c, \lambda_l) \right) e_{2z} \sqrt{a_{11}} \right] + p \sqrt{a} n_z,
 \end{aligned} \tag{1}$$

where  $\tilde{s}_1, \tilde{s}_2$  are the Lagrangian curvilinear orthogonal coordinates and  $t$  is time. The components of the velocity vector  $v_x, v_y$  and  $v_z$  are

$$v_x = \frac{dx}{dt}, \quad v_y = \frac{dy}{dt}, \quad v_z = \frac{dz}{dt}. \tag{2}$$

The rate of elongation (hereafter, the subscripts  $(l)$  and  $(c)$  are referred to the longitudinal and circular muscle layers, respectively), are calculated as

$$\lambda_c = \frac{dx}{d\tilde{s}_1}, \quad \lambda_l = \frac{dy}{d\tilde{s}_2}. \tag{3}$$

The components and the determinant of the metric tensor are defined by

$$\begin{aligned}
 a_{ij} &= \frac{\partial x}{\partial \tilde{s}_i} \frac{\partial x}{\partial \tilde{s}_j} + \frac{\partial y}{\partial \tilde{s}_i} \frac{\partial y}{\partial \tilde{s}_j} + \frac{\partial z}{\partial \tilde{s}_i} \frac{\partial z}{\partial \tilde{s}_j} \\
 a &= a_{11}a_{22} - a_{12}^2 \quad (i = 1, 2)
 \end{aligned} \tag{4}$$

and the cosines of the outward normal  $\bar{n}$  to the surface with respect to the  $x, y, z$  axes are calculated as

$$\begin{aligned}
e_{ix} &= \frac{1}{\sqrt{a_{ii}}} \frac{\partial x}{\partial \tilde{s}_i}, & e_{iy} &= \frac{1}{\sqrt{a_{ii}}} \frac{\partial y}{\partial \tilde{s}_i}, & e_{iz} &= \frac{1}{\sqrt{a_{ii}}} \frac{\partial z}{\partial \tilde{s}_i}, \\
\bar{n}_x &= (e_{1y}e_{2y} - e_{1z}e_{2z})\sqrt{a_{11}a_{22}}/\sqrt{a}, \\
\bar{n}_y &= (e_{1z}e_{2x} - e_{1x}e_{2z})\sqrt{a_{11}a_{22}}/\sqrt{a}, \\
\bar{n}_z &= (e_{1x}e_{2y} - e_{1y}e_{2x})\sqrt{a_{11}a_{22}}/\sqrt{a}.
\end{aligned} \tag{5}$$

The passive  $T_{c,l}^p$  and active  $T_{c,l}^a$  forces of the total membrane force are given by

$$T_{c,l}^p = \frac{\partial \rho_0 W}{\partial (\lambda_{c,l} - 1)}, \tag{6}$$

$$T_{c,l}^a = \begin{cases} 0, & [\text{Ca}^{2+}] \leq 0.1 \mu\text{M} \\ c_7 + c_8[\text{Ca}^{2+}]^4 + c_9[\text{Ca}^{2+}]^3 + c_{10}[\text{Ca}^{2+}]^2 + c_{11}[\text{Ca}^{2+}], & 0.1 < [\text{Ca}^{2+}] \leq 1 \mu\text{M} \\ \max T^a, & [\text{Ca}^{2+}] > 1 \mu\text{M} \end{cases} \tag{7}$$

where  $W$  is the strain energy density function of the connective tissue network and passive muscle tissue

$$\begin{aligned}
\rho_0 W &= \frac{1}{2} [c_1(\lambda_l - 1)^2 + 2c_3(\lambda_l - 1)(\lambda_c - 1) + c_2(\lambda_c - 1)^2 \\
&\quad + c_{14} \exp(c_4(\lambda_l - 1)^2 + c_5(\lambda_c - 1)^2 + 2c_6(\lambda_l - 1)(\lambda_c - 1))]
\end{aligned}$$

Here  $c_{1-11}$  are empirically defined mechanical constants, and  $[\text{Ca}^{2+}]$  is the concentration of free intracellular calcium.

The characteristic feature of thin soft shells is the possibility of the simultaneous coexistence of smooth (biaxially stress) and wrinkled (uniaxially stress) zones. The smooth surface is characterized by  $\lambda_{l,c} > 1.0$  ( $T_{l,c} > 0$ ); in a case of the development of wrinkles, either  $\lambda_l \leq 1.0$ ,  $\lambda_c \leq 1.0$  ( $T_l = 0$ ,  $T_c > 0$ ), or  $\lambda_c \leq 1.0$ ,  $\lambda_l > 1.0$  ( $T_l > 0$ ,  $T_c = 0$ ). The wrinkled zone is substituted by an ironed out zone made of a set of unbound muscle and connective tissue fibers aligned with the direction of positive tensile stress. This is determined by general requirements of the conservation of smoothness of the surface and the continuity of membrane forces of the shell. Thus, if creases appear then the shell is subjected to the uniaxial stress-strained state. Therefore, for  $T_{c,l}^p$  we have

$$T_{c,l}^p = \begin{cases} 0, & \lambda_{c,l} \leq 1, \\ c_{12}[\exp(c_{13}(\lambda_{c,l} - 1) - 1)], & \lambda_{c,l} > 1. \end{cases} \tag{8}$$

Changes in the free cytosolic calcium concentration yield

$$d[\text{Ca}^{2+}]/dt = 0.2z(\varphi_{\text{Ca}} - \varphi_{c,l})/(1 + \zeta[\text{Ca}^{2+}]) - 0.3[\text{Ca}^{2+}] \tag{9}$$

Here  $\varphi_{\text{Ca}}$  is the reversal potential for the calcium ion current;  $\zeta$  is the parameter of inhibition of the  $\text{Ca}^{2+}$  channels;  $z$  is the dynamic variable of the ionic channels whose kinetics is given by

$$\frac{dz}{dt} = \left( \frac{1}{1 + \exp(-0.15(\varphi_{c,l} + 42))} - z \right) / \tau_z, \tag{10}$$

$\tau_z$  is the time constant.

The dynamics of the propagation of the electrical wave,  $\varphi_l$ , along the anisotropic longitudinal muscle layer is given by

$$C_m \frac{\partial \varphi_l}{\partial t} = I_{m1}(\tilde{s}_1, \tilde{s}_2) + I_{m2}(\tilde{s}_1 - \tilde{s}'_1, \tilde{s}_2 - \tilde{s}'_2) + I_{\text{ionic}}^*, \quad (11)$$

where  $I_{m1}$ ,  $I_{m2}$  are the transmembrane currents

$$\begin{aligned} I_{m1}(\tilde{s}_1, \tilde{s}_2) &= M_{\text{vs}} \left\{ -\frac{2(\mu_{\tilde{s}_1} - \mu_{\tilde{s}_2})}{(1 + \mu_{\tilde{s}_1})(1 + \mu_{\tilde{s}_2})} \arctan \left( \frac{d\tilde{s}_1}{d\tilde{s}_2} \sqrt{\frac{G_{\tilde{s}_2}}{G_{\tilde{s}_1}}} \right) + \frac{g_{0,\tilde{s}_2}^*}{G_{\tilde{s}_1}} \right\} \\ &\quad \times \left( \frac{\partial}{\partial \tilde{s}_1} \left( \frac{g_{0,\tilde{s}_1}^*}{\lambda_c} \frac{\partial \varphi_l}{\partial \tilde{s}_1} \right) + \frac{\partial}{\partial \tilde{s}_2} \left( \frac{g_{0,\tilde{s}_2}^*}{\lambda_q} \frac{\partial \varphi_l}{\partial \tilde{s}_2} \right) \right), \\ I_{m2}(\tilde{s}_1, \tilde{s}_2) &= M_{\text{vs}} \iint_S \frac{\mu_{\tilde{s}_1} - \mu_{\tilde{s}_2}}{2\pi(1 + \mu_{\tilde{s}_1})(1 + \mu_{\tilde{s}_2})} \frac{(\tilde{s}_2 - \tilde{s}'_2)/G_{\tilde{s}_2} - (\tilde{s}_1 - \tilde{s}'_1)/G_{\tilde{s}_1}}{[(\tilde{s}_1 - \tilde{s}'_1)/G_{\tilde{s}_1} - (\tilde{s}_2 - \tilde{s}'_2)/G_{\tilde{s}_2}]^2} \\ &\quad \times \left( \frac{\partial}{\partial \tilde{s}_1} \left( \frac{g_{0,\tilde{s}_1}^*}{\lambda_c} \frac{\partial \varphi_l}{\partial \tilde{s}_1} \right) + \frac{\partial}{\partial \tilde{s}_2} \left( \frac{g_{0,\tilde{s}_2}^*}{\lambda_q} \frac{\partial \varphi_l}{\partial \tilde{s}_2} \right) \right) d\tilde{s}'_1 d\tilde{s}'_2, \\ \mu_{\tilde{s}_1} &= g_{0,\tilde{s}_1}^* / g_{i,\tilde{s}_1}^*, \quad \mu_{\tilde{s}_2} = g_{0,\tilde{s}_2}^* / g_{i,\tilde{s}_2}^*, \\ G_{\tilde{s}_1} &= \frac{g_{0,\tilde{s}_1}^* + g_{i,\tilde{s}_1}^*}{\lambda_c}, \quad G_{\tilde{s}_2} = \frac{g_{0,\tilde{s}_2}^* + g_{i,\tilde{s}_2}^*}{\lambda_q}, \quad G = \sqrt{G_{\tilde{s}_1} G_{\tilde{s}_2}} \end{aligned} \quad (12)$$

Here  $C_m$  is the capacitance of smooth muscle;  $g_{i,\tilde{s}_1}^*$ ,  $g_{i,\tilde{s}_2}^*$ ,  $g_{0,\tilde{s}_1}^*$ ,  $g_{0,\tilde{s}_2}^*$  are the maximal intracellular (*i*) and interstitial space (0) conductivities of the longitudinal and circular muscle layers;  $M_{\text{vs}}$  is the membrane volume-to-surface ratio. The total ion current,  $I_{\text{ionic}}^*$ , is defined as

$$I_{\text{ionic}}^* = \bar{g}_{\text{Na}} m^{*3} h^* (\varphi_{(c,l)} - \bar{\varphi}_{\text{Na}}) + \bar{g}_{\text{K}} n^{*4} (\varphi_{(c,l)} - \bar{\varphi}_{\text{K}}) + \bar{g}_{\theta} (\varphi_{(c,l)} - \bar{\varphi}_{\theta}), \quad (13)$$

where  $\bar{g}_{\text{Na}}$ ,  $\bar{g}_{\text{K}}$ ,  $\bar{g}_{\theta}$  are the maximal conductances and  $\bar{\varphi}_{\text{Na}}$ ,  $\bar{\varphi}_{\text{K}}$ ,  $\bar{\varphi}_{\theta}$  are the reversal potentials of  $\text{Na}^+$ ,  $\text{K}^+$ , and  $\text{Cl}^-$  currents. The dynamics of change in the probability variables  $m^*$ ,  $h^*$ , and  $n^*$  of opening of the ion gates are obtained from the solution of the first-order equation

$$\frac{d\eta}{dt} = a_{\eta}^* (1 - \eta) - \beta_{\eta}^* \eta, \quad (\eta = m^*, h^*, n^*)$$

The activation,  $a_{\eta}^*$ , and deactivation,  $\beta_{\eta}^*$ , parameters satisfy the empirical relations

$$\begin{aligned} a_m^* &= 0.005(\varphi_{(c,l)} - \bar{\varphi}_m) / [\exp 0.1(\varphi_{(c,l)} - \bar{\varphi}_m) - 1], \\ \beta_m^* &= 0.2 \exp(\varphi_{(c,l)} + \bar{\varphi}_m) / 38, \\ a_h^* &= 0.014 \exp[-(\bar{\varphi}_h + \varphi_{(c,l)}) / 20], \\ \beta_h^* &= 0.2 / [1 + \exp 0.2(\bar{\varphi}_h - \varphi_{(c,l)})], \\ a_n^* &= 0.006(\varphi_{(c,l)} - \bar{\varphi}_n) / [\exp 0.1(\varphi_{(c,l)} - \bar{\varphi}_n) - 1], \\ \beta_n^* &= 0.75 \exp(\bar{\varphi}_n - \varphi_{(c,l)}). \end{aligned} \quad (14)$$

The dynamics of the propagation of the electrical wave,  $\varphi_c$ , along the isotropic circular smooth muscle syncytium is given by

$$C_m \frac{\partial \varphi_c}{\partial t} = \frac{M_{\text{vs}}}{1 + \mu_{\tilde{s}_1}} \left\{ \frac{\partial}{\partial \tilde{s}_1} \left( \frac{g_{0,\tilde{s}_1}^*}{\lambda_c} \frac{\partial \varphi_c}{\partial \tilde{s}_1} \right) + \frac{\partial}{\partial \tilde{s}_2} \left( \frac{g_{0,\tilde{s}_1}^*}{\lambda_q} \frac{\partial \varphi_c}{\partial \tilde{s}_2} \right) \right\} - I_{\text{ionic}}^*, \quad (15)$$

where the above-mentioned abbreviations and relationships for  $I_{\text{ionic}}^*$ , eqns (11–13), are used.

The gastric pressure,  $p$ , changes according to the adiabatic law

$$p = p_0 \Delta V^{1.41}, \quad (16)$$

where  $p_0$  is the meaning of  $p$  at  $t = 0$ ;  $\Delta V = V_0/V$  is the ratio of a current intraluminal volume,  $V$ , to its initial value,  $V_0$ .

The cardiac and pyloric ends of the organ are clamped

$$t > 0: x(\tilde{s}_1, \tilde{s}_2) = y(\tilde{s}_1, \tilde{s}_2) = z(\tilde{s}_1, \tilde{s}_2) = 0. \quad (17)$$

The initial conditions assume that the stomach is in the resting state

$$t = 0: v_r = v_s = v_z = 0; \varphi_l = \varphi_c = 0. \quad (18)$$

Excitation to the system is provided by electrical discharges of the pacemaker cell that are modeled as an input impulse of a given amplitude,  $\varphi_0$ , and duration  $t_d$

$$\begin{aligned} \varphi_l(\tilde{s}_1, \tilde{s}_2) &= \begin{cases} \varphi_0, & 0 < t \leq t_d \\ 0, & t > t_d, \end{cases} \\ \varphi_c(\tilde{s}_1, \tilde{s}_2) &= \begin{cases} \varphi_0, & t_i < t \leq t_d + t_i \\ 0, & t > t_d + t_i, \end{cases} \end{aligned} \quad (19)$$

where  $t_i$  ( $t_i \geq 0$ ) is the time interval between discharges on the longitudinal and circular smooth muscle layers.

The combined nonlinear system of partial and ordinary differential equations was solved numerically. Hybrid finite difference and finite element methods of second-order accuracy, with respect to spatial and time variables, were employed. The numerical algorithm was implemented in the *ABS Technologies*® computational platform. The accuracy of the algorithm and robustness of the platform have been evaluated extensively through multiple numerical experiments (different levels of discretization and time steps of integration, etc.) and the variation of parameters and constants of the model.

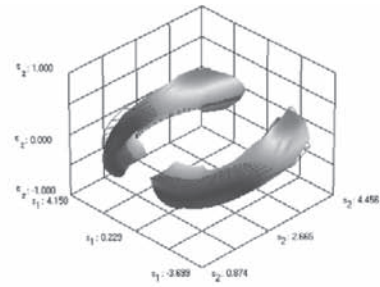
## 5 RESULTS OF SIMULATIONS

### 5.1 Inflated stomach

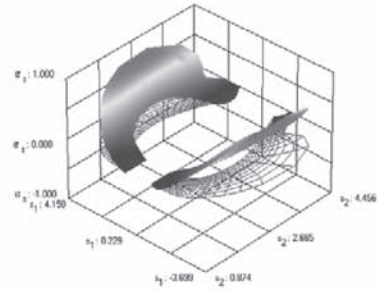
Consider a soft biological shell in the state of dynamic equilibrium. It is supported by intraluminal pressure  $p = 20$  kPa. The strain distribution in the wall of the bioshell is shown in Fig. 1. The maximal elongation of the longitudinal muscle fibers,  $\lambda_l = 1.35$ , is observed in the cardio-fundal region along the *greater* curvature of the organ. A part of the fundus bordering the body experiences the maximal biaxial extension with  $\lambda_l = 1.35$ ,  $\lambda_c = 1.04$  in that area. The cardia and the body of the stomach along the *lesser* curvature, both undergo biaxial deformation with  $\lambda_l = 1.01$ ,  $\lambda_c = 1.24$ , while the antrum-pyloric region along the *greater* curvature is under uniaxial strain,  $\lambda_l = 0.5$ ,  $\lambda_c = 1.16$ . Negative circumferential deformations are registered in the cardia and the pylorus. Thus, the fundus and the body of the organ undergo biaxial distension and the cardia and antrum-pyloric areas are subjects to uniaxial elongation.

Analysis of the total force distribution in the bioshell demonstrates that  $\max T_l = 9.3$  mN/cm,  $T_c = 14.5$  mN/cm are recorded in the fundus and the body. The maximum  $T_c = 34.7$  mN/cm is registered in a small area of the body along the *lesser* curvature of the stomach. In the antrum and the lower cardia, total forces of average intensity  $T_l = 4.1$  mN/cm,  $T_c = 14.5$  mN/cm are observed. Again, in the pylorus and the cardia the total force in the circumferential direction equals zero, while in the longitudinal direction,  $T_l = 3.0$  mN/cm. The proximal part of the cardia remains unstressed with  $T_l = T_c = 0$ .

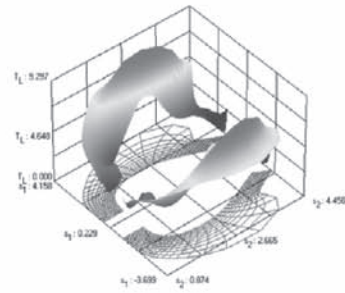




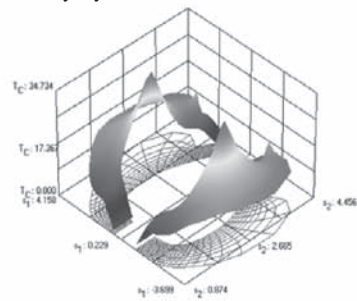
Longitudinal deformation



Circumferential deformation



Total force in the longitudinal syncytium



Total force in the circumferential syncytium

Figure 1: Static distribution of deformations and total forces in the longitudinal and circumferential smooth muscle syncytia of the inflated human stomach. Hereafter, results of simulations are presented on the entire stomach and the open surface envelope, respectively.

## 5.2 Electromechanical wave activity

Consider a case of two identical pacemaker cells located on the longitudinal and circular smooth muscle layers in the upper body along the greater curvature of the stomach. Let the cells discharge simultaneously multiple impulses ( $n = 5$ ) of amplitude  $\varphi_0 = 100$  mV and duration  $t_d = 0.1$  s. The activation of ion channels on the membrane of muscle causes the generation of the waves of depolarization of amplitude  $\varphi_{(l,c)} = 65\text{--}70$  mV (Fig. 2). The velocity of the propagation of excitation varies between the syncytia and regions of the organ. Thus the wave  $\varphi_l$  quickly spreads within the longitudinal muscle fibers to encase a narrow zone within the anterior surface of the organ ( $t = 0.8$  s). The wave  $\varphi_l$  sustains short wave-length and a constant amplitude 18 mV throughout  $2.0 < t < 5.6$  s. The high level of depolarization is observed in the pyloric region where  $\varphi_l = 25.2$  mV is registered.

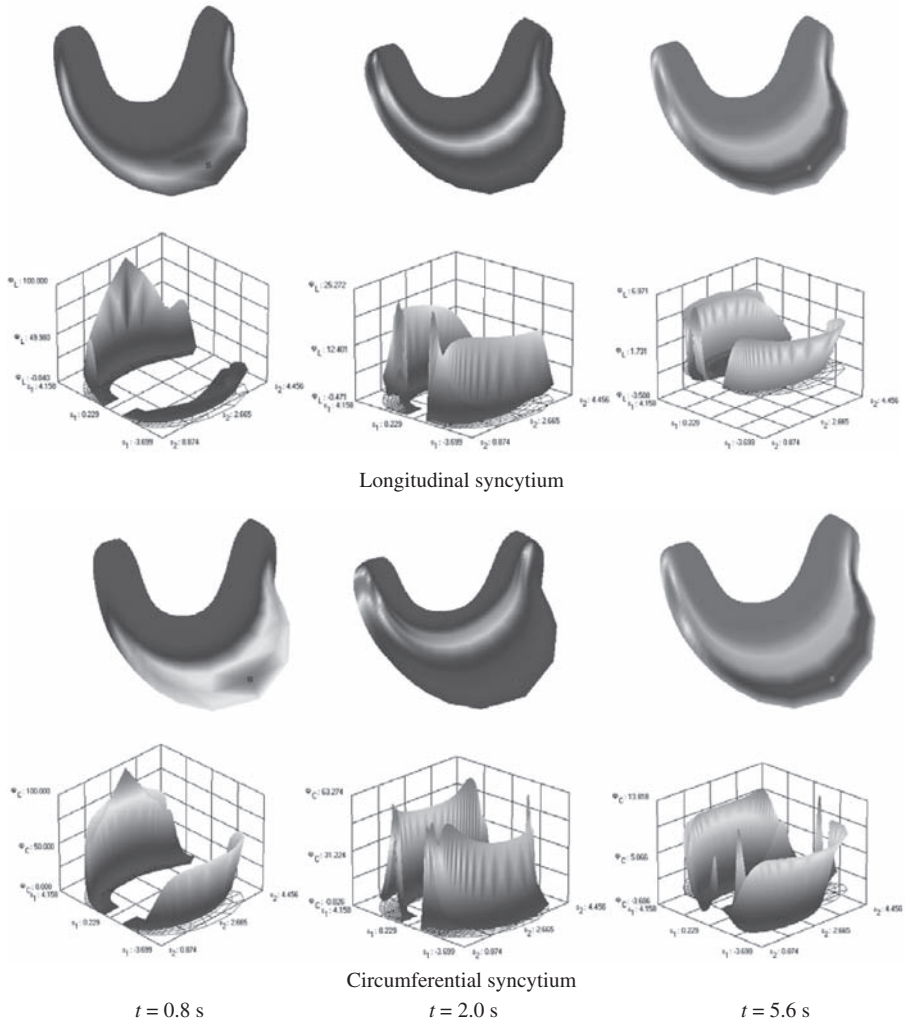


Figure 2: Dynamics of the propagation of the electrical wave of depolarization within different layers of the human stomach wall as a response to high frequency discharges of the pacemaker cell located in the body of the organ along its *greater* curvature.

The propagation of the wave  $\varphi_c$  within the isotropic circular smooth muscle layer is faster compared to  $\varphi_l$ . Thus, at  $t = 0.8$  s nearly a half of the anterior and posterior surfaces of the bioshell undergo even depolarization,  $60 < \varphi_c < 66.5$  (mV). The excitation quickly extends towards the lesser curvature. The cardiac and pyloric regions experience extensive depolarization with a max  $\varphi_c = 63.3$  mV. At  $t = 5.6$  s the longitudinal and circular smooth muscle syncytia of the stomach show a similar pattern in the distribution of depolarization with the average amplitude  $\varphi_l \approx 3.7$  mV,  $\varphi_c \approx 7.5$  mV.

The excitation of voltage-dependent calcium channels on the membrane of smooth muscle syncytia results in a rapid influx of  $\text{Ca}^{2+}$  ions and rise in the free cytosolic  $\text{Ca}^{2+}$  concentration to  $0.48 \mu\text{M}$ . The above lead to the activation of contractile proteins and the generation of active forces of contraction. There is a smooth distribution of active forces of contraction in the fundus and the body of the stomach where  $T_l^a = 6.1$  mN/cm and  $T_c^a = 7.4$  mN/cm are generated during  $0 < t \leq 5.0$  s (Fig. 3). The cardia and the antrum-pyloric regions generate less intense forces,  $T_l^a = 3.0\text{--}3.6$  mN/cm and  $T_c^a = 3.7\text{--}4.4$  mN/cm. At  $t = 5.6$  s of the dynamic process the redistribution in stresses occurs with the high level of contraction, max  $T_l^a = 7.9$  mN/cm, seen in the body of the organ. There is a concentration in active force development in the circular smooth muscle layer in the body along its lesser curvature with max  $T_c^a = 10.5$  mN/cm. The rest of the fundus and the body experience even contractions,  $T_l^a = 6.9$ ,  $T_c^a = 8.4$  (mN/cm).

At  $t = 5.6$  s the earlier existing zone of uniaxial stretching and wrinkling in the antrum-pyloric regions along the greater curvature has expanded to the lower part of the body. Sustained unidirectional longitudinal elongations persist in the cardia. However, a new zone of uniaxial stretch oriented along the longitudinal axis is generated along the lesser curvature of the bioshell.

The pattern of total force distribution is similar to that observed at the state of dynamic equilibrium. There is an increase in the intensity of forces, which is consistent with the generation of active forces of contraction by the syncytia (Fig. 3). Thus, max  $T_l = 15.1$  mN/cm,  $T_c = 22.4$  mN/cm are seen in the body, and  $T_l = 2.7$  mN/cm,  $T_c = 5.3$  mN/cm in the cardia and the pylorus of the stomach.

### 5.3 Time lag in firing of pacemakers

Consider the effect of time delay ( $t_i$ ) in discharges of pacemaker cells on the dynamics of the force – elongation development in the bioshell. The number of impulses, their amplitude and duration correspond to the experimental conditions as described above. The pacemaker located in the longitudinal muscle syncytium fires first, followed by a discharge of the pacemaker on the circular muscle syncytium at  $t_i = 0.75$  s.

Results of simulations show that there are no significant differences in the intensity of force development. However, the delay in activation of the circular smooth muscle layer results in early wrinkling ( $t = 0.8$  s) in the body along the lesser curvature which persists throughout. The delayed generation of contractions in the circular smooth layer results in a reciprocal contraction-relaxation relation between the two bisyncytia. The pattern of electromechanical activity resembles peristalsis, i.e. a propagating wave of contraction–relaxation that satisfies the condition of reciprocity (Fig. 4).

### 5.4 Multiple pacemakers

Consider three identical pacemaker cells spatially distributed along the anterior wall of the bioshell. The leading pacemaker is located in the upper part of the body, and the other two are positioned in the antrum and the pyloric regions of the stomach, respectively. The cells discharge impulses of amplitude  $\varphi_0 = 100$  mV and duration  $t_d = 0.1$  s. The time lag between the beginning of discharges of pacemakers is constant,  $t_i = 0.75$  s.

Results of simulations demonstrate that at  $t = 1.2$  s the entire organ undergoes higher levels of uniform depolarization,  $\varphi_l \approx \varphi_c \approx 55$  mV (Fig. 5). This pattern of excitation persists till  $t = 7$  s.

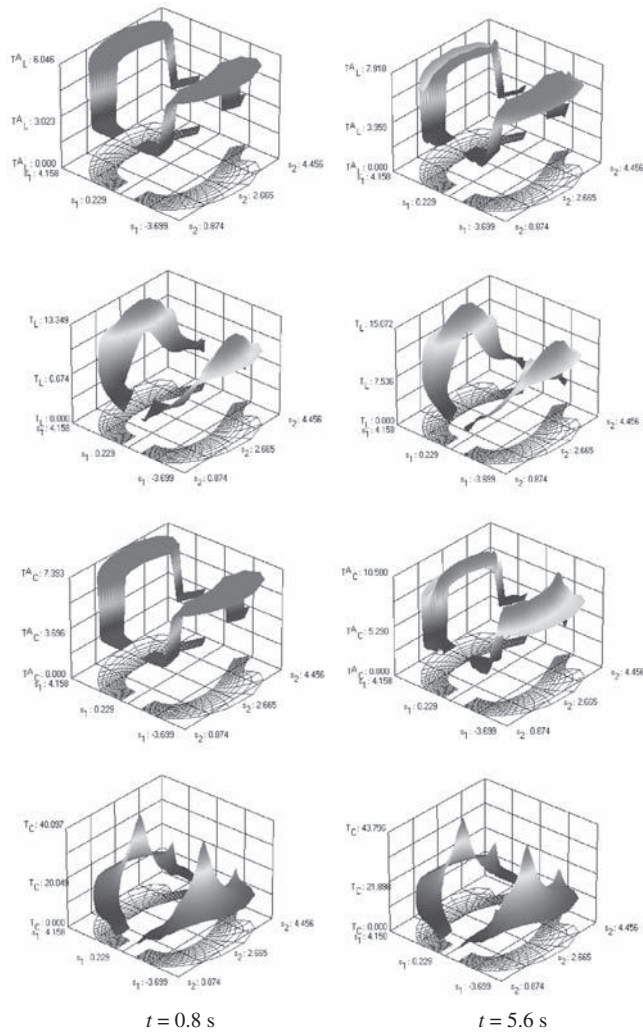


Figure 3: Development of active and total forces in the stomach as a result of the electromechanical coupling process in the myogenic syncytia.

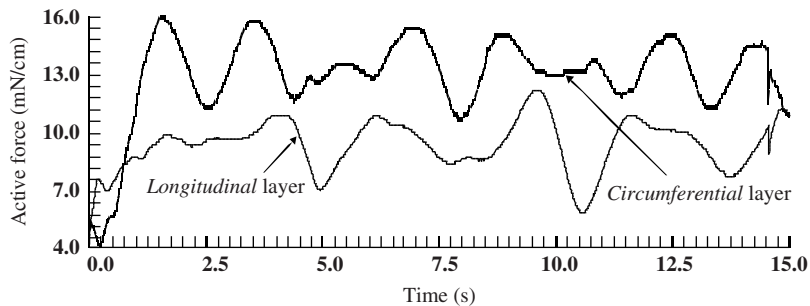


Figure 4: Changes in the active force dynamics in the longitudinal and circumferential smooth muscle layers at a “control” point in the body of the anterior surface of the human stomach.

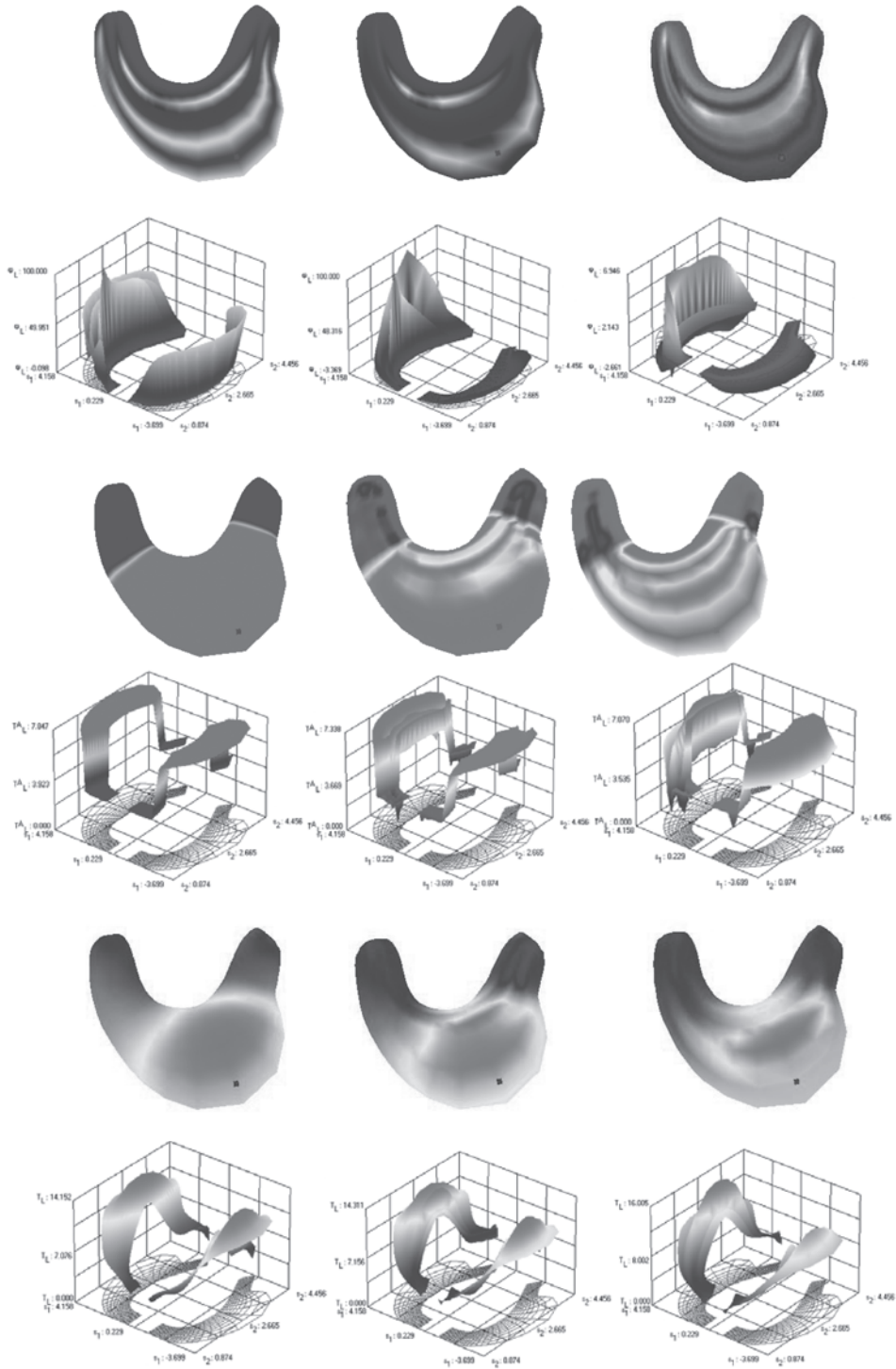


Figure 5: Dynamics of electromechanical responses of the soft biological shell – the human stomach, to high frequency stimulation by multiple pacemakers located in different regions of the organ.

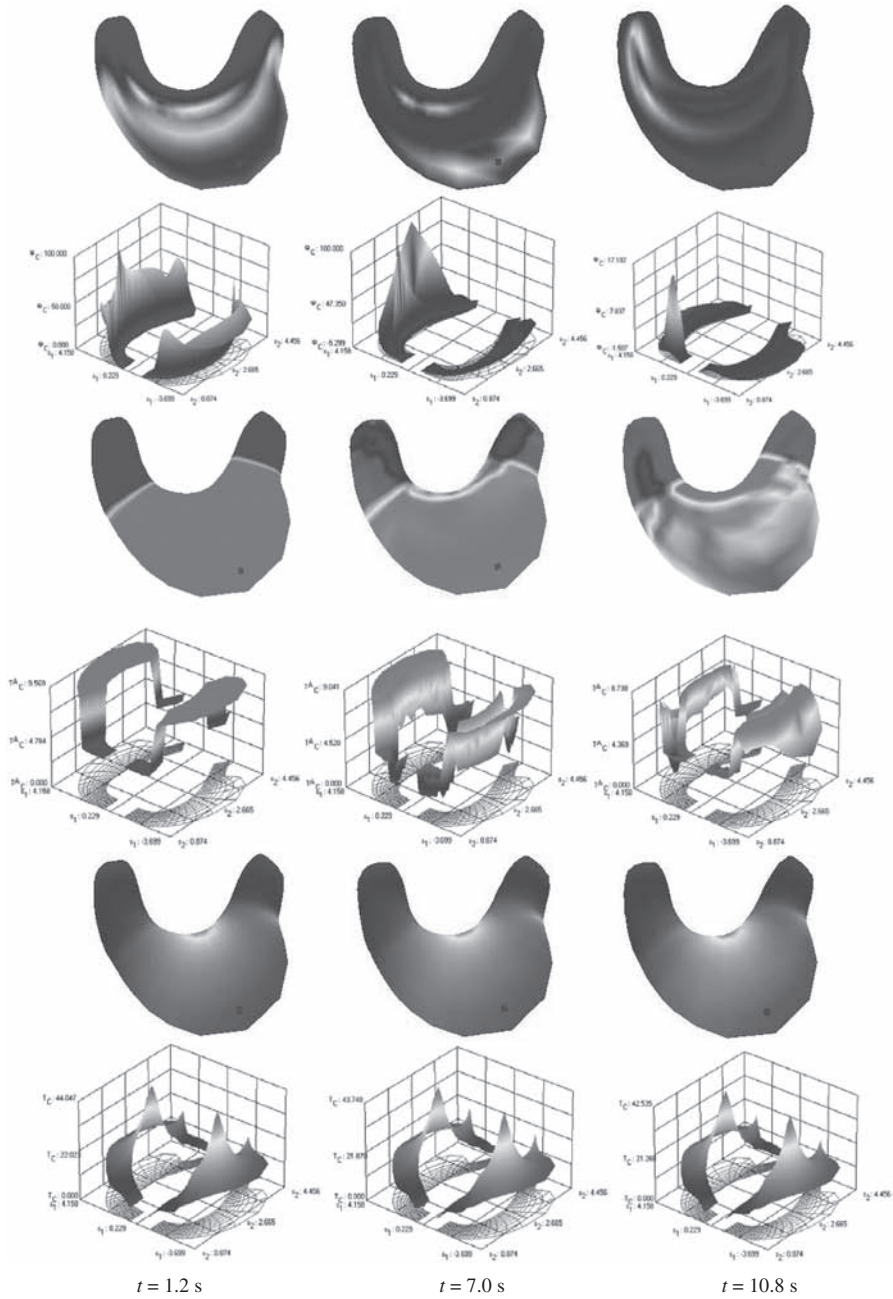


Figure 5: (continued)

For  $t = 10.8$  s the longitudinal smooth muscle layer of the anterior wall of the stomach in the projection of the body, antrum and pylorus remains excited,  $\phi_l \approx 6.8$  mV, while the circumferential layer experiences hyperpolarization  $\phi_c \approx -1.2$  mV. There is an area of high depolarization in the pyloric region where  $\phi_c \approx 17.1$  mV is recorded.



In the time interval  $1.2 \leq t \leq 7$  (s) the longitudinal and circumferential smooth muscle layers of the fundus, body and antrum generate smooth forces of contraction,  $T_l = 7.4$  mN/cm,  $T_c = 9.2$  mN/cm. Suffice it to note, that at the beginning of the process,  $t = 1.2$  s, the entire organ is stress-strained biaxially. At  $t = 7$  s the creases oriented longitudinally occur in the cardia and pyloric regions along the lesser curvature. With the redistribution of active forces,  $T_c$ , within the circular syncytium,  $t > 10$  s, they disappear. The most intense contractions are registered in the body at the *lesser* curvature,  $\max T_l = 7$ ,  $\max T_c = 8.7$  (mN/cm).

The involvement of the connective tissue network in the dynamics of load distribution provides 'smooth' deformation in all regions of the stomach and prevents the occurrence of gradients in  $T_{(c,l)}(\tilde{s}_1, \tilde{s}_2, t)$ . Thus, the bioshell passes through various stress-strain states without developing overstressed zones (Fig. 5). There is a persistent small area in the body along the *lesser* curvature where a  $\max T_c = 44$  mN/cm is registered. Other anatomical regions experience even biaxial stress states of average intensities:  $T_l = T_c = 2-3$  mN/cm in the cardia,  $T_l = 6.5$ ,  $T_c = 9.4$  (mN/cm) in the fundus,  $T_l = 10$ ,  $T_c = 15$  (mN/cm) in the body, and  $T_l = 5$ ,  $T_c = 9$  (mN/cm) in the antrum-pylorus.

## 6 DISCUSSION

The main hurdle that every computational modeler faces during the development of a biomechanical model of a living object is the paucity of reliable information about mechanical characteristics of biological tissues. Until now, there have been only a few correctly planned and executed experimental studies that are dedicated to the analysis of the human stomach from the quantitative mechanical perspective. The first uniaxial and biaxial tensile tests on tissue samples collected from various regions of the organ including the cardia, the fundus, the body, the antrum and the pylorus, were reported by Miftakhov [26–30]. The specimens were excised along two mutually orthogonal directions – longitudinal and circumferential, to study the axes of anisotropy. Results of investigations revealed that: (1) the wall of the stomach, like other soft tissues, exhibits nonlinear transversely anisotropic mechanical properties; (2) it undergoes large deformations  $\approx 160-180\%$ ; (3) there are regional and wall differences in mechanical properties, e.g. the anterior wall is more elastic and stretchable compared to the posterior wall; (4) there is stiffening of the biocomposite related to age changes. The experimentally obtained data on force-ratio of elongation served as a basis for the construction of phenomenological constitutive relations (3), (4), (8). They successfully described and offered robust estimates of the mechanical behavior of the stomach. Recent studies by different research groups performed on cadaveric, surgically removed human stomachs and healthy volunteers confirmed nonlinear anisotropic mechanical properties of the tissue and their regional dependence [31].

Miftakhov [32] was the first to formulate a biomechanical model of the organ as a soft multilayer biocomposite shell. Under general assumptions of curvilinear orthotropy, physical and geometrical nonlinearity, numerical and experimental investigations of the dynamics of stress-strain distribution in the organ under simple and complex loadings were performed. The dynamics of the development of uniaxial stress-strained states in the cardia and pylorus as a function of intraluminal pressure was demonstrated computationally and supported experimentally. Results offered a valuable insight into the mechanism of blunt abdominal trauma with rupture of the anterior wall of the stomach and gave a biomechanical explanation for the Mallory-Weiss syndrome. It was thought previously that atrophic changes in the gastric mucosa and submucous layer were responsible for longitudinal tears in the cardia-fundal region and life threatening intragastric bleeding. The model study proved that the anatomical structure and configuration of the stomach per se makes these regions more susceptible, than the others, to linear submucous breaks and ruptures.

The presented model is an extension of the previous model. It incorporates myoelectrical properties of the longitudinal and circular smooth muscle syncytia along with mechanical nonlinearity of the wall of the stomach. Special emphasis in the study was given to the questions of electromechanical coupling in smooth muscle syncytia and cable electromechanical wave activity.

Gastric motility is a result of electromechanical coupling that occurs at the cellular level and is manifested in the form of electromechanical wave activity within the organ wall. In the current study we restricted our attention to the cable, rather than to more general oscillatory, properties of smooth muscle syncytia. The network of interstitial cells of Cajal – pacemakers of gastric motility, was substituted by a single cell or a set of spatially distributed cells. They discharged *a priori* known electrical impulses. Even with these constructive simplifications, the model reproduced and predicted: (1) patterns of the propagation of the wave of excitation within the electrically anisotropic longitudinal and electrically isotropic circular smooth muscle syncytia; (2) small isolated contraction waves in the two smooth muscle syncytia and nonpropagating tonic simultaneous contractions of both muscle layers superimposed on small contractions; (3) the development of wrinkles in the cardia, the body along the lesser curvature and the pylorus, and (4) high levels of tension in the body of the stomach along the lesser curvature.

A note of caution though should be made at this point of discussion. Care should be taken in transferring the results of simulations to explain real biomechanics of the human stomach. One has to bear in mind that the biological plausibility of the model is constrained by the model assumptions, despite the fact that the theoretical results resemble qualitatively patterns of electrical and mechanical activity that are observed in mainly animal studies *in vivo* and *in vitro*. At the moment there is no direct affirmative experimental evidence obtained on human subjects to run a detailed quantitative evaluation and comparison of the computational data.

Unfortunately, it is still a common practice in the community of modelers to employ the system of Navier–Stokes equations when modeling the stomach as a ‘shell’ structure. Using commercially available software and highly flexible graphical tools they manage to fit results of numerical simulations to experimental data. The approach is utterly incorrect and results bring confusion, rather than provide solutions, to urgent clinical problems related to gastric function. Thus, it is erroneous to claim the dominant role of antral contraction wave activity on gastric fluid motions, based on the results of computer simulations of a flow caused by prescribed indentations of the surface boundaries [9, 10]. The latter is supposed to represent a two dimensional model of the stomach. And it is not surprising that the numerical method, that predetermines the desired patterns of flow, produced the results that resembled those observed in magnetic resonance imaging studies. An adequate mathematical model of the above phenomenon should have comprised of the combined system of the equations of motion of the bioshell – the stomach, and Navier–Stokes equations to model gastric content – thick semi-fluid mass of partly digested food and secretions (chyme). Suffice it to note, that until now no attempts have been made to describe the chyme as a chemically reactive medium. Also, in view of the fundamental mechanical property of the tissue, its softness, it is unwise to argue the dependence of tension-strain properties on the radii of curvature of the stomach [33]. It is the responsibility of an applied mathematician, a computer scientist, and a mechanical engineer to suggest an adequate descriptor and to give a rigorous mathematical formulation of the model.

Although the proposed model of the human stomach as a soft biological shell has a very limited biomedical value, at the moment, it is mathematically sound and is based on the accurate extension of general laws and hypotheses of the mechanics of thin soft shells. It incorporates electrophysiological and morphological data of the structure and function of the organ and reproduces quantitatively and qualitatively the dynamics of electromechanical wave activity and stress-strain distribution in it. It can serve as a starting point for further expansions and biological improvements.



## 7 FUTURE DIRECTIONS

As an example of further model improvements and development consider the following biologically plausible modifications.

### 7.1 Oscillatory myoelectrical activity

Incorporation of oscillatory myoelectrical phenomenon will complete the model of electromechanical conjugation with the generation and propagation of electromechanical waves in the stomach. The model description should be based on: (1) the Hodgkin-Huxley formalism in mathematical modeling of the dynamics of L- and T-type  $\text{Ca}^{2+}$  channels,  $\text{Ca}^{2+}$ -activated  $\text{K}^+$ , selective  $\text{K}^+$ ,  $\text{Na}^+$ , leak  $\text{Cl}^-$ , and nonselective cation channels, and (2) the concept of spatially distributed weakly connected oscillators. We should point up the use of Hodgkin-Huxley equations in the model that will become essential in future investigations of the effects of pharmacological compounds on gastric motility.

### 7.2 Neuronal networks and pacemaker activity

The myenteric and submucous nervous plexi are contained within the wall of the stomach and constitute only the first level in the hierarchy of neuronal systems that regulate gastric functions. The plexi are formed of multiple ganglia of the primary sensory, inter- and motor neurons, arranged in a planar neuronal network. Recent research has suggested another intrinsic network of interstitial cells of Cajal provides a modulatory signaling to the plexi. We possess ample experimental data on histomorphology, electrophysiology and neuropharmacology of neurons and cell of Cajal to construct a detailed mathematical model of the intrinsic regulatory neuronal network.

### 7.3 Electrochemical coupling and neurotransmitters

Neurons form chemical synapses within plexi. Immunohistochemical and radiolabeling studies revealed that neurons store and can release more than one neurotransmitter substance at a nerve terminal. The neurotransmitters may interact at many levels of their synthesis, storage, release, degradation and postsynaptic actions. Particular combinations of such substances correlate with specific functional classes of nerves. Mathematical modeling of the electrochemical coupling phenomenon – the process of transformation of chemical signals into electrical signals, is necessary for the full investigation of the effects of neurotransmitter co-localization for synaptic transmission. It will have enormous impact on the ability of the model to simulate and to predict the effects of different classes of drugs on gastric function.

### 7.4 Brain-stomach axis

The intramural nervous plexi function independently and in concert with the central nervous system. They communicate with the central nervous system (brain) through the sympathetic and parasympathetic nervous divisions of the autonomic nervous system. In the sympathetic nervous system, there are ganglia situated close to the stomach which participate in the control of contractions. These ganglia are connected to the spinal cord and to higher centers in the brain. The parasympathetic innervation is provided by the vagus nerve. It is of utmost importance to incorporate the above multilevel regulatory interactions in the model of the stomach.

## 7.5 Feedback regulation

The fact that gastric motility *in vivo* changes in response to mechanical and chemical stimulation of the organ indicates the existence of feedback regulation in the system. These effects, commonly attributed to reflex pathways and hormonal (gastrin, cholecystokinin, secretin, etc.) actions, are considered to be critical to the normal operation of the stomach. The integration of such feedback control mechanisms into a model of the neuromuscular apparatus of the stomach constitutes a major problem in this area.

When the model is complete it will offer unique insights and will provide otherwise inaccessible information on intrinsic physiological processes of gastric function. Such an approach will have enormous implication for our understanding of mechanisms of certain diseases, advancing of diagnostic accuracy, and planning of therapeutic interventions.

### REFERENCES

- [1] Cowin, S.C., How is a tissue built? *Transactions of ASME, Journal of Biomechanical Engineering*, **122**, pp. 553–559, 2000.
- [2] Humphrey, J.D., Continuum biomechanics of soft biological tissues. *Proceedings of the Royal Society, Ser. A*, **459**, pp. 3–46, 2003.
- [3] Hiroshi, Y., *Strength of Biological Materials*, Williams & Wilkins, 1970.
- [4] Miftakhov, R.N., Influence in the ion concentration changes on excitation propagation and mechanical response in smooth muscle. *Mechanics of Biological Solids*, The Academy of Sciences of the USSR, pp. 81–101, 1986 (in Russian).
- [5] Miftakhov, R.N., Applications of the theory of soft thin shells in problems of biomechanics. *Biomechanics: Problems and Investigations*, Zinatne: Riga, Vol. VI, pp. 51–56, 1988.
- [6] Pullan, A., Cheng, L., Yassi, R. & Buist, M., Modelling gastrointestinal bioelectric activity. *Progress in Biophysics and Molecular Biology*, **85**, pp. 523–550, 2004.
- [7] Cheng, L., Komuro, R., Austin, T.M., Buist, M.L. & Pullan A.J., Anatomically realistic multiscale models of normal and abnormal gastrointestinal electrical activity. *World Journal of Gastroenterology*, **13**, pp. 1378–1383, 2007.
- [8] Corrias, A. & Buist, M.L., A quantitative model of gastric smooth muscle cellular activation. *Annals of Biomedical Engineering*, **35**, pp. 1595–1607, 2007.
- [9] Pal, A., Brasseur, J. & Abrahamsson, B., A stomach road or “Magenstrasse” for gastric emptying. *Journal of Biomechanics*, **40**, pp. 1202–1210, 2007.
- [10] Pal, A., Indireskumar, K., Schwizer, W., Abrahamsson, B., Fried, M. & Brasseur, J.G., Gastric flow and mixing studied using computer simulation. *Proceedings of the Royal Society, Ser. B*, **271**, pp. 2587–2594, 2004.
- [11] Miftahof, R., *Biomechanics of the Small Intestine*, POSTECH University Press: Rep. Korea, 2005.
- [12] Miftahof, R., Nam, H.G. & Wingate D.L., *Mathematical Modeling and Simulation in Enteric Neurobiology*, World Scientific Publ.: Singapore, 2009
- [13] Suzuki, H., Cellular mechanisms of myogenic activity in gastric smooth muscle. *Japanese Journal of Physiology*, **50**, pp. 289–301, 2000.
- [14] Hirst, D.G.S. & Suzuki, H., Involvement of interstitial cells of Cajal in the control of smooth muscle excitability. *Journal of Physiology*, **576**, pp. 651–652, 2006.
- [15] Koh, S.D., Ward, S.M., Tamas, O., Sanders, K.M. & Horowitz, B., Conductances responsible for slow wave generation and propagation in interstitial cells of Cajal. *Current Opinion in Pharmacology*, **3**, pp. 579–582, 2003.

- [16] Carniero, A.A., Baffa, O. & Oliveira, R.B., Study of stomach motility using relaxation of magnetic tracers. *Physical and Medical Biology*, **44**, pp. 1691–1697, 1999.
- [17] Muraki, K., Imaizumi, Y. & Watanabe, M., Sodium currents in smooth muscle cells freshly isolated from stomach fundus of the rat and ureter of the guinea-pig. *Journal of Physiology*, **442**, 351–375, 1991.
- [18] Ou, Y., Strege, P., Miller, S.M., Makielski, J., Ackerman, M., Gibbons, S.J. & Farrugia, G., Syntrophin gamma 2 regulates SCN5A gating by a PDZ domain-mediated interaction. *Journal of Biological Chemistry*, **278**, pp. 1915–1923, 2003.
- [19] Lyford, G.L., Strege, P.R., Shepard, A., Ou, Y., Ermilov, L., Miller, S.M., Gibbons, S.J., Rae, J.L., Szurszewski, J.H. & Farrugia, G., Alpha 1C (Cav1.2) L-type calcium channel mediates mechanosensitive calcium regulation. *American Journal of Physiology, Cell Physiology*, **283**, pp. C1001–C1008, 2002.
- [20] Lyford, G.L. & Farrugia, G., Ion channels in gastrointestinal smooth muscle and interstitial cells of Cajal. *Current Opinion in Pharmacology*, **3**, pp. 583–587, 2003.
- [21] Dickens, E.J., Edwards, F.R. & Hirst, G.D.S., Selective knockout of intramuscular interstitial cells reveals their role in the generation of slow waves in mouse stomach. *Journal of Physiology*, **531**, pp. 827–833, 2001.
- [22] Hennig, G.W., Hirst, G.D.S., Park, K.J., Smith, C.B., Sanders, K.M., Ward, S.M. & Smith, T.K., Propagation of pacemaker activity in the guinea-pig antrum. *Journal of Physiology*, **556**, pp. 585–599, 2004.
- [23] Hirst, G.D.S., Garcia-London, A.P. & Edwards, F.R., Propagation of slow waves in the guinea-pig gastric antrum. *Journal of Physiology*, **571**, pp. 165–177, 2006.
- [24] Bárány, M., *Biochemistry of Smooth Muscle Contraction*, Academic Press, 1996.
- [25] Alvarez, W.C. & Zimmermann, A., Movements of the stomach. *American Journal of Physiology*, **84**, pp. 261–270, 1928.
- [26] Miftakhov, R.N., Age changes of the ‘quasi-equilibrium’ module of elasticity of the human stomach. *Shell Interactions with Fluids*, The Academy of Sciences of the USSR, pp. 197–204, 1981 (in Russian).
- [27] Miftakhov, R.N., Investigation of the human stomach tissue in uniaxial loading. *Hydroelasticity of Shells*, The Academy of Sciences of the USSR, pp. 163–171, 1983 (in Russian).
- [28] Miftakhov, R.N., Experimental investigation of the stomach tissue in biaxial loading. *Invest. in the Theory of Plates and Shells*, Kazan State Univ. Press: Kazan, XVIII, pt. I, pp. 35–46, 1985 (in Russian).
- [29] Miftakhov, R.N., Micromechanics of tissue fracture in uniaxial elongation. *Shell Interactions with Fluids*, The Academy of Sciences of the USSR, pp. 205–214, 1981 (in Russian).
- [30] Miftakhov, R.N., Experimental investigations of the stomach under complex loading. *Hydroelasticity of Shells*, The Academy of Sciences of the USSR, pp. 172–181, 1983 (in Russian).
- [31] Egorov, V.I., Schastlivtsev, I.V., Prut, E.V., Baranov, A.O. & Turusov, R.A., Mechanical properties of the human gastrointestinal tract, *Journal of Biomechanics*, **35**, pp. 1417–1425, 2002.
- [32] Miftakhov, R.N., *Experimental and Numerical Investigations of Soft Shells*, PhD Thesis, Kazan State University, Kazan, USSR, 1983 (in Russian).
- [33] Liao, D., Gregersen, H., Hausken, T., Gilja, O.H., Mundt, M. & Kassab, G., Analysis of surface geometry of the human stomach using real-time 3-D ultrasonography *in vivo*. *Neurogastroenterology & Motility*, **16**, pp. 315–324, 2004.

# A COMPUTER-ASSISTED INTERNAL EXAMINATION TRAINING SYSTEM USING BOTH ANATOMICAL AND VIRTUAL MODELS

A. DOI<sup>1</sup>, K. NOGUCHI<sup>1</sup>, K. KATAMACHI<sup>1</sup>, T. ISHII<sup>2</sup>, H. UNO<sup>3</sup>, Y. MEGA<sup>4</sup> & K. MATSUI<sup>4</sup>

<sup>1</sup>Iwate Prefectural University, Japan.

<sup>2</sup>The Japanese Red Cross Hokkaido College of Nursing, Japan.

<sup>3</sup>KOKEN Co., Ltd., Japan.

<sup>4</sup>JFP, Inc., Japan.

## ABSTRACT

For obstetricians and midwives, ‘internal examination’ refers to an important diagnostic technique in which the progress of labor is examined using the index and middle fingers inserted into the vagina or rectum. Training of this internal examination technique has been commonly performed using a model of the human body (manikin). However, with this method, it was impossible to determine visually where and how the examining fingers are touching, making it difficult for trainers to teach advanced examination skills efficiently and evaluate training achievements. Against this background, we have developed a training system for internal examination that enables simulation of normal and abnormal conditions of labor by detecting the position and direction of the examining fingers in real-time via tactile and visual perceptions using anatomical and virtual models. This system allows trainees to experience both normal and abnormal fetal descent into the pelvis. In addition to support the abnormal conditions, we propose the unique measurements function using magnetic sensors, in order to estimate the precise baby status, such as a gap of the uterine ostium or baby head. We conducted a survey of eight students at our university, and made inquiries for our system, and evaluated it for understanding where the position of ischiatic thor (spinal ischium), baby head, and uterine ostium. The result of the several questions shows that the understanding of all students is improved by using our system.

*Keywords: a training system, internal examination, magnetic sensor, manikin, virtual models, virtual reality.*

## 1 INTRODUCTION

Previously developed training systems for internal examination include our own system [1–3], ePelvis [4–6] developed by a group from Stanford University, and the peripartum diagnosis/delivery assistance training system [7], and the SIMone Childbirth Birthing Simulator/Manikin [8]. The ePelvis is a prototype pelvic simulator, and it attaches several sensors inside the mother’s body (manikin). The peripartum diagnosis/delivery assistance training system is basically a visual learning system using video images, and is suitable for teaching and explanation but not for training of the internal examination itself. The SIMone is a model of a female abdomen with a vulva and the spinal ischium as landmarks. Inside the simulator is a fetal head, and the 19” screen monitor shows the position and approach of the head. The ePelvis, the peripartum diagnosis/delivery assistance training system, and the SIMone are not suitable for close monitoring of fingers and the evaluation of examination techniques. Our approach in our training systems described in [1–3] is different in comparison with the three systems, ePelvis, the peripartum diagnosis/delivery assistance training system, and the SIMone. We utilize magnetic sensors that are attached with two fingers, and monitor the motions of two fingers in internal examination. Our previous system was used to simulate the normal labor condition and thus was not suitable for simulating various abnormalities that can occur during labor. We thus developed a system based on fetal models that could reproduce various abnormal labor conditions (frank breech presentation, complete breech presentation, placenta previa, and face presentation) [9]. Our newly developed internal examination training system consists of models of maternal body parts, including the vagina and the uterine ostium, and fetal body parts (anatomical models), a personal computer (PC), and a magnetic sensor (Fig. 1).

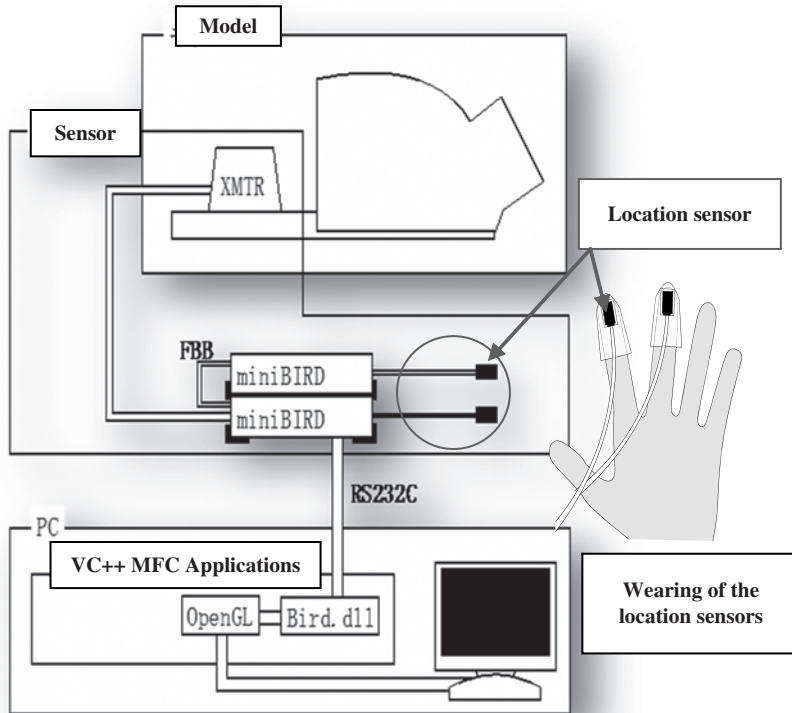


Figure 1: System configuration.

The tracking system consists of a transmitter (XMTR), a location sensor, and a controller (miniBIRD, Ascension Technology Corp.) [10–11]. Magnetic information transmitted from the transmitter is detected by the location sensor, and the location information is received by the PC. The location sensor is attached and fixed to a fingerstall made of silicon rubber, which is worn on the index and middle fingers, with which internal examination is performed. The accuracy of position and angle in miniBIRD are 1.8 mm RMS and 0.5°RMS. The update rate is up to 120 measurements per second. The sensor size (OD) of our miniBIRD is 5 mm (Model 500).

## 2 SYSTEM OVERVIEW

Figure 2 shows the external appearance of the training system. The system supports normal labor conditions of one-finger dilatation, two-finger dilatation, full dilatation and type C (another type of full dilatation) and abnormal labor conditions of frank breech presentation, complete breech presentation, placenta previa and face presentation. Other conditions can be added if necessary. The monitor displays geometric models (i.e. virtual models of human body, examining fingers, etc.) of the anatomical models. An advantage of the system is that it can display on the monitor the position and the direction of the examining fingers during internal examination via the magnetic sensors worn on the examining fingers. The teacher check the motion of trainers for internal examination in the monitor, and trainers can confirm their position of fingers, too. The system thus allows trainers to evaluate visually the skill level and accuracy of examination techniques on the monitor.

Inside the human body model shown in Fig. 3 is a guiding structure to install models of the pelvis and the fetus. The left top picture shows overview, and the right top picture shows the skin of vinyl



Figure 2: Our internal examination training system.

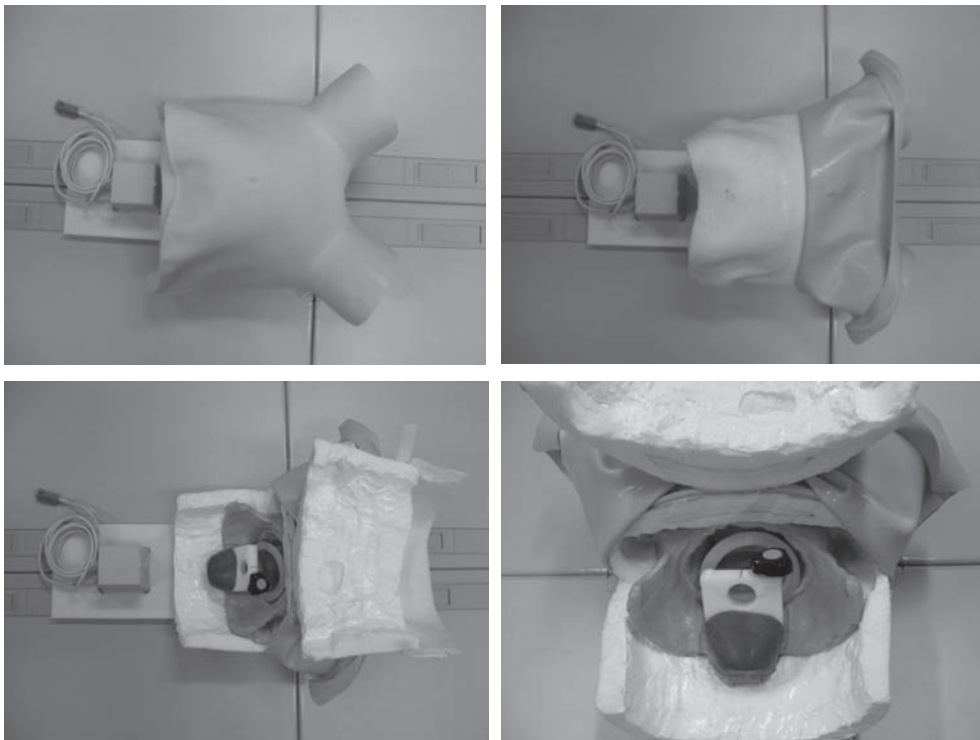


Figure 3: Overview inside the internal examination training system (left top: overview, right top: the skin of vinyl cloth and the body of foamed styrol, left bottom: the bone and guiding structure inside of the body, right bottom: the magnification of the guiding structure).

cloth and the body of foamed styrol. The left bottom picture shows the bone and guiding structure inside of the body, and the right bottom picture shows the detail of the guiding structure.

An appropriate anatomical model of the fetus should be placed in the human body model before starting training. The skin in the virtual model was created by measuring the skin with a noncontact 3D digitizer, and converting to polygonal shape.

The entire fetal models are created by a computer aided design (CAD) software. All generated polygonal models are combined, and both color and optical information are added. The anatomical models of the pelvis and the body were created as follows: a 3D image of the pelvis was taken with a 3D-computed tomography (CT) system, the 3D image was appropriately smoothed and iso-surfaced, and the surface shape of the pelvis and the body was created. The anatomical model of the pelvis and the fetus was made by rapid proto-typing device (3D printer). The skin of mother's body with enclosing the pelvis was created by plastic material and vinyl cloth.

### 3 OUR TRAINING METHOD

Eight anatomical models of the fetus, including 4 normal and 4 abnormal models, were prepared. Figure 4 shows both 4 normal cases (left top: type C (near full dilatation), right top: full dilatation, left bottom: two-finger dilatation, right bottom: one-finger dilatation) and 4 abnormal cases (left top: incomplete foot presentation, right top: complete breech presentation, left bottom: placenta previa, right bottom: face presentation), respectively. These models describe only the parts that are touched by the examining fingers, and are displayed together with the whole image of the fetus.

After a fetal model was placed in the system, the corresponding virtual model is selected on the dialog on the display and the anatomical model and the virtual model are adjusted. The position of both anatomical and virtual models is adjusted by using the location sensor interactively. Figure 5 shows how a fetal model is displayed when it has been changed (before and after change). In this case, the anatomical model of complete breech presentation is selected.

Figure 6 shows the dialog for the selection of an anatomical model of fetus (normal one-finger dilatation has been selected) and control displays of each model (i.e. models of the mother's skin,

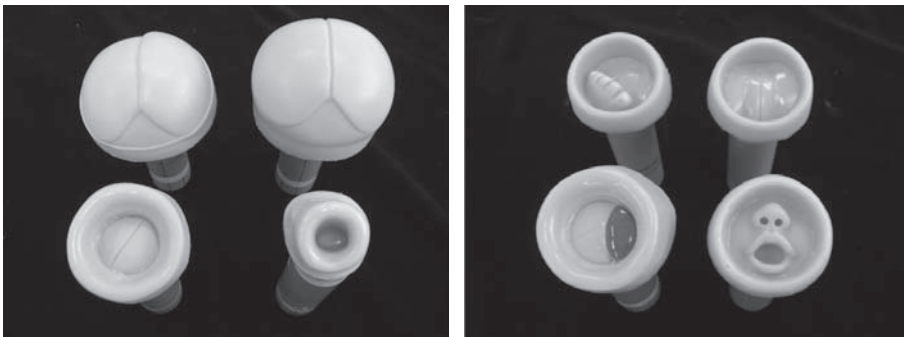


Figure 4: Anatomical models of fetus (left: normal cases, right: abnormal cases).

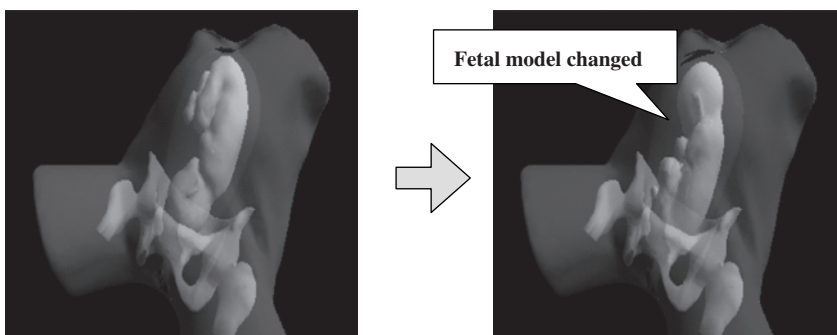


Figure 5: Change of a fetal model.

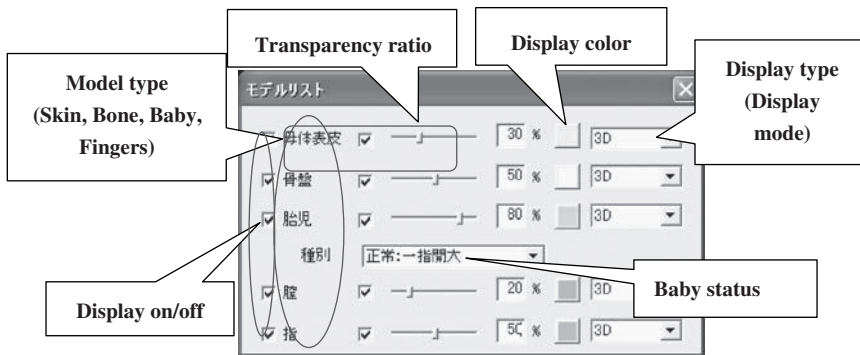


Figure 6: Fetal model selection dialog and display function.

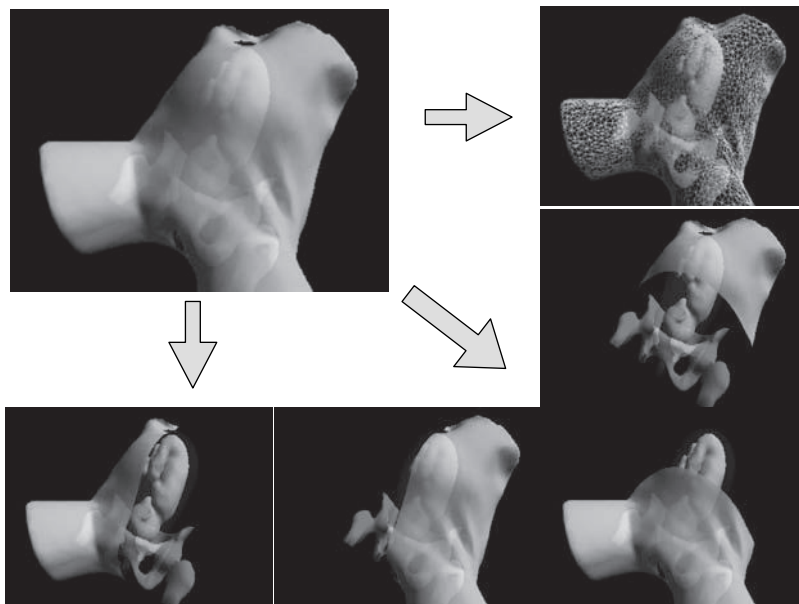


Figure 7: Display function of the internal examination training system.

pelvis, vagina, and fingers). The display control allows the selection of the constitutive models to display, the mode of display (i.e. wireframe (display with lines) or shading), transparency, and the display color. The system can also display internal views with 4 cross-sectional images (left, right, front, and back views). Figure 7 shows the example of the display control function. Normal and abnormal conditions of different fetuses can be incorporated into the system by performing the following actions: (1) creating an anatomical model of the fetus, (2) measuring or modeling the anatomical model to create a virtual model, and (3) registering the new anatomical and virtual models into the system. The positions of the anatomical and virtual models can be adjusted automatically simply by indicating the zero point of a scale called 'station' with an index finger pointer on the screen at the first application start-up.

#### 4 FETAL PRESENTATION

Fetal presentation refers to the orientation of the fetus in the uterus and is classified as 'longitudinal presentation', 'transverse presentation', or 'oblique presentation'. Longitudinal presentation is



further divided based on the position of the fetal head into the ‘head presentation’ (i.e. the fetal head is facing down) and ‘pelvic presentation’ (i.e. the fetal pelvis is facing down; also known as the breech position). All fetal presentations other than head position are considered abnormal. It is known that less than 5% of fetuses are delivered in breech position. Delivery of fetuses in breech position carries a higher risk of experiencing difficulty in pushing out the head and causing compression of the umbilical cord than does delivery of fetuses with their head facing down (i.e. head presentation).

Breech position is roughly divided into frank breech presentation, full breech presentation, knee presentation, and foot presentation. The fetal presentation in which fetal feet are facing up and the hips facing down is referred to as the frank breech presentation, that in which both feet are facing down is referred to as complete breech presentation, and that in which only one foot is facing up is referred to as incomplete breech presentation. ‘Knee presentation’ is the condition in which the fetal knee is flexed and facing down during delivery (i.e. the fetus descends with its knee presenting first), and is further divided into ‘complete knee presentation’ (i.e. both knees facing down) and ‘incomplete knee presentation’ (i.e. only one knee facing down). ‘Foot presentation’ is the condition in which the fetus descends with its extended legs presenting first during delivery. Some breech babies can be delivered naturally through the vaginal canal if they are in frank breech presentation or full breech presentation. Breech babies in knee or foot presentation have less chance to be delivered naturally and are usually delivered by Caesarian section (cutting) [12].

## 5 OPERATION OF INTERNAL EXAMINATION

### 5.1 Operation environment

In the training system for internal examination, it is possible to change the settings for manipulation and display. [Displacement] sets the displacement in the case where the viewpoint is manipulated with the mouse, the keyboard or the [viewpoint] dialog. Larger values in the settings induce larger displacement of the viewpoint for the same manipulation (dragging distance for the mouse, number of keystrokes for the keyboard and number of button clicks for the dialog). [Display curved surfaces] controls the smoothness of the displayed surface of the model, where setting it to [Smooth] makes the displayed surface smooth. [Displayed surfaces] controls whether one or both surfaces of the model are displayed and is used when it is difficult to see the model in cross-sectional view (Fig. 8). [Operation mode] sets the number of sensors used in operation. At present, the maximum supported number of sensors is two: one on the index finger and one on the middle finger. [Offset] adjusts the position of the displayed finger and is used for fine adjustment in cases where there is a discrepancy in the displayed position depending on where the sensor is placed on the finger. [Communication] is used to set the number of the COM port used for connection with the sensors. If the setting is changed, it is necessary to reset the sensor by clicking [Reset communication].

### 5.2 Correspondence between the sensor and the virtual model

When the application is started for the first time, it is necessary to match the coordinates of the virtual model and those of the finger displayed on the monitor. To simplify this process, a calibration scale referred to as ‘station’ is displayed in the virtual model, which facilitates the adjustment of the position of both the model and the displayed finger (Fig. 9). Specifically, their relative position with respect to each other can be adjusted by bringing the finger wearing the sensor to the station and pressing [Enter] on the keyboard. Figure 10 shows the coordinate system for the finger.

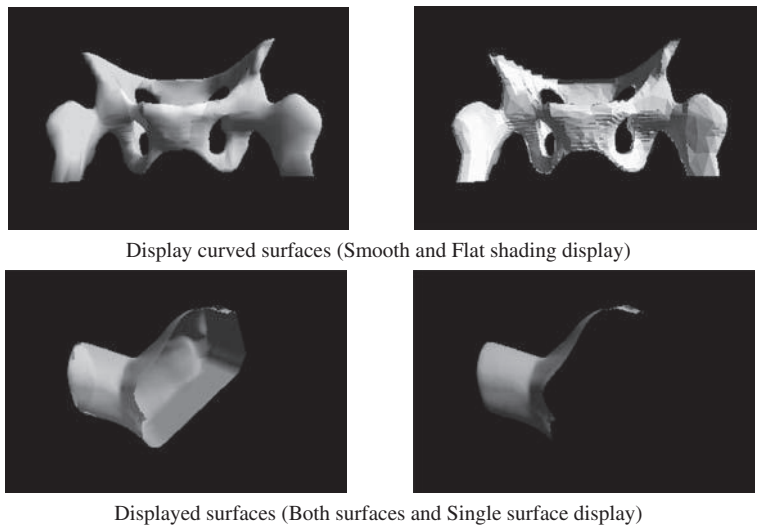


Figure 8: Display mode.

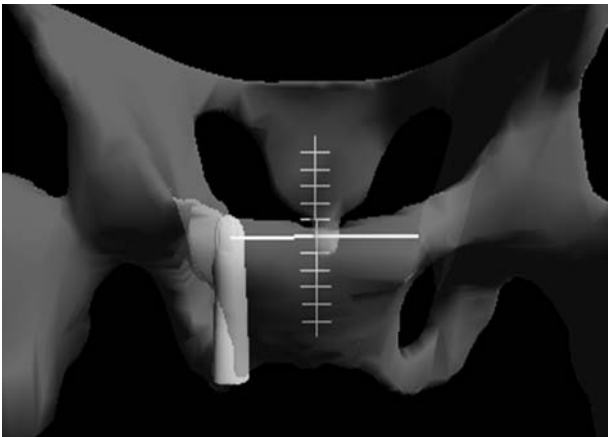


Figure 9: Correspondence between the station and the finger wearing the sensor.

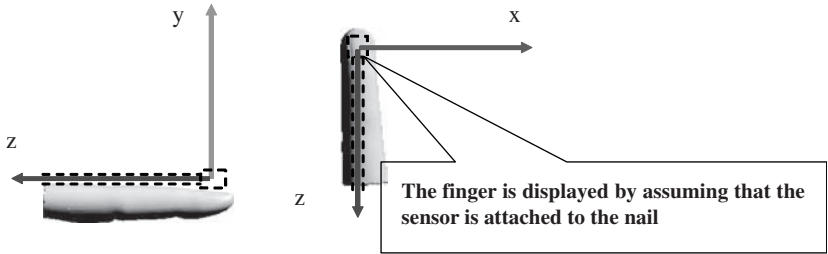
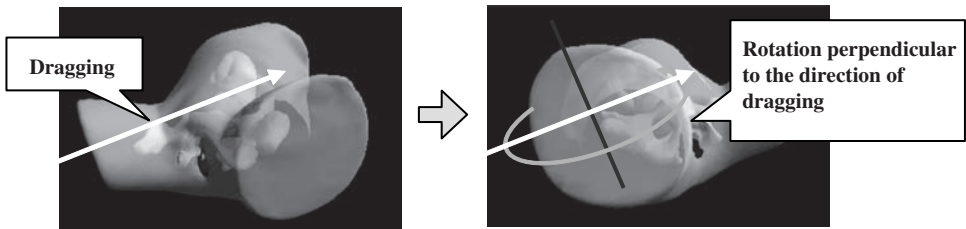
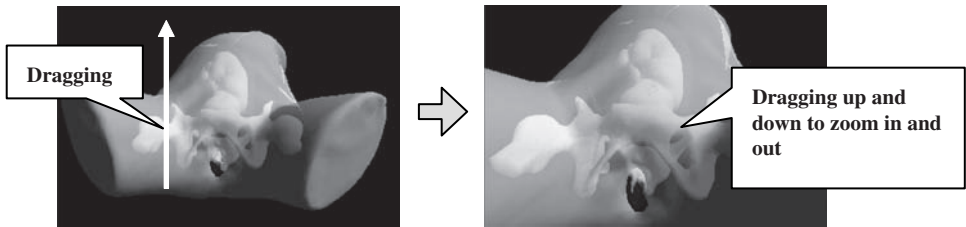


Figure 10: The coordinate system of the finger.

(Case A) Dragging with left button pressed: rotation



(Case B) Dragging with right button pressed: zoom in and zoom out



(Case C) [SHIFT] key and left button: translational motion in horizontal direction

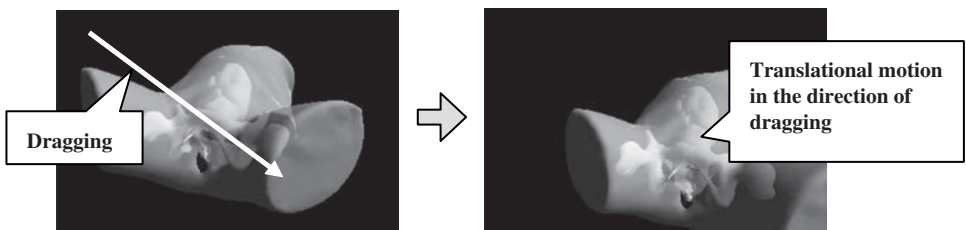


Figure 11: Operation with the mouse.

### 5.3 Changing the viewpoint

Viewing the model from different viewpoints is accomplished by dragging the cursor on the display with the mouse, where the left button controls rotation, the right button controls zooming in and out, and the model can be moved in horizontal direction by pressing the left button while holding down the [Shift] key (Fig. 11).

## 6 MEASUREMENTS

### 6.1 The measurement method

In order to measure a distance in three dimensional space, we have supported unique measurements functions using magnetic sensors. The functions are very important in order to estimate the baby status. For example, user can measure distances of a gap of the uterine ostium or baby head, a direction of baby, and so on. The teacher can also check against the measurements made by the trainees. In the training system for internal examination, distances are measured through the [Measurement]

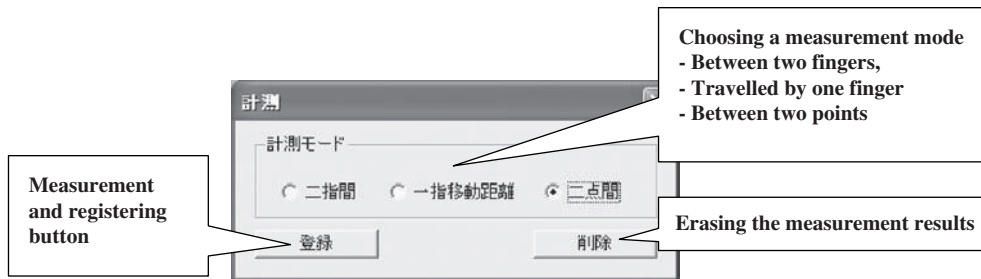


Figure 12: [Measurement] dialog.

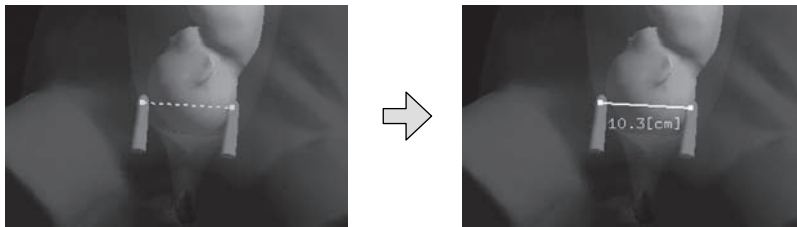


Figure 13: Measurement by between two fingers.

dialog (Fig. 12). Two measurement points are registered, and the distance between them is displayed in units of centimeter with an accuracy of one decimal place. There are three methods (measurement modes) for registering the measurement points, where the measurement method is different depending on the selected method:

- Between two fingers
- The distance travelled by one finger
- Between two points

### 6.2 Between two fingers

In this measurement mode, the measured distance is between two fingers wearing sensors. The positions of the two fingers are taken as the measurement points at the time of performing the measurement. In this case, if the mode [Between two fingers] is selected, the two fingers are moved to the region which should be measured. Measurement points are temporarily displayed on the tips of the fingers, and a dashed line is displayed between the two points. Upon pressing the [Measurement] button, the positions of the two fingers at that moment are registered as measurement points. The color of the registered measurement points is different from that of the temporary measurement points, and a solid line is displayed between them. The distance between the two points is displayed in units of centimeter with an accuracy of one decimal place (Fig. 13).

### 6.3 Distance traveled by one finger

This mode measures the distance travelled by one finger wearing a sensor. The measurement points are registered in two steps as the starting point and the ending point. Upon selecting [Distance travelled

by one finger], the text on the [Measurement] button in the [Measurement] dialog changes to [Register], and a button for selecting the finger used for the measurement is shown. Move the finger with the selected sensor to the region to be measured. A measurement point is registered upon pressing the [Register] button and the text on the [Register] button changes to [Measurement]. Next, the finger is moved to the end point in order to perform the measurement, and a dashed line is displayed between the starting point and the finger.

After moving the finger to the end point, it is registered by pressing the [Measurement] button and the distance between the starting point and the end point is displayed (Fig. 14).

#### 6.4 Between two points

Two points on the display are registered with the *mouse*, and the distance between them is measured. The starting point and the end point are registered in sequence, and the measurement results are displayed upon registering the end point. When the mode [Between two points] is selected, the text on the [Measurement] button in the [Measurement] dialog changes to [Register]. Upon pressing the [Register] button, the button becomes indented and waits for the registration of the measurement point. When the button is pressed again, the button restores its original shape and exits the waiting state. Move the mouse cursor to the starting point in the region to be measured. The first point is registered by clicking. Next, the mouse is moved again in order to record the end point. A dashed line is displayed between the starting point and the end point. After moving the mouse, the end point is registered by clicking and the distance between the starting point and the end point is displayed (Fig. 15).

As measurements are performed repeatedly, the results are displayed accumulatively on the display. The [Erase] button can be used for erasing the results (Fig. 16).

### 7 SYSTEM EVALUATION

We conducted a survey of eight students at our university, and made inquiries for our system, and evaluated it for understanding where the position of ischiatic thor (spinal ischium), baby head, and uterine ostium. We also checked that it was easy to understand the rotation of baby head and the open of the uterine ostium. In the lecture of an internal examination, first we teach an internal examination

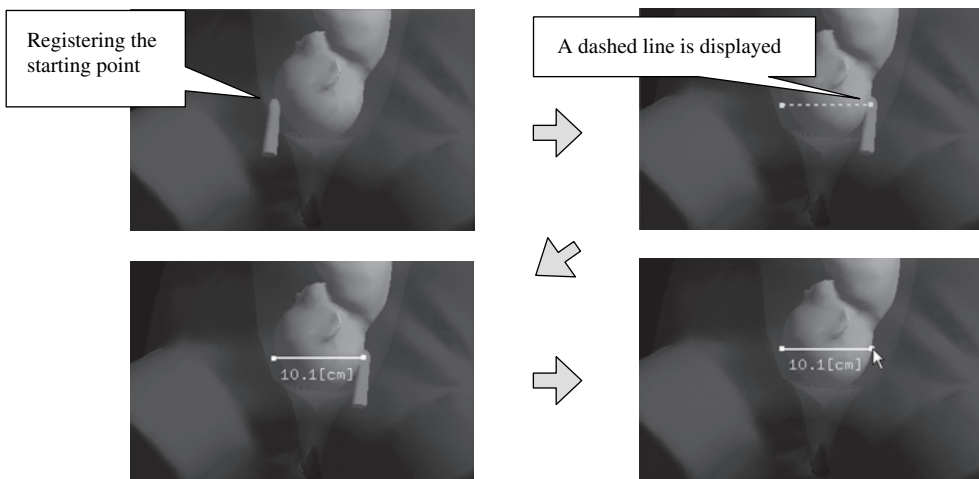


Figure 14: Measurement by distance travelled by one finger.

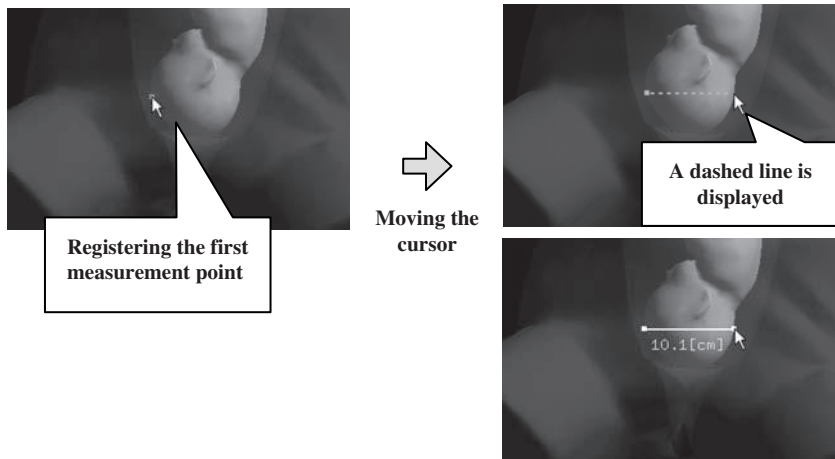


Figure 15: Measurement by between two points.



Figure 16: Erasing the measurement points.

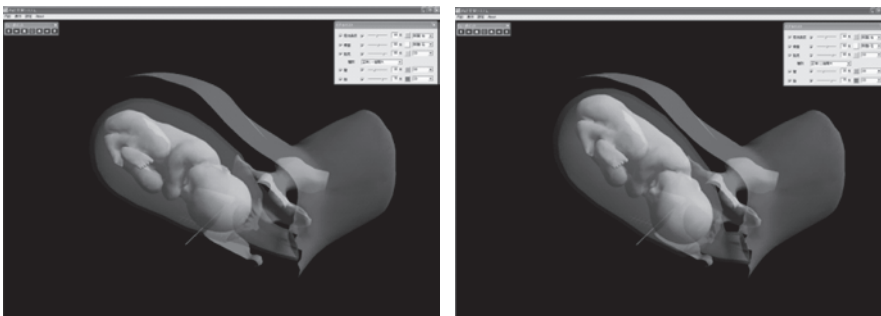


Figure 17: Fetal models of normal conditions (left: one-finger dilatation, right: two-finger dilatation).

in the classical method using a manikin only. Next, we teach them by using our system and make inquiries for our system with unregistered style. We check understanding of the students for several questions before and after looking images in our system. The result of several questions shows that the understanding of all students is improved by using our system [13]. Figures 17 and 18 show fetal models of normal conditions supported by the internal examination training system (i.e. one-finger dilatation, two-finger dilatation, type C (almost full dilatation), and full dilatation). Figures 19 and 20 show fetal models of abnormal conditions (incomplete foot presentation (frank breech presentation), complete breech presentation, placenta previa, and face presentation).

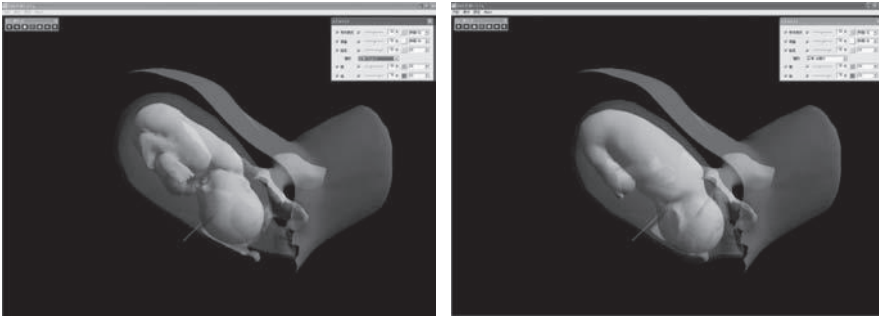


Figure 18: Fetal models of normal conditions (left: Type C, right: full dilatation).

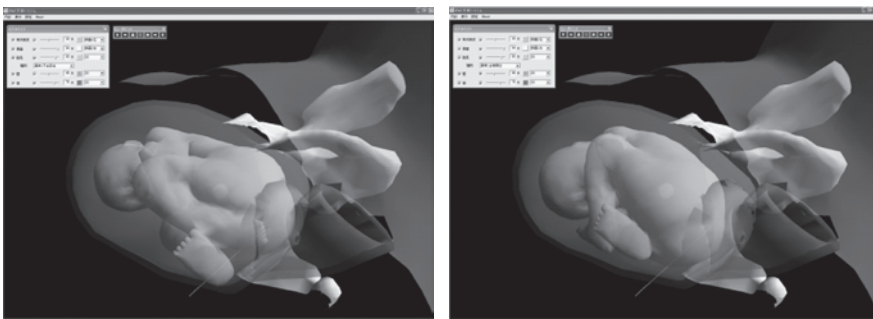


Figure 19: Fetal models of abnormal conditions (left: incomplete foot presentation, right: complete breech presentation).

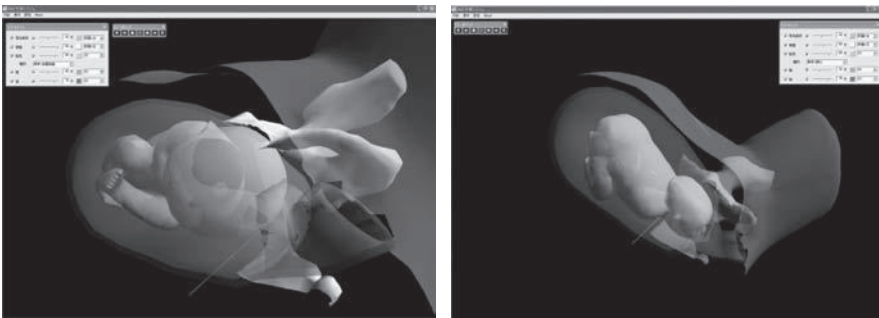


Figure 20: Fetal models of abnormal conditions (left: placenta previa, right: face presentation).

We have been evaluating the usefulness of the present technique by disseminating its use as a learning tool and presenting it at international meetings and exhibitions. At the exhibition of the 21st Japan Academy of Midwifery Scientific Meeting (Oita prefecture in Japan, March 10 and 11, 2007), we presented and demonstrated our internal examination training system and a number of people experienced the training procedure and answered a questionnaire about the usefulness of the system. Over 100 people attended our presentation, approximately 60 of whom experienced

the training procedure and provided feedback. Most of those who experienced the training system at the exhibition of the 21st Japan Academy of Midwifery Scientific Meeting provided positive comments, although some requested improvements or the addition of functions. These requests included the addition of various abnormal labor conditions, more measurement functions (e.g. distance between two fingers and distance to the head of fetus), and an internal examination rating function for each trainee. We have satisfied one of the requests by developing 4 abnormal labor conditions (frank breech presentation, complete breech presentation, placenta previa and face presentation) and have included them in the latest training system. We have also added measurement functions using one or two fingers; the location sensors mounted on the index and middle fingers enable the acquisition of position information in space (i.e. spatial position and rotation). Using this measurement function, we can precisely measure spatial distances estimated on the basis of the distance between the two fingers or the measurer's experience.

## 8 CONCLUSION

We have developed an internal examination training system that supports the learning of normal and abnormal labor conditions. The system provides a unique learning experience that cannot be gained in daily practice. The use of the system in teaching practice will help to nurture competent obstetricians and midwives in a short period. On the basis of specialist' feedback, we included both 4 normal and 4 abnormal fetal models in the training system. The availability of additional abnormal fetal models will make the system more relevant to actual clinical situations. The system supports several measurement functions using one or two fingers to which magnetic sensors are attached. Currently, we have developed the more real finger model, which represents finger bending by using 5DT Data Glove [14]. The glove itself does not contain any magnetic parts, and provides finger bending information by communicating with a control box via optical fiber. In order to construct the finger skin model, a human hand was captured by Magnetic Resonance Imaging device. We believe that the realistic finger model improves understanding of internal examination. Recently, Ascension Technology Corp. has announced the fourth generation of magnetic sensor, which is called trackSTAR [15–17]. The trackSTAR is the latest addition of the Ascension Technology Corp. magnetic sensors, and the sensor size for full six degrees-of-freedom tracking is just 1.5 mm in diameter. In order to utilize the device, we have incorporated the device drivers into our system. The differences between the previous magnetic sensors and the trackSTAR are the fast and dynamic tracking (240 to 420 measurements per second), compact transmitter, no external power supply, the small size of control box, and the support for the interchangeable sensor sizes. In comparison with miniBIRD, the trackSTAR has 4 ports for sensors, and can use by 4 sensors simultaneously. Therefore, our system configuration becomes more compact and simple. In future studies, we aim to perform more detailed examinations of abnormal labor conditions, and a useful internal examination rating feature for each trainee should be supported in our system. Although the present system was developed specifically for internal examination of the fetus, it can also be applied for such purposes as medical training and pre-operative planning for other parts of the body (e.g. thorax and abdomen) by using different anatomical and virtual models.

## ACKNOWLEDGEMENTS

This research was supported in part by Grants-in-Aid for Scientific Research (20500425), and grants aid for scientific research of Iwate Prefectural University (a basis research fund and cooperation research fund (2002)). We would like to thank the reviewers for helpful comments.



## REFERENCES

- [1] Ishii, T., Doi, A., Katamachi, K., Noguchi, K., & Uno, H., *Medical Training Device*, Japan Patent Application No. 2005-032614, Reference No. 4-1130, Receipt No. 50500225450, Patent Applicant: KOKEN Co., Ltd., 2004.
- [2] Ishii, T., Doi, A., Katamachi, K., Noguchi, K., & Uno, H., *Medical Training Device*, International patent application (European Patent Office), Reference No. GP05-1033PCT, Receipt No. 50600235406, Application No. Notification: PCT/JP2006/30219, Patent Applicant: KOKEN Co., Ltd., 2005.
- [3] Doi, A., Matsui, K., Katamachi, K., Noguchi, K., Ishii, T., Uno, H., A computer assisted medical training system for checking status of delivery by using virtual reality technique and physical models, CARS2007, pp. 156, 2007.
- [4] Carla M. Pugh, et al., *The E-Pelvis: A Pelvic Examination Simulator*, SUMMIT (Stanford University Medical Media & Information Technologies) Project Overview, On-line [http://summit.stanford.edu/publications/tear\\_index.htm](http://summit.stanford.edu/publications/tear_index.htm)
- [5] SUMMIT (Stanford University Medical Media & Information Technologies), *e-Pelvis*, On-line <http://summit.stanford.edu/research/epelvis.html>
- [6] AISR of Thomas Jefferson University, *Jefferson: Technology in the Classroom*, On-line <http://jeffline.jefferson.edu/AISR/Forum/04/07/pdfs/ClassTech.pdf>
- [7] MC Medical Shuppan, *3D CG Peripartum Diagnosis/Delivery Assistance Training System*, On-line <http://www.medica.co.jp/3d-bunben/#top>
- [8] [z]Buyamag Inc., SIMone Childbirth Birthing Simulator/Manikin, Online [http://www.buyamag.com/gynecological\\_models.php](http://www.buyamag.com/gynecological_models.php)
- [9] Doi, A., Noguchi, K., Katamachi, K., Ishii, T., Uno, H., Mega, Y., & Matsui, K., An internal examination training system supporting abnormal labor conditions. *Biomed 2009, Eighth International Conference on Modelling in Medicine and Biology*, 26–28 May 2009.
- [10] Mindflux, miniBIRD 500&800, On-line <http://www.mindflux.com.au/products/ascension/minibird-500-800.html>
- [11] 5DT Fifth Dimension Technology, *miniBIRD Model 800 and Model 500*, On-line <http://www.5dt.com/downloads/3rdparty/minibird.pdf>
- [12] Yajima, S., Nakano, H., & Taketani, Y., *NEW Gynecologic Sciences*, Nankodo; 2nd edn, 2004.
- [13] Noguchi, K., & Ishii, T., The development of teaching material for pelvic examination by combination of virtual reality techniques and physical model. *Journal of Japan Academy of Midwifery*, **20(3)**, pp. 134, 2007.
- [14] 5DT Fifth Dimension Technology, *5DT Data Glove 5 MRI/5DT Data Glove 16 MRI*, On-line <http://www.5dt.com/index.html>
- [15] Ascension Technology Corp., *Tracking 3D worlds*, On-line <http://www.ascension-tech.com/>
- [16] Ascension Technology Corp., *3D guidance trackSTAR*, On-line <http://www.ascension-tech.com/realtime/RTtrakSTAR.php>
- [17] Inition Corp., *3D Guidance driveBAY*, On-line [http://www.inition.com.au/inition/pdf/mocap\\_ascension\\_drivebay.pdf](http://www.inition.com.au/inition/pdf/mocap_ascension_drivebay.pdf)

# A NUMERICAL STUDY OF BLOOD FLOW PATTERNS IN CEREBRAL ANEURYSMS AND THE CAUSAL RELATIONSHIP WITH PLATELET AGGREGATION

K. SHIMANO<sup>1</sup>, T. KUDO<sup>1</sup>, S. YOSHIMOTO<sup>2</sup>, H. UJIIIE<sup>3</sup> & Y. ENOMOTO<sup>1</sup>

<sup>1</sup>Department of Mechanical Systems Engineering, Tokyo City University, Japan.

<sup>2</sup>Tokyo University of Science, Japan.

<sup>3</sup>Tokyo Rosai Hospital, Japan.

## ABSTRACT

Past statistical studies demonstrating the likelihood of slow blood flow in most ruptured aneurysms have suggested that thrombogenesis plays an important role in ruptures of cerebral artery aneurysms. In the authors' previous study, it was reported that the degree of platelet aggregation in an aneurysm had a significant correlation with the flow pattern in the aneurysmal dome. It is, therefore, crucial to investigate flow structures in various different aneurysms in order to understand better the relationship between thrombogenesis and ruptures. In this study, patterns of blood flow in three models of cerebral artery bifurcation aneurysms were numerically analysed and compared to discern the likelihood of platelet aggregation. The three model aneurysms had comparable aspect ratios (depth/neck width) but one model was larger in volume than the other two. Experimentally captured images of visualised flow in one of the three models were available and the calculated flow patterns in this model were seen to agree well with the images. Strong impingements of incoming main flows against aneurysmal necks were observed in all models regardless of the bifurcation angle and direction of the aneurysmal protrusion. These impingements presumably caused haemolysis, with ADP originating from haemolysed red blood cells inducing platelet aggregation. Dispersion of flow paths was observed only in the largest model and, consequently, fluid motion was slower than in the other two models. Thus, platelet aggregation was considered to be more active in the largest model. Validity of this discussion was confirmed by application of a platelet aggregation model, which had been proposed in the authors' previous study. It was concluded that the volume of the aneurysmal dome had a significant influence on formation of a low-speed region, which is held to be responsible for active platelet aggregation. Geometric features such as the bifurcation angle and direction of aneurysmal protrusion are considered to be secondary factors contributing to active platelet aggregation.

*Keywords: cerebral aneurysm, rupture, haemodynamics, computational fluid dynamics platelet aggregation thrombus formation*

## 1 INTRODUCTION

When a cerebral artery aneurysm ruptures, it results in a life-threatening subarachnoid haemorrhage, and although not all aneurysms rupture, it is difficult to predict precisely which are likely to do so. Ujiie *et al.* [1] reported a significant correlation between the probability of rupture and aspect ratio (AR) of aneurysmal dome depth to neck width: almost 80% of ruptured aneurysms had ARs higher than 1.6. Similar comparisons of ruptured and unruptured aneurysms were made by other researchers such as Weir *et al.* [2] and Nader-Sepahi *et al.* [3], who concurred with the correlation between AR and the probability of rupture. Some aneurysms, however, rupture even if their AR is lower than 1.6 and it is untrue that those with an AR higher than 1.6 always rupture. Due to this uncertainty, it is still dangerous to rely only on ARs for rupture prediction. For better rupture prediction, more understanding of the haemodynamics and physiology of cerebral aneurysms is necessary.

According to a theory proposed by Ujiie *et al.* [4], thrombogenesis is likely in aneurysms with high ARs due to extremely slow blood flow therein. Ensuing fibrinolysis in which thrombi are dissolved is considered to cause damage to the aneurysmal walls. In this context, the AR can be interpreted as a parameter which represents the degree of slowness of the blood flow within the aneurysmal dome and, consequently, the likelihood of thrombogenesis. The focus of Ujiie *et al.*

upon ARs seems reasonable because a narrow entrance to an aneurysm prevents kinetic energy from being actively transferred from the main arterial blood flow to the inside of the aneurysm and because greater dispersion of kinetic energy is promoted in larger aneurysms. In an experimental study by Takahashi *et al.* [5], evidence supporting Ujiie's theory was shown: canine blood flows in endothelialised model aneurysms made of glass were visualised and thrombogenesis was clearly observed in a model aneurysm with an AR of 2.3.

Ujiie's theory has been also supported through modelling. In the previous study [6], the authors tested a model aneurysm identical to one of the glass models in which thrombogenesis was observed in Takahashi's experiment. Assuming platelet aggregation in aneurysms is induced by adenosine diphosphate (ADP), the authors proposed a platelet aggregation model which mathematically describes the physiological reactions of platelets to ADP. This aggregation model was applied to the flow in the model aneurysm after instantaneous velocity profiles in the model had been calculated using an unsteady Navier–Stokes solver. The computational results clearly predicted aggregation of platelets along the aneurysmal wall where the blood flow was considerably slow. Followed by coagulation, active platelet aggregation is considered to lead to a great degree of thrombogenesis.

Although past studies suggest that Ujiie's theory regarding the process of rupture is promising, more detailed study of blood flow within aneurysms is necessary. Approaches based on numerical techniques such as computational fluid dynamics (CFD) are expected to be effective in the investigation of haemodynamic phenomena of which length-scales are small (say 1 mm or less).

In the previous study [6], it was also demonstrated that the flow pattern in an aneurysmal dome closely correlated with the location of platelet aggregation. It is important, therefore, to classify blood flow patterns into groups by investigation of a number of geometrically different aneurysms. Although a variety of CFD applications to blood flows in cerebral aneurysms have been reported [7–9], blood flow patterns in cerebral aneurysms were not discussed from a viewpoint of likelihood of thrombogenesis or platelet aggregation: those authors focused on parameters in dynamics such as wall shear stress and pressure. Indeed, wall shear stress and pressure are expected to play an important role in the process of aneurysmal growth, but more attention should be paid to the extent of correlation between the degree of thrombogenesis and the risk of rupture.

In this study, unsteady blood flow simulations with unstructured grids were conducted for three different model aneurysms in order to compare flow patterns and their impact on the likelihood of platelet aggregation. Details of the three model aneurysms are described in Section 2. Computational techniques are explained in Section 3, computational results are discussed in Section 4.

## 2 MODEL ANEURYSMS

Because it is known that a great number of cerebral aneurysms are found at bifurcations where anterior communicating arteries separate from anterior cerebral arteries, three models of aneurysms at cerebral artery bifurcations were investigated. The three models had comparable ARs ranging between 2.0 and 2.3 so that the influence of factors other than AR could be investigated. Note that each model had an AR of over 1.6, which equals to aneurysms with potential risk of rupture.

The important parameters of the fluid dynamics are summarised in Table 1. Reynolds numbers were based on inlet pipe diameter ( $D$ ) and mean velocity at the inlet ( $u_m$ ). The mean velocity was calculated from

$$u_m(t) = \frac{\int_A w dA}{\int_A dA} = \frac{4Q(t)}{\pi D^2} \quad (1)$$

Table 1: Important parameters of the geometry, fluid dynamics and computational conditions.

	Model 1	Model 2	Model 3
Reynolds number	Min.244 Max.485	Min.399 Max.797	Min.366 Max.728
Womersley number	2.39	2.40	2.25
Aspect ratio (AR)	2.3	2.0	2.0
Flow rate curve	Fig. 2 (measured)	Sinusoidal	Fig. 2
Reference experiment	Takahashi et al. [5]	Shimamura [11]	N/A
Computational cells	886,893	1,127,077	1,220,816

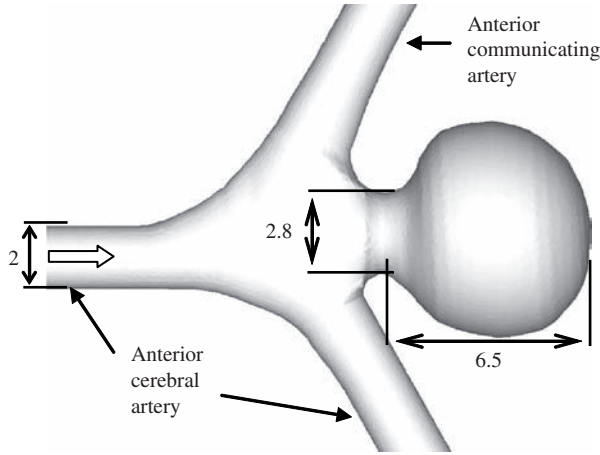


Figure 1: The geometry of Model 1 (all dimensions in mm).

where  $w$  and  $Q$  denote the incoming velocity component and flow rate, respectively. Due to the pulse, the flow rate and mean velocity displayed temporal variation.  $Q$  and  $u_m$ , therefore, represent instantaneous values of the respective parameters. The minimum and maximum Reynolds numbers shown in Table 1 were based on  $u_{m,\max} = \max(u_m)$  and  $u_{m,\min} = \min(u_m)$ , respectively. Womersley numbers were defined by inlet pipe radius and pulsation frequency.

Details of the geometry and computational conditions are explained in the following sections.

## 2.1 Model 1

Model 1 is shown in Fig. 1 where a thick arrow indicates the direction of incoming flow. The aneurysmal dome was located at a Y-shaped bifurcation. Each pipe was straight and 2 mm in diameter. The whole model was symmetrical about the central plane, which is, in Fig. 1, parallel to the surface of the page. Model 1 was identical to one of the glass aneurysms experimentally tested by Takahashi *et al.* [5]. Their original glass model was handcrafted and its fine geometric details could not be determined beforehand. The geometric data of Model 1 was, therefore, obtained manually from several digital images of the glass model. For ease of acquisition of geometric data, the glass model

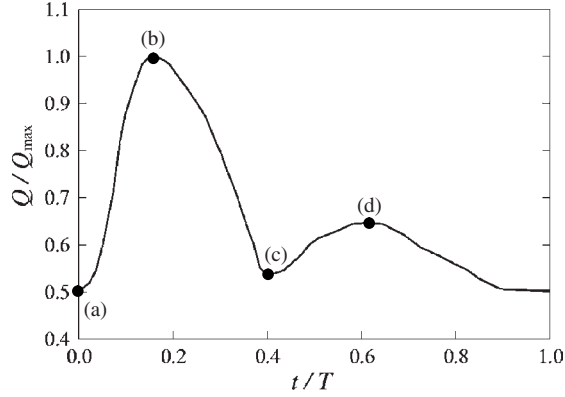


Figure 2: The curve of flow rate imposed at the inlets of Models 1 and 3.  $Q_{\max}$  and  $T$  stand for the maximum flow rate and pulsation period, respectively.

was cut in half and put on a piece of paper ruled into 1 mm squares. The depth of the aneurysmal dome and the neck width measured 6.5 and 2.8 mm, respectively, with an AR of 2.3.

During the experiment by Takahashi *et al.* [5], they recorded the instantaneous flow rate  $Q(t)$ . In this numerical study, the inlet boundary conditions were derived from their flow rate curve, which is shown in Fig. 2. Indices (a)–(d) in Fig. 2 represent time points of extrema. The period of the cyclic change,  $T$ , was 0.276 s and the Womersley number amounted to 2.39. The Reynolds number was at its lowest at point (a) and highest at (b), ranging between 244 and 485.

When inlet velocity profiles were calculated from the flow rate curve in Fig. 2, fully developed axisymmetric flow with no swirl was assumed. A profile of the incoming velocity component  $w$  was obtained as a function of radius  $r$  by solving the following set of equations at each time step:

$$\rho \frac{\partial w}{\partial t} = -\frac{dp}{dz} + \frac{1}{r} \cdot \frac{\partial}{\partial r} \left( \mu r \frac{\partial w}{\partial r} \right) \quad (2)$$

$$2\pi \int_0^R w r dr = Q(t) \quad (3)$$

where  $dp/dz$ ,  $\rho$  and  $\mu$  stand for pressure gradient, density and viscosity, respectively. Equation (2) is the equation of motion in the cylindrical coordinate system while eqn (3) expresses the flow rate condition. When the system of the equations was solved, the pressure gradient was treated as an unknown. Firstly, eqn (2) was solved with an initial approximation to  $dp/dz$ . Secondly,  $dp/dz$  was updated based on eqn (3) and also velocity components were corrected. These two steps of computation were repeated until both equations were satisfied. This solution process is similar to the SIMPLE method [10].

At the bifurcation, 40% of blood proceeded to the anterior communicating artery and the rest continued flowing in the anterior cerebral artery. This ratio of the outgoing flow rates was constant throughout the cycle.

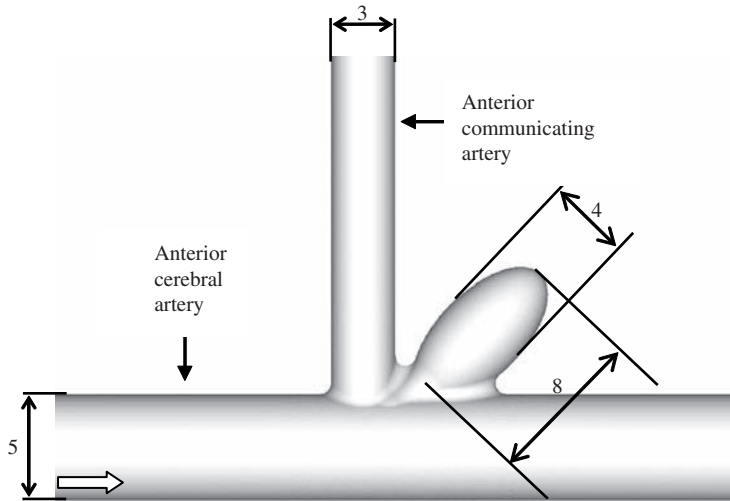


Figure 3: The geometry of Model 2 (all dimensions in mm).

## 2.2 Model 2

Model 2 was originally designed by Shimamura [11] who visualised the flow pattern in the dome. He made up the model by rapid prototyping. In this study, the authors reproduced the water flow in Shimamura's experiment using numerical techniques.

As shown in Fig. 3, Model 2 mimicked an ellipsoidal aneurysm at a T-shaped cerebral artery bifurcation where two arteries met at a right angle. Like Model 1, the whole model was symmetrical about the central plane. The main pipe (anterior cerebral artery) and branch (anterior communicating artery) were 5 and 3 mm in diameter, respectively. The diameters of these pipes in Model 2 were increased to exceed those typical of real human cerebral arteries for ease of visualisation of flow.

The aneurysmal dome inclined by 45 degrees. Its major and minor axes are 8 and 4 mm long, respectively. It is difficult to determine depth and neck width of the aneurysm precisely because the aneurysm was partially embedded within the two arteries. However, the length of the major axis, 8 mm, seems a good approximation to the dome depth and, similarly, the minor axis can be used instead of the neck width. Using these approximations, the AR was determined to be 2.0.

Generally, it is difficult in experiment to generate a flow rate curve which precisely mimics a real human pulsation curve. Therefore, a sinusoidal curve of the inlet flow rate was used in Shimamura's experiment. In this numerical study, inlet boundary conditions based on the same sinusoidal flow rate curve were imposed. Detailed velocity profiles at the inlet were calculated from the system of eqns (2) and (3) in the same manner as in Model 1.

In Shimamura's experiment, water was used instead of blood while the model aneurysms and arteries were larger than actual ones. According to the similarity law, flow features observed in such a model would be irrelevant to actual blood flow unless Womersley and Reynolds numbers in the model agreed with those in a real human cerebral artery. Therefore, the Womersley number and minimum and maximum Reynolds numbers were set at 2.40, 399 and 797, respectively, all of which were considered to be realistic values.

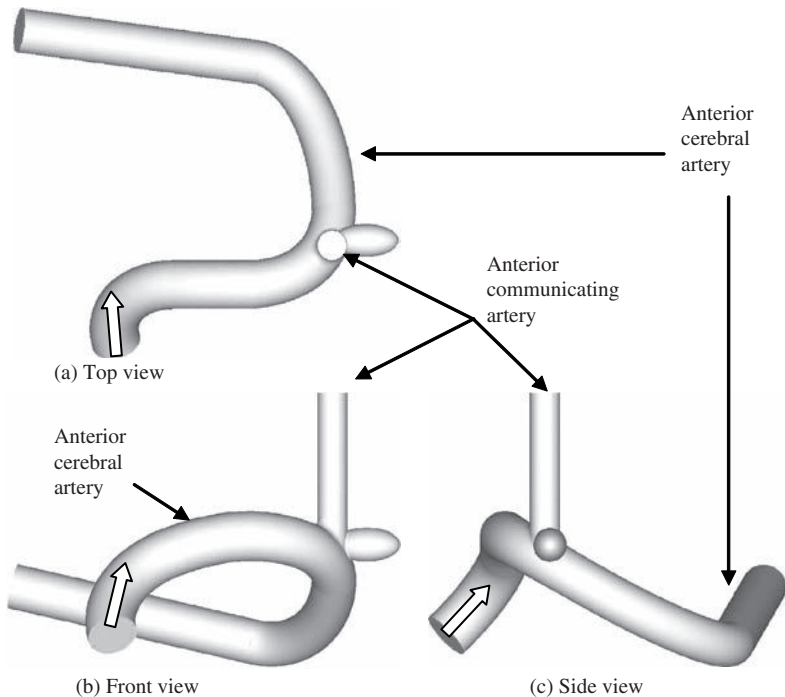


Figure 4: Views of Model 3 in three directions.

It was confirmed in Shimamura's experiment that, throughout the cycle, 26% of the incoming blood moved to the branch at the bifurcation.

### 2.3 Model 3

Models 1 and 2 had 3-dimensional geometry, but arteries in the two models were mimicked using simple straight pipes. This is unrepresentative of real cerebral artery bifurcations. The authors, therefore, tested Model 3 with more realistic features.

Model 3, shown in Fig. 4, consisted of a 3-dimensionally curved artery, a straight branch and an ellipsoidal aneurysm. The direction of protrusion of the dome was determined according to [12] in which the most likely features of anterior communicating artery aneurysms were mentioned. In Model 3, the anterior cerebral artery shrank a little: the diameter measured 3 mm at the inlet and 2.7 mm after the bifurcation. The branch (anterior communicating artery) was 1.8 mm in diameter. The dome was an ellipsoid with major and minor axes of 4 and 2 mm, respectively. The AR was determined to be 2.0 in the same manner as in Model 2.

A flow rate curve similar to that used for Model 1 was imposed when determining the inlet boundary conditions. The Womersley parameter was 2.25. The maximum and minimum Reynolds numbers at the inlet were 366 and 728, respectively. Thirty percent of the blood flowed into the anterior communicating artery.

## 3 COMPUTATIONAL TECHNIQUES

The unsteady incompressible Navier–Stokes equations (4) and continuity equation (5) were numerically solved.

$$\frac{\partial(\rho u^i)}{\partial t} + \frac{\partial(\rho u^j u^i)}{\partial x^j} = -\frac{dp}{dx^i} + \frac{\partial \tau^{ji}}{\partial x^j} \quad (i = 1, 2, 3) \quad (4)$$

$$\frac{\partial u^j}{\partial x^j} = 0 \quad (5)$$

where  $\rho$ ,  $\mu$  and  $u^i$  stand for fluid density, viscosity and the Cartesian component of velocity vector in the  $x^i$  direction, respectively. Einstein's summation rule is applied to these equations and  $j$  is a dummy index.  $\tau^{ji}$  is the component of viscous stress tensor associated with the strain rate through the following equation:

$$\tau^{ji} = \mu \left( \frac{\partial u^i}{\partial x^j} + \frac{\partial u^j}{\partial x^i} \right) \quad (6)$$

Note that eqn (4) is expressed in the conservation form for ease of application of the finite volume method (FVM). Flow was assumed to be laminar in all model aneurysms.

The SIMPLE algorithm [10] was employed for pressure–velocity linkage. The cell-centred finite volume approach in which all unknowns are defined at the centre of each computational cell was used for spatial discretisation of the governing equations. The cell-centred arrangement of unknowns is likely to cause a physically meaningless oscillation in calculated pressure fields. This error in solutions, known as ‘spurious error’, was avoided via Rhie and Chow’s method [13].

Unstructured grid systems were employed so that the complicated geometry of each model could be properly expressed. In unstructured grid systems, each computational cell is usually in the shape of a tetrahedron, triangular prism, pyramid or hexahedron. In this study, mainly tetrahedral cells were used. However, tetrahedral cells seemed undesirable for boundary layer flows which were parallel to wall surfaces and intersected surfaces of tetrahedral cells at oblique angles. This would lead to a loss of accuracy in the solution [10] and instability of calculation. Therefore, hexahedral and prismatic cells were allocated in near-wall regions.

The number of computational cells was 886,893 in Model 1, 1,127,077 in Model 2 and 1,220,816 in Model 3. The time dependent term in the L.H.S of eqn (4) was approximated by the 3rd order backward difference scheme and its treatment was fully implicit. For Model 1, two settings of time step  $\Delta t$  were tested:  $\Delta t = T/2760$  and  $T/500$ , where  $T$  represents the pulsation period. It was confirmed that there was no significant difference between the two solutions. The computational results for Model 1 presented in Section 4 are those obtained with  $\Delta t = T/2760$ . Considering experiences with Model 1, the authors determined the time step  $\Delta t$  for the other models:  $T/500$  for Model 2 and  $T/1000$  for Model 3. A longer time step was used for Model 2 because, as explained in Section 2, the inlet flow rate in Model 2 was expressed by a sinusoidal curve which was free from any rapid increase or decrease.

The authors’ original CFD code was used in solution of the N–S equations. The domain decomposition technique [14] was applied in order to enable parallel computing. The N–S solver was implemented on a PC cluster with sixteen Pentium-4 processors. The whole computational domain was partitioned into eight subdomains in Model 1 while the number of subdomains in Models 2 and 3 was sixteen. Connecting boundaries between neighbouring subdomains were treated with the overlap cell technique [15] in which computational cells along connecting boundaries are shared by the two corresponding subdomains. Communication between processors was provided by MPI



(message passing interface). In the parallelisation strategy, processors communicated with each other every time unknowns were updated so that any slowdown in convergence speed could be minimised [14].

Blood was assumed to be a Newtonian fluid in Models 1 and 3 while water flow was analysed in Model 2. Viscosity  $\mu$  was, therefore, fixed in all calculations. However, as blood is actually a non-Newtonian fluid, it seemed necessary to examine the influences of the Newtonian assumption on calculated flow patterns. The Carreau–Yasuda model [16] was applied to Model 1 so that Newtonian and non-Newtonian solutions could be compared. In the Carreau–Yasuda model, viscosity  $\mu$  is a function of strain rate  $\dot{\gamma}$  as follows:

$$\mu = \mu_{\infty} + \frac{\mu_0 - \mu_{\infty}}{\{1 + (\lambda\dot{\gamma})^b\}^a} \quad (7)$$

Values of the parameters in eqn (7) are shown in Table 2. Note that

$$\lim_{\dot{\gamma} \rightarrow 0} \mu = \mu_0, \quad \lim_{\dot{\gamma} \rightarrow \infty} \mu = \mu_{\infty}, \quad (8)$$

The relation between viscosity  $\mu$  and strain rate  $\dot{\gamma}$  is shown in Fig. 5. Before the non-Newtonian calculation was carried out, velocity profiles at the inlet had been calculated from the system of eqns (2), (3) and (7).

Table 2: Model parameters used in the Carreau–Yasuda model.

$\mu_0$	$\mu_{\infty}$	$a$	$b$	$\lambda$
0.16 Pa s	$3.5 \times 10^{-3}$ Pa s	1.23	0.64	8.2 s

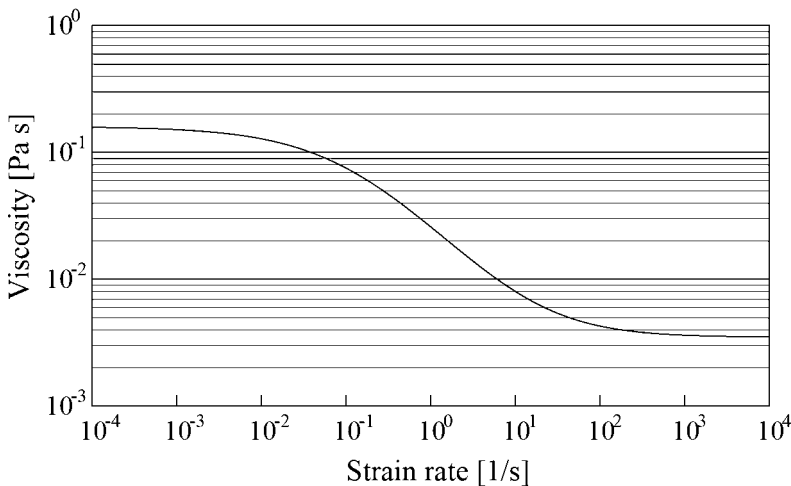


Figure 5: A non-Newtonian relation between viscosity and strain rate expressed by the Carreau–Yasuda model. The Carreau–Yasuda model was applied only to Model 1.

The time-marching process in unsteady incompressible flow calculation is mathematically equivalent to serial application of a non-linear vector mapping with a set of initial profiles of velocity and pressure, which usually contain physically meaningless components, and behaviours of the solution are determined by eigen values of the mapping. The non-physical components in the initial profiles continue to decline as the time-marching proceeds because they correspond to eigenvalues of which absolute values are less than unity [17] while eigenvalues of periodic fluctuations such as pulsatile blood flow correspond to unity [18]. However, solutions do not precisely reflect actual flow at an early stage until the non-physical components have become negligible. It is important for reduction in computational time to give the best possible initial profiles because the duration of unreliable early solutions depends on the quality of the initial profiles. In this study, initial profiles were obtained in the following way: a steady problem was solved with a flow rate identical to the highest flow rate of the corresponding unsteady problem. Subsequently, the unsteady flow calculation started at the moment of the highest flow rate with the steady flow solution used as the initial condition. This approach was based on a report by Wahap *et al.* [19], who found that calculated steady flow in an aneurysmal sac was close to the instantaneous flow in the corresponding unsteady problem at the moment of the highest flow rate. In every model, solutions agreed with those in the previous cycle after approximately 1.5 times the pulsation period had elapsed since the start of the time-marching.

## 4 RESULTS AND DISCUSSION

### 4.1 Model 1

Figure 6 shows velocity vectors on the central cross-sectional plane in Model 1 at the four time points (a)–(d), which are defined in Fig. 2. Each reference arrow in Fig. 6 represents 50% of the maximum mean velocity  $u_{m,max}$ , where  $u_{m,max} = 0.97$  m/s. All results in Fig. 6 were obtained on the assumption of a Newtonian fluid.

At each time point, the incoming flow approaching the entrance to the aneurysm from the left changed its direction slightly downward because the outgoing flow rate was higher in the anterior cerebral artery than in the anterior communicating artery. It can be clearly observed that the incoming flow hit the lower edge of the aneurysmal neck. More precisely, the flow dramatically decelerated near the apex of the aneurysmal neck. It is noteworthy that this rapid reduction in flow speed occurred across rather short distance in the vicinity of the neck. As a result, static pressure near the neck rapidly increased because, in accordance with Bernoulli's law, deceleration in flow causes an increase in static pressure. In fact, the apex of the neck was a stagnation point where the highest static pressure was recorded. The pressure gradient near the neck amounted to  $0.25 \text{ Pa}/\mu\text{m}$  at temporal point (a) and  $0.80 \text{ Pa}/\mu\text{m}$  at (b). As the characteristic length scale of a red blood cell (RBC) is  $8 \mu\text{m}$ , the pressure difference exerted on RBCs in the impingement region ranged approximately between 2.0 and 6.4 Pa. This pressure difference is considered to be large enough to cause haemolysis with Alkhamis *et al.* [20] having reported that ADP originally contained in RBCs escaped into plasma when a shear stress of only 2 or 3 Pa was exerted on RBCs. Here, the term 'haemolysis' does not mean destruction of RBC membranes but is used to express escape of RBC contents through the membranes into the surrounding plasma [21]. Although modes of RBC membrane deformation were different (compression in the present study and shearing in Alkhamis's), levels of strain were presumably comparable.

In addition, a dramatic rise in shear stress was observed immediately after the impingement. The highest wall shear stress was found at the point on the narrowest portion of the aneurysmal neck,

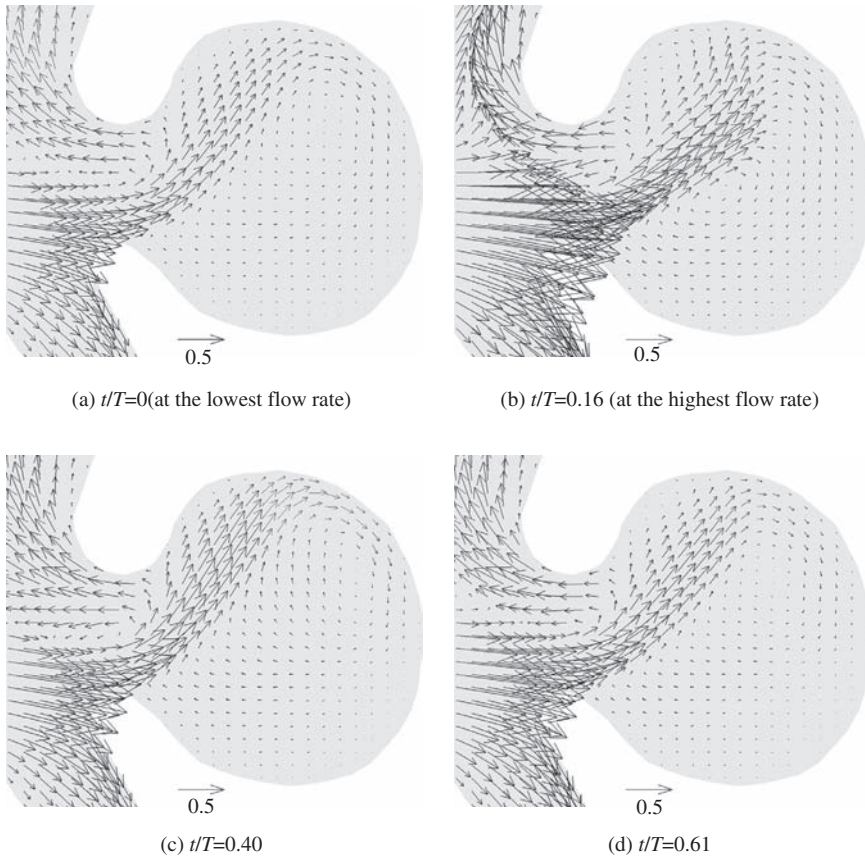


Figure 6: Calculated velocity vectors on the central plane in Model 1 at four time points with the Newtonian assumption. Each point in time is represented by the ratio of the time to the pulsation period  $T$ .

which was only 0.5 mm distant from the stagnation point along the wall. The wall shear stress at this point ranged between 14 and 32 Pa with its average being 20 Pa. It can be, therefore, concluded that RBCs sequentially received two types of force near the stagnation point:

1. compressing force caused by pressure gradient before the impingement;
2. shearing force due to velocity gradient after the impingement.

Both are considered to be responsible for haemolysis. This conclusion is supported by a finding in Takahashi *et al.* [5] that significant numbers of platelets were found in thrombi adhering to the wall of the model aneurysm. Note that the model aneurysm was endothelialised: there was no cause of platelet aggregation other than ADP originating from RBCs.

After the impingement upon the neck, some blood containing ADP proceeded to the aneurysmal dome and reached the upper part of the internal wall of the aneurysm. The exact position that the flow reached depend on the point in time because the flow rate and, therefore, inertia of the flow were

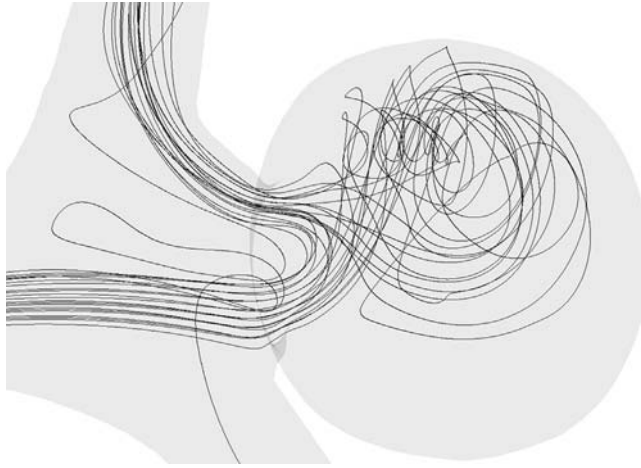


Figure 7: Flow paths in Model 1 (Newtonian). Particles were released at the inlet at  $t = 0$ .

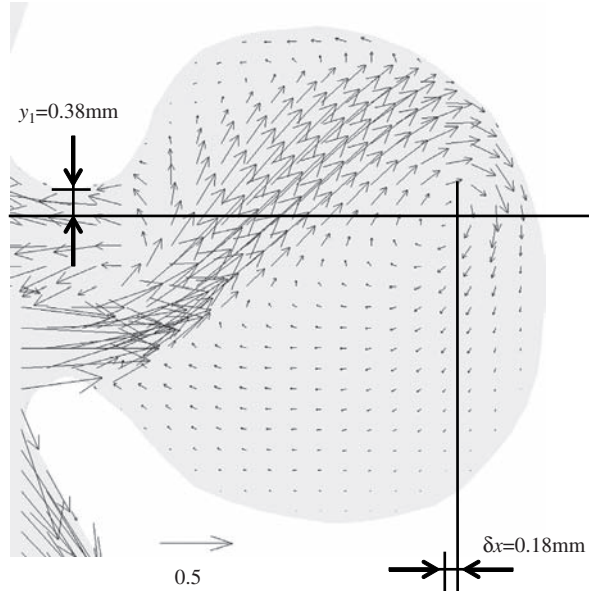
continually changing. The flow, then, changed its direction whilst fanning out in 3-dimensions and dramatically decreasing in speed. A low-speed region was consequently formed and came to occupy a large portion of the dome. The flow velocity was less than 10% of  $u_{m,max}$  at most points in the lower half of the aneurysm regardless of the timing. The blood motion in the dome after the 3-dimensional fanning was so slow that platelets had enough time to aggregate.

Flow paths within Model 1 are drawn in Fig. 7. In visualisation, imaginary particles were put into the flow at the inlet at temporal point (a). Only the paths of particles which entered the aneurysmal dome are included in Fig. 7 to avoid overlaying too great a number of paths. Flow features in Model 1 such as the impingement upon the neck and the 3-dimensional spread in the dome are clearly observed in Fig. 7. Some particles passing by the neck edge where haemolysis is considered to have occurred stretched across the aneurysmal dome and described long 3-dimensional curves. Blood moving slowly in the dome changed its direction towards the exit and proceeded to the anterior communicating artery.

Takahashi *et al.* [5] reported that a vortex was visualised in the glass model used in their study. Although no detailed picture of the vortex is included in Reference [5], the authors received the opportunity to have a close look at their video. The shape of the vortex observed in their experiment seemed to agree with the curved path lines in the aneurysm shown in Fig. 7.

Computational results at  $t/T = 0.230$  are compared in Fig. 8 between (a) Newtonian and (b) non-Newtonian calculations. In each image, the vortex centre (VC) is indicated by the intersection of the horizontal and vertical lines. Difference in the position of VC between the two calculations was  $\delta x = 0.18$  mm in the horizontal direction and  $y_1 - y_2 = 0.13$  mm in the vertical direction. The position of VC in the Newtonian calculation was located deeper and lower than in the calculation with the Carreau–Yamada model. This means that relative strength of inertia to viscosity in the Newtonian calculation exceeded that in the non-Newtonian. It follows that this difference resulted from the non-Newtonian characteristic that viscosity increases at a small strain rate. However, this is not of primary importance because the two flow fields showed the same overall features and because the difference in the VC position was less than 10% of the characteristic length scale (the neck width 2.8 mm).

(a) Newtonian  
 $t/T=0.230$



(b) non-Newtonian  
 $t/T=0.230$

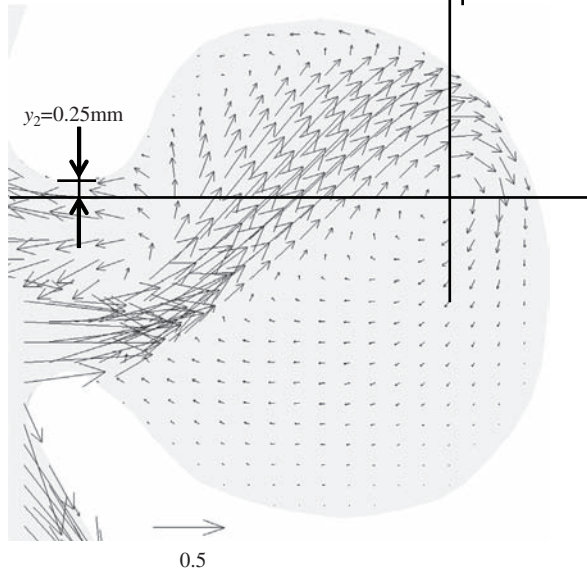


Figure 8: Comparison of vortex centres on the central plane in Model 1 between Newtonian and non-Newtonian calculations. Each snapshot is at  $t/T = 0.230$ .

Figure 9 shows velocity vectors on the central plane obtained with the Carreau–Yasuda model. The four time points are identical to those in Fig. 6. There was no noticeable difference between the Newtonian and non-Newtonian calculations. It is important that the large low-speed region observed in Fig. 6 is also found in Fig. 9 because this low-speed region is considered to be responsible for active platelet aggregation in the aneurysm. It can be concluded from the observations above that assumption of a Newtonian fluid is appropriate to discussion of blood flow patterns in aneurysms.

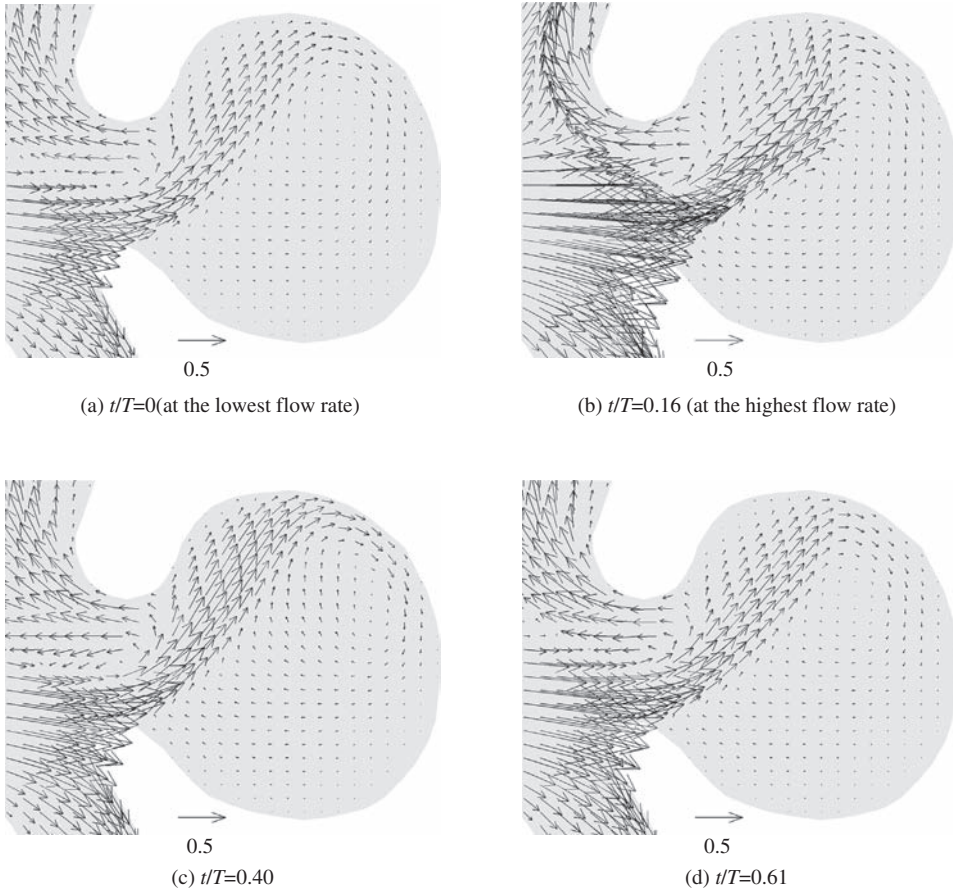


Figure 9: Calculated velocity vectors on the central plane in Model 1 at four time points with the Carreau–Yasuda. Each point in time is represented by the ratio of the time to the pulsation period  $T$ .

## 4.2 Model 2

Figure 10 shows velocity vectors on the central plane in Model 2 at four time points. The lowest and highest flow rates came at points (a) and (c), respectively. Acceleration and deceleration of the incoming flow was greatest at (b) and (d), respectively. As the flow rate curve was sinusoidal, the interval of the two neighbouring temporal points was exactly a quarter of the pulsation period. Each reference arrow in Fig. 10 represents 50% of the maximum mean velocity  $u_{m,\max}$ , where  $u_{m,\max} = 0.16$  m/s.

The main incoming stream was drawn upward by suction in the anterior communicating artery. The flow hit the right edge of the aneurysmal neck at each time point. This feature was commonly observed in Models 1 and 2. The flow decelerated before the neck so quickly that a strong pressure gradient was induced. After the impingement, however, the flow went into the dome and changed



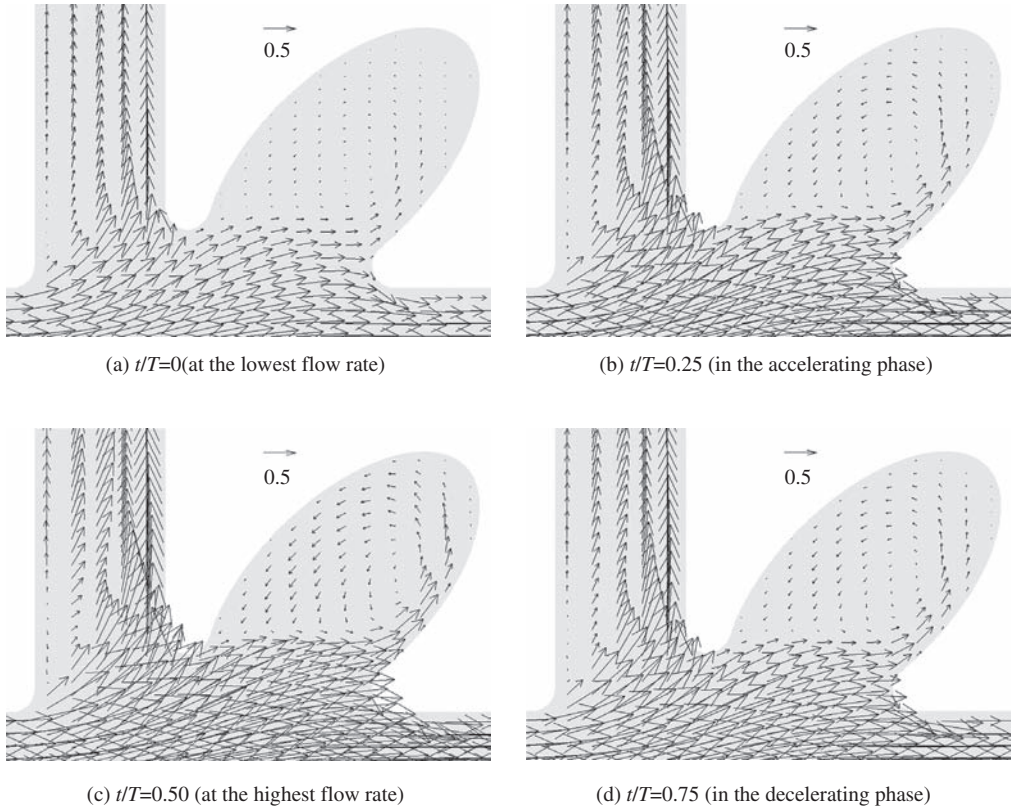


Figure 10: Calculated velocity vectors on the central plane in Model 2 at four time points. Each point in time is represented by the ratio of the time to the pulsation period  $T$ .

its direction, following the aneurysmal wall in Model 2. This is a sharp contrast to the flow in Model 1, which moved across the aneurysmal dome and kept away from the wall for a period after the impingement (see Fig. 6).

Another important difference between flow patterns in Models 1 and 2 was the magnitude of velocity. As shown in Fig. 6, the lower half of the aneurysm in Model 1 was filled with slowly moving blood of which velocity scale was less than 10% of  $u_{m,max}$  throughout the cycle. On the other hand, in Fig. 10, the magnitude of the flow velocity in the aneurysmal dome was 10% of  $u_{m,max}$  or more at time points (b)–(d), although the velocity magnitude was less than 10% at point (a). Thus, the blood entering the aneurysmal dome in Model 2 was quickly flushed out, a pattern not observed in Model 1. Platelet aggregation seems less likely in Model 2 than in Model 1 because platelets tended to exit the aneurysm before aggregation became active.

Figure 11 shows calculated flow paths in Model 2. Flow was visualised in the same manner as in Fig. 7. In Fig. 11, the model is rotated by 45 degrees around the vertical axis so that 3-dimensional structure of the flow can be seen. After entering the aneurysmal dome, the flow turned round, spreading slightly in the spanwise direction. Upon escaping from the dome in Model 2, the fluid returned to the original main passage and moved along the wall, not on or near the central plane.

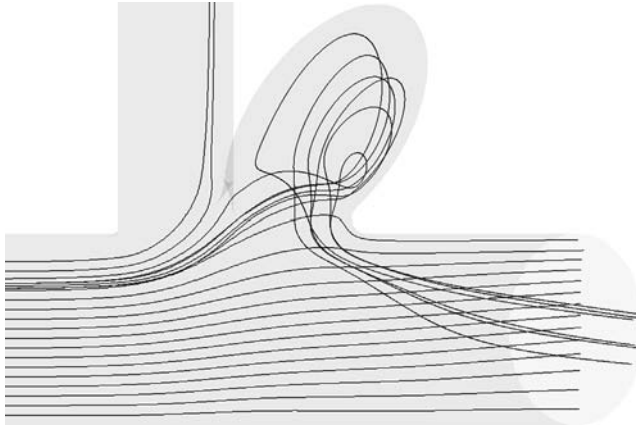


Figure 11: Flow paths in Model 2.

The degree of the spanwise spread in the dome was not great enough to cause the flow to lose much kinetic energy. This can be contrasted with Model 1 where flow paths dispersed within the aneurysm (see Fig. 7).

The calculated flow paths are compared with an experimentally obtained image in Fig. 12. The same flow paths as in Fig. 11 are projected onto the  $x$ - $y$  plane in Fig. 12(a). A snapshot from a video recorded in Shimamura's experiment [11] is shown in Fig. 12(b). In his experiment, the flow was visualised by filling the model with milk and the video was taken while the milk was being flushed out. It can clearly be seen that calculated flow paths in and out of the aneurysmal dome correlate well with the wisps of milk in Fig. 12(b).

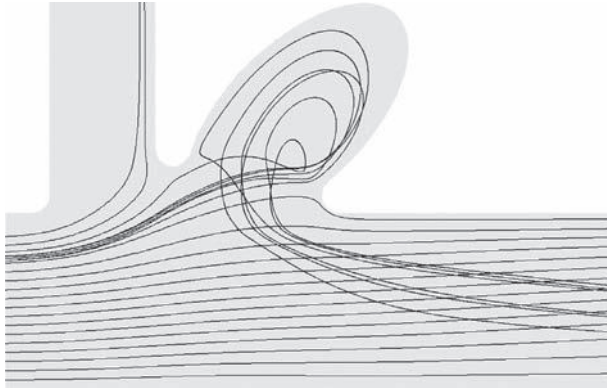
### 4.3 Model 3

Velocity vectors on the central plane of the aneurysmal dome in Model 3 are drawn in Fig. 13. The view direction of Fig. 13 is identical to that of Fig. 1(a). The four time points, (a)–(d) are defined in Fig. 2. Each reference arrow in Fig. 13 represents 50% of the maximum mean velocity  $u_{m,max}$ , where  $u_{m,max} = 0.97$  m/s. An impingement of the mainstream upon the aneurysmal neck is clearly seen in this figure. As, regardless of the bifurcation angles, similar impingements were observed in all models tested in this study, impingements of this kind and the resulting haemolysis are presumably common to most aneurysms located at artery bifurcations.

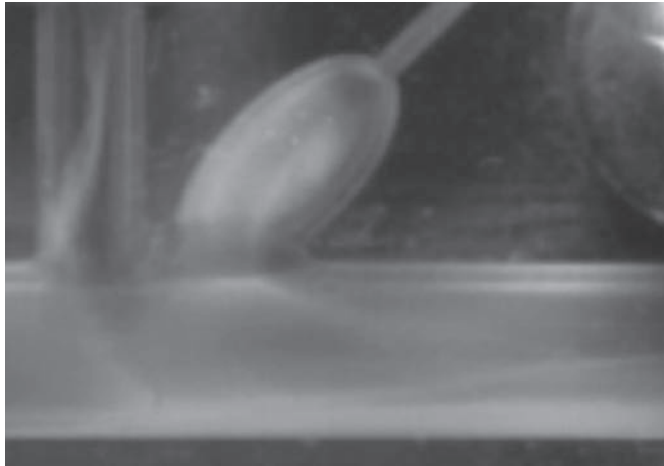
After the impingement, the flow proceeded along the aneurysmal wall and turned round. This feature was common to Models 2 and 3. Unlike Model 1, no sizable region of extremely slow flow was observed in Model 3. The flow speed was more than 10% of  $u_{m,max}$  in most part of the aneurysm: the exception being a region close to the deepest end. Therefore, the degree of platelet aggregation in Models 2 and 3 was presumably comparable: platelet aggregation in the two models was less active than in Model 1.

Figure 14 shows flow paths, which were calculated by releasing imaginary particles at the inlet at  $t = 0$ . Flow paths in Model 3 were similar to those in Model 2 because neither of the two models produced flow paths which dispersed within the aneurysmal dome (cf. Figs 11 and 14). This means that blood in the aneurysms lost little kinetic energy whilst maintaining a high flow speed. As a





(a) Calculated flow paths (projection onto the  $x$ - $y$  plane)



(b) A snapshot during the sweeping process of infused milk.  
(Courtesy of Tokyo University of Science)

Figure 12: Comparison between (a) calculated and (b) experimentally visualised flow patterns in Model 2.

whole, the flow structure in Model 3 was similar to that in Model 2 although the flow in Model 3 was more 3-dimensional.

#### 4.4 Likelihood of platelet aggregation

Every model tested had a chance of haemolysis and ensuing platelet aggregation in its aneurysm because the mainstream always hit the edge of the aneurysmal neck. The flow in Model 1 was characterised by dispersion, which resulted in a large low-speed region. In the other two models, by contrast, no low-speed region was observed. It can be concluded that platelet aggregation was less active in Models 2 and 3 because ADP released from RBCs due to the flow impingement was flushed out more quickly than in Model 1.

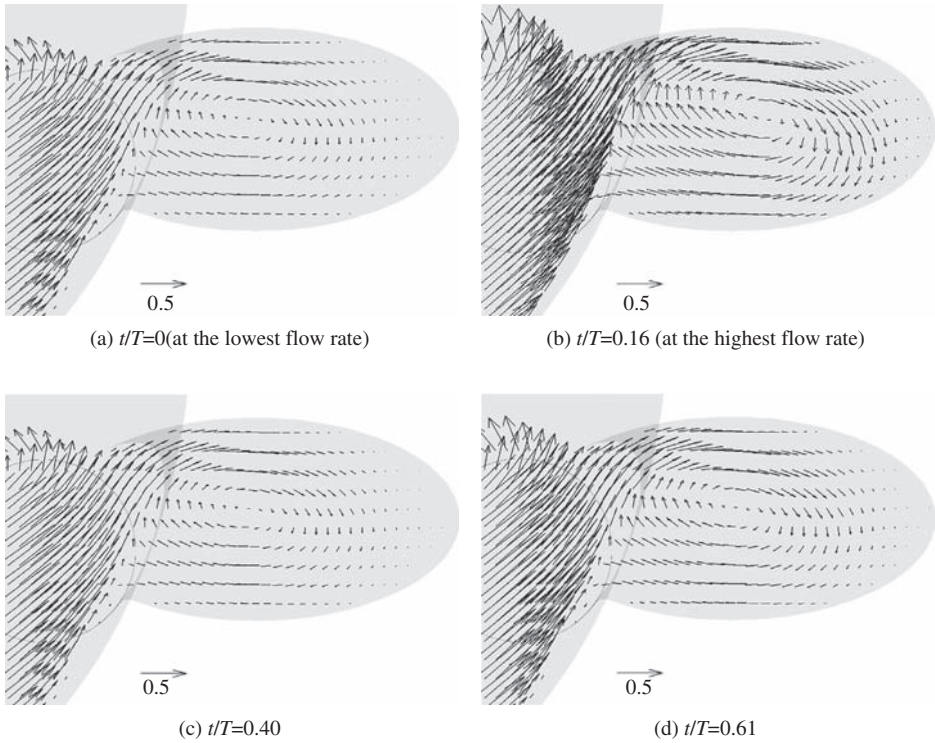


Figure 13: Calculated velocity vectors in Model 3 at four time points. Vectors are depicted on the central cross-section of the aneurysm and the view direction is identical to that of Fig. 3(a). Each point in time is represented by the ratio of the time to the pulsation period  $T$ .

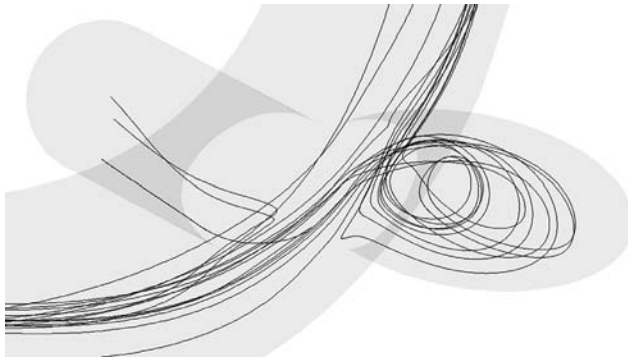


Figure 14: Calculated flow paths in Model 3.

Figures 15 and 16 show calculated distributions of  $N_1$  (density of aggregated platelets) in the vicinity of aneurysmal walls in Models 1 and 3. Here, the term ‘aggregated platelets’ is taken to mean those in primary aggregation. Density of aggregated platelets was calculated using the platelet aggregation model [6] on the assumption that 20% of ADP contained in RBCs was released into plasma in the region within a 1 mm radius of the stagnation point. Although this estimation of the

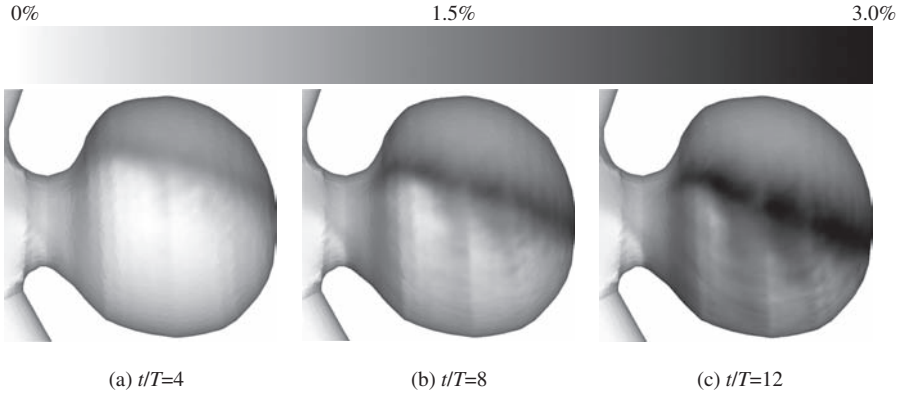


Figure 15: Distributions of  $N_1$  (density of primary-aggregated platelets) in the vicinity of the wall surface in Model 1.

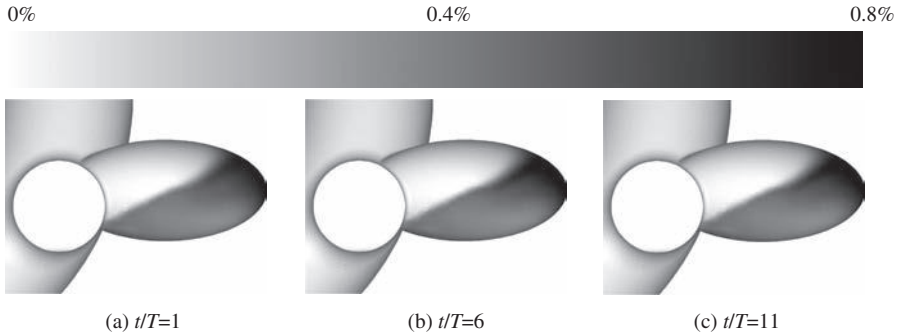


Figure 16: Distributions of  $N_1$  (density of primary-aggregated platelets) in the vicinity of the wall surface in Model 3.

degree of haemolysis was based on the time scale of thrombus formation reported by Takahashi *et al.* [5], its accuracy has not been ascertained. The following discussion will, therefore, concern only the platelet aggregation tendencies observed in Figs 15 and 16.

It can be seen in Fig. 15(a) that platelet aggregation in Model 1 started from the upper half of the aneurysm because ADP originating from RBCs was first brought to this region by blood flow (see Fig. 6). By the time eight pulse cycles had elapsed, a swathe of high  $N_1$  had been formed (Fig. 15(b)). The peak value of  $N_1$  reached 3% of the whole platelets after 12 pulsation periods (Fig. 15(c)) and continued to increase thereafter. In Model 3, on the other hand, platelet aggregation was mainly observed near the deep end of the aneurysm where the flow was slower. However, platelet aggregation was not found to progress after the first cycle: the maximum value of  $N_1$  would not exceed 0.8% of the whole platelets even after 11 cycles. This was due to the high-speed flow in Model 3 where ADP and aggregated platelets were quickly flushed out of the aneurysm. Thus, these results obtained by application of the platelet model support the discussion in the first paragraph of this section.

The AR (2.3 for Model 1 and 2.0 for Models 2 and 3) had an influence on the different flow patterns to some extent because the AR represents the relative size of the aneurysm in the longitudinal

direction. However, the larger volume of the aneurysmal dome in Model 1 seems to provide a more reasonable explanation for the dispersion and low-speed region therein. The volume of the dome was so large in Model 1 that the mainstream failed to provide fluid in the dome with enough kinetic energy to allow rapid motion. The degree of platelet aggregation is presumably influenced not only by the AR but also the size of the aneurysmal dome in the lateral direction. The bifurcation angle and direction of aneurysmal protrusion seem to be secondary factors contributing to the degree of platelet aggregation because Models 2 and 3 showed similar flow features in spite of different angles of bifurcation and dome protrusion.

## 5 CONCLUSIONS

Unsteady flow simulation was conducted for three different model aneurysms: Model 1 at a Y-shaped bifurcation, Model 2 at a T-shaped bifurcation and Model 3 which represented more realistic anatomical features of cerebral arteries. Impingements of the main flow upon the aneurysmal neck were observed in all the models. This suggests that haemolysis is likely to occur at the entry points of most cerebral aneurysms. A large region filled with low-speed fluid was found in Model 1 while fluid entering the domes was discharged quickly from aneurysms in Models 2 and 3. Therefore, it can be concluded that platelet aggregation was less active in Models 2 and 3. Computational results using an aggregation model supported this conclusion. The difference in flow patterns was attributed to the volume of the aneurysms. The present study suggests that not only AR but also aneurysmal size in the lateral direction should be taken into consideration when the likelihood of platelet aggregation in aneurysms is discussed.

## ACKNOWLEDGEMENTS

The authors would like to thank two postgraduates from Tokyo University of Science, Mr Noriyoshi Takahashi and Mr Takashi Shimamura, for providing their experimental data. Mr David H. McMahon's advice on English writing is also gratefully acknowledged.

## REFERENCES

- [1] Ujiie, H., Tamano, Y., Sasaki, K. & Hori, T., Is the aspect ratio a reliable index for predicting the rupture of a saccular aneurysm? *Neurosurgery*, **48**(3), pp. 495–503, 2001.
- [2] Weir, B., Amidei, C., Kongable, G., Findlay, J.M., Kassell, N.F., Kelly, J., Dai, L. & Karrison, T.G., The aspect ratio (dome/neck) of ruptured and unruptured aneurysms. *Journal of Neurosurgery*, **99**(3), pp. 447–451, 2003.
- [3] Nader-Sepahi, A., Casimiro, M., Sen, J. & Kitchen, N.D., Is Aspect Ratio A reliable Predictor of Intracranial Aneurysm Rupture? *Neurosurgery*, **54**(6), pp. 1343–1348, 2004.
- [4] Ujiie, H., Tachibana, H., Hiramatsu, O., Hazel, A.L., Matsumoto, T., Ogasawara, Y., Nakajima, H., Hori, T., Takakura, K. & Kajiya, F., Effects of size and shape (aspect ratio) on the hemodynamics of saccular aneurysms: a possible index for surgical treatment of intracranial aneurysms. *Neurosurgery*, **45**(1), pp. 110–130, 1999.
- [5] Takahashi, N., Ujiie, H., Yotoriyama, T., Suzuki, Y., Hori, T. & Kaibara, M., Flow visualization study of the endothelialized glass aneurysm model implanting canine carotid artery (in Japanese with English abs.). *Journal of Japanese Society of Biorheology*, **18**(4), pp. 143–148, 2004.
- [6] Shimano, K., Hayashi, T., Ujiie, H., Ono, T. & Enomoto, Y., Modelling of platelet aggregation in aneurysm, *Proc. of 7th Int. Conf. On Modelling In Medicine and Biology*, ed. C.A. Brebbia, WIT Press: Southampton, pp. 43–52, 2007.

- [7] Torii, R., Oshima, M., Kobayashi, T., Takagi, K. & Tezduyar, T.E., Influence of wall elasticity on image-based blood flow simulations (in Japanese with English abs.). *Transactions of Japan Society of Mechanical Engineers, Series A*, **70(697)**, pp. 1224–1231, 2004.
- [8] Funazaki, K., Higashi, M., Yamada, K., Taniguchi, H. & Tomura, N., Flow-Structure Coupled Analysis of Cerebrovascular Artery with an Aneurysm of Realistic Geometry (in Japanese with English abs.). *Transactions of Japan Society of Mechanical Engineers, Series B*, **73(731)**, pp. 1472–1479, 2007.
- [9] Utter, B. & Rossmann J.S., Numerical simulation of saccular aneurysm hemodynamics: Influence of morphology on rupture risk. *Journal of Biomechanics*, **40(12)**, pp. 2716–2722, 2007.
- [10] Patankar, S.V., *Numerical Heat Transfer and Fluid Flow*, Hemisphere publishing: Washington D.C., pp. 126–131, 1980.
- [11] Shimamura, T., *A Study on Flow in Aneurysms* (in Japanese), Graduation thesis, Tokyo University of Science, Tokyo, 2006.
- [12] Satoh, A., Nakamura, H., Kobayashi, S., Miyata, A., Tokunaga, H., Wada, M. & Watanabe, Y., Surgical approaches and techniques for anterior communicating artery aneurysms: from angioanatomical point of view (in Japanese with English abs.). *Surgery for Cerebral Stroke*, **30**, pp. 240–246, 2002.
- [13] Rhie, C.M. & Chow, W.L., Numerical study of the turbulent flow past an airfoil with trailing edge separation. *AIAA Journal*, **21(11)**, pp. 1525–1532, 1983.
- [14] Shimano, K. & Arakawa, C., Numerical simulation of incompressible flow on parallel computer with the domain decomposition technique, *Parallel Computational Fluid Dynamics: New Algorithms and Applications (Proc. of the Parallel CFD'94 Conference)*, eds N. Satofuka, J. Periaux & A. Ecer, Elsevier: Amsterdam, pp. 189–19, 1995.
- [15] Shimano, K., Okudera, K., Anaguchi, T., Utsumi, N., Saito, M., Sumie, C. & Enomoto, Y., Parallel Computing of Flow in Centrifugal Fan Volute Using Contravariant Physical Velocity, *Parallel Computational Fluid Dynamics: Multidisciplinary Applications (Proc. of the Parallel CFD 2004 Conference)*, eds G. Winter, A. Ecer, J. Periaux, N. Satofuka & P. Fox, Elsevier: Amsterdam, pp. 313–320, 2005.
- [16] Leuprecht, A. & Perktold, K., Computer simulation of non-Newtonian effects on blood flow in large arteries. *Computer Methods in Biomechanics and Biomedical Engineering*, **4**, pp. 149–163, 2001.
- [17] Shimano, K., Yonezu, S. and Enomoto, Y., Acceleration of Unsteady Incompressible Flow Calculation Using Extrapolation Method, *Transactions of Japan Society of Mechanical Engineers, Series B*, **74(745)**, pp. 1896–1902, 2008.
- [18] Shimano, K., Yonezu, S. and Enomoto, Y., Acceleration of Unsteady Incompressible Flow Calculation Using Extrapolation Method, *Proc. of the fourth International Conference on Computational Fluid Dynamics (ICCFD4)*, eds Deconinck, H. & Dick, E., Springer: Berlin, pp. 303–308, 2009.
- [19] Wahap, G., Kobori, T., Takakura, Y., Arai, N., Konishi, Y. & Fukasaku, K., Numerical simulation of Flows in a Pipe with an Aneurismal Sac (Effects of Aneurismal Models and Stents). *Advanced Materials Research*, **33–37**, pp. 1025–1030, 2008.
- [20] Alkhamis, T.M., Beissinger, R.L. & Chediak, J.R., Red blood cell effect on platelet adhesion and aggregation in low-stress shear flow -Myth of Fact? *Transactions of American Society of Artificial Internal Organs*, **34**, pp. 868–873, 1988.
- [21] Evans, E.A., Waugh, R. & Melnik, L., Elastic area compressibility modulus of red blood cell membrane. *Biophysical Journal*, **16**, pp. 585–595, 1976.

# EFFECTS OF DIFFERENT TYPES OF INPUT WAVEFORMS IN PATIENT-SPECIFIC RIGHT CORONARY ATHEROSCLEROSIS HEMODYNAMICS ANALYSIS

S.I. BERNAD<sup>1</sup>, E.S. BERNAD<sup>2</sup>, T. BARBAT<sup>1</sup>, V. ALBULESCU<sup>2</sup> & R. SUSAN-RESIGA<sup>3</sup>

<sup>1</sup>Romanian Academy - Timisoara Branch, Romania.

<sup>2</sup>University of Medicine and Pharmacy "Victor Babes" Timisoara, Romania.

<sup>3</sup>Department of Hydraulic Machinery, "Politehnica" University of Timisoara, Romania.

## ABSTRACT

Accurate fluid mechanics models are important tools for predicting the flow field in the coronary artery for understanding the relationship between hemodynamics and the initiation and progression of atherosclerosis. The purpose of this paper is to assess non-invasively hemodynamic parameters such as disturbed flows, pressure distribution and wall shear stress with computational fluid dynamics (CFD) in human right coronary artery (RCA) using patient-specific data from in vivo computed tomographic (CT) angiography, using two different pulsatile input waveforms. In order to produce a realistic three-dimensional model of the RCA anatomy, CT-datasets were acquired by a four-row-detector CT-scanner. Digital files in Digital Imaging and Communications in Medicine (DICOM) file format, containing cross-sectional information were then imported to CFD software package for reconstruction. The numerical analysis examines closely the effect of a different input waveforms model on the hemodynamic characteristics such as secondary flow, flow separation and wall shear stress in the multiple stenosed RCA.

*Keywords: hemodynamics, input velocity, wall shear stress, stenotic arteries, blood flow distortion, secondary flow, flow separation.*

## 1 INTRODUCTION

Atherosclerosis is a disease of large and medium-size arteries, which involves complex interactions between the artery wall and the blood flow. Both clinical reports and numerical simulations show that hemodynamics plays an important role in the pathogenesis of atherosclerosis [1–5]. It is widely believed that atherosclerosis development and progression are affected by many risk factors, such as static pressure, wall shear stress (WSS), blood viscosity, flow velocity, etc. Vascular geometry is another factor influencing strongly the flow patterns and generating a pre-existing atherogenic hemodynamic environment [6–9].

It is now well known that human atherosclerotic lesions originate preferably at the outer wall of vessel branches or bifurcations and at the inner wall of artery bends, where the blood vessel curvature creates dynamic environments of disturbed flow [6].

Although there are many factors that regulate the vascular remodeling, the endothelial cell and its interaction with the fluid-induced WSS play a key role in the adaptive response of vessels. The fluid-induced WSS is a very small frictional force induced by a viscous fluid flow moving on the surface of solid materials. The endothelial cell is capable of sensing the level and the direction of the WSS induced by the blood flow, and the biomechanical properties of endothelial cell are partially regulated by the WSS [2, 9–11].

Non-invasive imaging techniques coupled with CFD simulations are important tools for studying the flow field in individual human arterial models, and these numerical models are a convenient platform for evaluating the influence of vessel geometry on pathophysiologically relevant biomechanical properties [3, 5, 12].

A detailed hemodynamic evaluation of disturbed flow in the post-stenosis region may give additional insight to understand the progression of atherosclerosis and may have useful clinical value, such as early detection of a highly stenosed artery segment, prediction of future disease progression, and treatment planning [1, 13].

## 2 COMPUTATIONAL FLUID DYNAMICS IN VASCULAR CARDIOLOGY

Over the past two decades, the fluid mechanics of blood flow has been shown to play an important role in arterial adaptation and disease localization [14]. Flow patterns present within complex arterial geometries can be examined through experimental flow studies using large-scale in vitro models. These types of studies are also important for evaluation of diagnostic and therapeutic medical devices and flow measurement techniques. Furthermore, these types of studies are important for the validation of computational fluid dynamics (CFD) codes. With advances in computational speed and CFD codes, numerical simulation of blood flow has become a powerful tool.

Advances in CFD and computer technology are increasing the possibilities of simulation of blood flow in the cardiovascular system. CFD software provides a fast, non-invasive method of assessing surgical techniques, analyzing arterial diseases and examining blood flow in a number of diseased conditions [15–18]. These computational techniques can be used to predict the outcome of surgical and interventional procedures aiding the physicians to decide which is the best treatment for a given individual. Computer simulations can help to design less invasive and more precise procedures, to increase the quality and cost-effectiveness of the therapy and to provide better training for physicians.

## 3 MATERIALS AND METHOD

For the case presented in this paper, spiral CT (computed tomography) was performed for 4 days following the CA (coronary angiography) (44 year old, patient with typical angina symptoms is investigated). A Somatom Sensation 64 Scanner (Siemens Medical Systems, Erlangen, Germany) was used in non-enhanced spiral scan technique with a slice thickness of 2 mm, a table feed of 3 mm/s, and an increment of 2 mm. Data corresponding to the investigated patient is presented in Table 1.

The CA and the spiral CT investigation detected a multiple severe right coronary artery (RCA) stenosis (Fig. 1). According to the NASCET (North American Symptomatic Carotid Endarterectomy Trial) [19] and ECST (European Carotid Surgery Trial) [20] method of stenosis classification, the stenoses severity is illustrated in Table 2.

The percentage diameter reduction for a circular stenosis is  $1-d/D$ , where  $d$  is the diameter of the lumen and  $D$  the diameter of the unoccluded artery (for the present case diameter of section D3).

Table 1: Preoperative patient characteristics.

Variables	Value
Mean age	44
Gender (M/F)	Male
History of MI	No
Previous PTCA	No
Renal insufficiency	No
Cardiovascular risk factor	
Hypertension	Yes
Diabetes	No
Smoke	Yes
Obesity	Moderate
Angiographic data	
RCA stenosis	Multiple/severe

MI = myocardial infarction; PTCA = percutaneous transluminal coronary angioplasty;  
RCA = right coronary artery.

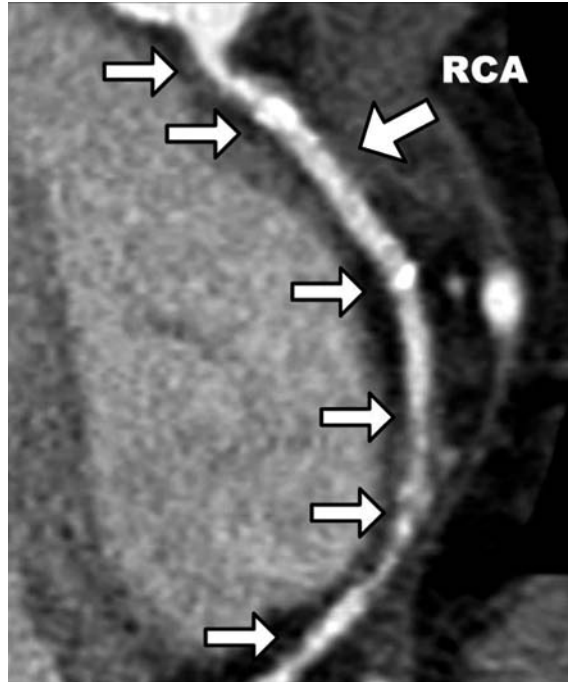


Figure 1: Patient-specific right coronary artery (RCA). Axial tomographic image which indicates a multiple coronary stenosis at the RCA (*arrows*) (64-slice CT).

Table 2: RCA stenosis severity (Fig. 2).

Section	Section diameter (mm)	Section area (mm <sup>2</sup> )	Diameter reduction percentage (%)
D0	3.8	11.3267	–
D1	1.76	2.4621	55
D2	1.81	2.5734	54
D3	3.96	11.7578	–
D4	2.6	5.3025	34
D5	3.84	11.3928	–
D6	1.68	2.2361	57
D7	3.6	10.1818	–
D8	1.6	2.008	60

### 3.1 Computational geometry

A computer aided design (CAD) model of a human RCA lumen was reconstructed from CT scans of a patient. The patient was a 44-year-old male who had a clinically identified stenosis in his RCA. The RCA geometry was reconstructed based on CT images. Images were then segmented in cross-sections perpendicular to the RCA centerline. Figure 1 shows the reconstructed lumen geometry of the RCA viewed from the epicardial, and pericardial sides. The lumen inlet diameter (hydraulic diameter) of the RCA was 3.8 mm. The RCA is modeled to be 52 mm in length with variable diameters,



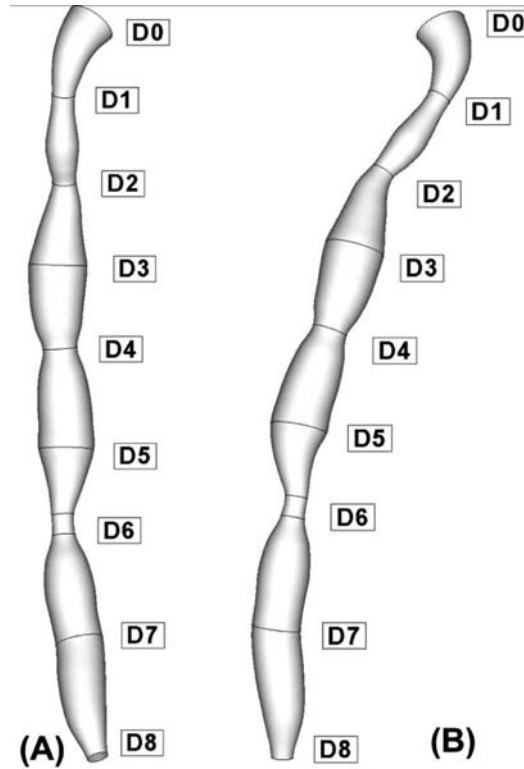


Figure 2: Patient-specific right coronary artery (RCA) geometry reconstruction. Reconstructed 3D geometry: (a) pericardial side; (b) epicardial side.

depending on the stenosis severity. Data corresponding to the reconstructed RCA is presented in Table 2. Good agreement has been demonstrated between coronary artery diameter measurements in the present case and the measurements done by transthoracic echocardiography (TTE) and quantitative coronary angiography (QCA) presented by Kiviniemi *et al.* [21].

An effective meshing procedure in this study is one that can mesh the CT scan image surface geometry without compromising the geometric features. To achieve this task the commercial grid generation software, GAMBIT 2.4.6 (ANSYS FLUENT, ANSYS, Inc.) was utilized [22].

The elements employed to mesh the 3D computational domain of the coronary arterial segment, consisted primarily of regular structured hexahedral elements as well as wedge elements wherever necessary. In order to carry out the mesh sensitivity analysis, numerical simulations were carried out by varying the number of mesh elements in the computational domain. The accuracy of the simulation results was then improved by employing a finer mesh that contained 1,598,752 elements. Figure 3 shows an enlarged view of the reconstructed mesh for the flow dynamic analysis.

### 3.2 Model assumptions

The blood is assumed to be incompressible, with a Newtonian behavior having dynamic viscosity ( $\mu$ ) of 0.00408 Pa and a density ( $\rho$ ) of 1050 kg/m<sup>3</sup>. Johnston *et al.* [23] compared the effects of different blood viscosity models on the WSS distributions in the RCA during the cardiac cycle. Their study

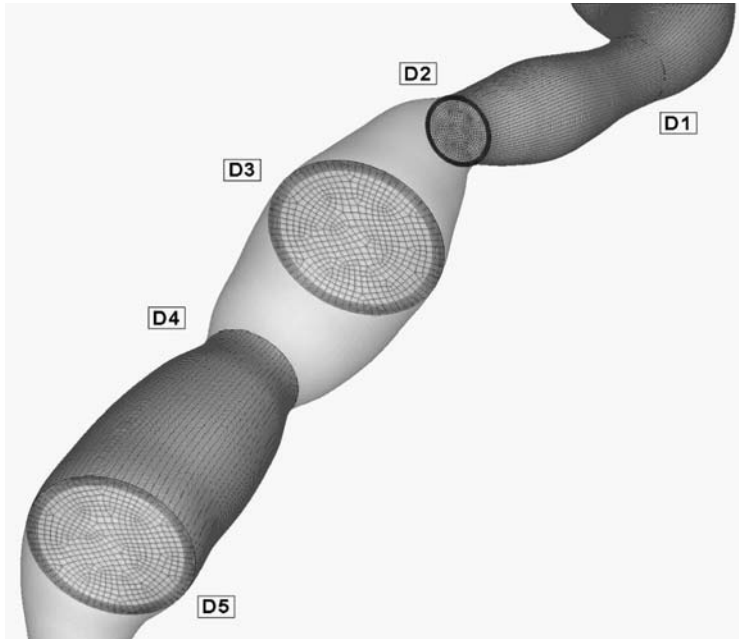


Figure 3: Reconstructed right coronary artery. Computational domain discretization using boundary layer techniques.

showed that the use of a Newtonian blood model is a reasonably good approximation when studying the WSS distribution for transient blood flow in arteries. The wall motion associated with pressure and flow pulsation is believed to be relatively small in constrictions with thickened intima because of the decreased flexibility of the wall. The walls were taken as solid and stiff, and a zero-velocity boundary condition was assumed for the walls, corresponding to a no-slip condition.

The governing equations of motion for the flow dynamic solution, i.e., the continuity equation and the time dependent 3D Navier-Stokes equations for an incompressible viscous fluid were applied in the numerical analysis. Commercial CFD FLUENT 6.3 package [22], parallelized across eight 3.2 GHz Intel processors of a TYANPSC T-650 Rx (Tyan Computer Corporation, Taiwan, parallel computing machine with sixteen 3.2 GHz processors) is used in order to perform the numerical analysis.

Three cycles were simulated to ensure that the flow was truly periodic [24]. Computations were repeated over different meshes to ensure that the numerical solutions were mesh independent. Computations were carried out with various values of physiological parameters to reveal the detailed characteristics of the flow in curved stenotic arteries and to examine the influence of stenosis on the blood flow pattern, including flow separation, secondary flow, WSS level and pressure drop. The time step employed for the unsteady simulations in the study is 0.001 s has been equivalent to using 1000 time steps to compute a single cardiac cycle.

Simulation results were visualized with TECPLOT (Tecplot, Inc., Bellevue, WA).

### 3.3 Flow conditions

In order to evaluate the effects of input function on flow patterns and WSS variation, we used two types of waveform models at the inlet section of the RCA geometry:

Case 1: Pulsatile inlet flow, which is a more realistic approximation of physiologic waveforms [25] presented in eqn (1), since it has a higher peak-to-mean ratio, is obtained using two harmonics and with  $a_1 = -a_2 = 0.75$  (Fig. 4).

$$\bar{u}(t) = \bar{u}_m \left[ 1 + a_1 \sin\left(\frac{2\pi t}{T}\right) + a_2 \cos\left(\frac{4\pi t}{T}\right) \right] \quad (1)$$

Case 2: Pulsatile inlet flow, which is the physiologically realistic case, based on flow and pressure waveforms acquired with an intravascular ultrasound Doppler probe in the RCA [26] (Fig. 5).

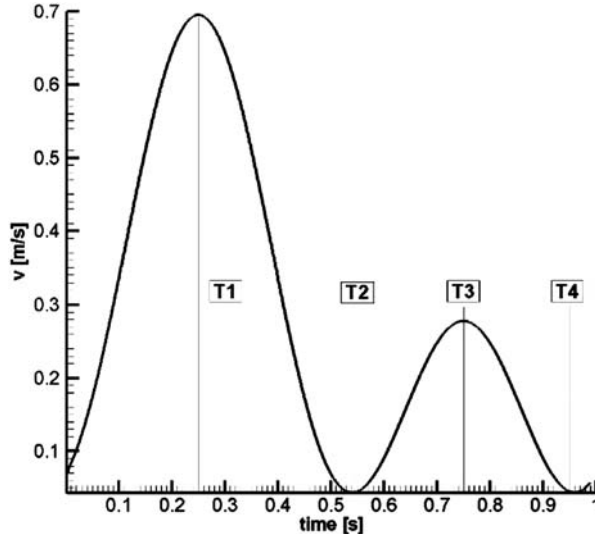


Figure 4: Pulsatile inlet flow waveforms throughout one cardiac cycle used as the input function at the RCA for case 1 (eqn (1)).

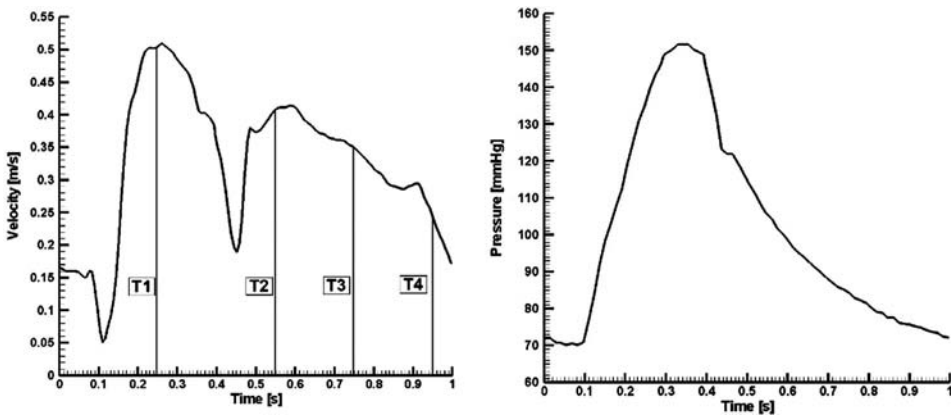


Figure 5: Velocity (left) used as the input function for case 2 and pressure (right) used as the outlet functions, throughout one cardiac cycle for patient with stenosed RCA. Values are based on measurements from the literature [26]. Reference phases at which results are presented are also indicated. The reference phases are the same for both the cases.

Comparisons between the two input wave models are presented in terms of hemodynamic factors (flow patterns, flow velocity, WSS distributions), as it is believed that WSS is a significant factor in the onset of coronary artery disease [27, 28].

For both cases a straight entrance length of 10 inlet cross-section diameters was included at the inlet to avoid the effect of inlet velocity profile on the fluid dynamics at the region of interest [29].

The velocity boundary condition was always specified normal to the inlet cross-section. Five diameter extensions on the downstream side was sufficient to avoid the effect of the outlet zero pressure boundary condition (for case 1) on the fluid dynamics in the stenosed region. For case 2 at the exit section of the outlet extension a physiologically realistic pressure waveform was applied.

Each extension consisted of a straight section that connected the reconstructed RCA geometry with the fixed straight section. Care was taken to ensure that there were smooth connections between the extension sections and the RCA geometry. The influence of the boundary condition on the solution in the region of interest was minimal.

## 4 RESULTS

In this work we modeled blood flow in a stenosed RCA using two different inlet waveforms (a physiologically realistic inlet velocity profile, and one realistic approximation of the physiologic waveforms described by the mean and two harmonic terms, eqn (1)).

Our goal was to quantify the importance of the inlet velocity waveforms for the RCA hemodynamics, in order to guide further modeling studies and to assess the potential importance of the input boundary condition for investigation and the validation of causal links between hemodynamic flow variables and coronary artery pathology.

The RCA is a common site of atherosclerosis, which is linked to hemodynamic factors such as low WSS [11, 26]. The effects of the difference in blood flow waveforms on coronary hemodynamics in RCA were investigated using CFD.

Transient simulations were performed for the stenosed RCA artery described above. Each simulation was from  $t = 0$  to 1.00 s, yielding a heart rate of approximately 64 beats per minute. For case 1, the cardiac cycle period was 1 s, with peak systolic flow occurring at 0.25 s, and peak diastolic flow at 0.75 s. The lengths of the systolic and diastolic phases were 0.6 and 0.4 s, respectively. For case 2, the cardiac cycle period is the same as for case 1, with peak systolic flow occurring at 0.27 s, and peak diastolic flow at 0.59 s. The lengths of the systolic and diastolic periods were 0.34 and 0.66 s, respectively.

Representative data set of the hemodynamics parameters in stenosed RCA are shown at the time values of 0.25 and 0.75 s through the cardiac cycle. These values were chosen as they are representative during the cardiac cycle:  $t = 0.35$  s is at the peak of the systolic phase, and  $t = 0.75$  s corresponds to the middle point of the diastolic phase.

### 4.1 Flow separation and secondary flow

The natural curvature of the RCA is expected to induce significant secondary flow motion or cross-flow motion within the artery. RCA curvature gradually changes the flow in sections D0, D3, D5, D7. Downstream of these sections, the flow is highly three-dimensional, being sharply skewed toward of the RCA wall.

In the spacing between successive constrictions (between: sections D2 and D4; sections D4 and D6; sections D6 and D8) the flow repeatedly undergoes an expansion after each constriction where the separation zone formed in sections D3, D5 and D6 (Fig. 6). Energy loss associated with such flow expansion after each constriction will be large and consequently the pressure drop will be higher (Tables 5 and 6).

Artery section constriction and post-constriction dilations have led to acceleration and rapid deceleration, respectively, including a distortion of flow. Large recirculation regions found in the vicinity of the each constricted section (Fig. 6).

Data corresponding to the velocity field obtained in the reconstructed RCA for both input velocity profiles is presented in Table 3 (at the investigated time  $T1 = 0.25$  s) and Table 4 (at the investigated time  $T4 = 0.75$  s). Good agreement has been demonstrated between coronary blood

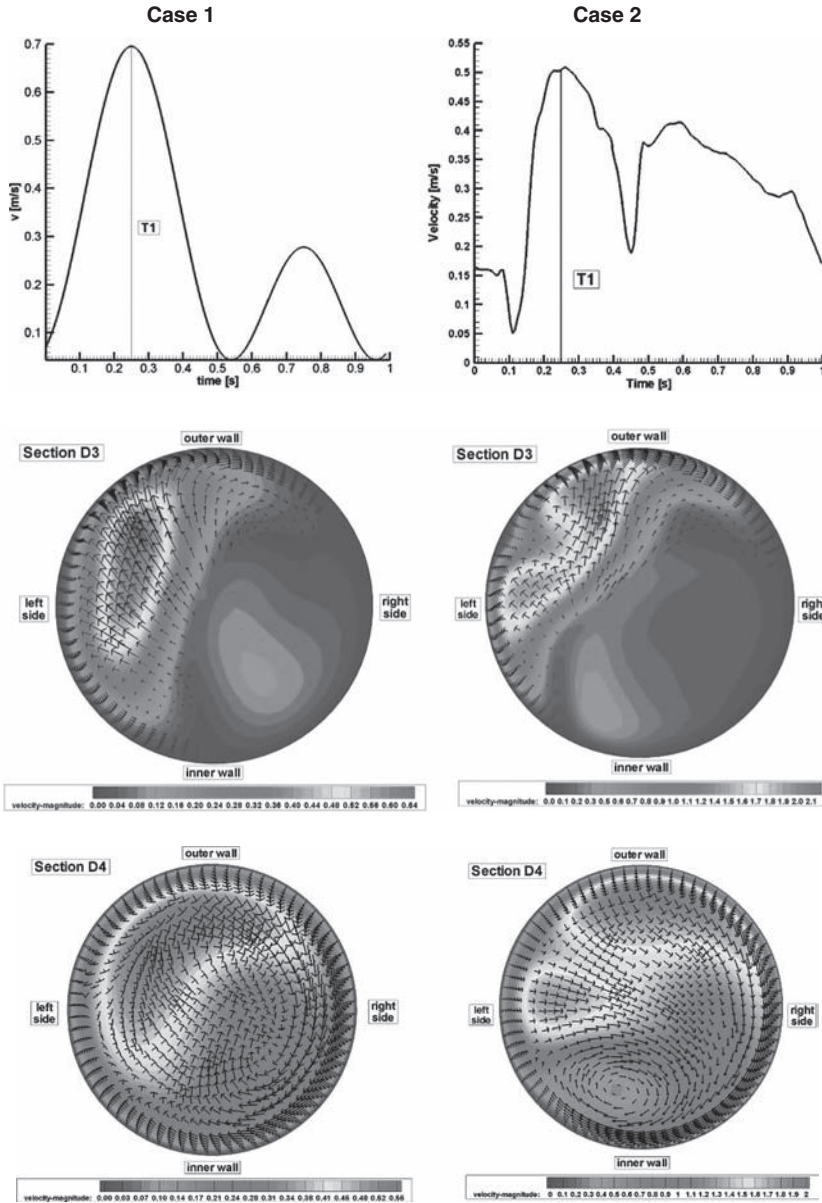


Figure 6: Transverse velocity profiles of the blood flow in stenosed RCA, in selected cross-sections for both input velocity waveforms at the time  $T1 = 0.25$  s.

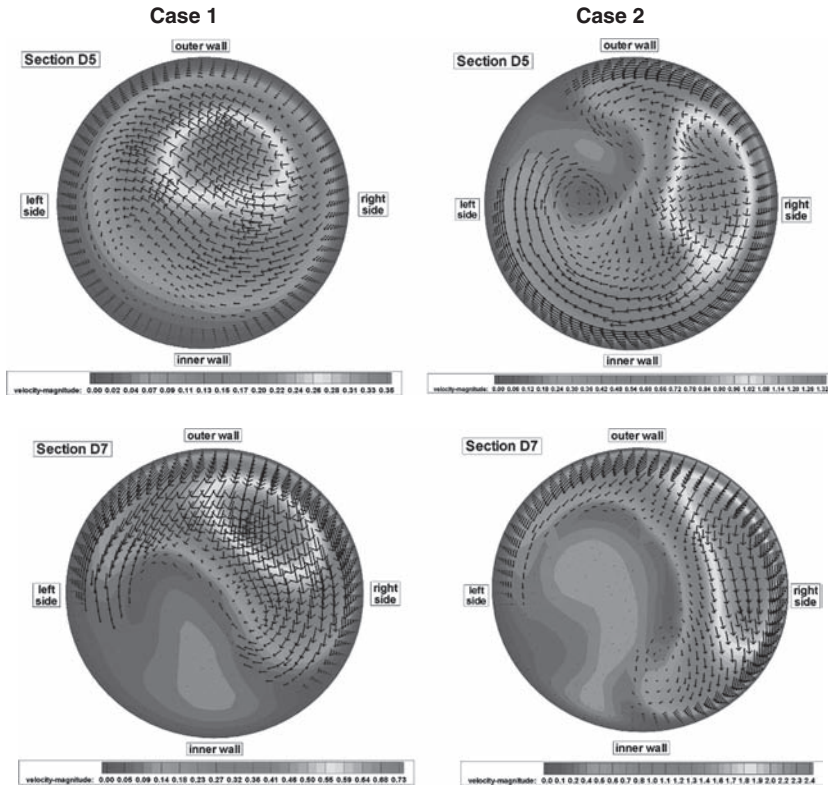


Figure 6: (continued).

Table 3: Blood velocities analysis in the cross-sections of interest defined in Fig. 2 at the time  $T1 = 0.25$  s.

Section	Time T1					
	Case 1		Case 2		Percent difference	
	Vc (m/s)	Vav (m/s)	Vc (m/s)	Vav (m/s)	Vc (%)	Vav (%)
D0	0.281	0.15	0.236	0.505	19	70.3
D1	0.859	0.69	0.905	2.338	5	70.3
D2	0.792	0.66	0.915	2.259	13.4	70.6
D3	0.061	0.15	0.146	0.550	58.2	72.7
D4	0.361	0.32	0.397	1.153	9	72.1
D5	0.253	0.12	0.201	0.470	25.8	74.4
D6	1.043	0.72	1.103	2.450	5.4	70.6
D7	0.100	0.21	0.419	0.780	76.13	73
D8	0.995	0.84	1.079	2.870	7.7	70.7

Vc – velocity magnitude in the center of the investigated sections.

Vav – area weighted average velocity magnitude in the cross-sections of interest.

Table 4: Blood velocities analysis in the cross-sections of interest at the time  $T_4 = 0.75$  s.

Section	Time $T_4$					
	Case 1		Case 2		Percent difference	
	Vc (m/s)	Vav (m/s)	Vc (m/s)	Vav (m/s)	Vc (%)	Vav (%)
D0	0.113	0.0096	0.589	0.349	80.8	97.2
D1	0.381	0.0447	1.863	1.618	79.5	97.2
D2	0.396	0.0429	1.673	1.561	76.3	97.2
D3	0.033	0.0140	0.171	0.379	80.7	96.3
D4	0.178	0.0209	1.003	0.788	82.2	97.3
D5	0.118	0.0083	0.104	0.317	13.4	97.3
D6	0.512	0.0461	2.020	1.681	74.6	97.2
D7	0.148	0.0151	0.221	0.529	33	97.1
D8	0.455	0.0547	2.103	1.985	78.3	97.2

Vc – velocity magnitude in the center of the investigated sections.

Vav – area weighted average velocity magnitude in the cross-sections of interest.

Table 5: Pressure variation in the sections of interest defined in Fig. 2 at the time  $T_1 = 0.25$  s.

Section	Time $T_1$					
	Case 1		Case 2		Percent difference	
	Pc (mmHg)	Pav (mmHg)	Pc (mmHg)	Pav (mmHg)	Pc (%)	Pav (%)
D0	28.21	28.22	324	324.47	91.29	91.30
D1	25.49	25.39	299	298.13	91.47	91.48
D2	24.04	23.81	290	287.69	91.71	91.72
D3	24.38	24.42	291	292.56	91.62	91.65
D4	24.32	24.24	292	291.81	91.67	91.69
D5	24.41	24.43	293	293.78	91.67	91.68
D6	21.38	20.63	260	260.87	91.78	92.09
D7	21.04	21.05	264	264.40	92.03	92.04
D8	17.58	17.45	234	232.68	92.49	92.50

Pc – pressure in the center of the investigated sections.

Pav – area weighted average pressure in the investigated sections.

velocity obtained in present work using input velocity described in case 2 and the measurements presented by Siebes *et al.* [30].

#### 4.2 Pressure

As the physiological pressure conditions were applied at the outlet for case 2 and pressure level 0 is selected at the outlet in case 1.

We selected the reference pressure as the pressure at the outlet in case 2 in order to estimate the percentage difference between the pressure variations in both cases, and to better compare the pressure drop under the effect of different sizes of stenosis.

To understand the pressure–flow relationship, pressure variations across the different sections of the RCA have been evaluated. In Fig. 7 the pressure field drop along the RCA has been plotted covering the total investigated length of the RCA.

Table 6: Pressure variation in the cross-sections of interest defined in Fig. 2 at the time  $T_4 = 0.75$  s.

Section	Time $T_4$					
	Case 1		Case 2		Percent difference	
	Pc (mmHg)	Pav (mmHg)	Pc (mmHg)	Pav (mmHg)	Pc (%)	Pav (%)
D0	8.78	8.78	191	191.42	95.41	95.42
D1	8.21	8.20	178	178.25	95.39	95.40
D2	7.79	7.75	173	172.61	95.50	95.51
D3	7.85	7.85	174	175.22	95.49	95.52
D4	7.79	7.79	175	174.79	95.55	95.55
D5	7.79	7.80	175	175.71	95.55	95.56
D6	7.14	6.97	159	159.27	95.51	95.62
D7	7.05	7.05	161	160.90	95.62	95.62
D8	6.29	6.26	145	144.69	95.67	95.67

Pc – pressure in the center of the investigated sections.

Pav – area weighted average pressure in the investigated sections.

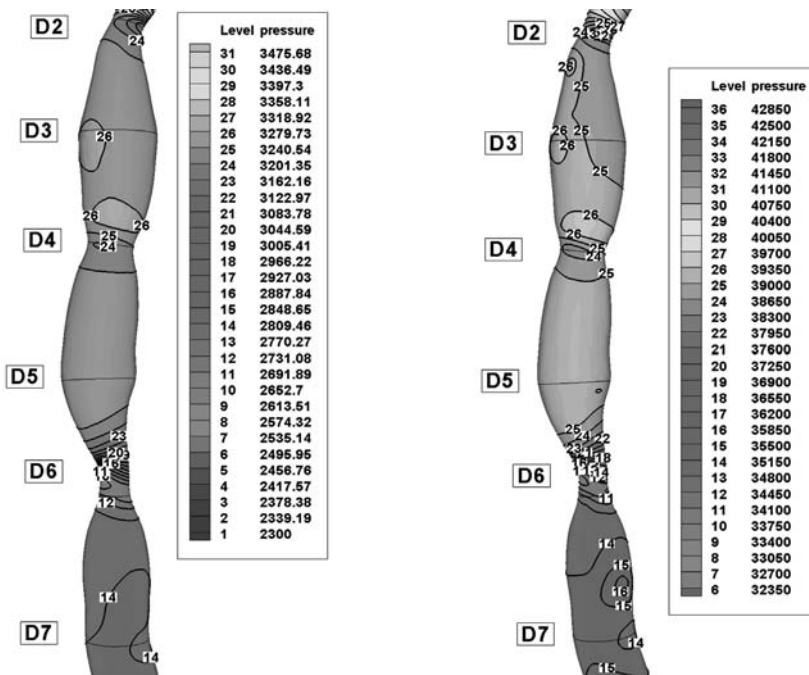


Figure 7: Pressure field (Pa) in stenosed RCA (Fig. 2) for both input velocity waveforms at the investigated time  $T_1 = 0.25$  s.

The knowledge of local pressure becomes mandatory when fluid structure interactions between the fluid and the vessel wall need to be considered. It would thus appear necessary to quantify the accurate pressure profiles within the coronary (Fig. 7).

The main function of wall pressure representing a map of the pressure inside the coronary artery is to push the blood into the capillaries and facilitate diffusion into the myocardium. For the patient



of this study, the wall pressure decreased towards the periphery of the coronary artery with elevated pressure drops in stenotic segments. The increased pressure drop in stenoses reflects the elevated energy needed to drive the flow through these regions.

#### 4.3 Wall shear rates

Wall shear stress and pressure are likely the most relevant parameters from the standpoint of the fluid mechanical involvement in the development of atherosclerosis.

The fluid-induced WSS is a very small frictional force induced by a viscous fluid flow moving on the surface of solid materials. The endothelial cell is capable of sensing the level and the direction of the WSS induced by the blood flow, and the biomechanical properties of endothelial cell are partially regulated by the WSS [2, 4]. The endothelial dysfunction induced by a certain hemodynamic condition is an elemental feature in the formation of atherosclerotic plaque. It is widely believed that atherosclerosis development and progression are affected by many risk factors, such as static pressure, WSS, blood viscosity, flow velocity, etc.

The magnitude and direction of WSS influence inflammatory processes in the vessels. Although the interaction of WSS and inflammation involves a complicated cascade, slow and turbulent flow condition has been shown to induce gene expression of proinflammatory molecules in the endothelial cells [9, 10].

The shear rate ( $\gamma$  (1/s)) for a Newtonian one-directional flow in a cylindrical tube is equal to the velocity gradient with respect to radial position:

$$\gamma = -\frac{dv}{dr} \quad (2)$$

where  $v$  (m/s) is the axial velocity and  $r$  (m) is the radial distance from the center of the vessel. The SS is the force per unit area applied to a fluid layer producing its movement relative to the adjacent layers and is equal to the product of shear rate and the viscosity:

$$\tau = \mu \cdot \gamma = -\mu \frac{dv}{dr} \quad (3)$$

Because the vessel narrows at the stenosis, the velocity at the center of the vessel increases due to the conservation of mass law. The velocity gradient at the wall and the resulting SS is maximum at the narrowest portion of the stenosis (Fig. 8). Along the stenosed arterial wall, the SS varies significantly from point to point. The SS, very low outside the stenosis, suddenly increases with the narrowing diameter, and reaches a maximum at the smallest diameter inside the stenosis (Fig. 8). Increasing the amount of stenosis usually reduced the flow through the stenosis. However, due to the cubic dependence of shear on diameter, the overall effect is to increase the SS.

Parallel to the changes of WSS, the flow pattern was more variable and inconsistent in the vicinity of the constriction (Tables 7 and 8). Artery section constriction and post-constriction dilatations have led to acceleration and rapid deceleration, respectively, including a flow distortion.

## 5 DISCUSSION

### 5.1 Flow separation

Various patterns of transverse velocity fields at radial cross-sections demonstrated a significant secondary flow in the curved arteries and a strong effect of stenosis on this flow dynamic phenomenon.

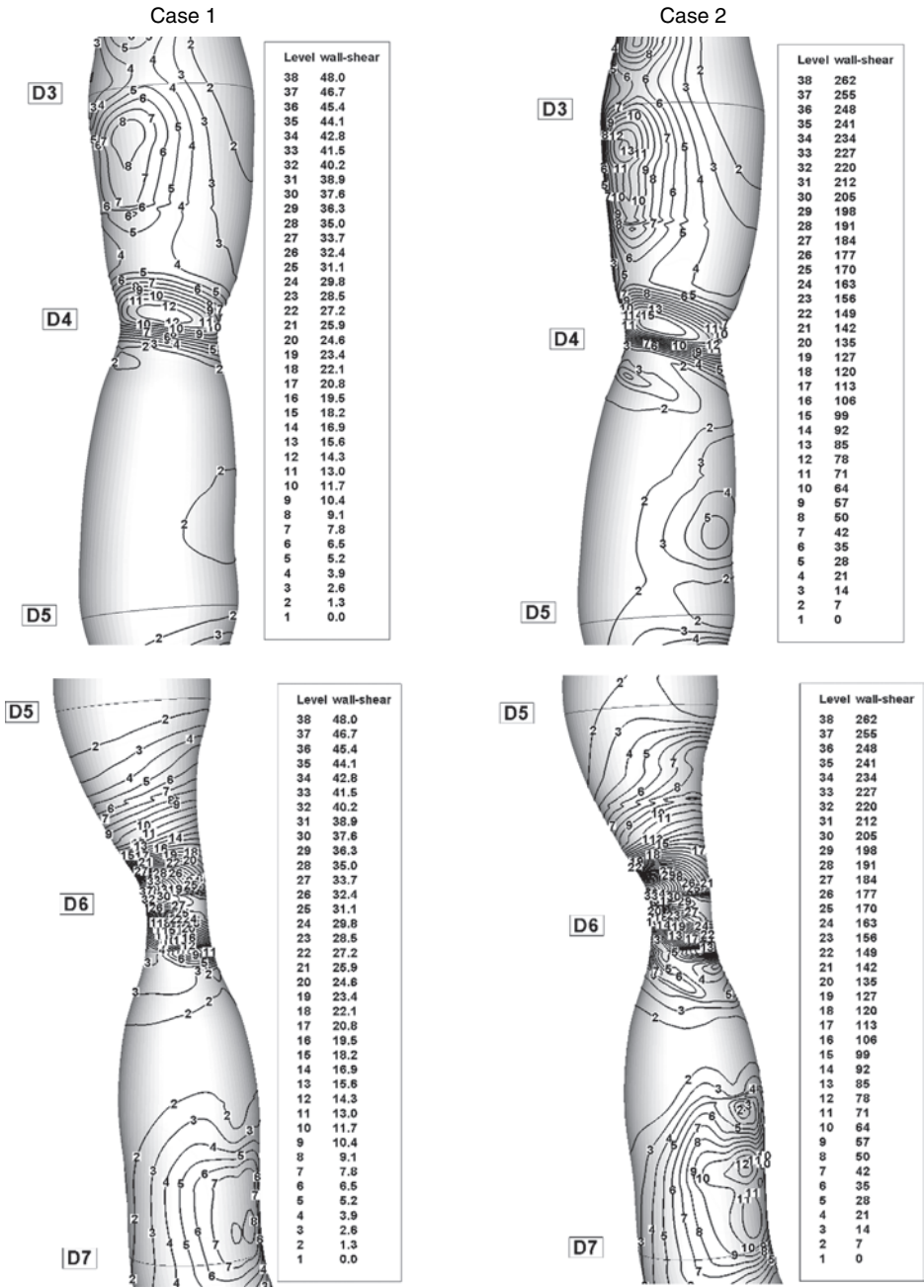


Figure 8: Contour plot of WSS magnitude in the sections of interest defined at the time  $T1 = 0.25$  s: case 1 (left column); case 2 (right column).

Table 7: Minimum/maximum shear rates (Pa) in the cross-sections (time T1 = 0.25 s).

Section	Time T1			
	Case 1		Case 2	
	WSS min (Pa)	WSS max (Pa)	WSS min (Pa)	WSS max (Pa)
D0	2.00	4.00	7	14.00
D1	26.00	31.00	140	168.00
D2	12.00	34.00	63	133.00
D3	1.00	2.00	7	49.00
D4	6.00	15.00	21	91.00
D5	1.00	2.00	7	9.00
D6	4.00	42.00	154	238.00
D7	2.00	4.00	7	56.00
D8	38.00	44.00	196	231.00

Table 8: Minimum/maximum shear rates (Pa) in the cross-sections (time T4 = 0.75 s).

Section	Time T4			
	Case 1		Case 2	
	WSS min (Pa)	WSS max (Pa)	WSS min (Pa)	WSS max (Pa)
D0	0.50	0.80	4	5.00
D1	6.30	8.50	88	100.00
D2	3.80	11.00	36	124.00
D3	0.40	0.50	4	28.00
D4	2.00	3.00	24	52.00
D5	0.20	0.30	4	8.00
D6	8.00	11.80	100	148.00
D7	0.30	1.30	4	32.00
D8	10.00	11.80	132	140.00

It was found that the secondary flow became stronger and the pattern varied irregularly in the downstream curved stenotic arteries due to the presence of a stenosis (Fig. 6).

Stenoses and post-stenotic dilatations have led to acceleration and rapid deceleration, respectively, including a distortion of flow. Large recirculation regions found in the vicinity of the each constricted section. Post-stenotic deceleration of blood flow induces flow separation and recirculation zones (vortices). Such regions of flow separation and stasis are favored sites for the development of thrombosis and atherosclerosis [8]. A closer inspection on these patterns reveals that complex recirculation zones develop in the vicinity of the sections D3, D5 and D7 of the RCA during systolic phase of both types of the input waveforms (Fig. 6). Appearance of these recirculation zones coincides with inflow deceleration during that period of the cardiac cycle. These particular areas coincide with the regions of minimum WSS (Fig. 8).

## 5.2 Pressure

Pressure wave propagation and reflection are not incorporated in the present model. In spite of that, the current approach is valid in the branchless RCA model given the expected long pressure wavelengths.

In patients with multiple stenoses within the same coronary artery, coronary pressure investigation can uniquely determine the separate hemodynamic effects of the individual stenoses in sequence [31]. For clinical practice, pressure recording at maximum hyperemia provides important information, which can help objectively select which of several stenoses is most appropriate for PTCA. This information will also allow clinicians to avoid performing unnecessary procedures that increase the risk of restenosis without a hemodynamic benefit.

### 5.3 Wall shear stress

Wall shear stress is another important parameter in the study of stenotic flow. Gibson *et al.* [11] investigated the relation between vessel WSS and the rate of atherosclerosis progression by means of quantitative angiography. Their results showed that there was a significant correlation between low shear stress and an increased rate of atherosclerosis progression.

The change of WSS throughout the cardiac cycle highly correlated to flow velocities. The WSS characterizes the forces that longitudinally act on the vessel wall. These forces were high when the blood flow parallel to the wall was fast. The maximum WSS spatial variation was approximately 46 Pa in stenosed sections D4 and D6 (Fig. 8 and Table 7) whereas the corresponding maximum wall pressure drop reached 460 Pa, for case 1 at the time  $T_1 = 0.25$  s. For case 2, the WSS maximum spatial variation is 260 Pa in sections D4 and D6, corresponding to the maximum pressure drop reached 1600 Pa.

### 5.4 Study limitations

Some limitations of our study should be pointed out. First, the heart movement and the movement of the coronary arteries due to muscle tension cannot be simulated yet, therefore, not included in the present calculations. Second, we modeled only the trunk of the RCA by ignoring all of its branches. Third, in this model vessel walls are assumed rigid.

Zeng *et al.* [32] have incorporated the effects of physiologically realistic arterial motion into a simulation of blood flow patterns in the RCA. Our results show that arterial motion had little effect on the WSS distribution within the RCA, and that flow in the moving artery followed the instantaneous dynamic geometry quite closely. These results agree with the findings of other groups [33, 34].

Localized high stresses in the vessel wall have been found to relate to local disease development [35]. Furthermore, it has been indicated by numerous studies that fluid dynamics plays an important role in the initiation and development of atherosclerosis [36, 37] and it is possible that certain arterial motion may promote atherosclerosis by creating or exacerbating a pathogenic fluid dynamic environment.

## 6 CONCLUSION

In the work described here, we compared the fluid dynamics for the same arterial segment using two different input pulsatile conditions.

Employing a pulsatile flow curve from the literature, we compared the computed axial velocity distribution, WSS and pressure distribution at selected cross-sections, between both input waveforms investigated. We therefore conclude that the effect of simplification of the real inlet velocity profile in the RCA will significantly affect conclusions drawn from the hemodynamic parameters of WSS, pressure distribution, velocity field and secondary flow development, in realistic models of the human stenosed RCA. However, it is conceptually important to realize that one stenosis influences the hemodynamic effects of another in a sequence that may result in a mutual underestimation of the severity of each unless stenosis interaction is accounted for.

The study also provides awareness that the presence of one stenosis in a coronary artery influences the hemodynamic appearance of the other and, consequently, that treating one lesion will unmask the true severity of the second. As shown in this study, it is possible to calculate this effect quantitatively by measuring pressures at the relevant sites within the artery.

The influence of a distal stenosis on the hemodynamic appearance of a proximal stenosis is generally larger than that of a proximal stenosis on a distal one (Tables 3–6).

The fluid, dynamic interaction of multiple sequential stenoses in coronary arteries is complex, often unexpected, and cannot be adequately assessed by visual interpretation on the coronary angiogram. Assessment of shear stress, along with percent stenosis, in arterial lesions might prove to be a valuable diagnostic tool to identify patients at risk of developing acute platelet thrombus formation in stenosed arteries. Computer flow models can be utilized in conjunction with human coronary angiography to study flow characteristics for plaques of different sizes and shapes in patients with stable and unstable angina.

Wall shear stress and its interaction with the endothelial cell and smooth muscle cell regulate not only the vessel diameter but also the proliferation of endothelial and smooth muscle cells, endothelial permeability, and inflammation in the vessels. Laminar and physiologic shear stress is one of the crucial factors to maintain the proper level of NO, a key mediator of vessel behavior. Attenuation of NO is one of the earliest changes preceding endothelial dysfunction. Endothelial dysfunction induced by slow or turbulent flow condition promotes atherosclerosis in conjunction with such systemic risk factors as hypercholesteremia, hypertension, diabetes, and smoking.

#### ACKNOWLEDGMENTS

The present research has been supported by the Romanian National Authority for Scientific Research through the CNCSIS 798/2008 project, contract no: 590/2009.

#### REFERENCES

- [1] Buchanan, J.R. & Kleinstreuer, C., Simulation of particle-hemodynamics in a partially occluded artery segment with implications to the initiation of microemboli and secondary stenoses. *Journal of Biomechanical Engineering*, **120**, pp. 446–454, 1998.
- [2] Ciu, J.-J., Wang, D.L., Chien, S., Skalak, R. & Usami S., Effects of disturbed flow on endothelial cells. *Journal of Biomechanical Engineering*, **120**, pp. 2–8, 1998.
- [3] Marsahall, I., Zhao, S., Papathanasopoulou P., Hoskins P. & Yun Xu X., MRI and CFD studies of pulsatile flow in healthy and stenosed carotid bifurcation models. *Journal of Biomechanics*, **37**, pp. 679–687, 2004.
- [4] Sun, N., Torii R., Wood, N.B., Hughes A.D., Thom S.A.M., & Xu Y.X., Computational modeling of LDL and albumin transport in an in vivo CT image-based human right coronary artery. *Journal of Biomechanical Engineering*, **131**, pp. 1–9, 2009.
- [5] Frauenfelder, T., Boutsianis, E., Schertler T., *et al.*, In-vivo flow simulation in coronary arteries based on computed tomography datasets: feasibility and initial results. *Eur Radiol*, **17**(5), pp. 1291–1300, 2007.
- [6] Liu, B., The influences of stenosis on the downstream flow pattern in curved arteries. *Medical Engineering & Physics*, **29**, pp. 868–876, 2007.
- [7] Sherwin, S.J. & Blackburn, H.M., Three-dimensional instabilities and transition of steady and pulsatile axisymmetric stenotic flows. *Journal Fluid Mechanics*, **533**, pp. 297–327, 2005.
- [8] Dodds, S.R., The haemodynamics of asymmetric stenoses. *European Journal of Vascular Endovascular Surgery*, **24**, pp. 332–337, 2002.

- [9] Zeng, D., Boutsianis, E., Ammann, M., Boomsma, K., Wildermuth, S. & Poulidakos, D., A study of the compliance of a right coronary artery and its impact on wall shear stress. *Journal of Biomechanical Engineering*, **130**, pp. 041014–11, 2008.
- [10] Truskey, G.A., Barber, K.M., Robey, T.C., Lauri, A.O. & Combs, M.P., Characterization of a sudden expansion flow chamber to study the response of endothelium to flow recirculation. *Journal of Biomechanical Engineering*, **117**, pp. 203–210, 1995.
- [11] Gibson, C.M., Diaz, L., Kandarpa, K., *et al.*, Relation of vessel wall shear stress to atherosclerosis progression in human coronary arteries. *Arteriosclerosis Thrombosis*, **13(2)**, pp. 310–315, 1993.
- [12] Tateshima, S., Tanishita, K. & Vinuela, F., Hemodynamics and cerebrovascular disease. *Surgical Neurology*, **70**, pp. 447–453, 2008.
- [13] Hyun, S., Kleinstreuer, C. & Archie, J.P. Jr, Computational particle-hemodynamics analysis and geometric reconstruction after carotid endarterectomy. *Computers in Biology and Medicine*, **31**, pp. 365–384, 2001.
- [14] Spicer, S.A. & Taylor, C.A., Simulation ased Medical Planning for Cardiovascular Disease: Visualization System Foundations. *Computer Aided Surgery*, **5**, pp. 82–89, 2000.
- [15] Bernad, S.I., Bernad, E. & Mihalas, G.I., Numerical investigation of blood flow in the arterial stenosis, *Proc. of the Medical Informatics Europe - MIE2003*, eds Baund, R., Fieschi, M., Le Beux, P. & Ruch, P., IOS Press: Amsterdam, The Netherlands, pp. 3–8, 2003.
- [16] Rathish Kumar, B.V., Yamaghuchi, T., Liu, H. & Himeno, R., A numerical study of an unsteady laminar flow in a doubly constricted 3D vessel. *International Journal for Numerical Methods in Fluids*, **38**, pp. 1159–1176, 2002.
- [17] Shahcheraghi, N., Dwyer, H.A., Cheer, A.Y., Barakat A.I. & Rutaganira T., Unsteady and tree-dimensional simulation of blood flow in the human aortic arch. *Journal of Biomechanical Engineering*, **124**, pp. 378–387, 2002.
- [18] Yung, C.N., De Witt, K.J., Subramanian, S., Afjeh, A.A. & Keith, T.G., Three-dimensional pulsatile flow through a bifurcation. *International Journal of Numerical Methods for Heat & Fluid Flow*, **7(8)**, pp. 843–862, 1997.
- [19] Eliasziw, M., Smith, R.F., Singh, N., *et al.*, Further comments on the measurement of carotid stenosis from angiograms: North American Symptomatic Carotid Endarterectomy Trial (NASCET) Group. *Stroke*, **25**, pp. 2445–49, 1994.
- [20] Rothwell, P.M., Eliasziw, M., Gutnikov, S.A., *et al.*, Analysis of pooled data from the randomized controlled trials of endarterectomy for symptomatic carotid stenosis. *Lancet*, **361**, pp. 107–16, 2003.
- [21] Kiviniemi, T.O., Saraste, M., Koskenvuo, J.W., *et al.*, Coronary artery diameter can be assessed reliably with transthoracic echocardiography. *American Journal Physiology. Heart Circulatory Physiology*, **286**, pp. H1515–H1520, 2004.
- [22] FLUENT 6.3 User's Guide, Ansys Fluent Incorporated, 2006.
- [23] Johnston, B.M., Johnston, P.R., Corney, S., Kilpatrick, D., Non-Newtonian blood flow in human right coronary arteries: transient simulations. *Journal of Biomechanics*, **39**, pp. 1116–1128, 2005.
- [24] Stroud, J.S., Berger, S.A. & Saloner, D., Numerical analysis of flow through a severely stenotic carotid artery bifurcation. *Journal of Biomechanical Engineering*, **124**, pp. 9–20, 2002.
- [25] Sherwin, S.J. & Blackburn, H.M., Three-dimensional instabilities and transition of steady and pulsatile axisymmetric stenotic flows. *Journal of Fluid Mechanics*, **533**, pp. 297–327, 2005.
- [26] Torii, R., Wood, N.B., Hadjiloizou, N., Dowsey, A.W., Wright, A.R., Hughes, A.D., Davies, J., Francis, D.P., Mayet, J., Yang, G-Z., Thom, S.A., & Yun, X.X., Differences in coronary artery haemodynamics due to changes in flow and vascular geometry after percutaneous coronary intervention. *Heart*, **94**, pp. A1–A4, 2008.

- [27] Giddens, D.P., Zarins, C.K., & Glagov, S., Response of arteries to near wall fluid dynamic behavior. *Applied Mechanics Review*, **43**(2), pp. S98–S102, 1990.
- [28] Ku, D., Giddens, D., Zarins, C., & Glagov, S., Pulsatile flow and atherosclerosis in the human carotid bifurcation: positive correlation between plaque and low and oscillating shear stress. *Arteriosclerosis*, **5**, pp. 293–302, 1985.
- [29] Liu, Y., Lai, Y., Nagaraj, A., Kane, B., Hamilton, A., Greene, R., McPherson, D.D., & Chandran, K. B., Pulsatile flow simulation in arterial vascular segments with intravascular ultrasound images. *Medical Engineering & Physics*, **23**(8), pp. 583–595, 2001.
- [30] Siebes, M., Verhoeff, B.-J., Meuwissen, M., de Winter, R.J., Spaan, J.A.E., & Piek, J.J., Single-wire pressure and flow velocity measurement to quantify coronary stenosis hemodynamics and effects of percutaneous interventions. *Circulation*, **109**, pp. 756–762, 2004.
- [31] Pijls, N.H.J., De Bruyne, B., Jan Willem Bech, G., Liistro, F., Heyndrickx, G.R., Bonnier, H.J.R.M & Koolen J.J., Coronary pressure measurement to assess the hemodynamic significance of serial stenoses within one coronary artery: validation in humans. *Circulation*, **102**, pp. 2371–2377, 2000.
- [32] Zeng, D., Ding, Z., Friedman, M.H., Ethier, C.R., Effects of cardiac motion on right coronary artery hemodynamics. *Annals of Biomedical Engineering*, **31**, pp. 420–429, 2003.
- [33] Qiu, Y. & Tarbell, J.M., Numerical simulation of pulsatile flow in a compliant curved tube model of a coronary artery. *Journal of Biomechanical Engineering*, **122**, pp. 77–85, 2000.
- [34] Santamarina, A., Weydahl, E., Siegel, J.M. Jr., & Moore, J.E. Jr., Computational analysis of flow in a curved tube model of the coronary arteries: effects of time-varying curvature. *Annals of Biomedical Engineering*, **26**, pp. 944–954, 1998.
- [35] Delfino, A., Stergiopulos, N., Moore, J.E. Jr., & Meister, J.J., Residual strain effects on the stress field in a thick-wall finite-element model of the human carotid bifurcation. *Journal of Biomechanics*, **30**, pp. 777–786, 1997.
- [36] Fry, D.L., Acute vascular endothelial changes associated with increased blood velocity gradients. *Circulation Research*, **22**, pp. 165–197, 1968.
- [37] Nerem, R.M., Vascular fluid mechanics, the arterial wall, and atherosclerosis. *Journal of Biomechanical Engineering*, **114**, pp. 274–282, 1992.

# THE INFLUENCE OF HEART STRESS ON THE BRAIN: A PRELIMINARY STUDY

A.K. MACPHERSON<sup>1</sup>, S. NETI<sup>1</sup>, M. AVERBACH<sup>2</sup>, P.A. MACPHERSON<sup>3</sup>, C. CHUTAKOSITKANON<sup>1</sup>  
& D. NATHANSON<sup>2</sup>

<sup>1</sup>Institute of Biomedical Engineering and Mathematical Biology, Lehigh University, USA.

<sup>2</sup>Division of Cardiology, St Lukes Hospital, USA.

<sup>3</sup>Department of Applied Technology, Rogers State University, USA.

## ABSTRACT

The interaction between the cardiac hemodynamics and brain activity has been extensively studied in the past. However these studies have involved not only an increase in heart rate but also an increase in blood pressure. One method to evaluate for underlying coronary artery disease is to perform stress testing. Often, myocardial stress is achieved by the patient walking on a treadmill or riding a stationary bicycle while being monitored. In patients that are unable to exercise, pharmacologic stress testing is performed, either with vasodilatory agents (e.g. adenosine) or dobutamine, which is a pro-inotropic and chronotropic drug. During dobutamine infusion, the heart rate increases, but there is a negligible increase in blood pressure. The result is that the heart rate increases as a function of the dosage. Thus by monitoring brain activity while patients are undergoing dobutamine stress testing the effect of increased blood pressure on the brain is removed. It was found in the results of one patient that there are five areas of the brain which show a change in the frequency of EEG activity that is a function of dobutamine dosage. Using Fourier transforms it was established that this change occurred at a frequency around 12.5 Hz. The regions of the brain where the increased activity were a function of heart rate occurred in the CZ-PZ, C4-P4, T5-O1, T4-T6 and C3-P3 regions. In undertaking these calculations it was realized that the stress on the ventricle could be calculated. The physicians monitor ECG of the patient to evaluate the cardiac status of the patient. Since currently the attending physician does not have data on the stress being applied to the myocardium, it would be useful to have this calculated on a real time basis. The motivation for the present preliminary study is to both investigate the feasibility of producing such information for clinicians as well as to investigate the variation between different patients as the heart rate varies. It was found that generally the surface shear stress increased with heart rate around most of the left ventricle. While the time averaged shear stress may be important for diagnosis the maximum shear stress probably is the limiting factor in terminating testing.

*Keywords: brain, diagnostic tool, echocardiogram, electroencephalogram, frequency, heart, stress.*

## 1 INTRODUCTION

The physically verified data on the interaction of the heart and brain is rather limited. It has not been possible to identify specific parts of the brain which results in specific actions of the heart. It may be that this is not the way the heart and brain interact. Such a conclusion is reached in [1]. An extensive review of the key experiments on how the brain regulates the cardiovascular system are examined. From this review it does not appear that there is sufficient compelling evidence to determine exactly which portions of the brain controls the heart. The control of the muscle fibers in the wall of blood vessel provides an indication of the difficulty of reaching final conclusions on the brain–heart interaction. It was discovered in the 19th century that there existed a vasomotor system of nerve fibers which controlled the muscle fibers in the wall of blood vessels. Today it is still unclear whether the spontaneous activity in the vasomotor nerves arises from the intrinsic activity of pacemaker cells or from assemblies of neurons. In addition it is suggested that the hypothalamus plays a significant role in different vascular responses. There are other open questions such as in heart failure [1] ‘Is it a signal from the heart to the brain that results in the CNS changes or are there changes occurring first in the supramedullary regions of the brain?’ Based on the ability of the body to deliver blood to



organs where the blood is needed the idea of command neurons is suggested. This could lead to the brain being the cause of hypertension and congestive heart failure.

There are some areas where the interaction is fairly well established. One is a system termed the baroflex which controls the arterial blood pressure. It is suggested in [2] that a complete physical description of the various components of the baroflex have been developed. As an understanding, based on physical observation, of the behavior of the baroflex is unknown a mathematical model is proposed in [2]. Based on that model it was shown there is considerable feedback between the pressure regulators and the heart rate. The interaction occurs both through the parasympathetic and the sympathetic systems.

An experiment close to the present work was undertaken in [3]. The objective of the study was to construct a model for determining the effect of stress on patients. As part of the study, physical load was induced in a subject by exercising on a bicycle. An extensive monitoring system of blood pressure, heart rate, respiration, body temperature, and electroencephalography (EEG) signals was setup. Although only one EEG recording site is mentioned in the paper it appears that a number of sites were recorded. The conclusions reached were 'Two circumscribed clusters of significant association between heartbeat-evoked potential (HEP) and cardiac output change (independent of changes in systolic blood pressure) were observed in left temporal and lateral frontal regions. We observed no overall alteration across electrodes in the amplitude of HEP (455–595 ms after R wave) as a function of mental stress'. This result suggests that a specific connection between heart rate and two regions of the brain were established. Unfortunately due to the exercise there were increases in blood pressure, temperature and respiration rate as well as heart rate. The analysis of the test results of 16 subjects indicated that these factors did not influence the heart-brain interaction. However for the purpose of the study, the tests were undertaken on healthy subjects. In a hospital environment involving a wide variety of patients, the results may be different. In [4] it was found on testing 10 patients with average age 59 years and all suffering from some heart disease that 'Across patients, HEP amplitude at left temporal and lateral frontal electrode locations correlated with stress-induced changes in cardiac output, consistent with an afferent cortical representation of myocardial function during stress'. It is known that the effects of shear stress on the heart are very extensive. Two surveys [5, 6] showed that stress can cause changes in the genetic structure of the heart.

Dobutamine acts to increase the heart rate and dilates the arteries. Thus the blood pressure does not increase so the baroreceptors do not transmit signals to the brain. In addition, the temperature does not change as in the standard exercise stress test. This provides a clean experiment where only the motion of the ventricle transmits signals to the brain. Thus the possible effects of these variables are removed from the results. This is achieved by the injection of dobutamine. Under conditions where, due to reduced physical capability, patients cannot undertake the usual exercise stress test, then the heart is stressed by dobutamine injections at various rates. For the purposes of analysis the results obtained are superior to those obtained from an exercise stress test as dobutamine dilates the arteries neither the patient's blood pressure nor temperature increases.

## 2 METHODS OF EXPERIMENTS AND CALCULATION

A patient who was scheduled to undergo a dobutamine stress test was instrumented with 19 electrodes in the standard positions on the scalp (Fig. 1). At the same time, ECG results were obtained while the dobutamine was administered. There were results from the use of three different dosages of dobutamine. These were 0, 1560 and 2750 mics/min. As the usual designation of the injection is 20 and 35 mics/kg/min these designations have been used below. In order to establish any frequency changes due to dobutamine the EEG results were analyzed using MATLAB to obtain the Fourier transforms.

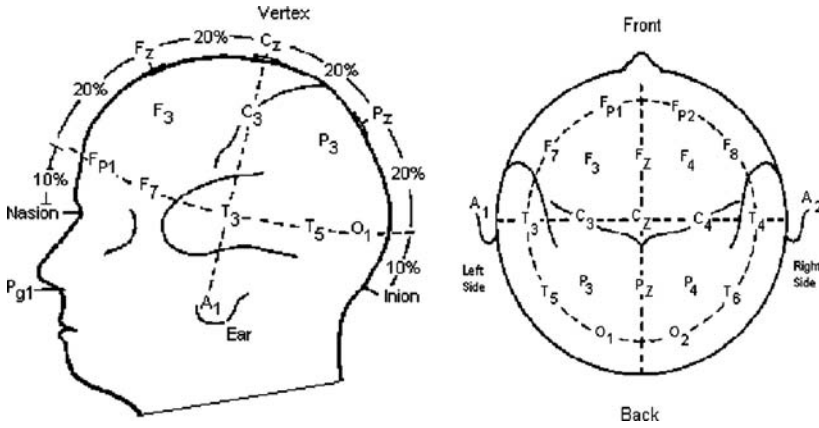


Figure 1: Electrode positions on skull. From website by Eric Chudler, University of Washington.

It was of interest to establish the stress level on the heart at each dosage. This was undertaken by firstly calculating the blood flow. The general method of calculation used here has been described previously [7–9]. The solution is in two dimensions. In the solution the blood flow into the left atrium is simulated by a source distributed throughout the atrium. In order to conserve mass sinks are distributed around the periphery of the integration domain. The change in shape is obtained from the echocardiograms and used as boundary conditions for the flow. The source strength has to match the change in volume of the ventricle. The valves have to be modeled as thicker than in reality as Lagrangian integration must go around both sides of the valve. The Navier-Stokes equations are then solved with a predictor corrector scheme [7].

The Navier–Stokes equations defined on an  $x$ - $y$  Cartesian co-ordinate system for an incompressible fluid are

$$\rho \left( \frac{\partial \hat{u}}{\partial t} + \hat{u} \cdot \nabla \hat{u} \right) + \nabla p = \mu \nabla^2 \hat{u} + \hat{F} \quad (1)$$

$$\nabla \hat{u} = 0 \quad (2)$$

where  $\hat{u}$  is the blood velocity vector,  $\rho$  the density,  $t$  the time,  $p$  the pressure, and the viscosity is  $\mu$ .

The boundary force  $\hat{F}$  arising from the heart muscles is

$$\hat{F}(\hat{x}, t) = \int_0^L \hat{f}(s, t) \delta(\hat{x} - \hat{X}(s, t)) ds \quad (3)$$

Here  $\hat{f}$  is the force on the boundary element at the point  $s$  defined on a Lagrangian system where  $\hat{x}$  is defined on the Cartesian system and  $\hat{X}^n$  is the  $n$ th point on the Lagrangian system,  $L$  the circumference of the ventricle. If  $\hat{f}$  is known then it would be used. In the present case the value of  $\hat{f}$  varies with time and position on the ventricle. The value of  $\hat{f}$  can be obtained by using the difference equation [7].

$$x_k^* = [x_k^n + (\Delta t)u_k^n] + \lambda \hat{f}_k \quad (4)$$

where  $k$  is a Cartesian grid point, the position  $x_k^*$  is the value of  $x_k^n$  at the next time step,  $u$  is the velocity and  $\lambda$  is a complex function of the source strength and a function to produce a linear resistance model of the blood flow through the arteries.  $\lambda$  is also dependent on the strength of the sinks external to the ventricle.

$$\lambda = \frac{9(\Delta t^2)\beta}{64h^2N} \quad (5)$$

where  $\beta$  is an adjustable parameter of order 1,  $h$  is the Cartesian grid spacing and  $N$  is the number of boundary points. The delta function is defined as

$$\delta_k = \delta(x)\delta(y)$$

$$\delta(x) = \frac{1}{4h} \left( 1 + \cos \frac{\pi x}{2h} \right) \quad \text{if } |x| \leq 2h \quad \text{otherwise } \delta^k = 0 \quad (6)$$

From echocardiograms of the patient the positions of the wall can be measured at various times. Thus the velocity of the wall can be calculated and hence  $\hat{f}_k$  can be obtained. This value of  $\hat{f}$  is both time dependent and spatially dependent.

The flow velocities and pressures can be used to calculate the stresses on the surface of the heart walls. These forces can then be used to examine the microscopic interaction with the cells in the heart wall (endocardium).

The first step in the solution involves obtaining the shape of the ventricle at various times. This is often difficult as echocardiogram images are sometimes indistinct. Following a method often used by echocardiographers only five images in a cardiac cycle were selected. One image when the valves were closed, a second image when the valves were fully open, a third just before the atrium starts to contract, one at the end of the ventricle filling (diastole) stage and a final one as the aortic valve opens. A linear variation was assumed between each image, time frame. It was assumed that the motion of the wall would be normal to the surface.

The second step required the simulation of the atrium. The atrium changes shape during the diastole stage and thus changes the pressure. However the use of a source in place of the correct inflow pattern to the atrium was an artifice which made the actual atrium shape unimportant. The atrium shape was fixed at near hemispherical shape with valves in the closed and early open positions. After some time the atrium contracts for a period before the mitral valve closed. The shape was expanded and contracted as required for the different sized mitral valves. The source strength was increased slowly as the valves opened in accordance with the increase in volume of the ventricle.

The stresses at the walls were calculated by selecting two points chosen as close to the wall as possible along a line normal to the surface. A finite difference method was used to obtain the derivative of the velocity along this line. Similarly the velocity normal to the wall was calculated along the same line. Thus if  $y$  is normal to the wall the fluid shear stress  $\tau_0$  is calculated to provide  $\tau = \mu \partial u / \partial y$  and the coupling to the wall is obtained from  $\mu d^2 u / d^2 y = Ku$  where  $K$  is the hydraulic resistivity of the wall.

### 3 RESULTS

The electrode traces after the first injection of dobutamine are shown in Fig. 2.

It can be seen that there were eye movement amplitude changes detected by the frontal electrodes.

The electrode traces after 35 mics of dobutamine are shown in Fig. 3.



Figure 2: Electrode traces after injection of 20 mics of dobtamine.



Figure 3: Electrode traces after injection of 35 mics of dobtamine.

By observation it was thought that there was a change in frequency in some of the transducers output. In order to examine this, Fourier transforms were performed on all of these results except for the ear tracings LOC-A1 and ROC-A2. The relevant results are shown in Figs 4–7 where the absolute values of the signals are shown.

Figure 4 is on the right just above the eye level swinging back from the ears.

Figure 5 is on the right just above the eye level. It is in a similar position to Fig. 4 but more to the center of the head. Again it moves to the rear of the skull.

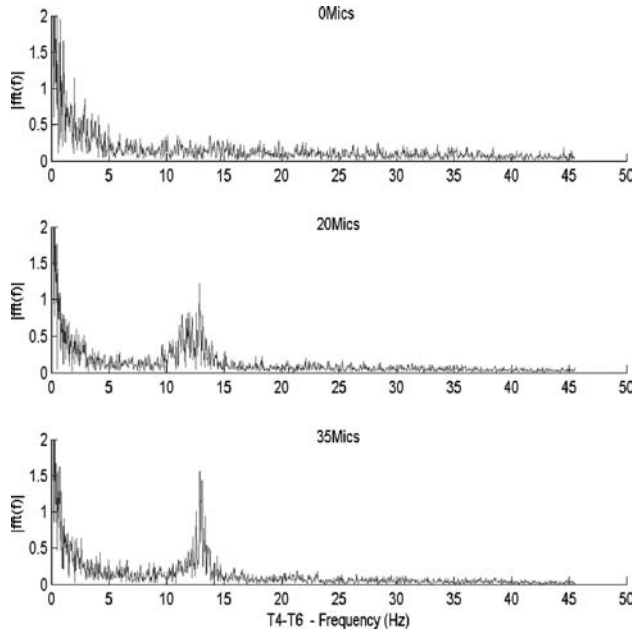


Figure 4: Fourier transforms of electrode traces at the T4-T6 (Fig. 1) location after varying injections of dobutamine.

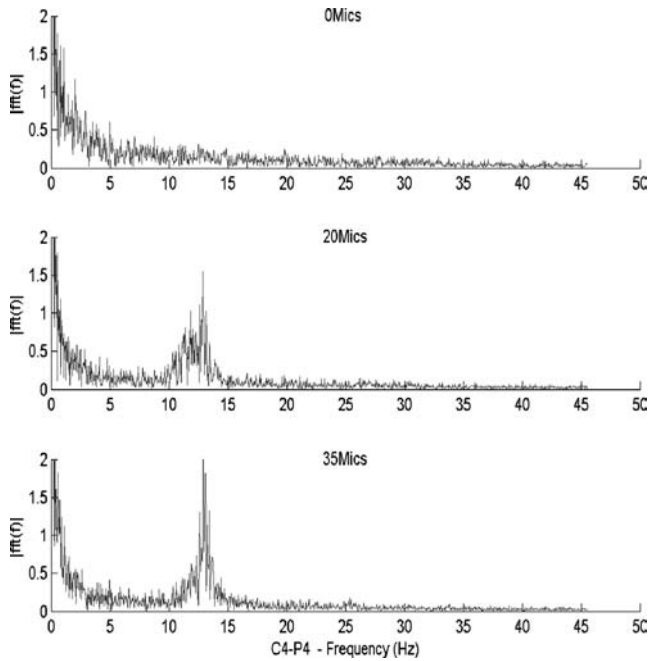


Figure 5: Fourier transforms of electrode traces at the C4-P4 (Fig. 1) location after varying injections of dobutamine.

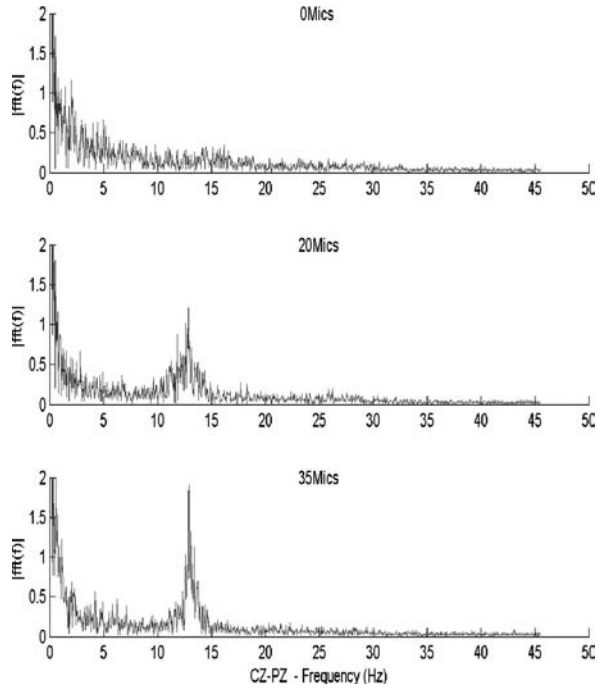


Figure 6: Fourier transforms of electrode traces at the CZ-PZ locations (Fig. 1) after injection of varying injections of dobutamine.

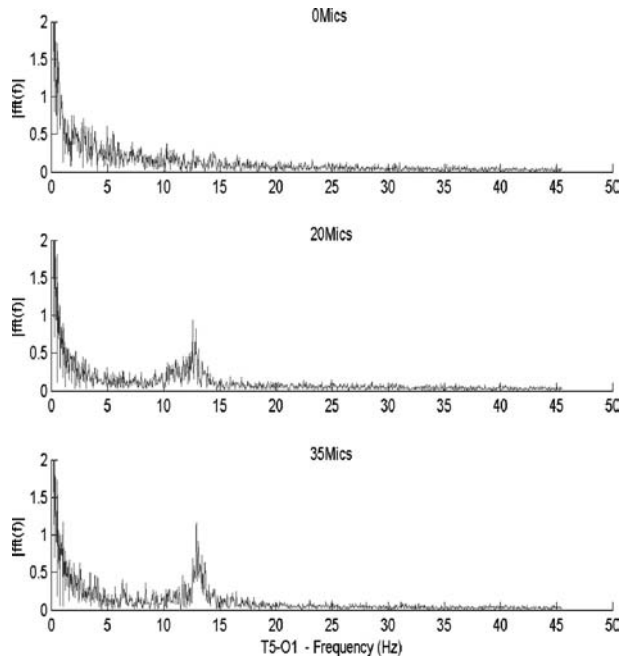


Figure 7: Fourier transforms of electrode traces at locations T5-O1 locations (Fig. 1) after injection of varying injections of dobutamine.

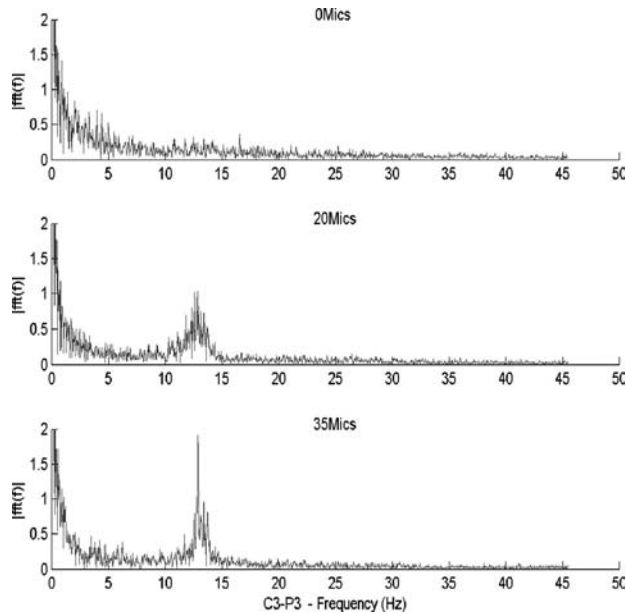


Figure 8: Fourier transforms of electrode traces at the C3-P3 (Fig. 1) location after varying injections of dobutamine.

Figure 6 is running from the top of the skull backwards to a similar extent as the T6 location.

Figure 7 is on the left side of the skull and extends backwards. In this case it starts on the opposite side of the skull at a location similar to T6.

Figure 8 is on the left just above the eye level but further towards the center of the head. It is a mirror position of Fig. 5.

It can be seen from Figs 4–8 that the power of the transform has a peak at a frequency close to 12.5 Hz that is the normal alpha rhythm. The locations in Figs 5 and 8 are towards the center of the skull. The signals from the right side appear stronger than the left. The center location Fig. 6 also shows a strong signal. The outer locations in Figs 5 and 7 do not show such strong transforms. Thus it would appear that the significant signal strength is found on the right side of the head arising towards the center of the skull. Certainly additional results are required to reach definite conclusions of its significance. It is interesting, although from only one result not necessarily significant, that the Fourier transform power has a peak at almost all locations at the same frequency.

Although the dosage of dobutamine is relevant to the load on the heart, the important variable in assessing the neural signals is probably the stress on the heart. In calculating this data it was realized that it could be expressed in a number of ways. One way is to show the variation of both the maximum and average shear stress over the ventricle as a function of time as shown in Fig. 9. The average was calculated over the regions shown in thick lines. For example the endocardium average shear stress is obtained by averaging the Lagrangian locations 5–9.

The results were obtained for three patients. Patient 1 was a 55 year old woman, Patient 2 was a 75 year old woman and Patient 3 was a 75 year old woman. The results in Figs 10 and 11 were for Patient 1.

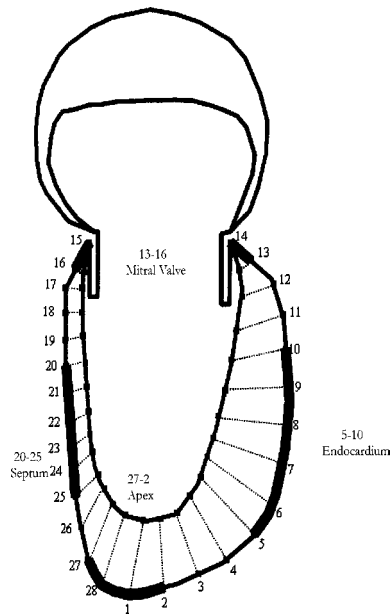


Figure 9: Areas over which averages taken.

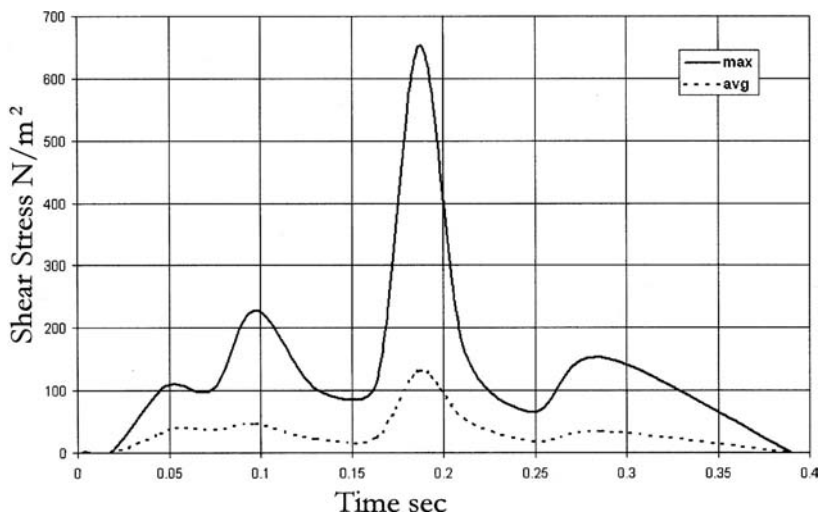


Figure 10: Variation of maximum and average shear stress over the ventricle.

It can be seen that the maximum occurs approximately when the mitral valves are open.

The maximum shear stress in the apex occurs just as the mitral valve is opening.

The shear stress over the apex is larger than that over the endocardium. However it is known that failure most often occurs in the endocardium. Further, sometimes the stress over the endocardium decreases with heart rate as shown in Fig. 12(c) whereas a patient feels stress as the heart rate increases. Thus the maximum shear stress at any point on the ventricle was examined as in Fig. 13.



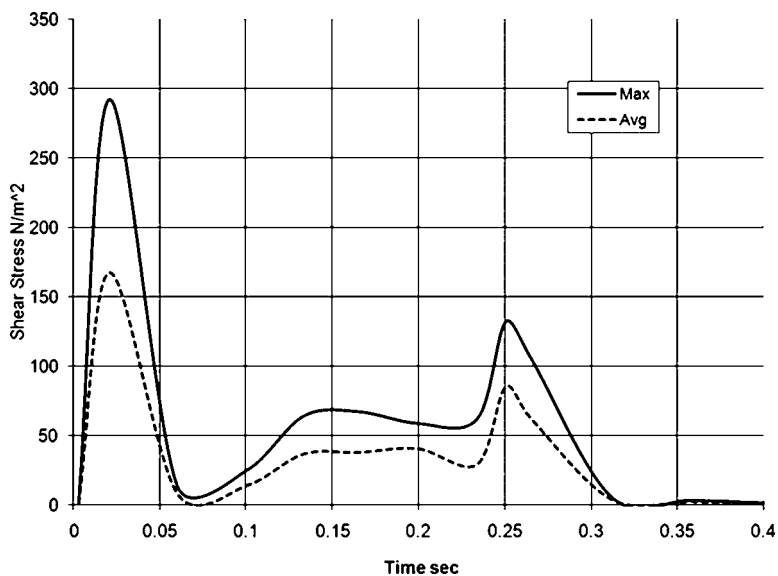


Figure 11: Variation of maximum and average shear stress over the apex.

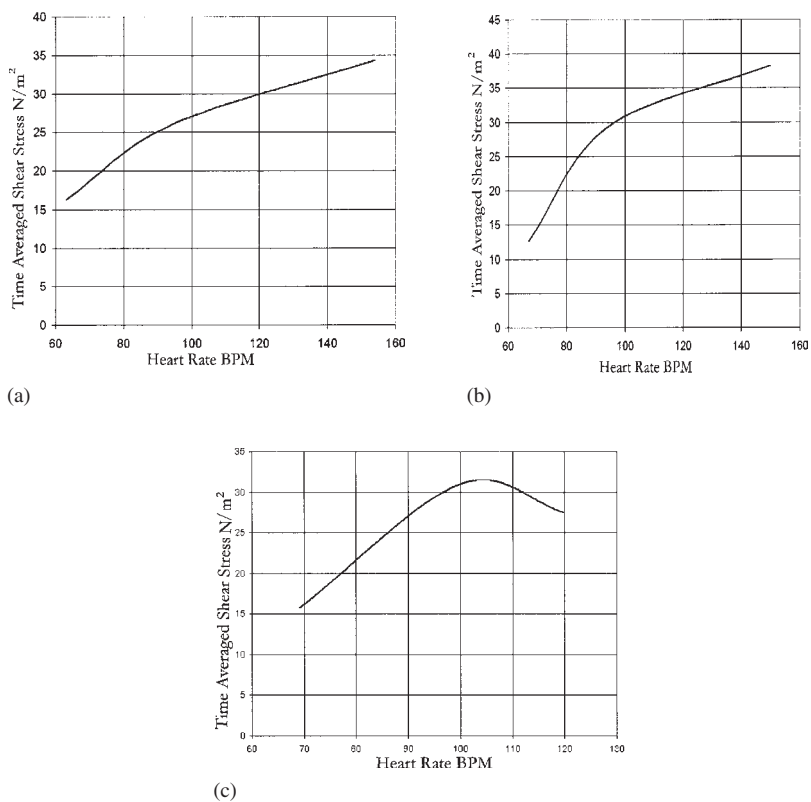


Figure 12: Variation of time averaged endocardium shear stress over on heart beat as a function of heart rate. (a) Patient 1, (b) Patient 2, (c) Patient 3.

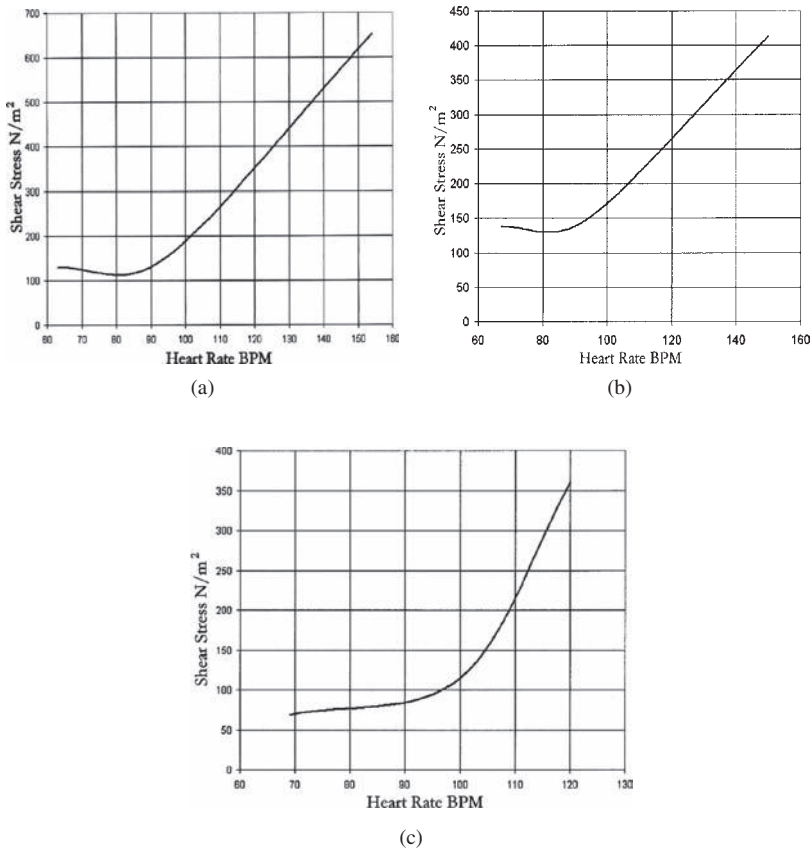


Figure 13: The Variation of the maximum shear stress on left ventricle with heart rate. (a) Patient 1, (b) Patient 2, (c) Patient 3.

It can be seen that the maximum shear stress shown in Fig. 12 increases rapidly as a function of heart rate and would appear to be the significantly important variable. It was realized that this data if calculated on a real time basis would be a useful input to a physician in deciding when to terminate the test. The measurement of surface shear stress would be very difficult and values are not available. Thus it is not possible to know the critical shear stress for a given patient. However for the proposed purpose the calculated values would be adequate.

#### 4 CONCLUSIONS AND FUTURE WORK

It has been shown that there is a definite relation between heart stress and certain brain activity. As there was only one set of data available general conclusions cannot be drawn. It is intended to continue the study with additional patients. This preliminary study has shown that data useful to a clinician monitoring dobutamine testing can be obtained. In addition, diagnostic results can be extracted from the data. It is intended to continue the study with additional patients in order to draw general conclusions.

#### ACKNOWLEDGEMENTS

We would like to acknowledge the assistance of a Lehigh student Kristy Caltabiano in setting up the initial MATLAB calculations.

## REFERENCES

- [1] John, H.C., Landmarks in understanding the central nervous control of the cardiovascular system. *Experimental Physiology*, 92.1 pp 3–18
- [2] Mauro, U., Interaction between carotid baroregulation and the pulsating heart: a mathematical model. *American Journal of Physiology. Heart and Circulatory Physiology*, **275**, pp. 1733–1747, 1998.
- [3] Emad, El-S., Mahdi, M., Derek, A.L., A closed-loop hybrid physiological model relating to subjects under physical stress. *Artificial Intelligence in Medicine*, **38**, pp. 257–274, 2006.
- [4] Marcus, A.G., Peter, T., Peter, M.S., David, G., Diana, R.H., David, B., David, B. & Hugo, D.C., A cortical potential reflecting cardiac function. *PNAS*, **104(16)**, pp. 6818–6823, 2007.
- [5] Sadoshima, J. & Izumo, S., The cellular and molecular response of cardiac myocytes to mechanical stress. *Annual Review of Physiology*, **59**, pp. 551–571, 1997.
- [6] Ruwhof, C. & van der Laarse, A., Mechanical stress-induced cardiac hypertrophy: mechanisms and signal transduction pathways. *Cardiovascular Research*, **47**, 23–37, 2000.
- [7] Macpherson, A.K. & Neti, S., The effect of angiotensin II on heart blood flow and hypertension. *Advances Fluid Mechanics IV*, eds M. Rahman, R. Verhoeven & C.A. Brebbia, WIT Press: Southampton, pp. 1–12, 2002.
- [8] Macpherson, A.K., Neti, S., Macpherson, P.A., Houser, S.R., Hari, M. & Marzillier, J., Mechanical stress and hypertrophy. *Modelling in Medicine and Biology VI*, eds M. Ursino, C.A. Brebbia, G. Pontrelli, & E. Magasso, WIT Press: Southampton, pp. 171–179, 2005.
- [9] Macpherson, A.K., Neti, S., Chutakostikanon, C., Averbach, M. & Macpherson, P.A., The variation of dobutamine induced heart stress with heart rate. *Modelling in Medicine and Biology VI*, ed C.A. Brebbia, WIT Press: Southampton, pp. 17–26, 2009.

The following comment has been provided by an anonymous reviewer.

Traditionally, echocardiography and other imaging modalities have provided the ability to measure radial motion of the myocardium on a regional or global basis. The development of strain and strain rate techniques has provided the ability not only to assess but also to quantify longitudinal motion (i.e. ventricular shortening).

More recent literature indicated a possible role of adenosine stress MR (magnetic resonance) perfusion (magnetic resonance perfusion – MRP) imaging in identifying patients at high risk for future cardiac events; however, as for dobutamine stress MR – DSMR. Cardiac MR imaging offers the advantage of conducting myocardial perfusion and wall motion measurements at rest and under stress conditions during a single-session examination, thereby ensuring superb comparability of test results [1].

Because many patients are unable to perform adequate exercise testing because of physical incapacity, dobutamine stress echo (DSE) has become a well-established modality for the diagnosis of myocardial ischemia.

Dobutamine stress echocardiography is used widely to assess coronary artery disease (CAD), its interpretation is demanding, and its accuracy depends on the experience and training of the reader [2]. Despite technical advances and digital image processing and display, both its reproducibility and accuracy are dependent on image quality. DSE also is limited by its relative insensitivity for mild single-vessel disease, low sensitivity for recognizing the presence of multivessel coronary disease, and difficulty in detection of ischemia within areas of abnormal resting wall motion (WM).

Quantification of DSE with tissue Doppler is less dependent on 2-dimensional image quality than quantification from 2-dimensional echocardiography, and several studies have shown the technique to be feasible for DSE using either velocity or strain rate imaging (SRI) [3]. SR and strain can characterize regional myocardial deformation at rest and can quantify normal or abnormal regional function during DSE [4].

Conventional DSE are two important problems. First, it remains a subjective tool; its accuracy depends on the skills of the user. Second, although the extent and severity of abnormality at peak stress are predictive of outcome [5], WM abnormality is known to be relatively poor for distinguishing the true extent of CAD.

A recent review of 28 major DSE studies [6] has reported sensitivity, specificity, and accuracy ranging from 54 to 96%, 60 to 100%, and 62 to 92%, respectively, depending on patient selection, study size, definition of coronary artery disease and technical equipment.

Connection between the nervous system and the cardiopulmonary system provides the unifying link that allows a coherent explanation for most, if not all, of the forms of neurocardiac damage. It has been known for a long time that stimulation of the hypothalamus can lead to autonomic cardiovascular disturbances [7], and many years ago lesions in the heart and gastrointestinal tract have been produced with hypothalamic stimulation.

Brain natriuretic peptide is produced by the ventricular myocardium in response to stretch; its vasodilator and natriuretic effects counteract the opposing actions of angiotensin II and aldosterone [8].

Increased levels of circulating neurohormones are only part of the response seen after an initial insult to the myocardium. Left ventricular remodeling is the process, by which mechanical, neurohormonal, and possibly genetic factors alter ventricular size, shape, and function.

## REFERENCES

- [1] Paetsch, I., Jahnke, C., Wahl, A., Gebker, R., Neuss, M., Fleck, E. & Nagel, E., Comparison of dobutamine stress magnetic resonance, adenosine stress magnetic resonance, and adenosine stress magnetic resonance perfusion. *Circulation*, **110**, pp. 835–842, 2004.
- [2] Picano, E., Lattanzi, F., Orlandini, A., Marini, C. & L'Abbate, A., Stress echocardiography and the human factor: the importance of being expert. *Journal of the American College of Cardiology*, **17**, pp. 666–669, 1991.
- [3] Madler, C.F., Payne, N., Wilkenshoff, U., Cohen, A., Derumeaux, G.A., Pierard, L.A., Engvall, J., Brodin, L.A., Sutherland, G.R. & Fraser, A.G., Non-invasive diagnosis of coronary artery disease by quantitative stress echocardiography: optimal diagnostic models using off-line tissue Doppler in the MYDISE study. *European Heart Journal*, **24**, pp. 1584–1594, 2003.
- [4] Voigt, J.U., Exner, B., Schmiedehausen, K., Huchzermeyer, C., Reulbach, U., Nixdorff, U., Platsch, G., Kuwert, T., Daniel, W.G., Flachskampf, F.A., Strain-rate imaging during dobutamine stress echocardiography provides objective evidence of inducible ischemia. *Circulation*, **107**, pp. 2120–2126, 2003.
- [5] Hoffman, R., Lethen, H., Kuhl, H., Lepper, W. & Hanrath, P., Extent and severity of test positivity during dobutamine stress echocardiography. *European Heart Journal*, **20**, pp. 1485–1492, 1999.
- [6] Geleijnse, M.L., Fioretti, P.M. & Roelandt, J.R., Methodology, feasibility, safety and diagnostic accuracy of dobutamine stress echocardiography. *Journal of the American College of Cardiology*, **30**, pp. 595–606, 1997.
- [7] Dikshit, B.B., The production of cardiac irregularities by excitation of the hypothalamic centres. *Journal of Physiology*, **81**, pp. 382–394, 1934.
- [8] Jessup, M., Brozena, S., Heart failure. *The New England Journal of Medicine*, **348**, pp. 2007–2018, 2003.

*This page intentionally left blank*

# MATHEMATICAL ASPECTS OF THE MECHANICS OF LEFT VENTRICULAR CONTRACTION

R.M. SHOUCRI

Department of Mathematics and Computer Science, Royal Military College of Canada, Kingston, Ontario, Canada.

## ABSTRACT

Large elastic deformation is used in order to model the mechanics of left ventricular contraction. The active force generated by the myocardium is modeled as force/unit myocardial volume in the mathematical formalism describing the local equilibrium of forces in the myocardium. Expressions for the stress components are derived by assuming a cylindrical geometry for the left ventricle, the total stress is expressed as the sum of a component due to the deformation of the passive medium of the myocardium and an active component induced by the tension in the muscular fibers. It is shown that knowledge of the tension generated by the muscular fiber in the myocardium can lead to useful information for the estimation of the pseudo-strain energy function used to express the stress-strain constitutive relations in a non-linear model.

*Keywords: active force of the myocardium, cardiac mechanics, mathematical modeling of ventricular contraction, pressure-volume relation in the left ventricle.*

## 1 INTRODUCTION

Many articles have been devoted to the study of stress-strain relations in the myocardium and how to formulate a pseudo-strain energy function  $W$  that is used to derive the constitutive relations between stress and strain [1–4]. Previous studies by the authors [5–9] have shown how the active force developed by the myocardium can be modeled as force generated by unit volume of the myocardium in the mathematical formalism used to describe the local equilibrium of forces. This mathematical approach was successfully developed by using large elastic deformation [5, 8] as well as linear elasticity [6]. For this purpose the total stress in the myocardium is expressed as the sum of a contribution due to the stress generated by the deformation of the passive isotropic medium of the myocardium, and a contribution coming from the stress induced by the active muscular fibers. A mathematical description of how this splitting is done can be found in the work of Spencer [10]. The approach used in this study is similar to the approach used in some studies in which the pseudo-strain energy function  $W$  is split into the sum of an isotropic component and an anisotropic component in the form  $W = W_{iso} + W_{aniso}$  [11], the link between the two approaches is evident from what follows. We also show in this study how the calculation of the stress in the myocardium can be based on the knowledge of the muscular fiber tension  $T$  without an explicit knowledge of the pseudo-strain energy function  $W$ , which presents a possible way to estimate  $W$  as a result of the method of calculation shown in this study.

## 2 ACTIVE FORCE OF THE MYOCARDIUM

The myocardium is represented as a thick-walled cylinder (see Fig. 1 & Fig. 2), with the myocardial muscular fibers arranged in a helical way in a passive soft incompressible medium assumed to be isotropic. Inertia forces and viscous forces are neglected in the quasi-static approximation used in this study. The unit tangent vector  $\mathbf{t}$  in the direction of the helical fiber makes an angle  $\gamma(r)$  with the unit vector  $\mathbf{e}_q$  pointing in the circumferential direction and can be expressed in the form (see Fig. 1)

$$\mathbf{t} = \mathbf{e}_q \cos \gamma(r) + \mathbf{e}_z \sin \gamma(r) \quad (1)$$

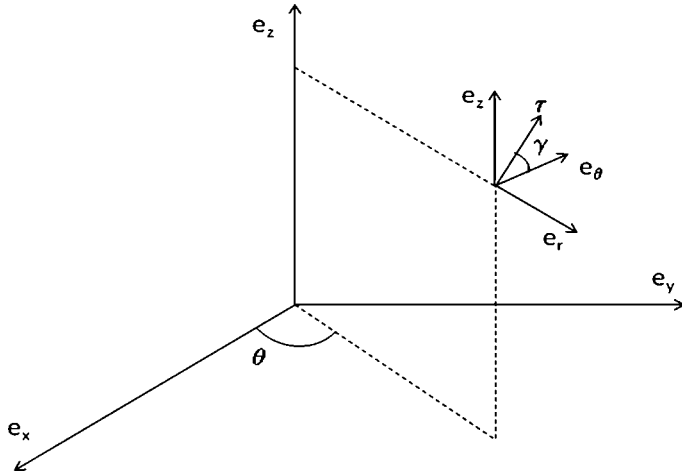


Figure 1:  $(e_r, e_\theta, e_z)$  are three unit vectors in a cylindrical coordinates system. A unit vector  $t$  tangent to the direction of a helical muscular fiber in the myocardium makes an angle  $\gamma(r)$  with the unit vector  $e_\theta$  in the circumferential direction.

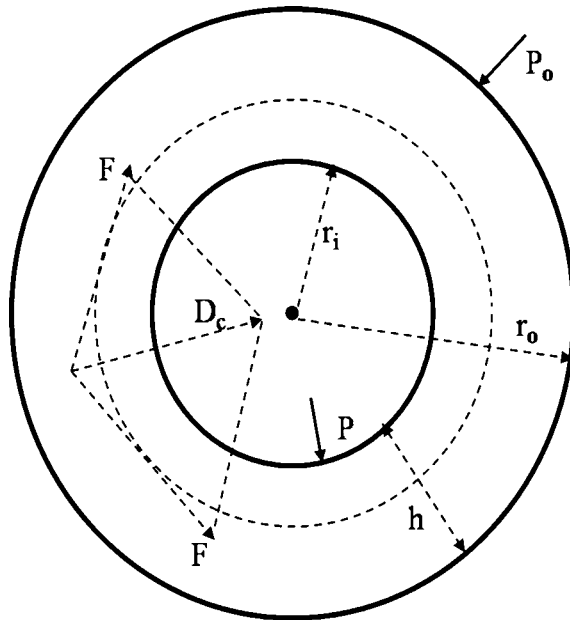


Figure 2: The left ventricle is represented as a thick-walled cylinder, with inner radius  $r_i$  and outer radius  $r_o$ , wall thickness  $h = r_o - r_i$ . A helical fiber is projected as a dotted circle on the cross-section. The radial active force/unit volume of the myocardium is  $D_c(r) = -D_r(r)$  in the notation of the text.  $P_i$  is the left ventricular pressure,  $P_o$  is the outer pressure on the epicardium.

Notice in this case  $\text{div } \mathbf{t} = 0$  which in conjunction with the result given by Peskin [12] allows one to express the active force/unit myocardial volume in the form

$$\mathbf{D} = (D_r, D_\theta, D_z) = \frac{d(T\mathbf{r})}{ds} \quad (2)$$

where  $T(r, z)$  is the tension/unit myocardial area generated by the muscular fibers,  $d/ds = \mathbf{t} \cdot \nabla$  with  $\nabla$  standing for the gradient symbol which in cylindrical coordinates is given by

$$\nabla = \mathbf{e}_r \frac{\partial}{\partial r} + \mathbf{e}_\theta \frac{1}{r} \frac{\partial}{\partial \theta} + \mathbf{e}_z \frac{\partial}{\partial z} \quad (3)$$

The unit vectors in cylindrical coordinates are given by  $\mathbf{e}_r$ ,  $\mathbf{e}_\theta$  and  $\mathbf{e}_z$ . Performing the differentiation on the right hand side of eqn (2) gives the following results

$$D_r = -\frac{(\cos \gamma(r))^2}{r} T \quad (4a)$$

$$D_\theta = \sin \gamma(r) \cos \gamma(r) \frac{\partial T}{\partial z} \quad (4b)$$

$$D_z = (\sin \gamma(r))^2 \frac{\partial T}{\partial z} \quad (4c)$$

The active stress tensor  $\mathbf{q}$  (components  $q_{ij}$ ) represents the stress components in an orthogonal cylindrical coordinate system induced by the muscular fiber stress  $T(r, z)$ . By taking into consideration eqn (1), the components of the active stress  $q_{ij} = T \mathbf{t}_{ij}$  (see [13]) are given in a cylindrical coordinate system by the following relations:

$$\begin{aligned} q_{\theta\theta} &= T(\cos \gamma(r))^2 & q_{zz} &= T(\sin \gamma(r))^2 \\ q_{\theta z} &= q_{z\theta} = T(\sin \gamma(r))(\cos \gamma(r)) & q_{r\theta} &= q_{r\theta} = q_{rz} = q_{rz} = 0 \end{aligned} \quad (5)$$

The relation between the active force/unit myocardial volume  $\mathbf{D} = (D_r, D_\theta, D_z)$  and the active stress tensor  $\mathbf{q}$  can be obtained by using Gauss theorem. The traction force  $\mathbf{F}_a$  acting on a closed surface  $A$  enclosing a volume  $V$  inside the myocardium can be expressed in the form

$$\mathbf{F}_a = \iint \mathbf{q} dA = \iiint (\text{div } \mathbf{q}) dV \quad (6)$$

Consequently the active force/unit myocardial volume can be expressed as

$$\mathbf{D} = \text{div } \mathbf{q} \quad (7)$$

We take into consideration eqn (5) and the fact that the solution is independent of the  $\theta$ -coordinate (symmetry around the  $z$ -axis). The expression of the divergence in cylindrical coordinates (see [8]) gives

$$(D_r, D_\theta, D_z) = -\mathbf{e}_r \frac{(\cos \gamma)^2}{r} T + \mathbf{e}_\theta (\sin \gamma)(\cos \gamma) \frac{\partial T}{\partial z} + \mathbf{e}_z (\sin \gamma)^2 \frac{\partial T}{\partial z} \quad (8)$$



from which we retrieve the relations given in eqn (4). We notice from eqns (4) and (5) that we have the relations

$$D_r = -\frac{q_{\theta\theta}}{r} \quad D_\theta = \frac{\partial q_{z\theta}}{\partial z} \quad D_z = \frac{\partial q_{zz}}{\partial z} \quad (9)$$

### 3 QUASI-STATIC EQUILIBRIUM CONDITION

We assume symmetry around the  $z$ -axis (solution independent of  $\theta$ ). Under this assumption the total stress components  $t_{ij}$  must satisfy the quasi-static equilibrium condition  $\text{div } \mathbf{t} = 0$ , which in cylindrical coordinates is expressed as follows:

$$\frac{\partial t_{rr}}{\partial r} + \frac{t_{rr} - t_{\theta\theta}}{r} + \frac{\partial t_{zr}}{\partial z} = 0 \quad (10a)$$

$$\frac{1}{r^2} \frac{\partial(r^2 t_{r\theta})}{\partial r} + \frac{\partial t_{z\theta}}{\partial z} = 0 \quad (10b)$$

$$\frac{1}{r} \frac{\partial(r t_{rz})}{\partial r} + \frac{\partial t_{zz}}{\partial z} = 0 \quad (10c)$$

We shall simplify the problem by assuming that  $t_{zr}$  and  $t_{z\theta}$  are independent of  $z$  variable, which gives

$$r^2 t_{r\theta} = \text{const} = H_1 \quad r t_{rz} = \text{const} = H_2 \quad (11)$$

The boundary conditions for the radial stress on the surface of the cylinder can be expressed as follows:

$$t_{rr}(r_i) = -p_i \quad t_{rr}(r_o) = -p_o \quad (12)$$

We now use the decomposition  $t_{ij} = \sigma_{ij} + q_{ij}$ . By using eqns (9), eqns (10) can be written in the form

$$\frac{\partial \sigma_{rr}}{\partial r} + \frac{\sigma_{rr} - \sigma_{\theta\theta}}{r} + \frac{\partial}{\partial z}(\sigma_{rr} + \int_z D_r dz) = 0 \quad (13a)$$

$$\frac{1}{r^2} \frac{\partial(r^2 \sigma_{r\theta})}{\partial r} + \frac{\partial}{\partial z}(\sigma_{z\theta} + \int_z D_\theta dz) = 0 \quad (13b)$$

$$\frac{1}{r} \frac{\partial(r \sigma_{rz})}{\partial r} + \frac{\partial}{\partial z}(\sigma_{zz} + \int_z D_z dz) = 0 \quad (13c)$$

The force/unit volume of the myocardium  $D_r$  appearing in eqn (13a) is similar, but not identical, to the introduction of the derivative of a hydrostatic pressure in eqn (26) of reference [14]. Another, but different, attempt to divide the stress in the myocardium into two components can be found in [15].

Some simplifying assumptions concerning the dependence on the  $z$  variable will be introduced. By noting that  $t_{r\theta} = \sigma_{r\theta}$  ( $q_{r\theta} = 0$ ),  $t_{rz} = \sigma_{rz}$  ( $q_{rz} = 0$ ) and  $t_{rr} = \sigma_{rr}$  ( $q_{rr} = 0$ ), one can write by referring to eqns (11) and (12)

$$r^2 \sigma_{r\theta} = \text{const} = H_1 \quad r \sigma_{rz} = \text{const} = H_2 \quad (14)$$

$$\sigma_{rr}(r_i) = -P_i \quad \sigma_{rr}(r_o) = -P_o \quad (15)$$

Two useful relations that we shall apply in our calculations are: first the moment of forces  $M$  around the  $z$ -axis is assumed zero (no external moment applied around the  $z$ -axis).

$$M = 2\pi \int_{r_i}^{r_o} (\sigma_{z\theta} + q_{z\theta}) r^2 dr = 0 \quad (16)$$

from which we can assume that

$$\sigma_{z\theta} = -q_{z\theta} \quad (17)$$

Second from the equilibrium of forces in the vertical direction we get

$$\sigma_{zz} + q_{zz} + \zeta = 0 \quad (18)$$

where  $\zeta$  is the traction on the cross-section and it is assumed to vary linearly over the cross-section

$$\zeta = \zeta_{end} \left( \frac{r_o - r}{r_o - r_i} \right) + \zeta_{epi} \left( \frac{r - r_i}{r_o - r_i} \right) \quad (19)$$

We have taken in our calculation the stress at the endocardium  $\zeta_{end} = 0.5P_i$  and at the epicardium  $\zeta_{epi} = -0.01P_i$  based on estimate of the average traction  $\zeta_{av} = (P_i r_i^2 - P_o r_o^2)/(r_o^2 - r_i^2)$ .

#### 4 DEFORMATION GRADIENT

The thick-walled cylindrical structure representing the left ventricle is supposed to have a stress free configuration with coordinates  $(R, \Theta, Z)$ , at end-diastole the cylindrical coordinates are represented by  $(r_{ed}, \theta_{ed}, z_{ed})$  and finally by  $(r, \theta, z)$  during the systolic phase. The coordinate transformation from one configuration to the other is expressed as follows:

$$r_{ed} = r_{ed}(R) \quad \theta_{ed} = a_1 \Theta \quad z_{ed} = k_1 Z \quad (20)$$

$$r = r(r_{ed}) \quad \theta = a_2 \theta_{ed} + \psi_2 z_{ed} + \chi(r_{ed}) \quad z = k_{2z} z_{ed} + k_{2\theta} \theta_{ed} + \omega(r_{ed}) \quad (21)$$

The two preceding equations can be combined together to give

$$r = r(R) \quad \theta = a\Theta + \psi Z + \chi(R) \quad z = k_z Z + k_\theta \Theta + \omega(R) \quad (22)$$

The deformation gradient  $F_1$  for the transformation  $(R, \Theta, Z) \rightarrow (r_{ed}, \theta_{ed}, z_{ed})$  can be expressed as follows (see [2]):

$$F_1 = \begin{bmatrix} \frac{\partial r_{ed}}{\partial R} & \frac{1}{R} \frac{\partial r_{ed}}{\partial \Theta} & \frac{\partial r_{ed}}{\partial Z} \\ r_{ed} \frac{\partial \theta_{ed}}{\partial R} & \frac{r_{ed}}{R} \frac{\partial \theta_{ed}}{\partial \Theta} & r_{ed} \frac{\partial \theta_{ed}}{\partial Z} \\ \frac{\partial z_{ed}}{\partial R} & \frac{1}{R} \frac{\partial z_{ed}}{\partial \Theta} & \frac{\partial z_{ed}}{\partial Z} \end{bmatrix} = \begin{bmatrix} \frac{dr_{ed}}{dR} & 0 & 0 \\ 0 & \alpha_1 \frac{r_{ed}}{R} & 0 \\ 0 & 0 & k_1 \end{bmatrix} \quad (23)$$

The deformation gradient  $F_2$  for the transformation  $(r_{ed}, \theta_{ed}, z_{ed}) \rightarrow (r, \theta, z)$  is given by

$$F_2 = \begin{bmatrix} \frac{\partial r}{\partial r_{ed}} & \frac{1}{r_{ed}} \frac{\partial r}{\partial \theta_{ed}} & \frac{\partial r}{\partial z_{ed}} \\ r \frac{\partial \theta}{\partial r_{ed}} & \frac{r}{r_{ed}} \frac{\partial \theta}{\partial \theta_{ed}} & r \frac{\partial \theta}{\partial z_{ed}} \\ \frac{\partial z}{\partial r_{ed}} & \frac{1}{r_{ed}} \frac{\partial z}{\partial \theta_{ed}} & \frac{\partial z}{\partial z_{ed}} \end{bmatrix} = \begin{bmatrix} \frac{dr}{dr_{ed}} & 0 & 0 \\ r \frac{d\chi}{dr_{ed}} & \alpha_2 \frac{r}{r_{ed}} & r\psi_2 \\ \frac{d\omega}{dr_{ed}} & \frac{k_{2\theta}}{r_{ed}} & k_{2z} \end{bmatrix} \quad (24)$$

The deformation gradient  $F = F_2 * F_1$  of the combined transformation is given by

$$F = \begin{bmatrix} \frac{\partial r}{\partial R} & \frac{1}{R} \frac{\partial r}{\partial \Theta} & \frac{\partial r}{\partial Z} \\ r \frac{\partial \theta}{\partial R} & \frac{r}{R} \frac{\partial \theta}{\partial \Theta} & r \frac{\partial \theta}{\partial Z} \\ \frac{\partial z}{\partial R} & \frac{r}{R} \frac{\partial z}{\partial \Theta} & \frac{\partial z}{\partial Z} \end{bmatrix} = \begin{bmatrix} \frac{dr}{dR} & 0 & 0 \\ r \frac{d\chi}{dR} & a \frac{r}{R} & r\psi \\ \frac{d\omega}{dR} & \frac{k_\theta}{R} & k_z \end{bmatrix} \quad (25)$$

By assuming that the contraction takes place at constant volume, the incompressibility constraint is expressed as follows:

$$I_3 = (\det F)^2 = (\det F_2)^2 * (\det F_1)^2 = 1 \quad (26)$$

where  $I_3$  is the third invariant of the matrix  $F$ . By calculating the determinants in eqn (26), equating to one and then integrating we get

$$\frac{dr}{dR} = \frac{R}{Kr}, \quad Kr^2 - R^2 = Kr_i^2 - R_i^2 \quad (27)$$

$$\frac{dr_{ed}}{dR} = \frac{R}{K_1 r_{ed}}, \quad K_1 r_{ed}^2 - R^2 = K_1 r_{ied}^2 - R_i^2 \quad (28)$$

$$\frac{dr}{dr_{ed}} = \frac{r_{ed}}{K_2 r}, \quad K_2 r^2 - r_{ed}^2 = K_2 r_i^2 - r_{ied}^2 \quad (29)$$

The constants in eqns (27)–(29) are defined as follows:  $K_1 = \alpha_1 k_1$ ,  $K_2 = \alpha_2 k_{2z} - \psi_2 k_{2\theta}$  and  $K = K_1 K_2 = \alpha_1 k_1 \alpha_2 k_{2z} - \alpha_1 k_{2\theta} k_1 \psi_2 = \alpha k_z - k_\theta \psi$ . The inner radius is  $R_i$  in the stress free configuration and  $r_i$  during the systolic phase.

The helical configuration of a muscular fiber in the myocardium is supposed to be confined to a cylindrical surface. A unit vector  $\mathbf{t}$  in the direction of the fiber in the deformed configuration will make an angle  $\gamma(r)$  calculated with respect to the circumferential direction (see Fig. 1), in the stress free configuration the corresponding unit vector is  $\mathbf{t}_o$  and the angle is  $\gamma_o(r)$ , the relation between these two vectors are given by

$$\mathbf{t} = \frac{1}{\lambda_f} F \mathbf{t}_o \quad (30)$$

where  $\lambda_f$  is the stretch ratio in the direction of the fiber. By using eqn (25) we can write

$$\cos(\gamma(r)) = \frac{1}{\lambda_f} \left[ \frac{ar}{R} \cos(\gamma_o(r)) + (r\psi) \sin(\gamma_o(r)) \right] \quad (31)$$

$$\sin(\gamma(r)) = \frac{1}{\lambda_f} \left[ \frac{k_\theta}{R} \cos(\gamma_o(r)) + k_z \sin(\gamma_o(r)) \right] \quad (32)$$

We can model first  $\gamma_o(r)$  and then use eqns (31, 32) to calculate  $\gamma(r)$ . But in view of the method of calculation we are going to use later on, it is easier to model directly  $\gamma(r)$  and then to calculate back  $\gamma_o(r)$  at the end if needed. Consequently we shall assume directly either a linear variation for  $\gamma(r)$  across the myocardium of the form

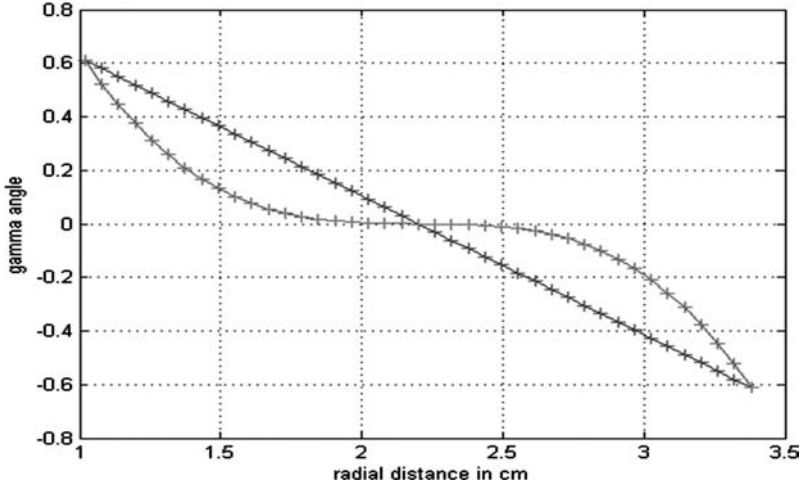


Figure 3: Linear model (eqn (33)) and non-linear model (eqn (34)) for the variation of  $\gamma(r)$  with the radial distance  $r$  from endocardium to epicardium.

$$\gamma(r) = \gamma_{end} \left( \frac{r_o - r}{r_o - r_i} \right) + \gamma_{epi} \left( \frac{r - r_i}{r_o - r_i} \right) \quad (33)$$

or a cubic variation of the form [16]

$$\gamma(r) = \gamma_{end} \left( \frac{r_o + r_i - 2r}{r_o - r_i} \right)^3 \quad (34)$$

In our calculation, we have taken  $\gamma_{end} = 35^\circ$  and  $\gamma_{epi} = -35^\circ$ . The radial variation for these two models is shown in Fig. 3.  $\lambda_f$  can be calculated from eqns (31) and (32) by eliminating  $\cos(\gamma_o)$  and  $\sin(\gamma_o)$  from these two equations.

## 5 CONSTITUTIVE RELATIONS

The relation between stress and strain is expressed with what is called constitutive relation. It is expressed by calculating the left or right Cauchy-Green deformation tensors, respectively,  $B = F^*F^T$  or  $C = F^T F$ . In this study we shall use the model of Humphrey and Yin [1] which focus on a subclass of transverse isotropic material with pseudo-strain energy function  $W$  given by

$$W = W(I_1, \lambda_p), \quad (35)$$

where  $I_1$  is the first invariant of the matrix  $B$ ,  $I_1 = \text{tr}(B)$ . Written explicitly the expression of  $B$  becomes

$$B = \begin{bmatrix} \left( \frac{dr}{dR} \right)^2 & r \frac{dr}{dR} \frac{d\chi}{dR} & \frac{dr}{dR} \frac{d\omega}{dR} \\ r \frac{dr}{dR} \frac{d\chi}{dR} & \left( r \frac{d\chi}{dR} \right)^2 + \left( \frac{ar}{R} \right)^2 + (r\psi)^2 & r \frac{d\chi}{dR} \frac{d\omega}{dR} + \frac{ark_\theta}{R^2} + r\psi k_z \\ \frac{dr}{dR} \frac{d\omega}{dR} & r \frac{d\chi}{dR} \frac{d\omega}{dR} + \frac{ark_\theta}{R^2} + r\psi k_z & \left( \frac{d\omega}{dR} \right)^2 + \frac{k_\theta^2}{R^2} + k_z^2 \end{bmatrix} \quad (36)$$

By using eqn (36) the Cauchy stress tensor  $t$  can be expressed as follows (see [1]):

$$t_{ij} = -p\delta_{ij} + 2W_{I_1}B_{ij} + W_{\lambda_f}\lambda_f\tau_i\tau_j \quad (37)$$

where  $W_{I_1} = \partial W / \partial I_1$  and  $W_{\lambda_f} = \partial W / \partial \lambda_f$ ,  $p$  is a Lagrange multiplier introduced to express the incompressibility condition that the contraction of the myocardium is assumed to take place at constant volume. By writing the total stress  $t_{ij} = \sigma_{ij} + q_{ij}$  it is possible to split eqn (37) into two parts. The first part has the form

$$\sigma_{ij} = -p\delta_{ij} + 2W_{I_1}B_{ij} \quad (38)$$

where  $\sigma_{ij}$  is the stress resulting from the deformation of the isotropic passive medium of the myocardium, and the second part has the form

$$q_{ij} = W_{\lambda_f}\lambda_f\tau_i\tau_j, \quad \text{with } T = W_{\lambda_f}\lambda_f \quad (39)$$

where  $q_{ij}$  is the stress induced by the muscular fiber tension  $T(r, z)$  and reflects the directional character of the stress. Equation (38) can be written in explicit form as follows:

$$\sigma_{r\theta} = 2W_{I_1}r \frac{dr}{dR} \frac{d\chi}{dR} = \frac{H_1}{r^2} \quad (40)$$

$$\sigma_{rz} = 2W_{I_1} \frac{dr}{dR} \frac{d\omega}{dR} = \frac{H_2}{r} \quad (41)$$

$$\sigma_{z\theta} = 2W_{I_1} \left[ r \frac{d\chi}{dR} \frac{d\omega}{dR} + \frac{ark_\theta}{R^2} + r\psi k_z \right] \quad (42)$$

$$\sigma_{zz} = -p + 2W_{I_1} \left[ \left( \frac{d\omega}{dR} \right)^2 + \frac{k_\theta^2}{R^2} + k_z^2 \right] \quad (43)$$

$$\sigma_{\theta\theta} = -p + 2W_{I_1} \left[ \left( r \frac{d\chi}{dR} \right)^2 + \left( \frac{ar}{R} \right)^2 + (r\psi)^2 \right] \quad (44)$$

$$\sigma_{rr} = -p + 2W_{I_1} \left( \frac{dr}{dR} \right)^2 = -p + 2W_{I_1} \left( \frac{R}{Kr} \right)^2 \quad (45)$$

In the applications that follow, we shall neglect  $d\chi/dR$  and  $d\omega/dR$  that are relatively small. This simplifies the numerical procedure of calculation used in what follows.

## 6 MATHEMATICAL PROCEDURE OF CALCULATION

The numerical procedure used in what follows avoids an explicit knowledge of the pseudo-strain energy function  $W(I_1, \lambda_f)$ . If the values of the fiber tension  $T$  are known, then we can calculate directly  $D_r$ ,  $\sigma_{z\theta}$  and  $\sigma_{zz}$  from eqns (4a), (17) and (18). We then proceed by eliminating  $-p$  and  $W_{I_1}$  from eqns (42–45) and we get

$$\frac{\sigma_{z\theta}}{\sigma_{zz} - \sigma_{rr}} = \frac{\frac{(k_\theta ar)}{R^2} + k_z \psi r}{\frac{k_\theta^2}{R^2} + k_z^2 - \frac{R^2}{(Kr)^2}} \quad (46)$$

and

$$\frac{\sigma_{z\theta}}{\sigma_{\theta\theta} - \sigma_{rr}} = \frac{\frac{(k_\theta ar)}{R^2} + k_z \psi r}{\frac{(ar)^2}{R^2} + (\psi r)^2 - \frac{R^2}{(Kr)^2}} \quad (47)$$

Equations (46) and (47) are the basis of the calculation outlined in what follows. We notice for instance from Fig. 5 that  $\sigma_{z\theta}$  is zero for a value of  $r$  we indicate by  $r_z$ , the corresponding value  $R_z$  is calculated from eqn (27). The numerator of eqn (46) gives

$$ak_\theta + \psi k_z R_z^2 = 0 \quad (48)$$

and we have from the incompressibility condition

$$ak_z - \psi k_\theta = K \quad (49)$$

where  $K = (R_o^2 - R_i^2) / (r_o^2 - r_i^2)$  from eqn (27). By solving eqns (48) and (49) we get

$$a = \frac{k_z K R_z^2}{k_\theta^2 + k_z^2 R_z^2} \quad (50)$$

$$\psi = -\frac{k_\theta K}{k_\theta^2 + k_z^2 R_z^2} \quad (51)$$

These two values are then substituted in eqn (46) evaluated at  $r_i$  and  $r_o$  with the boundary conditions given by eqn (15). We get the two following relations:

$$f(k_z, k_\theta) = cf_i * \left[ k_\theta^2 + R_i^2 \left( k_z^2 - \left( \frac{R_i}{K r_i} \right)^2 \right) \right] * \det + k_\theta k_z K (R_i^2 - R_z^2) = 0 \quad (52)$$

$$g(k_z, k_\theta) = cf_o * \left[ k_\theta^2 + R_o^2 \left( k_z^2 - \left( \frac{R_o}{K r_o} \right)^2 \right) \right] * \det + k_\theta k_z K (R_o^2 - R_z^2) = 0 \quad (53)$$

where  $cf_i = \sigma_{z\theta}(r_i) / (\sigma_{zz}(r_i) + P_i)$  evaluated at  $r_i$ ,  $cf_o = \sigma_{z\theta}(r_o) / (\sigma_{zz}(r_o) + P_o)$  evaluated at  $r_o$  and  $\det = k_\theta^2 + k_z^2 R_z^2$ . The two roots  $k_\theta$  and  $k_z$  of eqns (52) and (53) are calculated by using Newton iteration procedure. For this purpose we calculate the Jacobian

$$J = \begin{bmatrix} \frac{\partial f}{\partial k_z} & \frac{\partial f}{\partial k_\theta} \\ \frac{\partial g}{\partial k_z} & \frac{\partial g}{\partial k_\theta} \end{bmatrix} \quad (54)$$

We start with an approximation of  $k_z$  and  $k_\theta$ . The iteration process is expressed in the form

$$\begin{bmatrix} k_z \\ k_\theta \end{bmatrix}_{j+1} = \begin{bmatrix} k_z \\ k_\theta \end{bmatrix}_j - J^{-1} \begin{bmatrix} f(k_z, k_\theta) \\ g(k_z, k_\theta) \end{bmatrix}_j \quad (55)$$

which gives the values of  $k_z$  and  $k_\theta$  at the  $(j + 1)$ th iteration in terms of the preceding  $j$ th iteration. Having calculated these two parameters we can then calculate  $\alpha$  and  $\psi$ .  $\sigma_{rr}$  is then calculated from eqn (46) and  $\sigma_{\theta\theta}$  from eqn (47).

## 7 NUMERICAL APPLICATIONS

The three simulations described in what follows follow the same steps of calculation. Simulation #1 is based on data for the fiber tension  $T$  calculated from Fig. 7A of Feit [17], and simulations #2 and #3 are based on data of  $T/P_i$  calculated from Fig. 5 of Chadwick [13] who uses in his simulation the same dimension  $r_o$  and  $r_i$  reproduced from Feit. Consequently the three simulations use the same values for the outer radius  $r_o = 3.38$  cm, the inner radius  $r_i = 1.02$  cm and length  $l = 3.06$  cm.

### 7.1 Simulation #1

A linear variation of  $\gamma(r)$  is assumed (see eqn (33)). The radial contraction force  $D_c = -D_r$  is positive during the systolic phase or late diastolic phase and it is calculated from eqn (4a), both  $T$  and  $D_c$  are

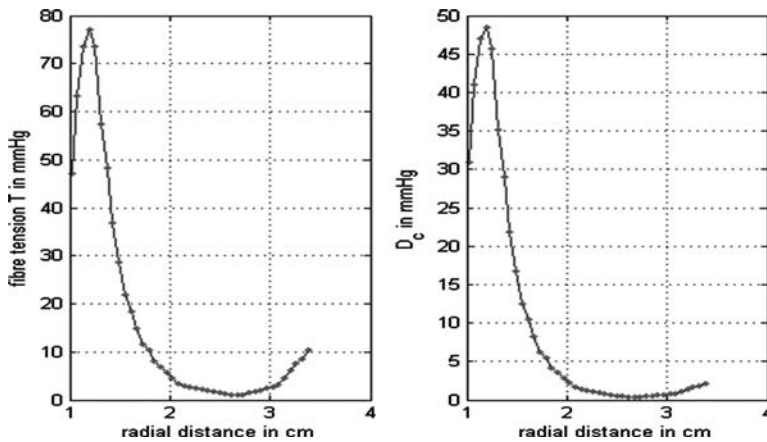


Figure 4: Simulation #1, radial variation from endocardium to epicardium of the fiber tension  $T$  (left), and of the radial active force/unit volume of the myocardium  $D_c = -D_r$  (right).

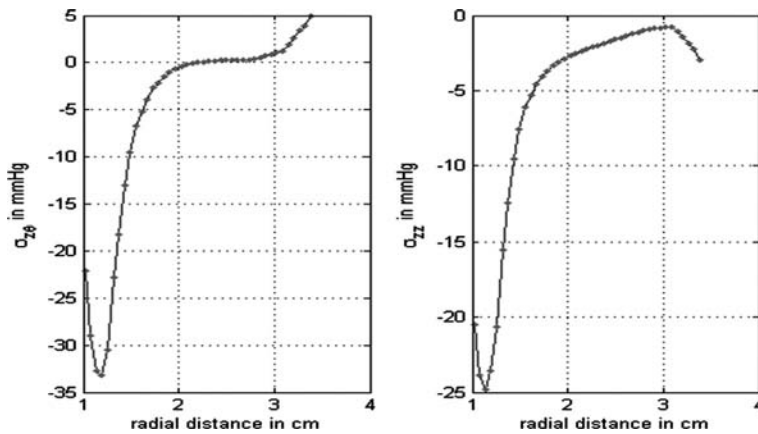


Figure 5: Simulation #1, radial variation from endocardium to epicardium of the stress component  $\sigma_{z\theta}$  (left), and of the axial stress  $\sigma_{zz}$  (right).

plotted against  $r$  in Fig. 4. The variation of  $\sigma_{z\theta}$  (see eqn (17)) and  $\sigma_{zz}$  (see eqn (18)) with  $r$  is shown in Fig. 5,  $\sigma_{z\theta} = 0$  for  $r_z = 2.2$  cm which is used to calculate  $R_z$  in eqn (48). We have taken in our calculation the inner pressure  $P_i = 10$  mmHg from the work of Feit [17] and we have assumed that the outer pressure  $P_o \approx 0.05P_i$ . The corresponding dimensions in the stress free configuration were estimated as  $R_o = 3.48$  cm and  $R_i = 1.15$  cm,  $\sigma_{rr} = t_{rr}$  ( $q_{rr} = 0$ ) and  $\sigma_{\theta\theta}$  are calculated as indicated in Section 6 and the results are shown in Fig. 6 together with  $q_{\theta\theta}$  and  $t_{\theta\theta} = q_{\theta\theta} + \sigma_{\theta\theta}$ . Calculated values of  $k_\theta = -0.4699$ ,  $k_z = 0.9350$ ,  $\alpha = 1.0603$  and  $\psi = 0.1011$ . Finally the variation with respect to  $r$  of  $W_{\lambda n}$  and  $W_{\Pi}$  is shown in Fig. 7.

## 7.2 Simulation #2

A linear variation of  $\gamma(r)$  is assumed (see eqn (33)). The radial contraction force  $D_c = -D_r$  is positive during the systolic phase or late diastolic phase and it is calculated from eqn (4a), both  $T/P_i$  and  $D_c$  are plotted against  $r$  in Fig. 8. The variation with respect to  $r$  of  $\sigma_{z\theta}$  (see eqn (17)) and  $\sigma_{zz}$  (see eqn (18)) is shown in Fig. 9,  $\sigma_{z\theta} = 0$  for  $r_z = 2.2$  cm which is used to calculate  $R_z$  in eqn (48). We have

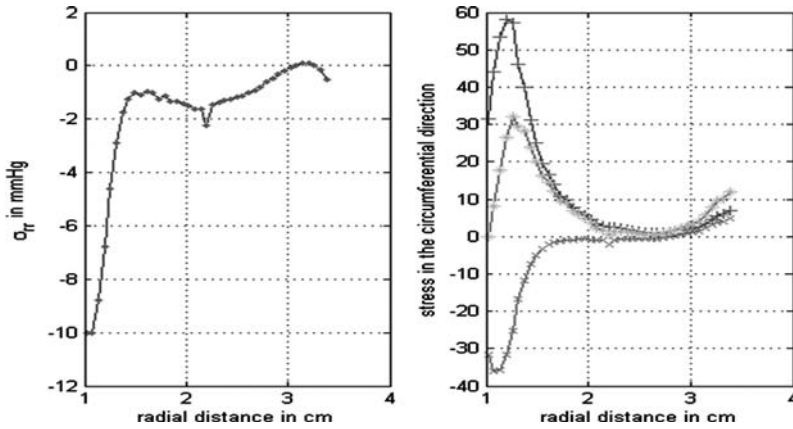


Figure 6. Simulation #1, radial variation from endocardium to epicardium of the radial stress  $\sigma_{rr}$  (left), and of the circumferential stress  $q_{\theta\theta}$  (+),  $\sigma_{\theta\theta}$  (x) and (\*)  $t_{\theta\theta} = q_{\theta\theta} + \sigma_{\theta\theta}$  (right).

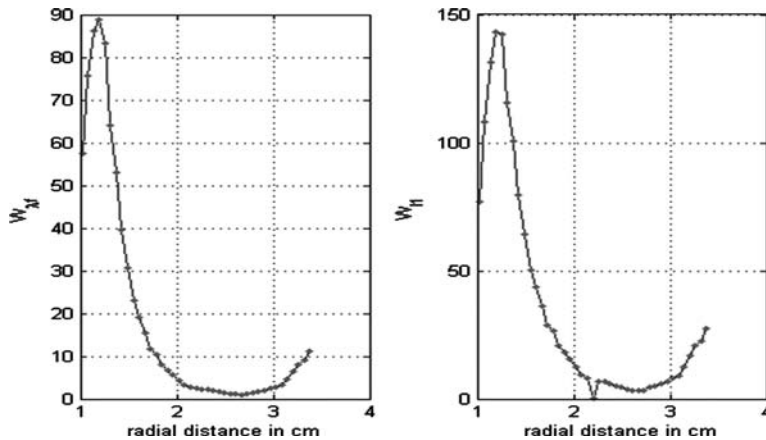


Figure 7: Simulation #1, radial variation from endocardium to epicardium of  $W_{\lambda f}$  (eqn (39)) (left), and  $W_{\Pi}$  (eqn (42)) (right).



taken in our calculation the inner pressure  $P_i = 1$  mmHg based on the work of Chadwick [13] and we have assumed that the outer pressure  $P_o \approx 0$ . The corresponding dimensions in the stress free configuration were estimated as  $R_o = 3.455$  cm and  $R_i = 1.08$  cm,  $\sigma_{rr} = t_{rr}$  ( $q_{rr} = 0$ ) and  $\sigma_{\theta\theta}$  are calculated as indicated in Section 6 and the results are shown in Fig. 10 together with  $q_{\theta\theta}$  and  $t_{\theta\theta} = q_{\theta\theta} + \sigma_{\theta\theta}$ . Calculated values of  $k_\theta = 0.2011$ ,  $k_z = 0.9905$ ,  $\alpha = 1.0388$  and  $\psi = -0.0413$ . Finally the variation with respect to  $r$  of  $W_{\lambda n}$  and  $W_{I1}$  is shown in Fig. 11.

### 7.3 Simulation #3

A cubic variation of  $\gamma(r)$  is assumed (see eqn (34)). The radial contraction force  $D_c = -D_r$  is positive during the systolic phase or late diastolic phase and it is calculated from eqn (4a), both  $T/P_i$  and  $D_c$  are plotted against  $r$  in Fig. 12. The variation with respect to  $r$  of  $\sigma_{z\theta}$  (see eqn (17)) and  $\sigma_{zz}$  (see eqn (18)) is shown in Fig. 13,  $\sigma_{z\theta} = 0$  for  $r_z = 2.2$  cm which is used to calculate

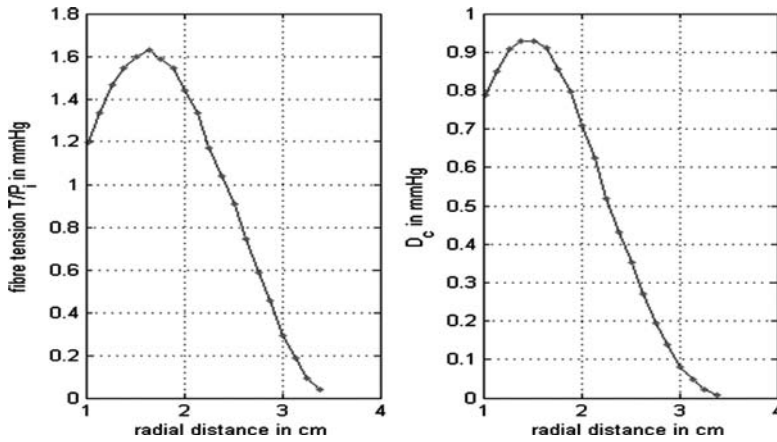


Figure 8: Simulation #2, radial variation from endocardium to epicardium of the fiber tension  $T/P_i$  (left), and of the radial active force/unit volume of the myocardium  $D_c = -D_r$  (right).

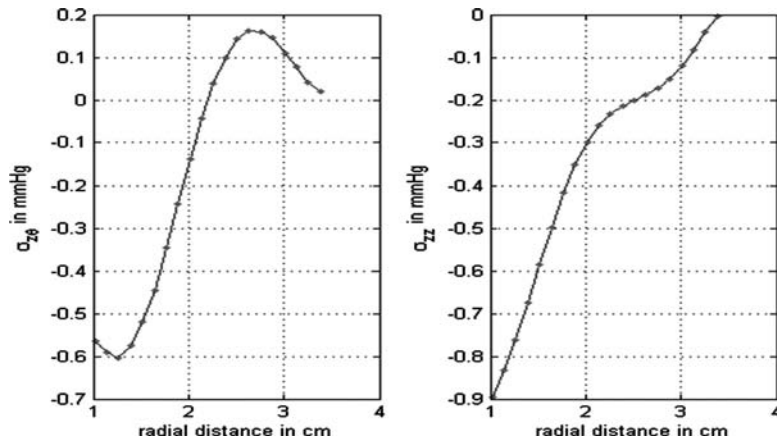


Figure 9: Simulation #2, radial variation from endocardium to epicardium of the stress component  $\sigma_{z\theta}$  (left), and of the axial stress  $\sigma_{zz}$  (right).

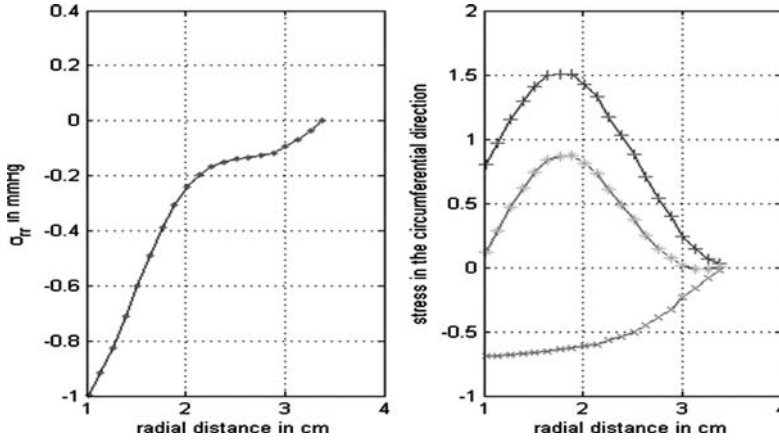


Figure 10: Simulation #2, radial variation from endocardium to epicardium of the radial stress  $\sigma_{rr}$  (left), and of the circumferential stress  $q_{\theta\theta}$  (+),  $\sigma_{\theta\theta}$  (x) and (\*)  $t_{\theta\theta} = q_{\theta\theta} + \sigma_{\theta\theta}$  (right).

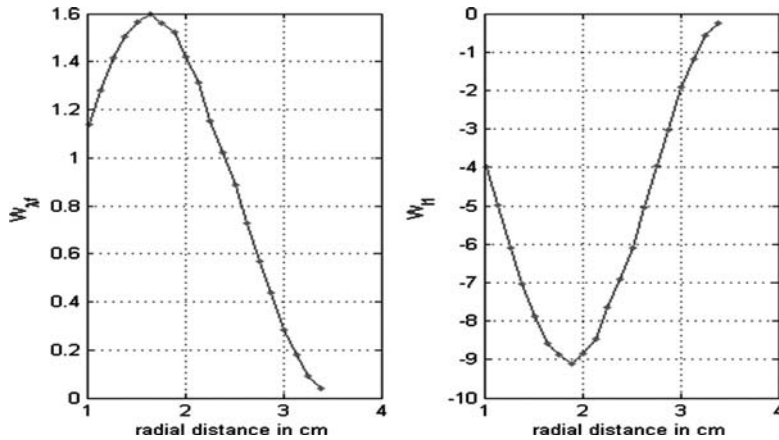


Figure 11: Simulation #2, radial variation from endocardium to epicardium of  $W_{\lambda f}$  (eqn (39)) (left), and  $W_{II}$  (eqn (42)) (right).

$R_z$  in eqn (48). We have taken in our calculation the inner pressure  $P_i = 1$  mmHg based on the work of Chadwick [13] and we have assumed that the outer pressure  $P_o \approx 0$ . The corresponding dimensions in the stress free configuration were estimated as  $R_o = 3.455$  cm and  $R_i = 1.08$  cm,  $\sigma_{rr} = t_{rr}$  ( $q_{rr} = 0$ ) and  $\sigma_{\theta\theta}$  are calculated as indicated in Section 6 and the results are shown in Fig. 14 together with  $q_{\theta\theta}$  and  $t_{\theta\theta} = q_{\theta\theta} + \sigma_{\theta\theta}$ . Calculated values of  $k_\theta = 0.2011$ ,  $k_z = 0.9905$ ,  $\alpha = 1.0388$  and  $\psi = -0.0413$ . Finally the variation with respect to  $r$  of  $W_{\lambda n}$  and  $W_{II}$  is shown in Fig. 15.

The three examples show the wide variation of  $W_{II}$  from one example to another. The values of  $R_o$  and  $R_i$  chosen are not unique, the simulation is very sensitive to the values of the parameters chosen and there is unfortunately no systematic and simultaneous measurement of all the parameters needed for our simulation. On the other hand one should notice the similarity of

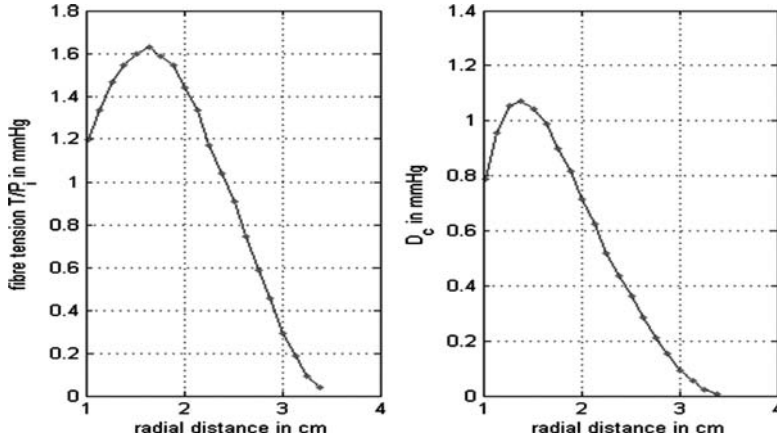


Figure 12: Simulation #3, radial variation from endocardium to epicardium of the fiber tension  $T/P_i$  (left), and of the radial active force/unit volume of the myocardium  $D_c = -D_r$  (right).

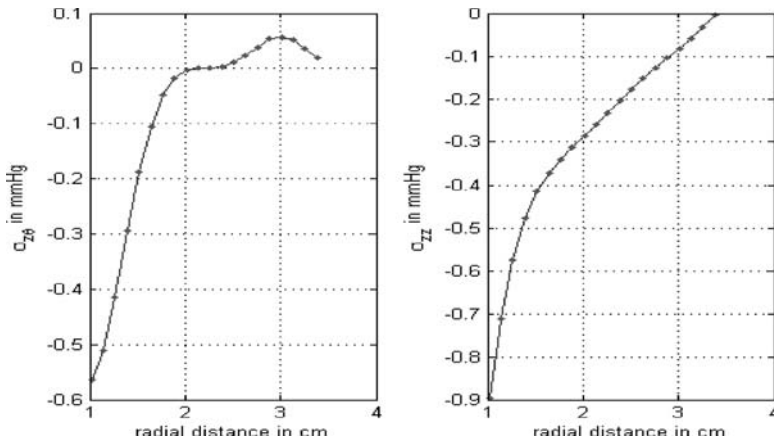


Figure 13: Simulation #3, radial variation from endocardium to epicardium of the stress component  $\sigma_{z\theta}$  (left), and of the axial stress  $\sigma_{zz}$  (right).

the curves for  $W_{\lambda_n}$  and  $T$  (or  $T/P_i$ ), which is due to the fact that the stretch ratio  $\lambda_n$  is varying around unity (see eqn (39)). The calculation of the components of the stress has been carried out without explicit knowledge of the pseudo-strain energy function  $W(I_1, \lambda_p)$ . The next step is to study a procedure by which one can recover  $W(I_1, \lambda_p)$  from the knowledge of the partial derivatives  $W_{\lambda_f}$  and  $W_{I_1}$ .

## 8 CONCLUSION

The total stress in the myocardium can be split into two components, a component due to the deformation of the passive isotropic medium of the myocardium and a component induced by the active muscular fibers  $T$ . By using this approach we have been able under some assumptions to derive these

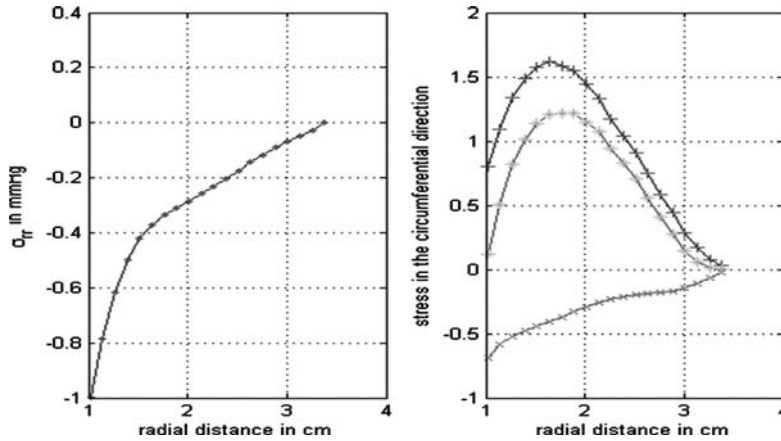


Figure 14: Simulation #3, radial variation from endocardium to epicardium of the radial stress  $\sigma_{rr}$  (left), and of the circumferential stress  $q_{\theta\theta}$  (+),  $\sigma_{\theta\theta}$  (x) and (\*)  $t_{\theta\theta} = q_{\theta\theta} + \sigma_{\theta\theta}$  (right).

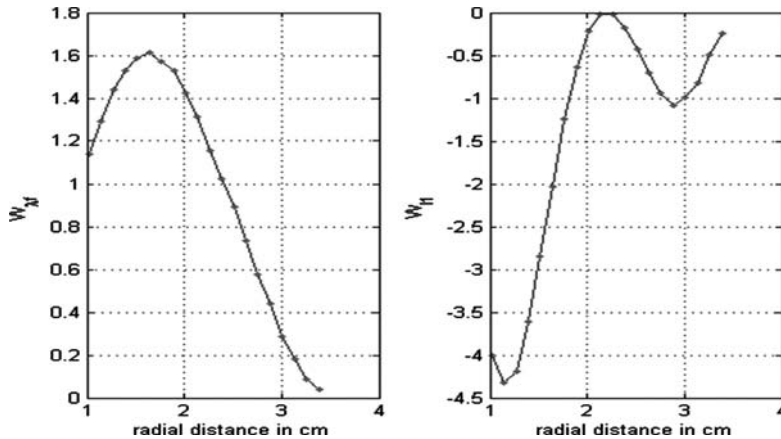


Figure 15: Simulation #3, radial variation from endocardium to epicardium of  $W_{\lambda_f}$  (eqn (39)) (left), and  $W_{I1}$  (eqn (42)) (right).

parts of the stress without explicit knowledge of the pseudo-strain energy function  $W$ . This method is sensitive to the parameters chosen in the calculation, unfortunately not all are measured simultaneously. By integrating the partial derivatives of  $W$  one can possibly gain better understanding of how one can choose directly a mathematical model for  $W$ .

#### REFERENCES

- [1] Humphrey, J.D. & Yin, F.C.P., Constitutive relations and finite deformations of passive cardiac tissue II: stress analysis in the left ventricle. *Circulation Research*, **65**, pp. 805–817, 1989.
- [2] Guccione, J.M., McCulloch, A.D. & Waldman, L.K., Passive material properties of intact ventricular myocardium determined from a cylindrical model. *Journal of Biomechanical Engineering*, **113**, pp.42–55, 1991. Comment by Chaudhry, H.R., *Journal of Biomechanical Engineering*, **118**, pp. 262–263, 1996.

- [3] Yang, M., Taber, L.A. & Clark, E.B., A nonlinear poroelastic model for the trabecular embryonic heart. *Journal of Biomechanical Engineering*, **116**, pp. 213–223, 1994.
- [4] Demiray, H., Stresses in ventricular wall. *Journal of Applied Mechanics*, **43**, pp. 194–197, 1976.
- [5] Shoucri, R.M., Equivalence of two approaches to study the stress-strain relation in the myocardium. *Modelling in Medicine and Biology VIII*, eds C.A. Brebbia, WIT Press: Southampton & Boston, pp. 3–16, 2009.
- [6] Shoucri, R.M., Active and passive stresses in the myocardium. *American Journal of Physiology*, **279**, pp. H2519–H2528, 2000.
- [7] Shoucri, R.M., Studying the mechanics of left ventricular contraction. *IEEE Engineering in Medicine and Biology Magazine*, **17**, pp. 95–101, 1998.
- [8] Shoucri, R.M., Theoretical study of pressure-volume relation in left ventricle. *American Journal of Physiology*, **260**, pp. H282–H291, 1991.
- [9] Shoucri, R.M., The pressure-volume relation and the mechanics of left ventricular contraction. *Japanese Heart Journal*, **31**, pp. 713–729, 1990.
- [10] Spencer, A.J.M., *Deformation of Fiber-reinforced Materials*, Clarendon Press: Oxford, UK, 1972.
- [11] Holzapfel, G.A., Gasser, T.C. & Ogden, R.W., Comparison of a multi-layer structural model for arterial walls with a Fung-type model, and issues of material stability. *Journal of Biomechanical Engineering*, **126**, pp. 264–274, 2004.
- [12] Peskin, C.S., *Mathematical aspects of heart physiology*, New York University, Courant Institute of Mathematical Sciences, 1975.
- [13] Chadwick, R.S., The myocardium as a fluid-fiber continuum: passive equilibrium configurations. *Advances in Bioengineering* ed D.C. Viano, The American Society of Mechanical Engineers, pp. 135–138, 1981.
- [14] Nevo, E. & Lanir, Y., Structural finite deformation model of the left ventricle during diastole and systole. *Journal of Biomechanical Engineering*, **111**, pp. 342–349, 1989.
- [15] Arts, T., Bovendeerd, P.H.M., Prinzen, F.W. & Reneman, R.S., Relation between left ventricular cavity pressure and volume and systolic fiber stress and strain in the wall. *Biophysical Journal*, **59**, pp. 93–102, 1991.
- [16] Tözeren, A., Static analysis of the left ventricle. *Journal of Biomechanical Engineering*, **105**, pp. 39–46, 1983.
- [17] Feit, T.S., Diastolic pressure-volume relations and distribution of pressure and fiber extension across the wall of a model left ventricle. *Biophysical Journal*, **28**, pp. 143–166, 1979.

# UNIVERSAL FEATURES IN THE LAWS OF GROWTH

P.P. DELSANTO<sup>1</sup>, A. GLIOZZI<sup>1</sup>, D. ALEXANDRU IORDACHE<sup>2</sup> & C. GUIOT<sup>3</sup>

<sup>1</sup>Department of Physics, Politecnico di Torino, C.so Duca degli Abruzzi 24, 10129 Torino, Italy.

<sup>2</sup>Department of Physics, University "Politehnica" of Bucharest, Splaiul Independenței 313, Bucharest, Romania.

<sup>3</sup>Department of Neuroscience, Università di Torino, C.so Raffaello 30, 10125 Torino, Italy.

## ABSTRACT

Computational models and simulations can be powerful tools for gaining an insight into the complex world of the biological mechanisms. Among them the growth processes are perhaps the most challenging and elusive to describe, for the different time scales and species specific features involved. Using a recently proposed technique for the analysis of experimental datasets (the Phenomenological Universalities Approach: PUN), we have succeeded to reproduce, to an excellent level of reliability, many results from experimental ‘*in vitro*’ and ‘*in vivo*’ tumor growth studies (e.g. the ‘multipassaged’ tumors described in the paper). Also the description of human growth, with its important implications for monitoring children development and diagnosing metabolic diseases, can be approached using the PUN method.

*Keywords: best fitting, biological models, complexity, human growth, metabolic diseases, nonlinearity, phenomenological universalities, scaling, simulations, tumor growth.*

## 1 INTRODUCTION

Growth of living beings and biological entities (e.g. tumors) has been extensively studied in the past. Most of the proposed laws are based on phenomenology, and simply fit experimental data in a (more or less) satisfactory manner.

More recently, some efforts have been devoted to find a scientific basis (mainly related to physics) for the proposed algorithms. In particular, West and collaborators have published their allometric model based on both the principle of energy conservation and the assumption that the development of a proper vascular network is the basis for growth in all living beings [1, 2] and its main limiting factor, explaining growth saturation.

For most living organisms the vascular network develops according to some ‘optimality principles’ [3]: provided eight assumptions are done, regarding network scaling and hierarchical structure, constant branching ratio and space-filling properties and assuming that the network should minimize the energy losses and maximize exchange surfaces.

The growth law can be written as

$$dV/dt = a V^{3/4} - b V \quad (1)$$

where  $V$  is the volume and  $a$  and  $b$  are suitable parameters. Note that the term  $V^{3/4}$  can be interpreted as an ‘effective exchange surface’, e.g. in the case of a cell assuming nutrients only by diffusion through its membrane  $S = V^{2/3}$ . This formalism has been extended by Guiot *et al.* [4] for tumors.

Another very important application is human growth. Height, weight and body mass index (BMI) growth charts are universally adopted to monitor children growth and diagnose metabolic diseases, and are the basis of the field of auxology. Human growth has been described by a plethora of different algorithms, many of which simply aiming at best fitting average data [5].

## 2 PHENOMENOLOGICAL UNIVERSALITIES

Mathematical relationships, such as algebraic equations, ordinary differential equations (ODE), partial differential equations (PDE), etc. can be considered as true universalities, since their validity is

completely independent from the field of application, be it physics, biology, economics or any other science. They are, however, ‘*a priori*’ (or ‘top-down’ [6]) universalities, even if they are the ultimate result of a considerable amount of experimental or observational work, since they no longer contain any reference to the experiments and observations from which they have been inferred. In other words, they are stated as valid or applicable ‘*per se*’ and often include the effect of intellectual manipulations, such as generalizations or corrections due to analogies, intuition or formal elegance. Their usefulness may be immediately appreciated in any kind of ‘top-down’ approach, in which they are applied to the solution of the most diverse problems in all fields of science.

In the present context we are concerned with Phenomenological Universalities (PUN), which represent an attempt to classify in well defined classes of universality datasets collected in all fields of science, based on simple unifying criteria. Thus, apart from their epistemologic interest, PUN’s allow to set up a ‘bottom-up approach, in which ‘laws’ or ‘models’ are inferred ‘*a posteriori*’, i.e. directly from data.

To be more specific, we define PUN’s as a tool for solving the following problem:

Given the string of data  $z_i = z(t_i)$ , ( $i = 1, \dots, J$ ) with  $t$  being the time (or any other suitable variable), then:

1. Find a best fitting function  $z(t)$ , based not on a given numerical procedure, but on a general formalism independent of the field of application.
2. From the fitting function obtain a model for the proposed phenomenology.

The above problem can be easily extended to vectorial datasets, such as  $z_{ki} = z_k(t_i)$ , ( $k = 1, \dots, K$ ), in which correlations exist among several variables  $z_k$ , all functions of the same independent variable  $t$ , which might also be vectorialized. In the case  $K = 2$ , the use of a complex notation both for the variables and the parameters, allows to use, for the solution of the problem, the same formalism developed in the following sections.

## 2.1 Procedure

Assuming for brevity to have a single dataset  $z(t_i)$ , the problem defined above can be solved by searching for a relationship of the kind

$$G^N(a, b, p_1, p_2, \dots, p_N) = 0 \quad (2)$$

which represents the truncation of a suitable expansion to the  $N$ -th term, with  $N$  fitting parameters  $p_n$ . In eqn (1)  $a = \dot{z}$ ,  $b = \ddot{z}$ , with dots denoting differentiation with respect to the independent variable, i.e.  $\dot{z} = dz/dt$ . In general  $a = a(z, t)$ , but in the following we restrict ourselves to the case  $a = a(z)$ . The cases  $a = a(t)$  and  $a$  given by a sum of contributions from two terms,  $\bar{a}(z)$  and  $\tilde{a}(t)$ , each depending on only one of the two variables, are discussed in Ref. [7].

As a simple but very important example, we consider the sub-case of eqn (2), in which  $b = b(a)$ . Since

$$b = \dot{a} = \frac{da}{dz} \dot{z} = a \frac{da}{dz} \quad (3)$$

assuming

$$\frac{da}{dz} = \beta + \gamma a + \delta a^2 + \dots, \quad (4)$$

if we truncate the expansion at the  $N$ -th term, then we call the corresponding PUN class UN. It follows, in the case  $N = 2$  (i.e. U2):

$$b = \sum_{n=1}^2 \alpha_n^{(N)} a^n = \beta a + \gamma a^2 \quad (5)$$

Eqn (5), or its generalization to UN with  $N > 2$ , has a very simple interpretation (or justification). Even if the experimentally measured quantity is  $z(t)$ , the relevant observable, for what concerns the evolution of the system, is  $a$ . In a linear approximation we would expect its derivative  $b$  to be proportional to  $a$ , for reasons of scaling. But our overwhelming experience in all fields of science points out to a nonlinear Universe, with the linearity being just an approximation or a special (often ad hoc) case. Therefore we should also expect a nonlinear  $b(a)$ .

One could, of course, in addition to the ‘space’  $(a, b)$ , consider others, such as  $(z, a)$  or  $(z, b)$ , but we do not do it here, since they would lead to already well explored ODE’s (or PDE’s). Other PUN classes in the space  $(a, b)$  may also be considered, e.g. the extended UN class EUN, for which

$$b = \sum_{n=0}^N \alpha_n^{(N)} a^n = a + \beta a + \gamma a^2 + \dots \quad (6)$$

or the VN class, defined by

$$a = \sum_{n=1}^N \beta_n^{(N)} b^n. \quad (7)$$

The classes EUN will be considered in the next section.

Obviously such PUN classes are of interest only if some phenomenology described by them may be found. For example, EU2 seems to be able to represent the growth of successive implantations of tumoral lines in cavies or other lab animals.

## 2.2 The class UN

The class U1 and its correspondence with the well known (and most extensively used) Gompertz law are discussed in Ref. [8] Therefore in the following we limit ourselves to derive the basic formalism for the class U2, which includes, as special cases, the well known law for ontogenetic growth of West and collaborators [1–3] and its extension to tumoral growth [9]. From the differential equations  $\dot{a} = b$  and eqn (5), it follows:

$$a = a_0 \left[ (1 + \psi) e^{-\beta t} - \psi \right]^{-1} \quad (8)$$

where  $\psi = (\gamma/\beta)a_0$  and  $a_0 = a(z(0))$ . Then from  $\dot{z} = a$  and  $z(0) = 0$ , which does not represent a real restriction (since a translation can be performed), it easily follows:

$$z = -\frac{1}{\gamma} \ln \left[ 1 + \psi (1 - e^{\beta t}) \right] \quad (9)$$



A specially relevant case can be obtained by letting  $z = \ln y$ . Then we have the usual growth equation:

$$\dot{y} = a(y)y \quad (10)$$

with the solution

$$y = \left[ 1 + \psi(1 - e^{\beta t}) \right]^{-1/\gamma} \quad (11)$$

It can be easily proven that  $y$  satisfies the ODE

$$c_1 y^p = \frac{dy}{dt} + c_2 y \quad (12)$$

where  $p = 1 + \gamma$ ,  $c_2 = \beta/\gamma$ ,  $c_1 = c_2(1 + \psi)$ .

In many applications (e.g. in biology, see [10]), a very important interpretation can be attached to eqn (12). That is, we may consider  $c_1 y^p$  as the energy input,  $dy/dt$  the growth of the system and  $c_2 y$  the energy consumption (e.g. due to the metabolism). Then saturation (i.e. no further growth:  $dy/dt = 0$ ) follows when  $c_1 y^p = c_2 y$ .

According to the 1st law expressed per unit time, any variation in the internal energy is related to the difference between the input energy (1st term of the RHS of eqn (1), accounting for the nutrient/oxygen inlet from the surface by diffusion, or through the vascular network) and the energy required for metabolism, which is normally dependent on the volume of the system. Any positive variation in the internal energy can be stored in the system (e.g. by adipose mass) or, alternatively, used for growth (LHS of eqn (1)).

This interpretation, which implies that eqn (12) is an expression of the energy conservation of the system (or of the First Principle of Thermodynamics), is very intriguing, since it suggests that, as a direct result of the nonlinearity of eqn (5), fractality follows (since in general  $p$  is not integer, unless the energy input is uniformly distributed over the whole system). If the energy enters the system through its external (e.g. spherical) surface, then  $p = 2/3$ . In the model of West and collaborators  $p = 3/4$ . In a recent model by Guiot *et al.* [11] the exponent  $p$  varies between a first avascular phase of tumoral growth and the onset of angiogenesis.

It is interesting to remark that in the next PUN class U3, eqn (12) becomes

$$c_1 y^p = c_2 \frac{dy}{dt} + c_3 \frac{dy^p}{dt} - c_4 y \quad (13)$$

that is an additional term  $c_3(dy^p/dt)$  appears as a fractal-like dimensioned contribution to the growth. The coefficients  $c_1$ ,  $c_2$ ,  $c_3$  and  $c_4$  are not reported here for brevity.

From eqn (11), by defining

$$u = y^{-\gamma} - 1 \quad (14)$$

and

$$\tau = 1 - e^{\beta t} \quad (15)$$

it follows

$$u = \psi\tau \quad (16)$$

that is, the scaling invariance, which was lost in eqn (10), due to its nonlinearity, is regained by means of the adoption of the fractal-dimensioned variables  $u$  and  $\tau$ .

### 2.3 The class EUN

In Section 2.1, eqn (6) may be ‘justified’ as a plausible generator of PUN classes on aesthetical grounds, since it completes the power expansion of  $b(a)$ , which in the UN formalism (see eqns 3–5) lacks the  $n = 0$  term  $a$ . A correlation between the classes EUM and UN, with  $N = M + 1$ , may be easily obtained by defining:

$$f(a) = \sum_{n=0}^M a_n a^n = a_M \prod_{n=1}^M (a - r_n), \quad (17)$$

where  $r_n$  are the roots of  $f(a)$ , including possibly multiple ones and complex conjugate (c.c.) pairs.

In the case EUM, from  $b(a) = f(a) = da/dt$  it follows:

$$t = t(a) = I = \int \frac{da}{f(a)} \quad (18)$$

whereas, in the case UN, from  $b(a) = a f(a) = da/dt$  it follows:

$$t = t(a) = J = \int \frac{da}{a f(a)} \quad (19)$$

The integral  $I$  can be easily evaluated, starting from the formula [12]:

$$\frac{1}{f(a)} = \sum_{n=1}^M \frac{1}{f'(r_n)(a - r_n)} = \sum_{n=1}^M \frac{p_n}{a - r_n} \quad (20)$$

where the prime denotes derivation with respect to  $a$  and

$$p_n = [f'(r_n)]^{-1} \quad (21)$$

It follows for EUM, apart from an integration constant:

$$t(a) = \sum_{n=1}^M p_n \ln(a - r_n) = \ln \prod_{n=1}^M (a - r_n)^{p_n} \quad (22)$$

For the evaluation of  $J$  we can apply eqn (20) to the function  $g(a) = a f(a)$  and let  $n = 0, M$  with  $r_0 = 0$ . Then

$$\frac{1}{a f(a)} = \frac{1}{a f(0)} + \sum_{n=1}^M \frac{q_n}{a - r_n} = \sum_{n=0}^M \frac{q_n}{a - r_n} \quad (23)$$

where  $q_0 = 1/f(0)$  and  $q_n = p_n/r_n$  for  $n = 1, M$ .

It follows for UN (with  $N = M + 1$  and apart from an integration constant):

$$t(a) = \sum_{n=0}^M q_n \ln(a - r_n) = \ln \prod_{n=0}^M (a - r_n)^{q_n} \quad (24)$$

It is important to recall that, in case of c.c. pairs of roots,

$$\ln(x + iy) = \ln(r \exp(i \Phi)) = \ln r + i \Phi$$

where and  $r = \sqrt{x^2 + y^2}$   $\Phi = \arctg y/x$  ( $0 \leq \Phi < \pi$ ),

So that, instead of logarithms of complex numbers, it is possible to express the results in terms of arctg of real numbers [12, idem, eqn 2.172, p. 68].

In order to obtain the solution  $z(t)$ , or  $y(t) = \exp z(t)$ , one must integrate the ODE  $dz/dt = a(t)$ . The prerequisite for this, of course, is the inversion of the relationship  $t(a)$ , given by eqns (22) and (24) for EUM and UN, respectively.

This can be easily done up to  $M$  or  $N = 2$ . The results are summarized in Tables 1 and 2 for EUM and UN, respectively.

Table 1: Solutions for the PUN classes EUM,  $M = 0, 1, 2$ .

	$b(a)$	$a(t)$	$z(t)$
EU0	$a$	$a t + a_0$	$\frac{1}{2} a t^2 + a_0 t$
EU1	$a + \beta a$	$r + (a_0 - r) B$	$r t + 1/\beta (a_0 - r) (B - 1)$
EU2	$a + \beta a + \gamma a^2$	$a_0 (p - q E)/(1 - E)$	$p t - 1/\gamma \ln((1 - E)/(1 - E_0))$

The following notations have been used:  $a_0 = a(0)$ ;  $B = \text{ext}(\beta t)$ ;  $E_0 = (1 - p)/(1 - q)$ ;  $E = E_0 \exp(\gamma (p - q)t)$ ,  $r = a/\beta$ ,  $p$  and  $q$  are the roots of the equation  $b(a) = 0$  for EU2.

Table 2: Solutions for the PUN classes UN,  $N = 0, 1, 2$ .

	$b(a)$	$a(t)$	$z(t)$
U0	0	$a_0$	$a_0 t$
U1	$\beta a$	$a_0 B$	$a_0 (B - 1)/\beta$
U2	$\beta a + \gamma a^2$	$a_0 B/(1 + \Phi - \Phi B)$	$-1/\gamma \ln(1 + \Phi (1 - B))$

The following notations have been used:  $a_0 = a(0)$ ;  $B = \text{ext}(\beta t)$ ;  $\Phi = \gamma a_0/\beta$ . The reported solutions are, of course, in agreement with the ones found in Section 2.2.

Many plots obtained for U1, U2 (and its generalizations UN/TM, obtained when  $a(t, z) = \bar{a}(t) + \bar{a}(z)$ ) may be found elsewhere [7]. No plots of EUM growth curves have been reported so far. Figure 1 accounts for the first four members of the family.

Therefore, in the next section, we present some representative examples, in the spirit of building up an ‘Atlas of PUN classes’ helping experimentalists to select a suitable class for novel datasets. We wish to recall that an extremely beautiful and comprehensive ‘Atlas of Functions’ [13] has been recently compiled for the ‘mathematical universalities’.

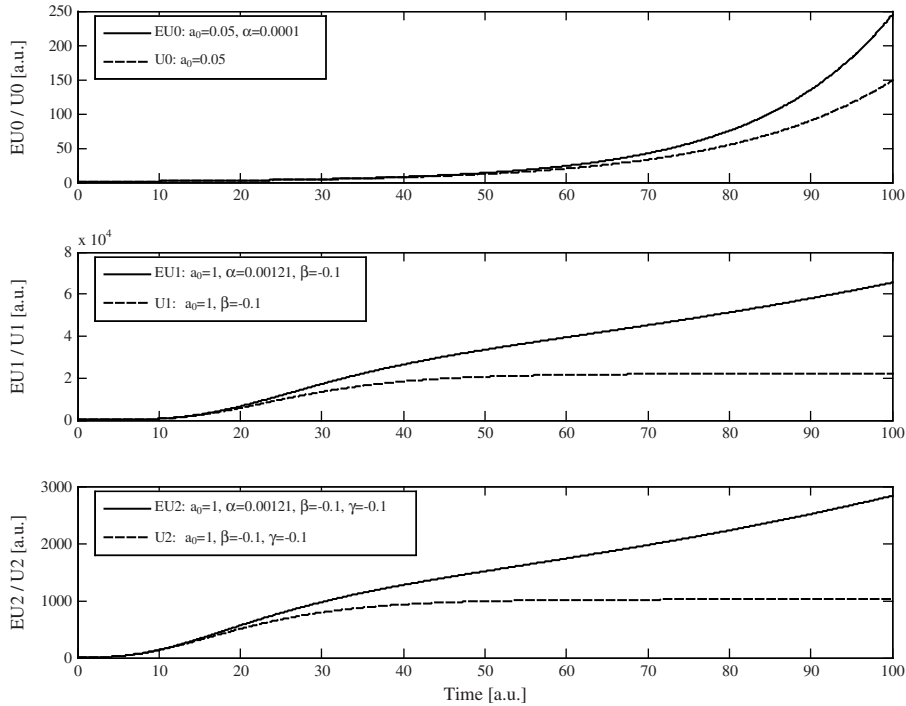


Figure 1: Some examples of different behaviors for the universal classes EUN and the corresponding class UN.

### 3 NOTABLE APPLICATIONS OF THE PUN CLASSES UN: TUMOR GROWTH

The PUN class U0 describes a simple exponential growth law, which properly applies to tumoral cells keeping on replicating with a constant duplication time in the absence of mechanical or nutritional restrictions. Contrary to expectations, such a model is not totally unrealistic. In fact, U0 represents the first phase of any '*in vitro*' experiment, and also the initial phase of all tumors.

Such an unrestricted growth may last for days, months or even years provided a healthy, nutrient rich environment is available, as in the biological model of the Multi Passage Tumor (MPT), where tumors grow following the subcutaneous implantation on the back of a lab animal (usually mice) of  $\sim 10^6$  tumor cells (from cell cultures or surgical resection). Tumor cells are then passaged from one mouse to another by harvesting them from a growing tumor and implanting a given number of them into another healthy animal. Once the tumor has grown above a certain volume, it is harvested again [14, 15]. For example, McCredie *et al.* reported the case of a spontaneous mammary tumor in a C3H mouse, from which the first syngenic transplant was done in 1946 and which has been serially transplanted into the C3H/HeJ strain, reaching in 1971 the 900th generation.

As shown in Figure 2, tumors grow at a larger rate in each successive transplant, i.e. the growth curves become progressively steeper, which can be explained by observing that, being the new seed reimplanted each time after a short time  $T$  (e.g. 10 days) into a new healthy, nutrient rich environment; thus we can assume at each 'passage' an experimental growth law with approximately the same rate  $c$ . The tumor mass, after  $n$  passages in which the same amount  $m_0$  of tumor

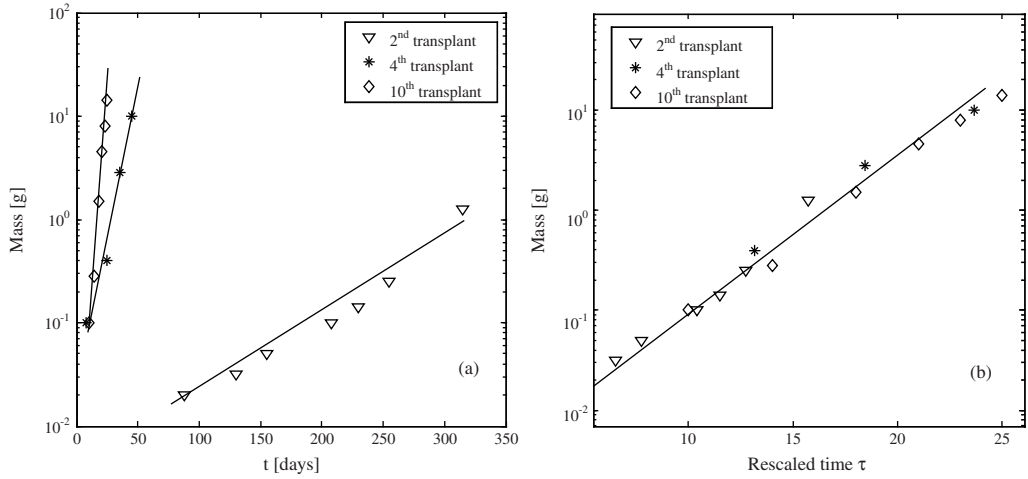


Figure 2: Results from Steel [14]. Up to 10 transplants of cells from the tumoral line rat fibroadenoma have been performed, but the curves corresponding to only three of them have been reported [9] in logarithmic scale. As discussed in the text, the averaged growth curves become increasingly steeper with successive passages, due to the aging of the newly transplanted tumor cells. By rescaling the time, we obtain a plot (b), in which all the curves are collapsed into a unique one.

is reimplanted, and at a time from the beginning of the whole procedure equal to  $t = nT + \Delta t$ , will be given by [17]:

$$m(t) = m_0 (1 + \exp(ncT)(\exp(c\Delta t) - 1)) \quad (25)$$

Eqn (25) shows that the exponential trend is corrected by a term, which accounts for the real age of the tumor and increases at each transplant, thus accelerating the growth.

If we follow the tumor growth curve for a longer time (even ‘*in vitro*’), a necrotic core will develop, due to the ‘screening’ of the nutrients flow from the cells of the outer layers, so that a saturation level is reached. This corresponds to the PUN class U1, predicting a saturation value:

$$V_\infty = V_0 \exp(c_0/\beta) \quad (26)$$

which is normally seen in MTS and is normally described using the Gompertz law [17]. Most aggressive tumors overcome nutrients deprivation by means of angiogenesis, and the neo-vascular network partly supports growth, as discussed by Guiot *et al.* [18], following the model of West and collaborators [1–3]. Often this third phase is complemented, in ‘*in vivo*’ or ‘*ex vivo*’ tumors by the processes of tumor invasion and metastasis. Starting from West’s law (1), a generalized expression for growth is then:

$$dV/dt = a S - b V \quad (27)$$

where  $S$  is the embedding layer acting as boundary with the host (i.e. the effective ‘surface’ from which nutrients come and waste products are removed), and  $V$  the volume, to which the energy consumption for metabolism is assumed to be proportional. Note:  $S$  is not in general a 2D surface.

This stage of tumor growth corresponds to the PUN class U2. The class U2 includes, besides Gompertz as a special case, all the growth models proposed to date in all fields of research, i.e. besides the already mentioned model of West and collaborators [1–3], also the exponential, logistic, thetalogistic, potential, von Bertalanffy, etc. (see for a review De Vladar [19]).

The choice of the specific ‘strategy’ for maximizing the exchange surface depends on many factors, according to the characteristics of the host and the ‘molecular weapons’ available.

This encompasses the possibility that the tumor evolves by changing the ‘degree of fractality’ of its nutrient input system and may imply that the fractal parameter  $p$  varies dynamically through tumor growth [11, 20], which requires resorting to the PUN class U3.

#### 4 NOTABLE APPLICATIONS OF THE PUN CLASSES EUN: HUMAN GROWTH

Understanding human growth, and particularly some phases, such as the perinatal and the juvenile ones, has always been challenging. Simple curves based on well established assumptions, and widely applied to other fields (such as the Gompertz curve) are inadequate, and therefore purely phenomenological curves, selected on the basis of their ‘fitting’, were traditionally used.

Contrary to most mammals, the growth curve of some ‘social’ species, such as elephants, lions, primates and men, cannot be described by a simple curve, but requires at least two Gompertz- or logistic-like curves (or three for humans, see for instance [21]), describing the early growth and the juvenile phases separately.

According to Devenport [22], the human growth rate exhibits three maxima: one intrauterine, a second around the 6-th year and the third around the 16-th year, possibly activated by the secretions of the pituitary gland or the anterior lobe of the hypophysis.

In addition to the above main accelerations, many authors have pointed out that short-term oscillations are detectable looking at longitudinal data. In the classical paper of Butler *et al.* [23], 135 children were monitored at six monthly intervals from 2 to 18 years of age.

Longitudinal studies made apparent a cyclic, rhythmic pattern, as a cycle of spurts and lags occurring from the age of 2 until adolescence.

Actually, in the historical paper of Wales [5] even very short time cyclicities, such as the postural changes in height throughout the day, due to spinal disc compression, are reported. Variations in height velocity have been described with the season of the year, possibly modulated through the higher central nervous system and secretion of melatonin and other hormones with circadian rhythmicity.

All the above effects cannot obviously be deduced by phenomenologic models. Moreover, being the algorithms different and selected ‘ad hoc’, to compare the results from studies performed in different institutions, or between normal vs. pathological growth (normally described by different growth charts) is virtually impossible. The PUN model, and in particular the EUM family seems, on the contrary, to be able to describe the growth using few, unifying variables.

Figure 3 represents the various types of growth which can be found in human growth reported in the variables  $dz/dt$  vs.  $z$ .

Actually, in many phases of human growth (as, for instance, fetal growth [24], see Figure 4) the relationship  $a$  vs.  $z$  exhibits some non-monotonicity, i.e. some ‘spurts’. Contrary to UN, the EUN family, proved to account for such spurts.

The analysis of the obtained results (starting from some existing data concerning the human body growth) suggests that the use of the similitude ‘phases space’  $(z, \dot{z})$  allows the identification of the main types of growth stages, which can be reproduced by the EUM universality class.

Further work is needed to estimate the parameter values which best fit the various human growth phases and to better exploit all the model features, and possibly to explore its implications for

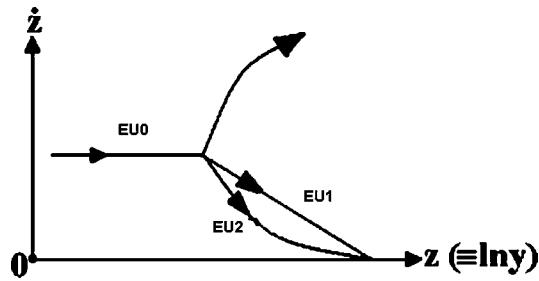


Figure 3: A sketch of the growth curves which can be found in various phases of human growth reproducible with the EU0, EU1 and EU2 models.

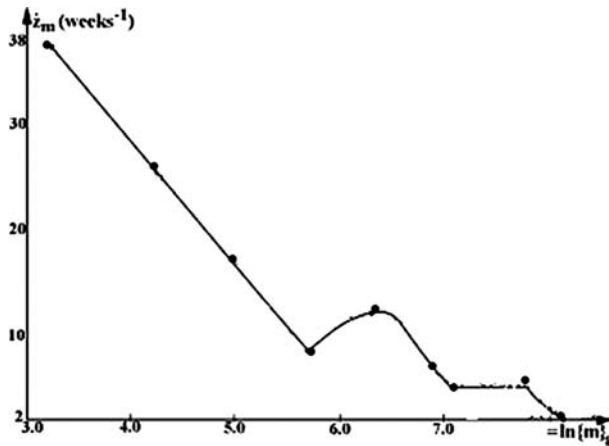


Figure 4: Fetal growth: sketch of the line connecting the experimental data (estimated mass reported in Ref. [24]). Data are represented using the logarithm of the mass on the  $x$ -axis and its time derivative on the  $y$ -axis).

diagnosing various growth pathologies. For instance, by assuming that different ‘clones’ of cells can be activated at different times (e.g. by hormones, such as GH or sexual hormones), the EUM curves can be further modulated to better resemble the realistic human growth curves.

By comparison between any specific individual growth curve and the collection of many representative ones, the numerical evaluation of the timing and the amplitude at the onset of the ‘growth spurts’ could eventually lead to a better diagnostics of some hormonal disorders as well as to a better monitoring of the related therapies.

## 5 ACKNOWLEDGEMENTS

One of the authors (ASG) acknowledges the support of a Lagrange fellowship from the C.R.T. Foundation. CG kindly acknowledges the contribution from Regione Piemonte (Progetti Sanitari Finalizzati 2008) and Università di Torino.

## REFERENCES

- [1] West, G.B., Brown, J.H. & Enquist, B.J., A general model for ontogenetic growth. *Nature*, **413**, pp. 628–631, 2001.
- [2] West, G.B. & Brown, J.H., Life’s universal scaling laws. *Physics Today*, **57**, pp. 36–43, 2004.

- [3] Savage, V.M., Deeds, E.J. & Fontana, W., Sizing up allometric scaling theory. *PLoS Comput Biol*, **4**, pp. e1000171, 2008.
- [4] Guiot, C., Degiorgis, P.G., Delsanto, P.P., Gabriele, P. & Deisboeck, T.S., Does tumor growth follow a “universal law”? *J Theor Biol*, **225**, pp. 147–151, 2003.
- [5] Wales, J.K.H., A brief history of the study of human growth dynamics. *Ann Human Biol*, **25**, pp. 175–184, 1998; see also Canessa, E., Modeling of body mass index by Newton’s second law. *J Theor Biol*, **248**, pp. 646–656, 2007.
- [6] Bejan, A. & Marden, J.H., Unifying constructal theory for scale effects in running, swimming and flying. *J Exp Biol*, **209**, pp. 238–248, 2006.
- [7] Delsanto, P.P., Gliozzi, A.S. & Guiot, C., Scaling, growth and Ciclicità in biology: a new computational approach. *Theoretical Biology and Medical Modelling*, **5**, p. 5, 2008, doi:10.1186/1742-4682-5-5.
- [8] Delsanto, P.P., Gliozzi, A.S. & Bosia, F., A comparison of different instances of phenomenological universalities, *Proceedings of the 9th WSEAS International Conference on Mathematics & Computers In Biology & Chemistry*, Bucharest, Romania, pp. 36–41, 2008.
- [9] Delsanto, P.P., Griffa, M., Condat, C.A., Delsanto, S. & Morra, L., Bridging the gap between mesoscopic and macroscopic models: the case of multicellular tumor spheroids. *Phys. Rev. Lett.*, **94**, pp. 148105, 2005.
- [10] Castorina, P., Delsanto, P.P. & Guiot, C., Classification scheme for phenomenological universalities in growth problems in physics and other sciences. *Phys Rev Lett*, **96**, pp. 188701, 2006.
- [11] Guiot, C., Delsanto, P.P., Carpinteri, A., Pugno, N., Mansury, Y. & Deisboeck, T.S., The dynamic evolution of the power exponent in a universal growth model of tumors. *J Theor Biol*, **240**, pp. 459, 2006.
- [12] Gradshteyn, I.S. & Ryzhik, I.M., *Tables of Integrals, Series and Products*, Academic Press: New York, pp. 56–7, 1980.
- [13] Oldham, K., Myland, J. & Spanier, J., *An Atlas of Functions*, Springer: New York, 2008.
- [14] Steel, G.G., *Growth Kinetics of Tumors*, Clarendon Press: Oxford, 1977.
- [15] McCredie, J.A. & Sutherland, R.M., Differences in growth and morphology between the spontaneous C3H mammary carcinoma in the mouse and its syngenic transplants. *Cancer*, **27**, pp. 635–642, 1971.
- [16] Gliozzi, A.S., Guiot, C. & Delsanto, P.P., A new computational tool for the phenomenological analysis of multipassage tumor growth curves. *PLoS ONE*, **4**, e5358, 2009, doi:10.1371/journal.pone.0005358.
- [17] Gompertz, B., On the nature of the function expressive of the law of human mortality and a new mode of determining life contingencies. *Phil Trans R Soc*, **115**, pp. 513–585, 1825.
- [18] Guiot, C., Pugno, N., Delsanto, P.P. & Deisboeck, T.S., Physical aspects of cancer invasion. *Phys. Biol.*, **4**, P1–P6, 2007, doi:10.1088/1478-3975/4/4/P01.
- [19] De Vladar, H.P., Density-dependence as a size-independent regulatory mechanism, *J Theor Biol*, **238**, pp. 245–256, 2006.
- [20] Delsanto, P., Gliozzi, A.S., Bruno, C.L.E., Pugno, N. & Carpinteri, A., Scaling laws and fractality in the framework of a phenomenological approach. *Chaos, Solitons & Fractals*, ISSN: 0960-0779, 2008.
- [21] Lozy, M.E., A critical analysis of the double and triple logistic growth curves. *Ann Hum Biol*, **5**, pp. 389–394, 1978.



- [22] Devenport, C.B., Human growth curve. *J Gen Physiol*, **10**, pp. 205–216, 1926.
- [23] Butler, G.E., McKie, M. & Ratcliffe, S.G., The cyclical nature of prepubertal growth. *Ann Hum Biol*, **17**, pp. 177–198, 1990.
- [24] (a) <http://embriology.med.unsw.edu.au/wwwhuman/Stages/Cstages.htm>, (b) <http://embriology.med.unsw.edu.au/wwwhuman/Stages/Cst800.jpg>, (c) <http://embriology.med.unsw.edu.au/wwwhuman/Hum.10wk/Images/fetalweight.jpg>.

# MODELING STENT EXPANSION DYNAMICS AND BLOOD FLOW PATTERNS IN A STENOTIC ARTERY

M.R. HYRE<sup>1</sup>, R.M. PULLIAM<sup>2</sup> & J.C. SQUIRE<sup>1</sup>

<sup>1</sup>Department of Mechanical Engineering, Virginia Military Institute, USA.

<sup>2</sup>Department of Mechanical Engineering, Villanova University, USA.

## ABSTRACT

Restenosis remains a significant problem in coronary intervention. Although stent migrations, collapses, and positioning difficulties remain serious issues, it is the problem of restenosis which is the most common long term problem in treating atherosclerotic coronary arteries with stents. Although much attention has focused on biocompatibility, thrombosis and neointimal pathology, less attention has been given to matching stents to the inflation balloon, artery and occlusion size. Balloons are typically sized 1–2 mm longer than endovascular stents, yet the effects of the degree of balloon overhang are unknown. In this study, a computational model capable of predicting balloon/stent/artery interactions and their effects on arterial stresses was developed to assess the effects of length mismatch on stent expansion characteristics and arterial stresses. Results from this study indicate that maximum arterial stress at balloon contact is approximately proportional to the degree of balloon overhang. A 100% increase in balloon overhang results in a 4% increase in maximum endflare and a 39% change in the peak arterial stress. However, at the end of expansion, which is of the most clinical importance, the increase in maximum endflare is 2% and the increase in maximum arterial stress is 93% at the balloon point of contact and 45% at the point of contact with the far proximal and distal ends of the stent. When comparing the results of calcified and cellular plaque, a maximum endflare of about 55% was observed for both the calcified and cellular plaque cases during expansion. At the end of expansion the increase in maximum endflare was 10% for the cellular plaque and 40% of the calcified plaque. The peak equivalent stress seen by the artery was about 100% larger in the cellular case than in the calcified plaque case.

*Keywords: balloon inflation, finite element modeling, stenosis, stent inflation.*

## 1 INTRODUCTION

Atherosclerotic stenosis and its ischemic complications necessitate arterial reconstruction. Current strategies to restore normal blood flow in stenotic coronary arteries include angioplasty, intracoronary stents, and coronary artery bypass surgery. Depending on the method of treatment, the incidence of restenosis is high: up to 40% within 6 months after angioplasty [1], 25% after stenting [2], and 20% after bypass surgery [3]. Therefore, restenosis remains a significant problem in coronary intervention.

Advances in prosthetic science and engineering have spurred the rapid development of many new permanent implants such as arterial reinforcement grafts, venous filters, myocardial perforation-sealing clamshells, and stents that strengthen and scaffold the biliary duct, urethra, veins, and arteries. These devices are typically attached to a delivery catheter and threaded to the site of interest where they are expanded. The very nature of the remote delivery systems make the mechanical details of implantation difficult to ascertain, yet this is important to quantify since there may be a link between how the devices are emplaced and the body's acute and chronic response. Endovascular stents in particular are ideal devices to quantify these relationships because of the extreme levels of stress they impose and because of their ubiquity; more than one million are annually implanted in the U.S. alone [4].

These studies suggest an upper limit exists to the success of purely biomedical approaches for managing post-device implantation, and a return to examining the mechanical initiators of vascular injury that occur during implantation. A complete understanding of the manner that stents expand

may thus lead to both a new understanding of the processes of vascular adaptation to implants and possibly to the design and development of less-injurious devices. Experimental data are indirect; stents are too thin to be fully radio-opaque, and methods of bringing a camera to the stent, such as intravascular ultrasound, are blocked by the balloon that expands the stent during the critical moments of implantation. Postmortem examinations indicate that restenosis is paradoxically more severe in the parts of the artery immediately outside the stented region, and animal studies have shown an unusual pattern of endothelial cell denudation occurring at a regular pattern at the center of stent struts, a superficial injury that may be a marker for deep vascular injury [5]. These data are not explained by current finite element analyses of arterial stresses in a stent-expanded artery [6–9] because no finite element models included the expansion of a balloon catheter in the model of a plastically deformed stent.

The inclusion of the balloon catheter in the stent expansion model is not trivial. The problem is highly nonlinear and includes complex contact problems among the stent, balloon, and arterial wall. Additionally, the balloon properties change dramatically depending on whether it is fully or partially inflated.

## 2 GEOMETRY

The finite element stress analysis was performed on a three-dimensional stent/balloon/plaque/artery geometry. In addition to the usual difficulties in modeling the mechanical behavior of soft tissue, the overall system response is highly nonlinear due to the large plastic/multilinear-elastic/hyperelastic deformations of the individual components. The component geometries and constitutive material models are described below.

### 2.1 Artery

The coronary artery model was 30 mm in length, with an inside diameter of 2.8 mm and thickness of 0.3 mm. Average element size was about 0.5 mm long with a thickness of 0.15 mm. This configuration yielded a total of 7,680 elements. The artery elements were defined by eight nodes capable of large deflections and hyperelasticity.

### 2.2 Plaque

The plaque has a semi-parabolic profile and corresponds to percent blockage data presented by Lally *et al.* [9]. The plaque was 16 mm in length with a maximum thickness of 0.48 mm. This configuration corresponds to a maximum percent blockage of about 60%. The characteristic shape of the plaque can be seen in Fig. 1.

### 2.3 Balloon

The balloon was modeled in its unfolded state, and already assumed to be in contact with the stent. The balloon dimensions are given at 0 Pa, before stent expansion occurs. Depending on the amount of balloon overhang, the overall length of the balloon can range from 22 to 23 mm. For 1 mm balloon overhang, the total length of end balloon is 1 mm, or 0.5 mm on each side of the balloon, yielding a total balloon length of 22 mm. For 2 mm balloon overhang, the total length of balloon overhang is 2 mm, or 1 mm on each side, yielding a total balloon length of 23 mm (Fig. 2).

The balloon was meshed using triangular shell elements with an average base size of 0.05 mm and an average side length of 0.05 mm. This yielded 54,456 elements for the 2-mm overhang case and

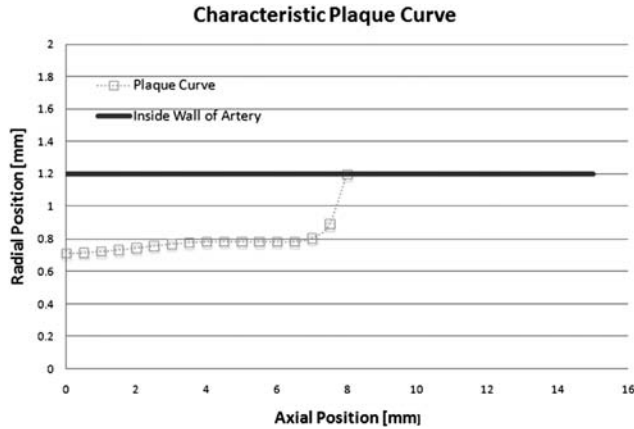


Figure 1: Characteristic plaque curve.

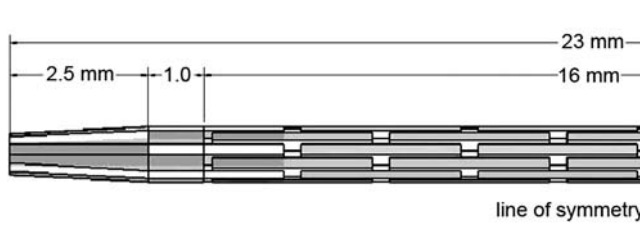


Figure 2: Balloon geometry shown with mounted slotted tube stent.

51,616 elements for the 1-mm overhang case. For finite element analysis, elements capable of modeling shell structures, large deflections and plasticity were used.

#### 2.4 Stent

A three-dimensional model of the slotted tube geometry intravascular stent was created. The stent is 16 mm in length ( $L$ ), with an inside diameter ( $ID$ ) of 1 mm, and a thickness ( $t$ ) of 0.1 mm. The diamond-shaped stent consists of 5 slots in the longitudinal direction and 12 slots in the circumferential direction with a length of 2.88 mm. The slots were cut such that in a cross-section, the angle describing the slot was approximately 23 degrees, and the angle describing the metal between slots was 6.9 degrees (Figs 3 and 4). These dimensions refer to the model in an unexpanded state [7, 9].

The stent was meshed using hexahedral elements. There are two elements through the thickness of the stent yielding a total of 12,036 elements. The stent was assigned an element type solid45 for analysis in ANSYS. These elements are defined by eight nodes and capable of large deflections and plasticity.

The stent and balloon mesh is shown in Fig. 5. A cross-section of the final model geometry with the stent/balloon/artery and plaque is shown in Fig. 6.

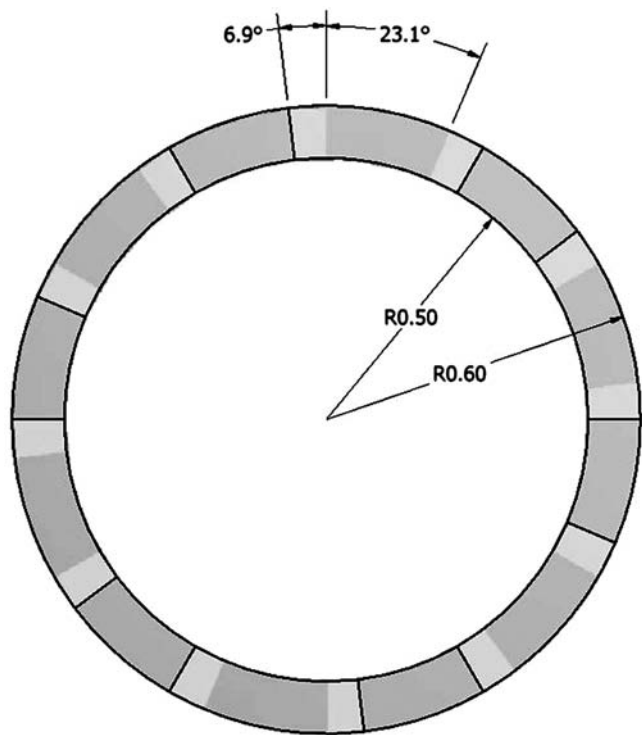


Figure 3: Medial slice of modeled slotted tube stent.

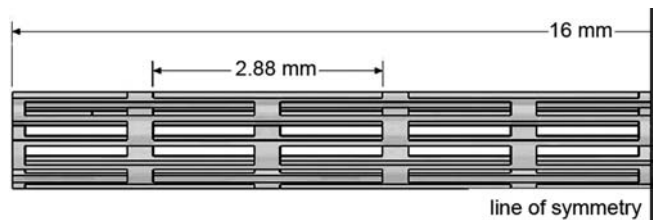


Figure 4: Side view of stent geometry.

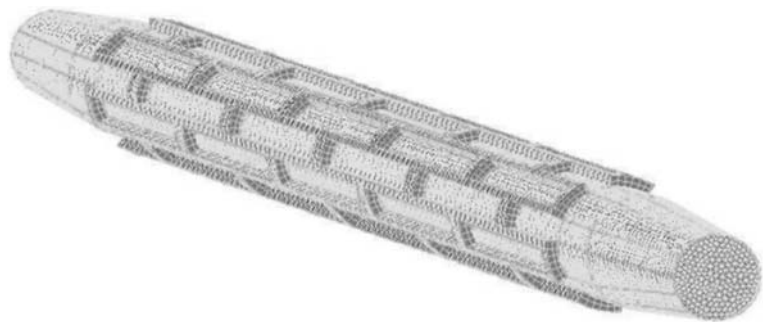


Figure 5: Balloon/stent mesh.

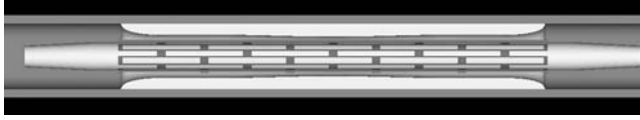


Figure 6: Final model geometry.

### 3 MATERIALS

#### 3.1 Artery

The material properties of the artery are based on a previous study by Lally *et al.* [6]. This model describes the behavior of the artery using a five-parameter, third-order, Mooney–Rivlin hyperelastic constitutive equation. This model has been found to be suitable for modeling an incompressible isotropic material [10].

Lally *et al.* developed the constants for this model by fitting the five-parameter Mooney–Rivlin expression to uniaxial and equibiaxial tension tests of human femoral arterial tissue data [11] (see Table 1).

The material properties of the plaque are based on a previous study by Loree *et al.* [12]. Two histological classifications of plaques were modeled: cellular and calcified. The cellular and calcified specimen results were chosen to provide models of stent expansion dynamics with plaques whose stress–strain slopes differed significantly. This model describes the behavior of the plaque using a five-parameter, third-order Mooney–Rivlin hyperelastic constitutive equation. This model for plaque behavior neglects the artery laminate compositions, tissue anisotropy as well as the residual strain and active smooth muscle stresses [13]. The final form of the strain density function used to model the artery is given in eqn (1). The constants were developed for this model by fitting the five-parameter Mooney–Rivlin expression to uniaxial tension tests of human aortic atherosclerotic tissue data [12]. The hyperelastic constants for the plaques are given in Table 2.

#### 3.2 Balloon

To model the mechanical properties of the balloon without evaluating the balloon’s behavior during unfolding, empirical data were used (Fig. 7). The stress–strain curve for the full expansion of the balloon produced a linear piecewise function. The first segment of the piecewise function is representative of the unfolding balloon, whereas the second is of the balloon expansion after unfolding.

Table 1: Hyperelastic constants for artery.

---

Hyperelastic constants [Pa]

---

$$a_{10} = 0.01890$$

$$a_{01} = 0.00275$$

$$a_{20} = 0.08572$$

$$a_{11} = 0.59043$$

$$a_{02} = 0$$


---

Table 2: Hyperelastic constants for plaque.

Hyperelastic constants [Pa]	
Cellular plaque	Calcified plaque
$a_{10} = -0.088314$	$a_{10} = -3.0254$
$a_{01} = 0.10619$	$a_{01} = 3.1073$
$a_{20} = 0.11373$	$a_{20} = 107.39$
$a_{11} = 0.89382$	$a_{11} = -234.7$
$a_{02} = -0.96676$	$a_{02} = 137.22$

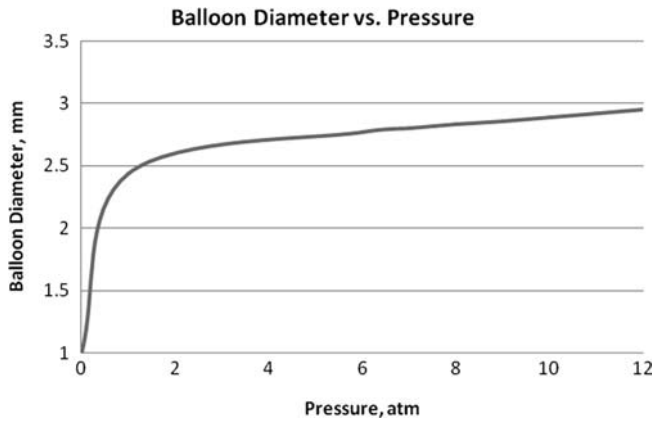


Figure 7: Experimentally determined balloon inflation curve.

### 3.3 Stent

The stent was modeled after the slotted tube geometry given by Migliavacca *et al.* [7]. This model assumes the stent to be made of 316LN stainless steel. The Poisson ratio is 0.3 and the Young Modulus is 200 GPa. The plastic region of the stress–strain curve is shown in Fig. 8.

## 4 BOUNDARY CONDITIONS

The artery, balloon, plaque, and stent were all constrained in the rotational directions allowing no rotation. The artery was constrained axially at the distal ends. The artery was at a minimum 7 mm longer than the stent on each side and 3.5 mm longer than the end of the balloon on each side. This constraint on the artery did not affect the behavior of the artery at the point of contact with the stent or balloon because of the extra length of the artery on both sides. The same axial constraint was placed on the balloon. To model the expansion of the balloon, the balloon was assigned a ramped internal pressure load.

## 5 DEFORMED GEOMETRY EXPORT AND SOLUTION

In order to examine the blood flow patterns through the stented artery, a script was written to export the final expanded stent/plaque/artery geometry for meshing. This mesh was then used within a finite volume computational fluid dynamics code (FLUENT/UNS) to predict arterial wall shear

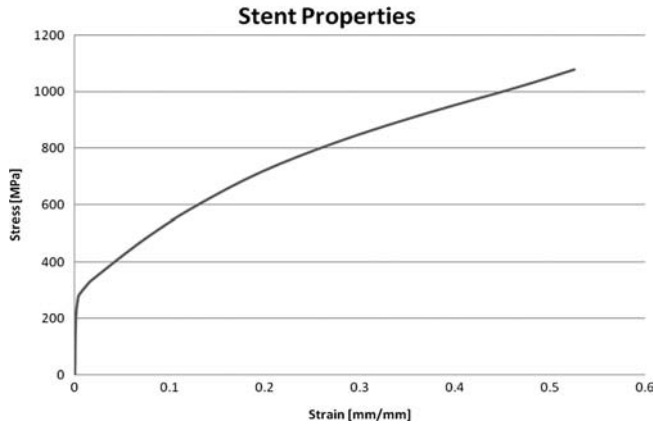


Figure 8: Stent stress–strain curve.

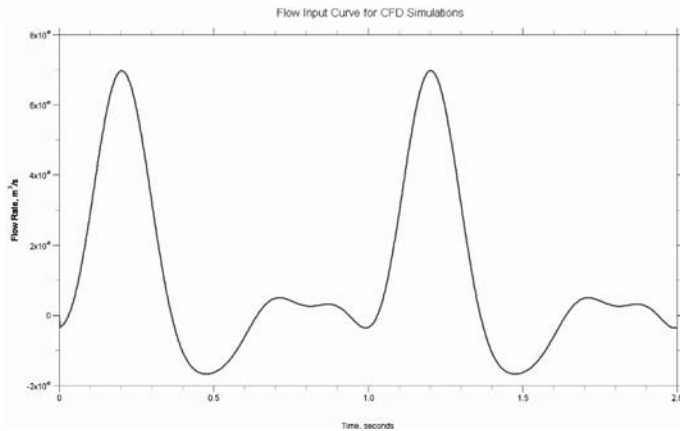


Figure 9: Flow inlet boundary condition for CFD simulations.

stresses and blood velocity and strain rate distributions. The deformed geometry was exported to STL format and the internal geometry (solid mirror of the stent/plaque/artery) was meshed using a hex dominant grid. Holes and seams between the various geometry parts were automatically filled within the meshing algorithms.

The inlet boundary condition was specified as a velocity inlet using the time dependent flow rate equation of Womersley [14] (Fig. 9). The flow was assumed to enter the simulation with a constant cross-sectional velocity. A no-slip condition where the stent/plaque/artery surfaces were in contact with the blood was assumed. The Casson model was used to evaluate the viscosity of the blood since the artery was relatively large and inhomogeneities associated with Fahraeus effects were negligible.

## 6 RESULTS AND DISCUSSION

Figure 10 shows the endflare during stent expansion for the 1 mm and 2 mm balloon overhang cases when there is no plaque included in the models. Endflare is defined as the ratio of the stent diameter at the distal ends to the diameter at the stent centerline. Figure 11 shows the condition of the stent/



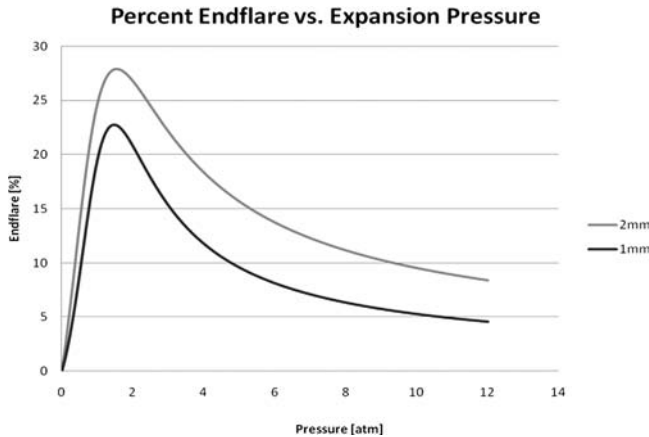


Figure 10: Endflare without plaque for 2 mm (top curve) and 1 mm (bottom curve) overhang.

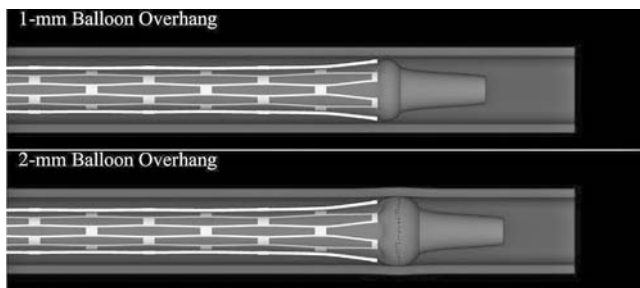


Figure 11: Stent/balloon/artery system at the point of maximum endflare.

balloon/artery system at the point of maximum endflare. There is a significant difference in the endflare both at the point of peak endflare and at the end of expansion, indicating that the amount of balloon overhang can have a significant impact on vascular injury.

Figure 12 shows the amount of balloon/artery interaction during stent inflation. As one would expect, there is a significant increase in the area of balloon/artery contact of approximately 33%.

Figure 13 shows the endflare during stent expansion for the 2 mm balloon overhang case when calcified and cellular plaques are included in the models. The endflare with plaque present in the model is significantly higher than when it was not included. This is because the distal ends of the stent were located such that they did not contact the plaque. Therefore, the effective diameter against which the stent was expanding was significantly larger in this area leading to a lower expansion resistance. There is a significant difference in the endflare both at the point of peak endflare and at the end of expansion, indicating that the amount of balloon overhang can have a significant impact on vascular injury.

Figure 14 shows the arterial stresses at the end of stent expansion when calcified and cellular plaque was included in the model. At the end of expansion the increase in maximum endflare for the cellular plaque geometry over the calcified plaque geometry is about 200%. The increase in maximum arterial stress is 200% at the point of stent contact at the proximal and distal ends. Figure 15 shows the max arterial stress during the expansion process for the cellular and calcified plaque cases.

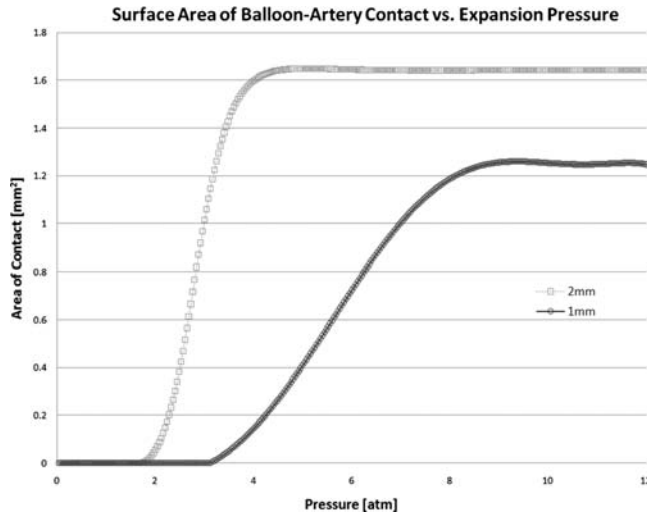


Figure 12: Comparison of balloon/artery contact areas.

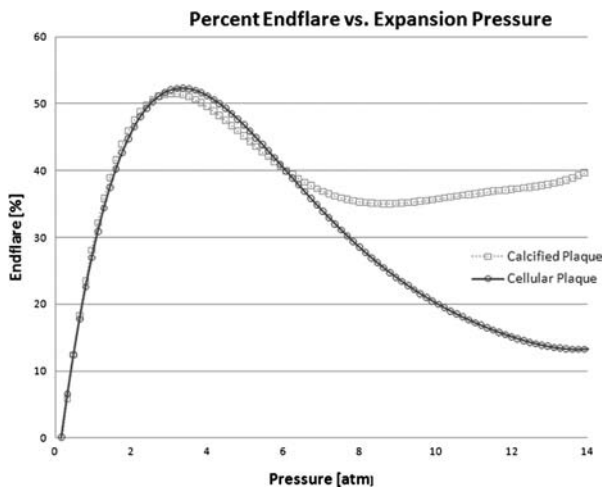


Figure 13: Endflare with plaque for calcified (blue) and cellular (red) plaque.

The cellular plaque case results in much higher stresses at a given balloon expansion pressure than the calcified plaque case.

Figures 16 and 17 show the directional stresses when calcified and cellular plaque are included in the model. As expected, the arterial stresses were significantly lower for the calcified plaque cases when compared to the cellular case. This is the result of the much higher rigidity of the calcified plaque layer over the cellular plaque. This is further supported by the higher stresses seen by the plaque in the calcified case as compared to the cellular case.

It should be mentioned that no plaque breakup model was included in the simulations. It would be expected that the calcified plaque would break up before the high stresses at the end of expansion predicted by the model.

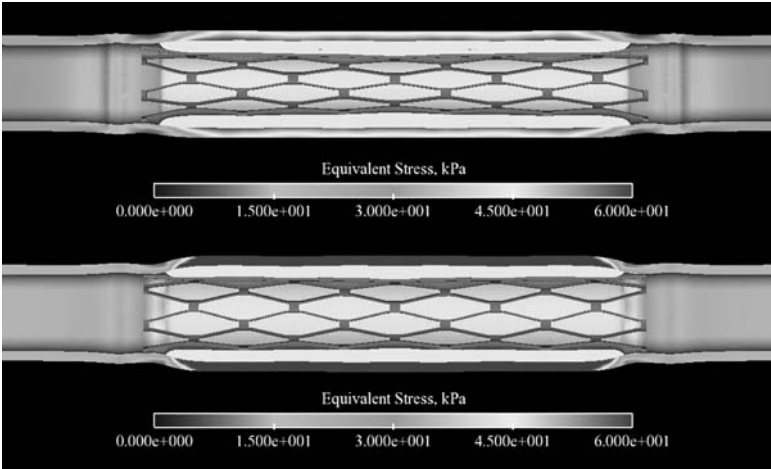


Figure 14: Arterial/plaque stresses for calcified (top) and cellular plaque (bottom).

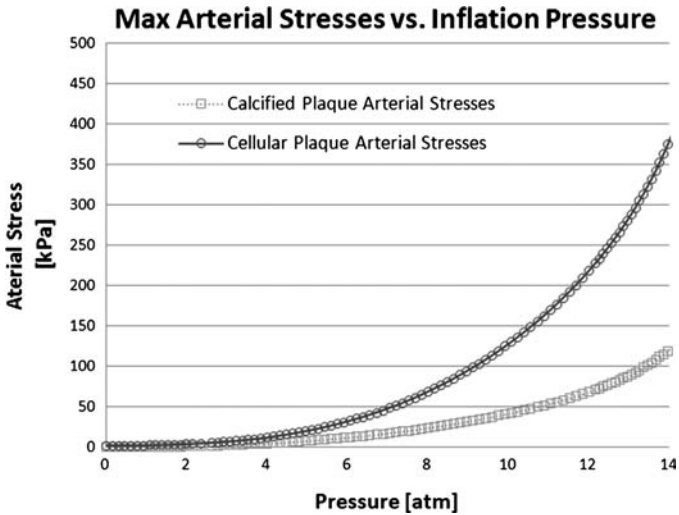


Figure 15: Max arterial stresses for calcified and cellular plaque.

As one would expect, the most significant component of stress is the hoop. The smallest component is the axial. The clinical significance of the directional stresses on vascular injury is unclear. Future experimental studies will be aimed at determining the most appropriate stress to analyze when evaluating vascular injury (von Misses, maximum principal, directional, etc.). The current model does not include the anisotropic behavior of the artery and plaque materials. Additionally, no distinction was made between the passive arterial medium and the active fibers, the orientations of which may vary from inner to the outer layers of the arterial wall. This is currently being included in a more sophisticated model which also includes arterial prestresses.

Finally, Fig. 18 shows the preliminary results of the flow pattern within the final stented geometry. The development of Poiseuille flow is apparent as the blood moves from the model entrance along

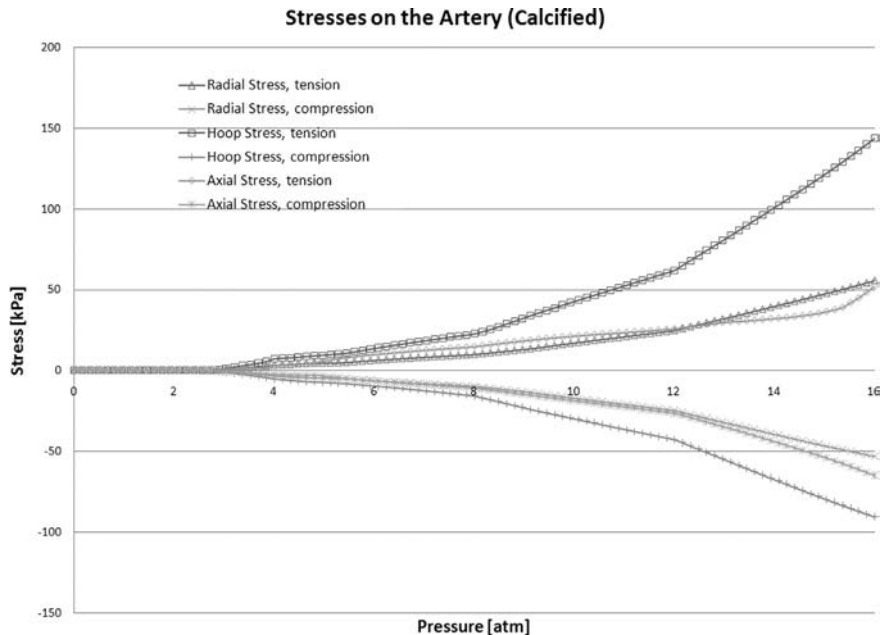


Figure 16: Arterial stresses (radial, hoop, and axial) for calcified plaque.

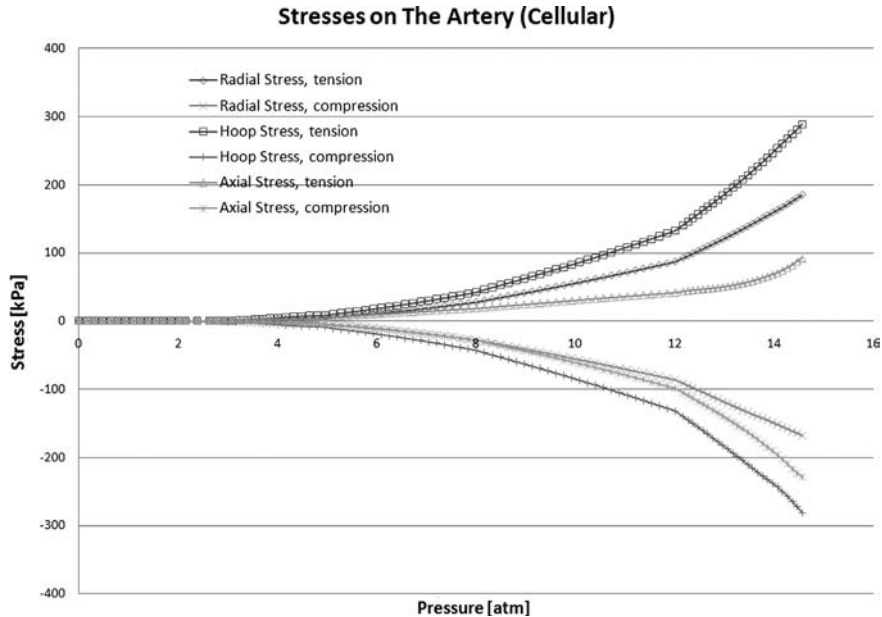


Figure 17: Arterial stresses (radial, hoop, and axial) for cellular plaque.

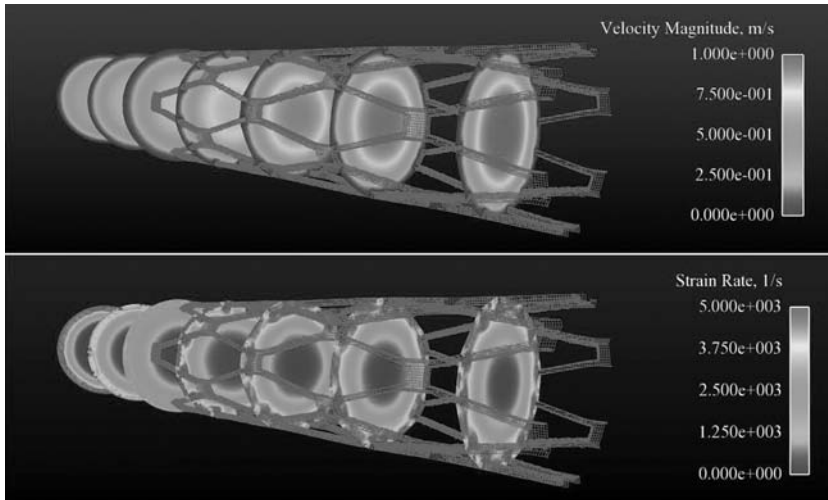


Figure 18: Velocity magnitudes and strain rates in stented artery.

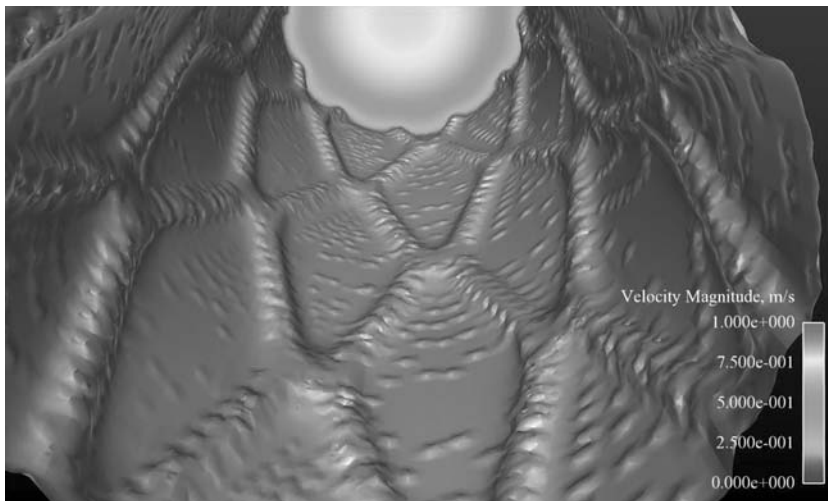


Figure 19: Iso-contour at 0.05 m/s on region near plaque/stent interface.

the artery and plaque surface (not shown) and through the stented portion of the artery. The strain rates are quite interesting and show a decrease after the initial entry into the arterial section. However, they rapidly increase as the blood travels through the stented portion of the artery.

This CFD model is now being used to evaluate the diffusion process associated with drug eluting stents, as well as modeling neointima formation, thrombus formation mechanics, and blood flow patterns. It has been found that standing vortices and regions of stagnation are responsible for the rise in concentrations of platelet-activating agents within those regions. Platelets accumulate preferentially in the regions of large platelet-activating agent concentrations and low fluid velocities. Figure 19 shows a contour plot at 0.05 m/s. Regions of the domain near where the stent contacts the

plaque exhibit zones of low velocity. These regions are potential locations for thrombus formation. Additionally, the wall shear rates and blood strain rates at the wall can be evaluated to determine if they exceed a critical embolizing limit.

## 7 CLINICAL SIGNIFICANCE OF REPORT

Concerns that drug-eluting stents interfere with the process of re-endothelization and thus may encourage long-term thrombosis have spurred interest in understanding the mechanisms causing acute de-endothelization during the stenting procedure [15, 16]. This model aids in the prediction of regions of endothelial cell (EC) denudation during stent implantation. This is an important phenomenon since regions of EC denudation profoundly impact drug absorption/loading profiles of anti-proliferative agents in drug-eluting stents (DES). Additionally, anti-proliferative drugs are hypothesized to inhibit EC regrowth causing increased rates of long-term thrombosis, so predictive capability of regions of EC denudation during implantation provides the tool to reduce thrombosis rates of DES.

The model developed also helps in the prediction of regions of high arterial stresses which may cause vascular injury. Acute superficial and deep vascular injury has been found to be a strong predictor of chronic restenosis. This method provides a predictive tool to evaluate the degree of acute vascular injury of new stent geometries prior to *in vivo* studies.

Finally, the ability to examine blood flow patterns in stented arteries allows for the prediction of standing vortices and high platelet-activating substances capable of trapping and stimulating platelets for aggregation. It also allows for the evaluation of embolizing stresses acting on a thrombus.

## REFERENCES

- [1] Schillinger, M., Exner, M., Mlekusch, W., Haumer, M., Sabeti, S., Ahmadi, R., Schwarzingner, I., Wagner, O. & Minar, E., Restenosis after femoropopliteal PTA and elective stent implantation: predictive value of monocyte counts. *Journal of Endovascular Therapy*, **10**, pp. 557–565, 2003.
- [2] Antonucci, D., Valenti, R., Santoro, G., Bolognese, L., Trapani, M., Cerisano, G. & Fazzini, P., Restenosis after coronary stenting in current clinical practice. *American Heart Journal*, **135**(3), pp. 510–518, 1998.
- [3] Griffiths, H., Bakhai, A., West, D., Petrou, M., De Souza, T., Moat, N., Pepper, J. & Di Mario, C., Feasibility and cost of treatment with drug eluting stents of surgical candidates with multi-vessel coronary disease. *European Journal of Cardiothoracic Surgery*, **26**, pp. 528–534, 2004.
- [4] Feder, B.J., Panel urges caution on coated stents. *New York Times – Health* p. 1, 2006.
- [5] Rogers, C., Parikh, S., Seifert, P. & Edelman, E.R., Endogenous cell seeding: remnant endothelium after stenting enhances vascular repair. *Circulation*, **11**, pp. 2909–2914, 1996.
- [6] Auricchio, F., Di Loreto, M. & Sacco, E., Finite element analysis of a stenotic artery revascularization through stent insertion. *Computer Methods in Biomechanics and Biomedical Engineering*, **4**, pp. 249–263, 2001.
- [7] Migliavacca, F., Petrini, L., Colombo, M. *et al.*, Mechanical behavior of coronary stents investigated through the finite element method. *Journal of Biomechanics*, **35**, pp. 803–811, 2002.
- [8] Petrini, L., Migliavacca, F., Dubini, G. & Auricchio, F., Evaluation of intravascular stent flexibility by means of numerical analysis. *Proceedings of the 2003 Summer Bioengineering Conference*, Key Biscayne: FL, pp. 251–252, 2003.
- [9] Lally, C., Dolan, F. & Prendergast, P.J., Cardiovascular stent design and vessel stresses: a finite element analysis. *Journal of Biomechanics*, **38**, pp. 1574–1581, 2005.

- [10] Lally, C. & Prendergast, P.J., An investigation into the applicability of a Mooney–Rivlin constitutive equation for modeling vascular tissue in cardiovascular stenting procedures. *Proceedings of the International Congress on Computational Biomechanics*, Zaragoza: Spain, pp. 542–550, 2003.
- [11] Prendergast, P.J., Lally, C., Daly, S., Reid, A.J., Lee, T.C., Quinn, D. & Dolan, F., Analysis of prolapse in cardiovascular stents: a constitutive equation for vascular tissue and finite element modelling. *ASME Journal of Biomechanical Engineering*, **125**, pp. 692–699, 2003.
- [12] Loree, H.M., Grodzinsky, A.J., Park, S.Y., Gibson, L.J. & Lee, R.T., Static circumferential tangential modulus of human atherosclerotic tissue. *Journal of Biomechanics*, **27**, pp. 195–204, 1994.
- [13] McFadden, E.P., Stabile, E., Regar, E., Cheneau, E. *et al.*, Late thrombosis in drug-eluting coronary stents after discontinuation of antiplatelet therapy. *The Lancet*, **364**, pp. 1519–1521, 2004.
- [14] Nichols, W.W. & O'Rourke, M.F., *McDonald's Blood Flow in Arteries Theoretical, Experimental and Clinical Principles*, Oxford University Press: New York, 1998.
- [15] Kuchulakanti, P.K., Chu, W.W., Torguson, R., Ohlmann, P. *et al.*, Correlates and long-term outcomes of angiographically proven stent thrombosis with sirolimus- and paclitaxel-eluting stents. *Circulation*, **113**, pp. 1108–1113, 2006.
- [16] Ong, A.T., McFadden, E.P., Regar, E., de Jaegere, P.P., van Domburg, R.T. & Serruys, P.W., Late angiographic stent thrombosis events with drug eluting stents. *Journal of the American College of Cardiology*, **45**, pp. 2088–2092, 2005.

# BLOOD FLOW UNDER EXTERNAL STRAINS: PHENOMENOLOGICAL APPROACH, THEORETICAL DEVELOPMENTS AND NUMERICAL ANALYSIS

R. PAULUS<sup>1,2</sup>, S. ERPICUM<sup>1,2</sup>, B.J. DEWALS<sup>1,2,3</sup>, S. CESCOTTO<sup>2</sup> & M. PIROTTON<sup>1,2</sup>

<sup>1</sup>HACH (Hydrology, Applied Hydrodynamics and Hydraulic Constructions), University of Liège, Belgium.

<sup>2</sup>ArGEnCo (Architecture, Geology, Environment and Constructions), University of Liège, Belgium.

<sup>3</sup>F.R.S – FNRS (Belgian Fund for Scientific Research), Belgium.

## ABSTRACT

In the medical field, the measurement of blood flow characteristics is often necessary. More specifically, blood pressure is an essential measure when it comes to assessing health. All over the world, many people suffer from hyper- or hypotension, and as it is known that these diseases can lead to serious complications, it is of great interest to determine the blood pressure with high accuracy. Nowadays, such information requires the use of specific materials; the present method for the measurement of the arterial pressure, by applying pressure using an armband (with a control device called sphygmomanometer), is known to introduce significant errors due to the inadequacy of the band dimensions (both the length and the circumference). The objective of the present research is to study and simulate the discharge of the blood in an artery subjected to external strains using theoretical developments and a numerical approach. Based on these modelling results, the response of the fluid to the external pressure of the band can be studied, and finally appropriate corrective factors for the true pressure and the measured pressure could be assessed. This research has been carried out with the aim of sharing medical and engineering views on the subject. The artery can be modelled as a deformable pipe, where the blood flowing in it is a fluid with specific properties. Thus, two complementary and interconnected domains are covered, solid mechanics (to obtain analytic relations between the strains and the deformations, using either linear or non-linear theories) and fluid mechanics (to study the discharge of blood in a deformable pipe, using finite volume methods), therefore considering the problem as a loose fluid–structure interaction (FSI). These two domains, which are well studied for common materials in civil engineering applications, are applied here not only to specific materials but especially to uncommon structures that, besides the somehow common FSI developments, lead to the investigation and research of very specific boundary conditions, giving them a physically based behaviour. At present, the research has reached the penultimate step, with the two main mentioned axes being fully developed and tested on their own. In particular, the boundary conditions developed for the models have been investigated and modelled in depth.

*Keywords: 1D numerical flow modelling, capillary behaviour, (non)-linear material analysis, original outflow boundary conditions.*

## 1 INTRODUCTION

Blood pressure is by far one of the most essential measures when it comes to assessing human health. Although it is well known that hyper- and hypotension diseases are widespread all over the world, one does not always know the impact of a physiologically abnormal measure. For instance, an increase of 5 mmHg will double the risks of cardiovascular diseases; it is therefore essential not to underestimate the blood pressure. It is also important not to overestimate it because that would lead to unnecessary treatments which are costly and sometimes risky if the patient is in good health.

The principal method used to measure blood pressure at present is based on Korotkoff's [1] and Riva-Rocci's [2] discoveries and developments and it follows a well-established medical procedure [3]. Although very widespread all over the world, this technique is known to induce potentially significant errors in the measurement, and modern medical approaches are currently being developed in order to avoid the use of this technique [4–6]. At our unit, the objective has been to simulate this operating mode, postulating that a numerical approach to the phenomenon would enhance the accuracy of the common surgical appliance.



For many years, fluid–structure interaction (FSI) has been widely used in order to simulate blood propagation in vessels, and, more generally, to study biomechanics as well as haemodynamic problems [7–9]. The interaction between the fluid and the surrounding structure can vary from loose to strong, and so the coupling between the two models follows the same scheme; interactions with materials of high deformability should be modelled using strong coupling [10, 11], whereas interactions with rigid materials can be modelled using loose coupling [12–14]. The method chosen in our unit is based on a strong interaction that is required here due to the strong deformability of the vessels. The mechanical behaviour is taken into account in a direct way in the flow modelling, using an ingenious modelling device called the Preismann slot for this purpose.

This coupled approach is somehow classical in this field [7–9, 15, 16], but the way the boundary conditions are represented still remains a challenge. Indeed, most of the time, the downstream boundary condition is linked to a pressure signal. But, since this signal is, in a way, the unknown that our research focuses on, it is rather awkward to consider it fixed and known downstream. Therefore, physically based boundary conditions have been identified, thus avoiding the imposition of a downstream signal.

The solution method is explained briefly in Section 2. Then the two independent models representing, respectively, the solid mechanics and the fluid mechanics are presented and discussed in Sections 3 and 4, before the boundary conditions are discussed at the end of the latest. Finally, the results obtained for the boundary condition developments are presented, analysed and discussed in Section 5.

## 2 SOLUTION METHOD

The goal of this research is to simulate the discharge of the blood in the arteries, more specifically when the arteries are subjected to external strains, as is the case during blood pressure measurement.

The artery can be modelled as a deformable pipe, where the blood flowing in it is a fluid with specific properties which is pulsed into the artery. The cardiovascular system has a specific architecture and structure that requires specific boundary conditions. Thus, the research involves two complementary and interconnected domains, namely solid mechanics and fluid mechanics; therefore, the FSI problem of interest here is the simulation of the discharge of a specific fluid into a network of deformable pipes. The analytic relations between the external strains (not only the arm-band pressure but also the blood pressure) and the deformations can be obtained using either linear or non-linear theories. In this manner, the way the artery changes its shape may be determined. Given the mathematically known deformations for the artery, the discharge of the blood in this deformable pipe, comprising vessels with a very wide range of diameters, has been studied based on the WOLF modelling system, fully developed at the University of Liège.

## 3 MECHANICAL ANALYSIS OF THE ARTERY

The first part of the research focuses on solid mechanics. As mentioned before, hydraulic modelling requires knowing the way in which the artery deflates under specific strains (be it internal or external pressures). The analytic relations between the section and the pressures have been derived. First, the necessary hypothesis are presented, followed by a detailed description of the mathematical developments.

### 3.1 Specificities of the artery

The arm is a complex material composed of muscles, bones, vessels and tendons among others.

Although a complete study of the limb could be undertaken (by means of numerical modelling), analytic equations are sought here. Therefore, assumptions are needed, both about the geometry and

about the mechanical behaviour of the material. The arm is considered to be composed of two coaxial materials, namely the artery and the muscle, and the contacts between them have been neglected, thus assuming that the pressures are uniformly applied (cf. Fig. 1a). Besides, it is known that the materials are subject to long deformations and that they can be assumed to be elastic materials.

To obtain the analytic results, two additional hypotheses are necessary, one concerning the material properties and the other concerning the material's behaviour under strain. The muscle and the artery are supposed to be transversely isotropic and to follow a plane state of strain. These two assumptions are supported by observations about the material's structure, as discussed in previous papers [17–19]; the structures of both the artery and the muscle are assumed to be concentric (and so present a cylindrical symmetry), the stresses are perpendicular to the solids generatrix, and one can reasonably accept that the longitudinal extensions are insignificant (the vessels are confined axially).

### 3.2 Mathematical analysis

As the artery and the muscle are viewed as a two-material coaxial pipe, one can develop the problem using the cylindrical coordinate and following the law of the solid mechanics.

Following the previous assumptions, a non-linear analysis is obviously required. However, for now, only the theoretical developments of this analysis as well as the implementation of a numerical model based on the mathematical results have been done. The last step would be to calibrate this model in order to make it usable in the final model.

The linear analysis, based on the more restrictive assumption that the displacement is relatively small, has been done in a similar manner and is already available since the parameters of the model are mostly available in literature [20–22].

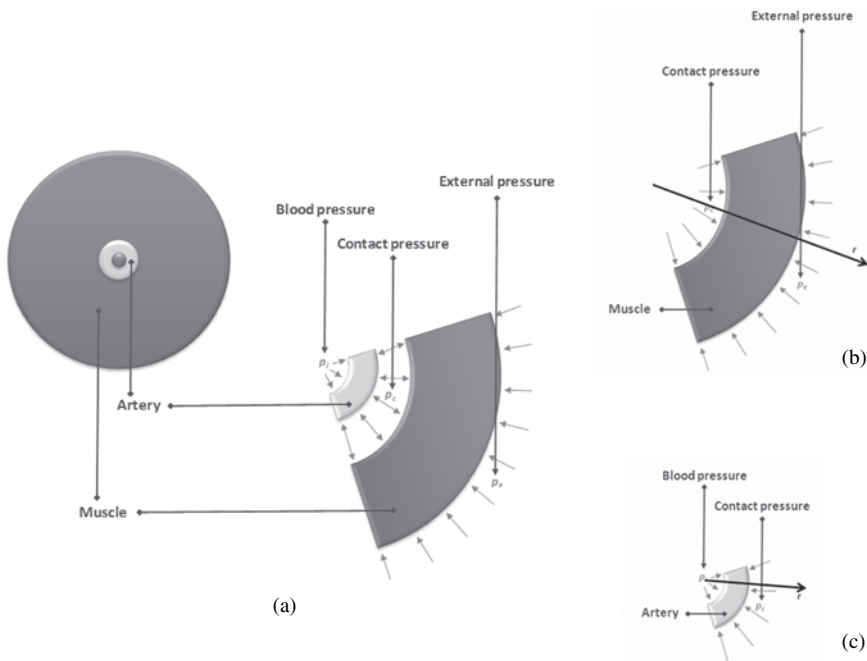


Figure 1: (a) Transverse section of the arm, idealized situation; (b) muscle with external and contact pressures; and (c) artery with contact and internal pressures.

### 3.2.1 Linear analysis

The linear analysis gives the first approach to the problem, and the different developments are rather obvious. Successively, the two cylinders are considered to be subjected to the concerned pressures (e.g. when the muscle has been considered, the internal and contact pressures have been taken into account), and the displacements are expressed as a function of the respective pressures (see Fig. 1b and c).

Finally, by setting the displacements at the contact zone as equal, an analytic relation is obtained for the section of the artery, function of the different materials (Hooke's parameters for the artery and the muscle), the dimensions and the pressures [17, 18]. The results are shown below and represent the radial displacement for the artery (eqn (1)), the equilibrium contact pressure (eqn (2)) and the section (eqn (3)).

$$u_r(r = r_i) = \frac{1}{2} \frac{1}{G_1} \left( \frac{1}{r_c^2 - r_i^2} \right) ((1 - 2\nu_1)(r_i^3 p_i - r_c^2 r_i p_c^x) + (p_i - p_c) r_i r_c^2), \quad (1)$$

$$p_c = 2 \frac{\frac{1}{G_1} \left( \frac{1}{r_c^2 - r_i^2} \right) (1 - \nu_1) r_i^2 p_i + \frac{1}{G_2} \left( \frac{1}{r_e^2 - r_c^2} \right) (1 - \nu_2) r_e^2 p_e}{\left( \frac{1}{G_2} \left( \frac{1}{r_e^2 - r_c^2} \right) (r_c^2 (1 - 2\nu_2) r_e^2) + \frac{1}{G_1} \left( \frac{1}{r_c^2 - r_i^2} \right) (r_c^2 (1 - 2\nu_1) + r_i^2) \right)}, \quad (2)$$

$$\Omega = \pi(r_i + u_r(r = r_i))^2, \quad (3)$$

where  $u_r$  [m] is the axial distortion;  $r$  [m] is the radial position;  $r_e$ ,  $r_i$  and  $r_c$  [m] are, respectively, the external, internal and contact radii;  $G_1$  and  $G_2$  [Pa] are, respectively, the artery and muscle bulk modulus;  $\nu_1$  and  $\nu_2$  [–] are, respectively, the artery and muscle Poisson coefficients;  $p_e$ ,  $p_i$  and  $p_c$  [Pa] are, respectively, the external, internal and contact pressures;  $\Omega$  [m<sup>2</sup>] is the section. This set of equations is valid only under the assumptions detailed in Section 3.1.

### 3.2.2 Non-linear analysis

A Mooney–Rivlin function, which is one of the most simple and comprehensive strain energy density functions, has been chosen to represent the hyperelastic material. It takes the form of  $W = C_1(I_1 - 3) + C_2(I_1 - 3)^2$ , where  $I_1$  [m] and  $I_2$  [m] are the first and second invariant of the deviatoric component of the Finger tensor and  $C_1$  [Pa] and  $C_2$  [Pa] are parameters inherent to the materials.

The equations obtained [17] are presented below:

$$u_r = r - R, \quad (4)$$

$$r = \sqrt{\frac{R^2 + C(1+k)}{1+k}}, \quad (5)$$

$$\begin{aligned} A^* = -q_b & \\ & - \frac{R_b^2 \left[ 2C_1(1+k) + 2C_2 + 2C_2(1+k)^3 + [C_1 + C_2(1+k)^2](1+k) \left\{ \frac{C(1+k)}{R_b^2 + C(1+k)} + 2 \ln R_b - \ln(R_b^2 + C(1+k)) \right\} \right]}{(1+k)^2 (R_b^2 + C(1+k))} \\ & + \frac{2C_2 C(1+k) + C(1+k)^2 (C_1 + C_2(1+k)^2) \left( \frac{C(1+k)}{R_b^2 + C(1+k)} + 2 \ln R_b - \ln(R_b^2 + C(1+k)) \right)}{\dots}, \end{aligned} \quad (6)$$

$$\begin{aligned}
\sigma_r(R = R_A) &= -q_A \\
&= \frac{R_A^2 \left[ 2C_1(1+k) + 2C_2 + 2C_2(1+k)^3 + \left( A^x + \frac{[C_1 + C_2(1+k)^2]}{1+k} \left\{ \frac{C(1+k)}{R_A^2 + C(1+k)} + 2 \ln R_A - \ln(R_A^2 + C(1+k)) \right\} \right) (1+k)^2 \right]}{(1+k)^2 (R_A^2 + C(1+k))} \\
&\quad + \frac{2C_2 C + \left( A^x + \frac{[C_1 + C_2(1+k)^2]}{1+k} \left\{ \frac{C(1+k)}{R_A^2 + C(1+k)} + 2 \ln R_A - \ln(R_A^2 + C(1+k)) \right\} \right) C(1+k)^2}{(1+k)(R_A^2 + C(1+k))}, \tag{7}
\end{aligned}$$

$$\Omega = \pi(r_A)^2, \tag{8}$$

where  $u_r$  [m] is the axial displacement,  $r$  [m] is the radius position after distortion,  $R$  [m] is the radius position before distortion,  $R_A$  and  $R_B$  [m] are, respectively, the internal and external radii,  $C$  [Pa] and  $A^x$  [Pa] are integrative constants (determined from the boundary behaviour),  $\Omega$  [m<sup>2</sup>] is the section,  $q_A$  and  $q_B$  [Pa] are, respectively, the internal and external pressures,  $C_1$  [Pa] and  $C_2$  [Pa] are parameters inherent to the materials,  $k$  [-] is a factor of longitudinal distortion and  $\sigma_r$  [Pa] is the radial constraint.

These equations need some explanations about their signification and use. Equations (4), (5) and (8) are obvious and, when combined, give the section function of  $C$  and  $k$ ,  $k$  being zero in plane state of strain. The two integrative constants are given considering the boundary behaviour through eqns (6) and (7).

The presented equations apply to one material considered individually, and the complete resolution must thus be iterative in order to give a stable solution (the contact zone is then taken as the equilibrium zone, and the goal of the iterative method is to balance the relative displacements of this zone). This set of equations is also only valid under the assumptions introduced in Section 3.1.

### 3.3 Results and discussion

The established equations give the response of both the artery and the muscle to the external strains, but the material parameters have not yet been calibrated from the comprehensive set of experiments. The geometrical and mechanical parameters of the materials make up the data of the model. The pressures are the input parameters, and the output data are the radial displacement, from which the section can be obtained. The initial condition consists of a situation without any external constraint. The model evaluates the displacements at the contact zone for both materials, and iterates until they are independent of the considered material, with an error of 0.05% on the relative displacement.

The results presented here (Figs 2 and 3) involve a comparison of both models for parameters representing the same materials, thus enabling the assessment of the sensitivity of the model.

The presented results correspond to the following data [17]:  $r_i = 1,950 \mu\text{m}$ ,  $r_c = 2,950 \mu\text{m}$ ,  $r_e = 1,950 \mu\text{m}$ ,  $E_{\text{Mat1}} = 1.7 \text{ MPa}$ ,  $\nu_{\text{Mat1}} = 0.5$ ,  $E_{\text{Mat2}} = 0.003 \text{ MPa}$ ,  $\nu_{\text{Mat2}} = 0.5$ ,  $C_{1, \text{Mat1}} = 0.159 \text{ MPa}$ ,  $C_{2, \text{Mat1}} = 0.116 \text{ MPa}$ ,  $C_{1, \text{Mat2}} = 0.015 \text{ MPa}$ ,  $C_{2, \text{Mat2}} = 0.007 \text{ MPa}$ .

The analytic developments presented in this section are based on realistic assumptions (Section 3.1), and the models may already be used in a number of applications. The next step will be to calibrate the models and to further analyse their sensitivity and assumed validity to simulate the physical behaviour of the arm during blood pressure measurement.

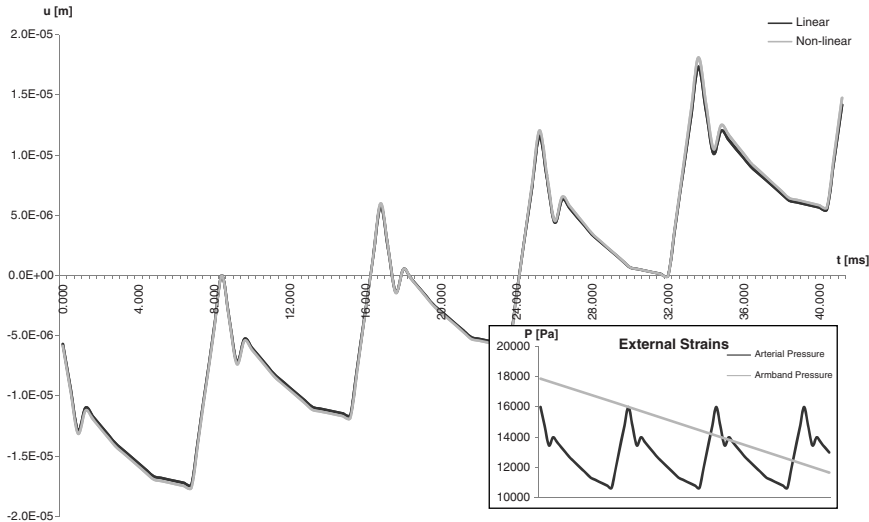


Figure 2: Evolution of the radial displacements [m] due to external strain [Pa], as a function of time.

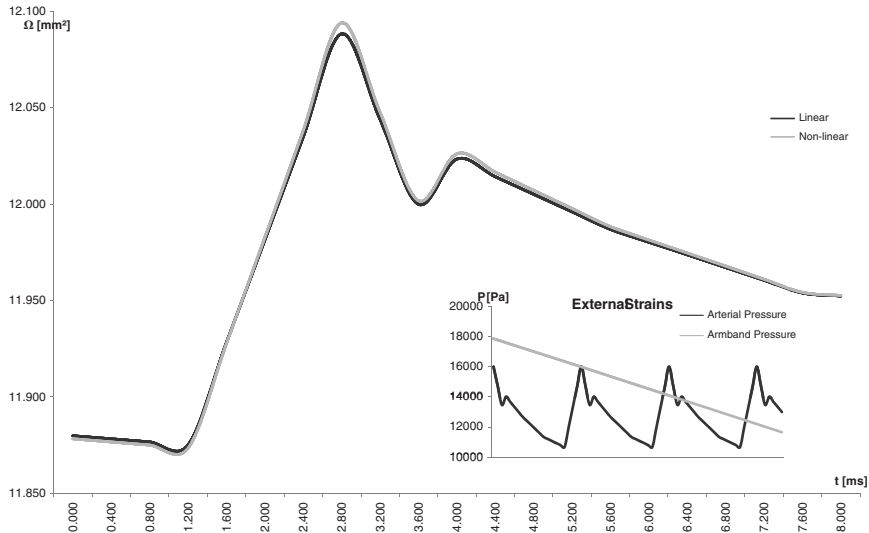


Figure 3: Evolution of the section [mm²] due to external strain [Pa], as a function of time.

#### 4 HYDRAULIC ANALYSIS OF THE FLOW IN THE ARTERY

This part of the research is dedicated to the study of the blood discharge in the artery, modelled as the particular deformable pipe described above.

First, the characteristics of blood have to be investigated. Then, the mathematical and numerical developments are outlined based on these assumptions.

While all these developments are common for hydraulic phenomena, Section 4.4, concerning the boundary conditions, will present an original method, as well as its results, developed in order to model the downstream boundary conditions of the artery as a result of the behaviour of the fluid in the capillary network.

#### 4.1 Characteristics of blood

Blood can be distinguished from other fluids based on its viscosity, determined by the haematocrit, and it is obviously a non-Newtonian fluid, but can acceptably be assumed as incompressible [23]. Blood behaves like a Bingham fluid, with its viscosity being a function of the velocity gradient. The latter is thus often expressed as a relative viscosity, being the ratio of the blood viscosity to the plasma viscosity, which is Newtonian. However, in large vessels, the fluid can be considered as Newtonian and homogeneous [24, 25], as the boundary layer is very small compared to the vessel radius. In the capillaries, this assumption is no longer acceptable, the flow being determined mainly by viscous stresses. Besides, it can reasonably be assumed that blood is incompressible, the Mach number being globally quite small. Finally, the turbulent effects have been neglected. It is well known that some sources of instabilities create local turbulence, but analysis of both Reynolds and Womersley numbers shows that this last hypothesis is acceptable [23]. For the smaller vessels, however, these assumptions have to be reconsidered, but for now they have not been updated, and it has been considered that the properties of the fluid remains constant in the whole domain, independent of the vessel dimensions.

#### 4.2 Mathematical model

The equations governing the fluid mechanics problem are the Navier–Stokes equations:

$$\begin{cases} \frac{\partial \rho}{\partial t} + \nabla(\rho \cdot U) = 0, \\ \frac{\partial U}{\partial t} + U \cdot \nabla U = \frac{-1}{\rho} \nabla p + \nu \cdot \nabla^2 U. \end{cases} \quad (9)$$

They represent, respectively, the conservation of the mass and the momentum. The two variables are the density ( $\rho$ ) [kg/m<sup>3</sup>] and the velocity ( $U$ ) [m/s], with respect to the time ( $t$ ) [s] and the coordinates  $x$ ,  $y$  and  $z$  [m]. The other parameters in this system are the pressure ( $p$ ) [Pa] and the kinematic viscosity ( $\nu$ ) [m<sup>2</sup>/s].

In the specific framework of blood flow, the flow is mostly one-dimensional (1D) and the cross-sectional velocities are small. In addition, despite the fact that the streamline curvature cannot actually be considered as small, no serious mistakes are made if these are neglected. With these three acceptable assumptions in mind, the Navier–Stokes equations can be area-integrated [26] into the following form:

$$\begin{cases} \frac{\partial \Omega}{\partial t} + \frac{\partial Q}{\partial x} = q_l, \\ \frac{\partial Q}{\partial t} + \frac{\partial}{\partial x} \left( \frac{Q^2}{\Omega} + g^* I_1 \right) = g^* I_2 + \frac{F_x}{\rho} + U q_l, \end{cases} \quad (10)$$

$$\begin{cases} I_1(h) = \int_{-h_b}^{h_s} (h - \xi) l(x, \xi) d\xi, \\ I_2(h) = \int_{-h_b}^{h_s} (h - \xi) \frac{\partial l(x, \xi)}{\partial x} d\xi, \end{cases} \quad (11)$$

where  $x$  [m] is the axial position,  $\Omega$  [m<sup>2</sup>] is the section,  $Q$  [m<sup>3</sup>/s] is the discharge,  $q_l$  [m<sup>2</sup>/s] is the lateral in- or outflow,  $g^*$  [m/s<sup>2</sup>] is the projected gravity acceleration,  $F_x$  [kg/s<sup>2</sup>] is the global effect of roughness,  $h_b$  [m] is the bottom height,  $h_s$  [m] is the slot height.

The Preismann slot model [27] allows the modelling of pressurized flow using equations similar to those for free surface flows. It consists of a narrow slot on the top of a closed pipe [28, 29].

The width of the slot ( $T_f$  [m]) is chosen in order to represent the behaviour of the conceptual free surface flow, with a gravity wave speed ( $c$ ) [m/s] represented by

$$c = \sqrt{\frac{g^* \Omega}{T_f}}, \quad \frac{1}{c^2} = \frac{\rho}{\Omega} \frac{\partial \Omega}{\partial p}, \quad (12)$$

where  $c$  [m/s] is the wave speed. The section  $\Omega$  and its derivative with respect to the pressure  $p$  refer to the law of solid mechanics developed above.

### 4.3 Numerical resolution

The set of non-linear equations introduced above (cf. Section 4.2) requires the use of a numerical resolution. As for many of the hydraulic applications, a finite volume method is an appropriate way to solve the problem.

The set of equations can be written as follows:

$$\frac{\partial}{\partial x} \mathbf{U} + \frac{\partial}{\partial x} \mathbf{F}(\mathbf{U}) = \mathbf{S}(\mathbf{U}), \quad (13)$$

where the vectors of conservative variables and sources are, respectively,

$$\mathbf{U} = \begin{pmatrix} \Omega \\ Q \end{pmatrix}, \quad \mathbf{S}(\mathbf{U}) = \begin{pmatrix} q_l \\ g^* I_2 + \frac{F_x}{\rho} + U q_l \end{pmatrix}, \quad \mathbf{F}(\mathbf{U}) = \begin{pmatrix} Q \\ \frac{Q^2}{\Omega} + g^* I_1 \end{pmatrix}. \quad (14)$$

The flux is computed using a flux-vector splitting [30], involving fractioning the flux into two distinct components

$$\mathbf{F}(\mathbf{U}) = \mathbf{F}^+(\mathbf{U}_l) + \mathbf{F}^-(\mathbf{U}_r), \quad (15)$$

where  $\mathbf{U}_l$  and  $\mathbf{U}_r$  are the reconstructed value of the conservative variables at the edge of the mesh, respectively, built at the left and right edges. This division takes the following form:

$$\mathbf{F}^+ = \begin{cases} \mathbf{F}^{\text{up}}, \\ \mathbf{F}^{\text{down}}, \end{cases} \quad \mathbf{F}^- = \begin{cases} \mathbf{F}^{\text{down}}, \\ \mathbf{F}^{\text{up}}, \end{cases} \quad \text{if } \begin{cases} Q \geq 0, \\ Q < 0, \end{cases} \quad (16)$$

where  $Q$  is the characteristic value of the speed at the interface between two meshes, and  $(\mathbf{F}^{\text{up}}, \mathbf{F}^{\text{down}})$  are the relative fluxes for variables taken, respectively, up- and downstream:

$$\mathbf{F}^{\text{up}} = \begin{cases} Q, \\ \varphi Q^2 / \Omega, \end{cases} \quad \mathbf{F}^{\text{down}} = \begin{cases} 0, \\ g I_1. \end{cases} \quad (17)$$

Finally, the integration of eqn (13) leads to the following conservative formulation:

$$\mathbf{U}_i^{n+1} = \mathbf{U}_i^n - \Delta t \left[ \frac{\mathbf{F}_{i+1/2} - \mathbf{F}_{i-1/2}}{\Delta x} + \mathbf{S} \right]. \quad (18)$$

The numerical resolution uses a three-step Runge–Kutta time-integration scheme, with the three following substep evaluations ( $k = 1, 2, 3$ , with  $k = 0$  corresponding to the value of the vectors of conservative variables at step  $n$ ):

$$\mathbf{U}_i^{n,k} = \mathbf{U}_i^n - \Delta t \left[ \frac{\mathbf{F}_{i+1/2}(\mathbf{U}_i^{n,k-1}) - \mathbf{F}_{i-1/2}(\mathbf{U}_i^{n,k-1})}{\Delta x} + \mathbf{S}(\mathbf{U}_i^{n,k-1}) \right]. \quad (19)$$

And the final solution is given by

$$\mathbf{U}_i^{n+1} = RK_1 \mathbf{U}_i^{n,1} + RK_2 \mathbf{U}_i^{n,2} + RK_3 \mathbf{U}_i^{n,3}, \quad (20)$$

with  $\sum_i RK_i = 1$ .

This numerical model has been fully developed within the HACH unit. Its robustness and ability to handle a very wide range of problems has been shown, tested and successfully validated in many steady as well as unsteady cases [31].

#### 4.4 Boundary conditions

The numerical resolution requires the prescription of boundary conditions. The hydraulic conditions observed in this specific case require the forcing of the upstream discharge and the downstream pressure. While it is acceptable to assume that the upstream discharge can be estimated with some accuracy at the upstream of the brachial artery, for instance around the shoulder [22, 32, 33], this is not the case for the downstream quantity. Indeed, the downstream boundary condition is linked to a pressure signal. But, since this signal is the unknown that our research focus on, it may not be considered as fixed and known downstream.

By contrast, we exploit the fact that the behaviour of both velocities and pressures is known in the capillaries. The pressure decays and stabilizes in the capillary network of blood flowing to the veins [18, 19], whereas the velocity tends to zero. Moreover, the capillary network presents a somewhat fractal structure with very dense ramifications.

The idea therefore is to impose downstream boundary conditions as capillary conditions so that the imposition of a constant low pressure, at the end of a certain ramified structure, can be done using branches following the architecture of vessels in the arm.

Along the artery, punctual pumping is considered, in order to represent the local branches bringing the blood to the veins through the capillary network, schematized as in Fig. 4a. In this network, the equations of flow are the same as those presented before (4.2.1), but, since only one way is

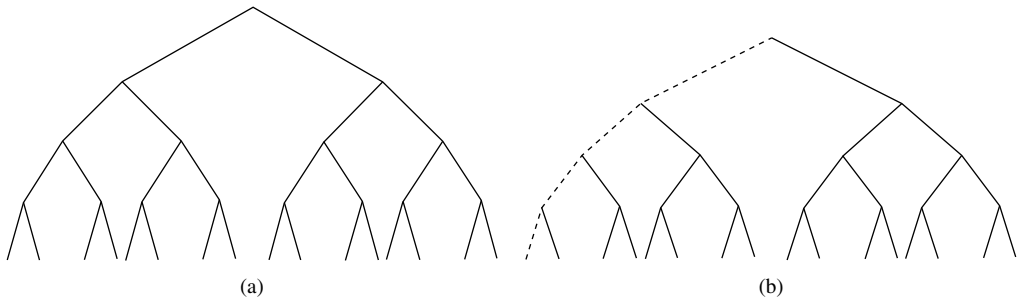


Figure 4: Schematization of the capillary network as modelled in the capillary flow: (a) global scheme and (b) one way considered.



considered (dashed line in Fig. 4b), the fluxes are re-evaluated at each junction, in order to obtain the true discharge to the capillaries.

For this approach to remain valid, the assumptions concerning blood rheology should still hold, which is questionable for the non-Newtonian effects. Nevertheless, since the purpose of modelling the capillary network is to obtain boundary conditions for the artery flow, using a pumping law that will be calibrated, it is reasonable to assume the behaviour as Newtonian, as a preliminary step to a physically based boundary condition.

## 5 RESULTS AND DISCUSSION

For now, the final model coupling both the structure and the fluid model is yet to be built. Nevertheless, the innovative developments in the boundary conditions can be tested and discussed. The remaining developments required before reaching the last step are well known in the current researches on FSI. Therefore, we focus here on the specific results concerning the so-called boundary model.

First, the boundary conditions are modelled on their own, with the aim of assessing their effectiveness. Next, their effect as a downstream boundary condition is compared with more classical outflow conditions, in order to judge the reliability of the original method that is presented in this paper.

The behaviour of the flow is influenced by two main parameters: the slot width and the friction coefficient. The slot represents, through its relation with the wave speed, the deformability of the pipe (see eqn (12)). For instance, a small wave speed (obtained with a relatively high slot width) leads to the representation of a deformable material for the pipe.

If these two parameters are appropriately chosen, the required dampening and the known drop can be well represented. Examples of this process have already been discussed in Ref. [19], and appropriate parameter values have been discussed in the same paper.

The results shown in Figs 5–7 illustrate the evolution of both the dimensional discharge and the dimensional head along the axial position of a single capillary and the evolution of the head as a

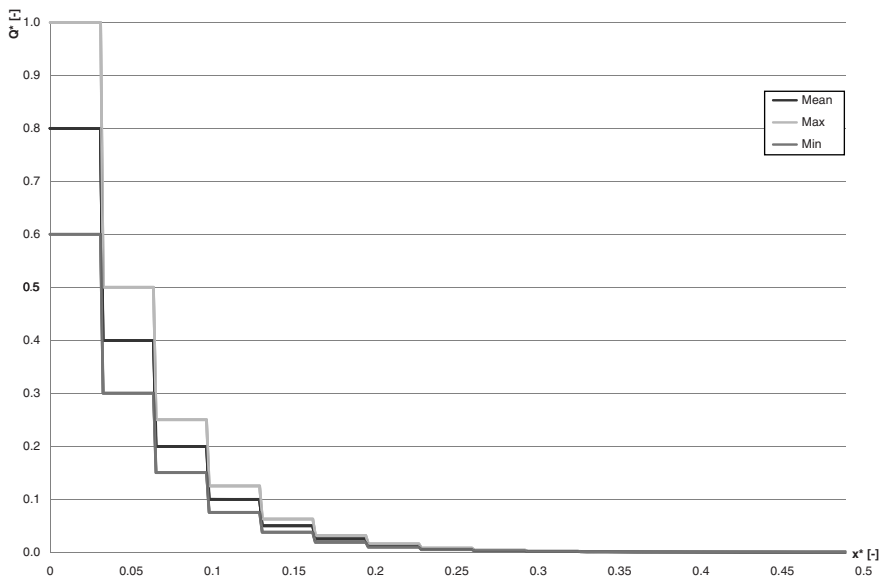


Figure 5: Evolution of the dimensional discharge [–] as a function of the axial position [–].

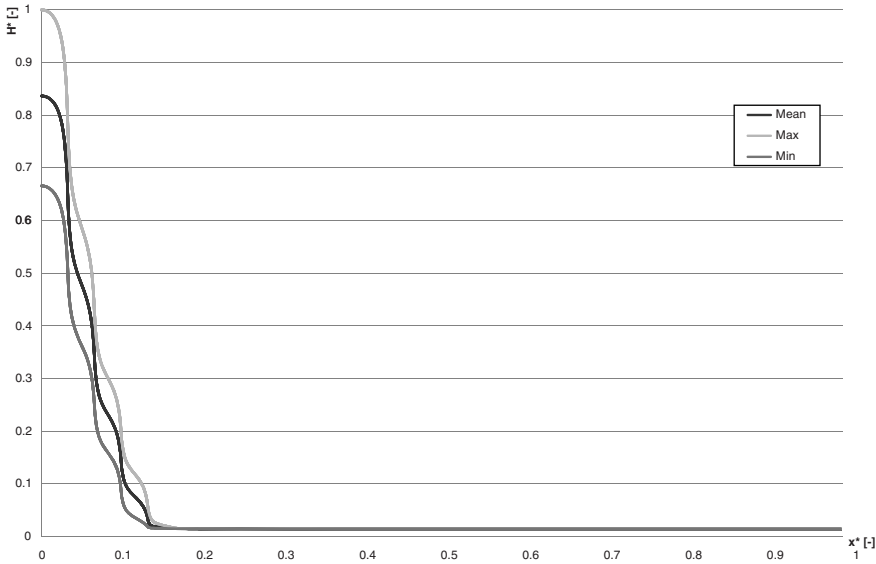


Figure 6: Evolution of the dimensional head  $[-]$  as a function of the axial position  $[-]$ .

function of time. In Fig. 5, the evolution of the dimensional discharge as a function of the axial position is depicted, for three different times corresponding, respectively, to the maximum, the minimum and the mean value of the sinusoidal signal. In Fig. 6, the same technique is used to represent the evolution of the head as a function of the axial position.

In Fig. 7, the evolution of the dimensional head as a function of time is depicted at different locations: successively at the upstream location of the network and at five different branches, from the first to the fifth branch.

The presented results correspond to the following numerical data:  $RK_1 = 0.15$ ,  $RK_2 = 0.45$ ,  $RK_3 = 0.4$ . The fluid characteristics are the following:  $\rho = 1,025 \text{ kg/m}^3$ ,  $\mu = 3.2 \text{ cP}$  for a haematocrit of 40–45%. The boundary conditions used for these simulations are indeed a constant pressure at the downstream position of the capillary network, combined with a sinusoidal upstream discharge signal, which enables, even if it is a long way from the read signal, interpreting the influence of the parameters and visualizing the required effects.

It is effectively clear that the consideration of a wide capillary subdivision combined with appropriate parameters representing the dissipative behaviour of the materials lead to the observation of the required dampening pretty quickly.

With these observations in mind, it remains now to assess the reliability of the proposed method as a boundary condition. For this purpose, a simple case of a prismatic pipe is simulated using two different types of outflow boundary conditions, namely our original proposition and the more basic concept of peripheral resistance, as proposed among others by Anliker *et al.* [34]. Both concepts rely on the fact that the terminal pressure is assumed to be constant, after vanishing in the capillaries. More comparisons are possible, but due to the lack of validation and the uncompleted integration of the whole model at the present time, it has been decided that the validation compared to the most basic and common downstream boundary condition was a first significant step available for an objective comparison. Once our model is finally integrated and calibrated, it will be time to compare it with existing more advanced models.

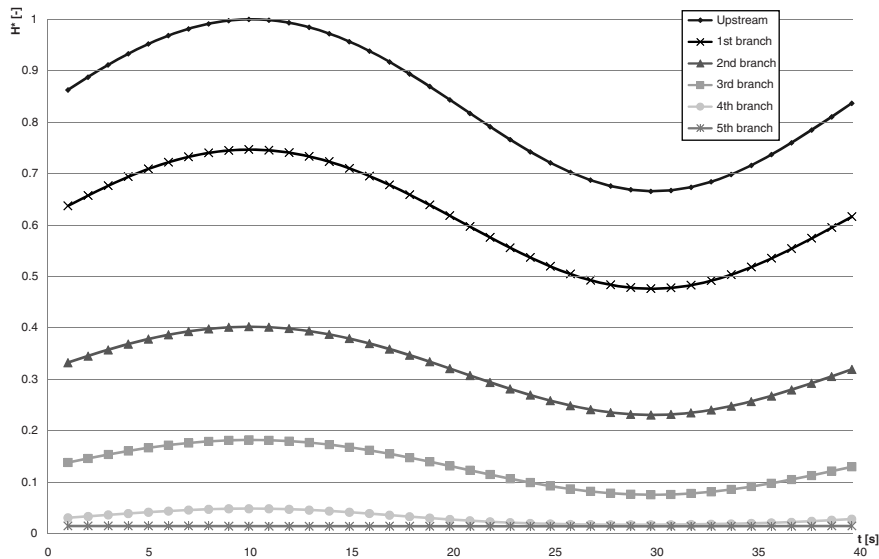


Figure 7: Evolution of the dimensional head  $[-]$  as a function of the time  $[s]$  at the very upstream of different branches.

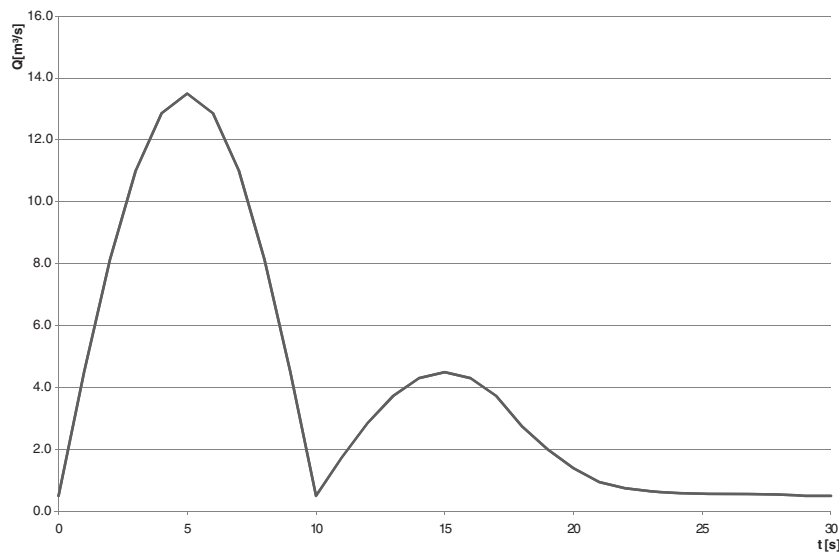


Figure 8: Evolution of the upstream discharge  $[m^3/s]$  as a function of time  $[s]$ .

The upstream boundary condition consists of a discharge signal, as presented in Fig. 8.

Besides, the initial condition is the situation corresponding to a uniform flow of  $0.5 \text{ m}^3/\text{s}$ . The results are presented in Fig. 9 as: (a) model with a peripheral resistance as the downstream boundary condition; (b) model with a capillary network as the downstream boundary condition.

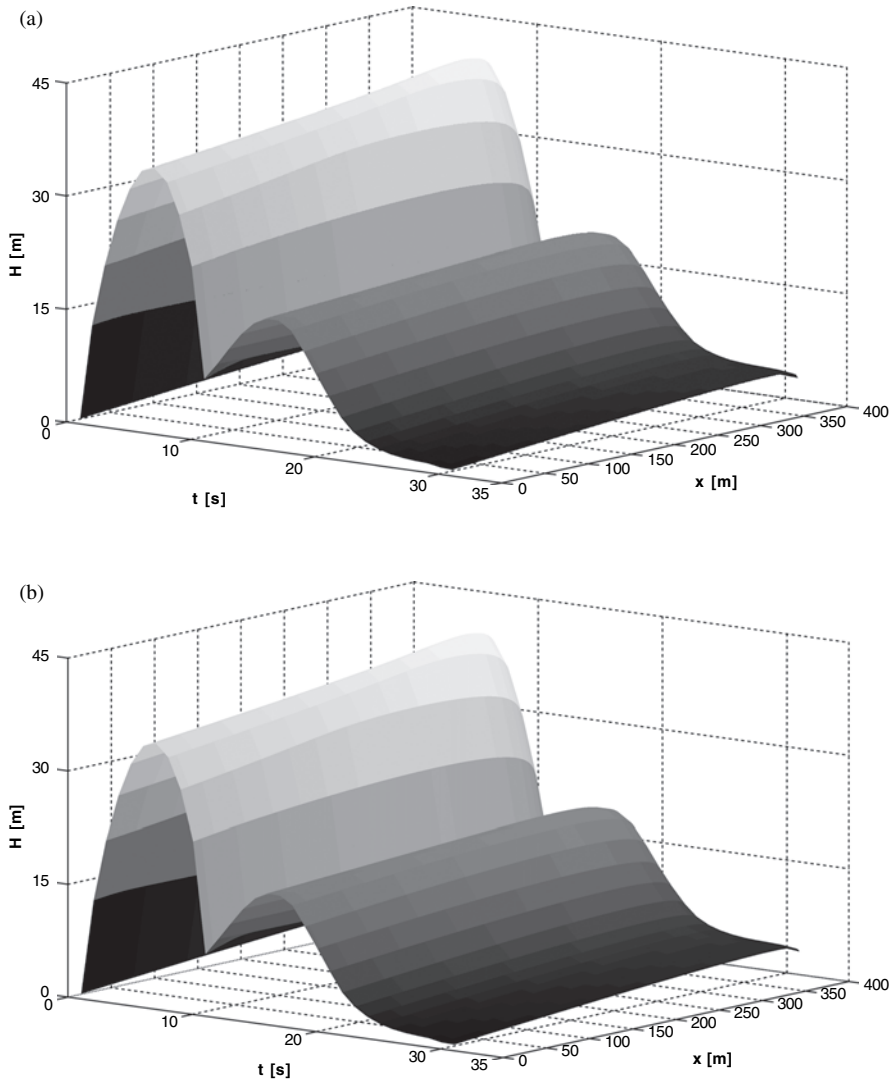


Figure 9: Evolution of the head [m] as a function of the time [s] and the axial position [m] for the whole pipe: (a) peripheral resistance case; (b) capillary network case.

The pipe is a 10 m long pipe, with a radius varying from 0.35 to 0.15 cm. The fluid characteristics are  $\rho = 1,025 \text{ kg/m}^3$  and  $\mu = 3.2 \text{ cP}$  for a haematocrit of 40–45%. The other parameters are the following:  $RK_1 = 0.15$ ,  $RK_2 = 0.45$ ,  $RK_3 = 0.4$ ,  $dx = 0.025 \text{ m}$ .

In both sets of figures, it is clear that the proposed boundary conditions are suitable to represent the phenomenon, the behaviour of the flow being, from a global point of view, similar no matter what the boundary conditions are.

More specifically, at the very downstream position, as can be seen in Fig. 10 ( $x = L_{\text{Max}}$ ), significant differences can be observed. In fact, the numerical value of the terminal pressure influences the behaviour in the case of the peripheral resistance, and not in the case of the capillary network case, which is another advantage of the method.

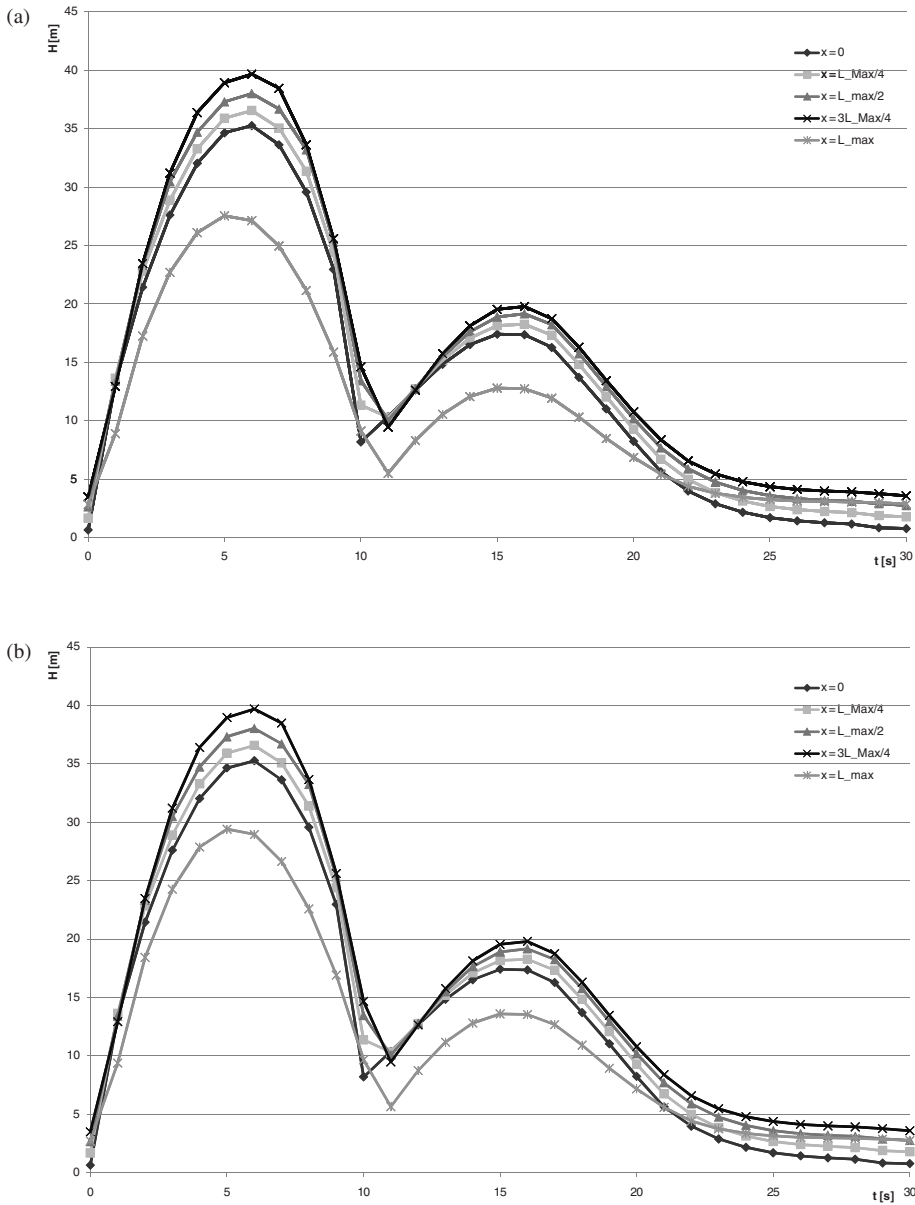


Figure 10: Evolution of the head [m] as a function of the time [s] for severe axial positions: (a) peripheral resistance case; (b) capillary network case.

## 6 CONCLUSIONS

The presented research for now keeps to the development of the coupled hydraulic model, whereas the final integration of this model with the boundary conditions still remains to be done.

The few results that have been developed and analysed within these researches clearly show interesting tendencies, and also provides information on the physical behaviour of the method. Moreover,

the work that has already been done indicates clear ways of developments for the final model, which is the last step of the research project.

First, the mechanical analysis of the artery has been done and a mathematical model has been developed such that the implementation of the equations through the final integrated model should be almost direct. Moreover, the numerical model established highlights the sensitivity of the parameters.

Second, a standard 1D flow solver has been implemented using finite volume methods, and enables the modelling of the blood flow through the artery. Although this model does not especially concern blood flow, it is suitable because it handles reliably stiff variation in the flow files, using an original numerical scheme adapted to flows governed by convective effects. Moreover, it enables straightforward modelling at junctions and therefore the physically based simulation of boundary conditions. It has been demonstrated that phenomena such as the dampening of the signal in the capillary network can be reproduced without spurious numerical oscillations. Finally, it has been shown, in a simple case study, that the proposed boundary conditions lead to an accurate prediction of the flow by comparison with classical boundary conditions.

## 7 PERSPECTIVES: THE INTEGRATED MODEL

Now that the different independent parts of the model have all been introduced and developed, the general framework of integration of these models can be described.

It consists of a main model coupled with secondary models and with boundary conditions following the capillary model.

The main model is simply the original hydraulic model presented in Section 4. In the framework depicted in Fig. 12, it is called ‘main flow’. The upstream condition requires the prescription of an upstream discharge. The downstream condition refers to the capillary model, as developed in Section 4.4. Basically, depending on the hypothetical presence of capillaries, a certain amount of fluid will be pumped out of the artery and propelled into the capillary following the capillary model.

The presence or lack of capillaries will depend on the geometry chosen at the beginning and obviously on the spatial discretization (see Fig. 11). As shown in Fig. 12, the capillary model uses the modified original main flow model (as explained in Section 4.4 and schematized in Fig. 11), and iteratively evaluates the pressure gradient between the artery and the capillary until the so-called equilibrium capillary discharge is determined.

Two final parameters have to be exploited: the external pressure and the way the fluid is pumped out of the artery have to be considered.

As mentioned in eqns (1–8), the external pressure modifies the cross section of the pipe. Therefore, this parameter somehow influences the original shape of the pipe. The pipe section for an empty slot (noted hereafter in Fig. 12,  $\Omega^*$ ) and the wave speed will both be modified at each time step in order to represent the external strain.

Besides, the artery/capillary interface is modelled based on a pumping law such that the fluid is taken out of the artery and propelled into the capillary as a function of the pressure difference between the two pipes.

Finally, the model is run as summarized in Fig. 12.

Considering at each time step the new external pressure and re-evaluating the nil-slot parameters, the main flow is evaluated and corrected (or not) due to the presence (or absence) of capillary, and so on, until the information has been propagated in the whole domain.

Finally, many elements, for example, the mechanical parameters of the living tissues (depending on the chosen material model), have to be investigated using experiments. Therefore, the authors plan to conduct a number of parallel researches about anatomical and physiological data, with the purpose of completing and calibrating the models and to finally validate their accuracy.

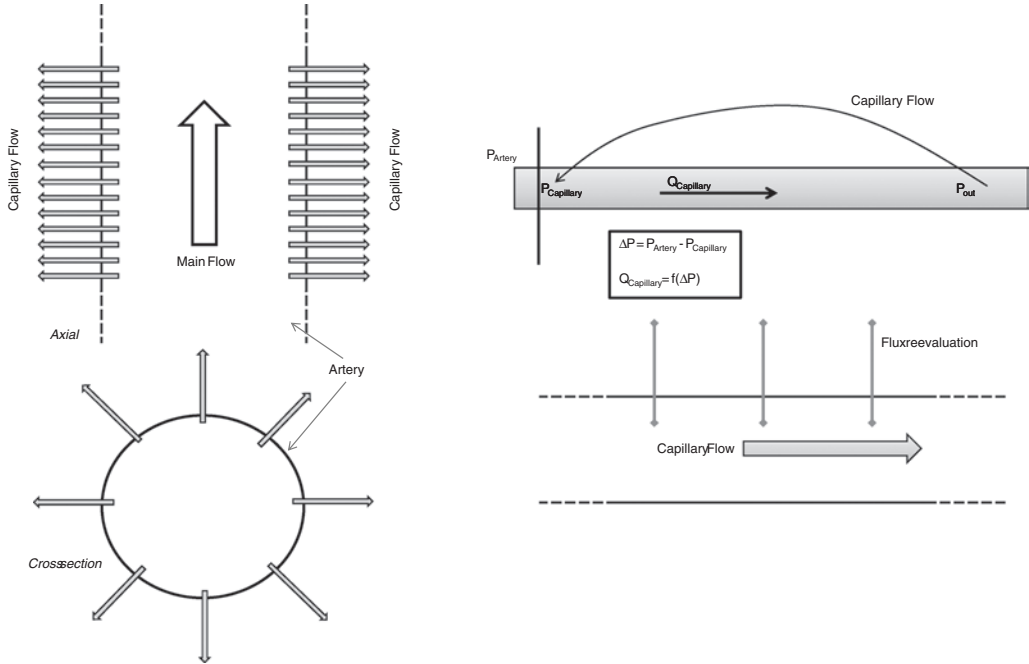


Figure 11: Schematization of the integrated model: (a) global model, (b) artery/capillary interface and (c) capillary model.

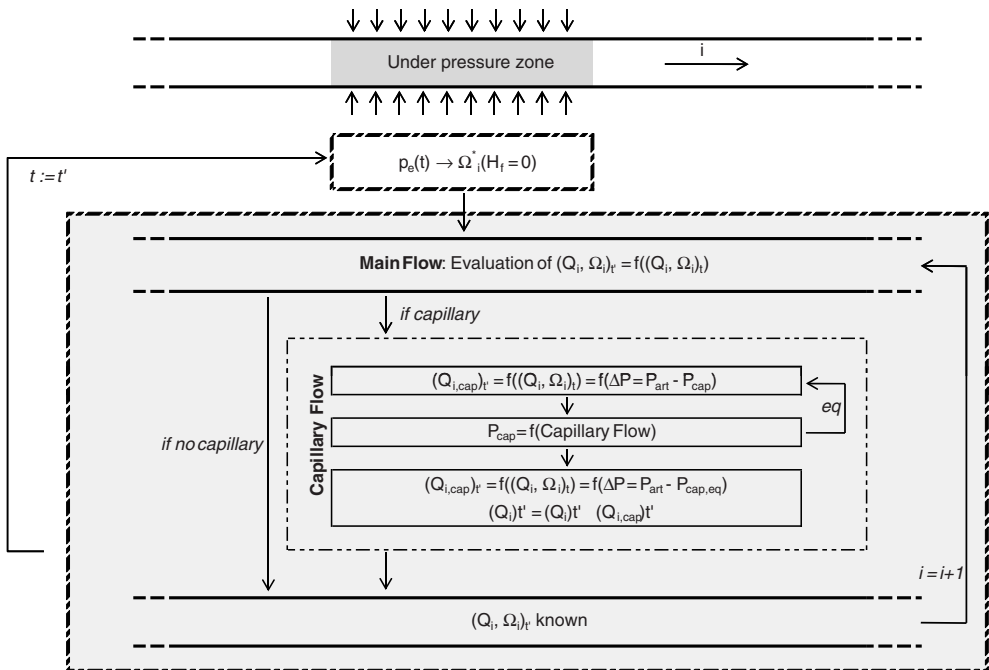


Figure 12: Final model.

## REFERENCES

- [1] Korotkoff, N., On methods of studying blood pressure. *Bull Imperial Mil Med*, **11**, pp. 365–367, 1905.
- [2] Riva-Rocci, S., Un nuovo sifigmomanometro. *Gazzeta Medica di Torino*, **47**, pp. 981–996, 1896.
- [3] Petrie, J.C., O'Brien, E.T., Littler, W.A. & de Swiet, M., Recommendations on blood pressure measurement. *British Medical Journal*, **293**, pp. 611–615, 1986.
- [4] O'Brien, E., Blood pressure measurement is changing! *Hearts*, **85-1**, p. 3–5, 2001.
- [5] O'Brien, E., Fitzgerald, D. & O'Malley, K., Blood pressure measurement: current practice and future trends. *British Medical Journal*, **290**, pp. 729–734, 1985.
- [6] Staessen, J., O'Brien, E., Thijs, L. & Fagard, R., Modern approaches to blood pressure measurement. *Occupational and Environmental Medicine*, **57-8**, pp. 510–520, 2000.
- [7] Bathe, M., *A Fluid–Structure Interaction Finite Element Analysis of Pulsatile Blood Flow through a Compliant Stenotic Artery*, PhD Thesis, Department of Mechanical Engineering, Massachusetts Institute of Technology, 1998.
- [8] Deparis, S., PhD Thesis, *Numerical Analysis of Axisymmetric Flows and Methods for Fluid–Structure Interaction Arising in Blood Flow Simulation*, Section de Mathématique, Ecole Polytechnique Fédérale de Lausanne, 2004.
- [9] Gerbeau, J.-F., Vidrascu, M. & Frey, P., Fluid–structure interaction in blood flows on geometries based on medical imaging. *Computers & Structures*, **83**, pp. 155–165, 2005.
- [10] Capron, N., Mompean, G. & Naji, H., Strong coupling for fluid structure interaction problems. *European Journal of Computational Mechanics*, **16(3–4)**, pp. 477–501, 2007.
- [11] Yang, J., Preidikman, S. & Balaras, E., A strong coupling scheme for fluid–structure interaction problems with dynamically moving boundaries in viscous incompressible flows. *Mecánica Computacional Vol XXIV*, Buenos Aires: Argentina, 2005.
- [12] Löhner, R., Cebal, J.R., Chi, Y., Baum, J.D., Meastream, E.L. & Soto, O., Extending the range and applicability of the loose coupling approach for FSI simulations. *Fluid–Structure Interaction; Modelling, Simulation, Optimisation*, eds H.-J. Bungartz, M. Schäfer, Springer: Berlin, Heidelberg, pp. 82–100, 2006.
- [13] Löhner, R., Cebal, J.R., Chi, Y., Baum, J.D., Mestreau, E., Charman, C. & Pelessone, D., Large-scale fluid–structure interaction simulations. *Computing in Science and Engineering*, **6(3)**, pp. 27–37, 2004.
- [14] Sieber, M.S.G., *Numerical Simulation of Fluid–Structure Interaction using Loose Coupling Methods*, Numerical Methods in Mechanical Engineering, PhD Thesis, Darmstadt Teknik University, 2001.
- [15] Lanoye, L., Swillens, A., Segers, P., Vierendeels, J. & Verdonck, P., Fluid structure interaction model of an axisymmetrical abdominal aortic aneurysm: decoupled versus fully coupled approach. *Advanced Computational Methods in Engineering*, Liège, Belgium: LTAS, 2008.
- [16] Vierendeels, J., Implicit coupling of partitioned fluid–structure interaction solvers using reduced-order models. *Fluid–Structure Interaction; Modelling, Simulation, Optimisation*, eds H.-J. Bungartz, M. Schäfer, pp. 1–18, 2006.
- [17] Paulus, R., Master Thesis, *Analyse des effets mécaniques et hydrauliques induits dans le bras par un brassard de mesure de la pression artérielle*, ArGenCo, ULg, 2007.
- [18] Paulus, R., Dewals, B.J., Erpicum, S., Cescotto, S. & Piroton, M., Numerical analysis of coupled mechanical and hydraulic effects induced by a blood pressure meter, *4th Advanced Computational Methods in Engineering*, Liège, Belgium: LTAS, 2008.



- [19] Paulus, R., Erpicum, S., Dewals, B.J., Cescotto, S. & Piroton, M., Computational hemodynamics coupled with mechanical behaviour of the surrounded materials, in the specific case of the brachial artery, *8th International Conference on Modelling in Medicine and Biology*, WIT: Crete, Greece, 2009.
- [20] Dobrin, P.B., Mechanical properties of arteries. *Physiol. Rev.*, **58(2)**, pp. 397–460, 1978.
- [21] Hayashi, K., Experimental approaches on measuring the mechanical properties and constitutive laws of arterial walls. *Journal of Biomechanical Engineering*, **115(4B)**, pp. 481–488, 1993.
- [22] Peterson, L.H., Jensen, R.E. & Parnell, J., Mechanical properties of arteries in vivo. *Circ Res*, **8(3)**, pp. 622–638, 1960.
- [23] Pochet, T., Master Thesis, *Ecoulement pulsatoire d'un fluide dans une conduite à parois déformables*, ULg, 1986.
- [24] Fung, Y.C., *Biomechanics, Mechanical Properties of Living Tissues*, Springer Science: New York, USA, 1993.
- [25] Fung, Y.C., *Biomechanics, Circulation*, Springer Science: New York, USA, 1996.
- [26] Archambeau, P., PhD Thesis, *Contribution à la modélisation de la genèse et de la propagation des crues et inondations*, ArGENCo, ULg, 2006.
- [27] Preismann, A., Propagation des intumescences dans les canaux et rivières, *1st Congress of the French Association for Computation*, Grenoble, France, 1961.
- [28] Kerger, F., Archambeau, P., Erpicum, S., Dewals, B.J. & Piroton, M., Simulation numérique des écoulements mixtes hautement transitoires dans les conduites d'évacuation des eaux. *Houille Blanche-Rev. Int.*, pp. 159–167, 2009.
- [29] Kerger, F., Erpicum, S., Archambeau, P., Dewals, B.J. & Piroton, M., Numerical simulation of 1D mixed flow with air/water interaction. *Multiphase Flow*, New Forest, 2009.
- [30] Dewals, B.J., Thesis, *Une approche unifiée pour la modélisation d'écoulements à surface libre, de leur effet érosif sur une structure et de leur interaction avec divers constituants*, University of Liege, 2006.
- [31] Kerger, F., Archambeau, P., Erpicum, S., Dewals, B.J. & Piroton, M., A fast universal solver for 1D continuous and discontinuous steady flows in rivers and pipes. *International Journal for Numerical Methods in Fluids*, 2009. Published online, DOI: 10.1002/fld.2243
- [32] Levenson, J.A., Peronneau, P.A., Simon, A. & Safar, M.E., Pulsed Doppler: determination of diameter, blood flow velocity, and volumic flow of brachial artery in man. *Cardiovasc Res*, **15(3)**, pp. 164–170, 1981
- [33] Morse, O.C. & Singer, J.R., Blood velocity measurements in intact subjects. *Science*, **170(3956)**, pp. 440–441, 1970.
- [34] Anliker, M., Rockwell, R.L. & Ogden, E., Nonlinear analysis of flow pulses and shock waves in arteries. *Zeitschrift für Angewandte Mathematik und Physik (ZAMP)*, **22(3)**, pp. 563–581, 1971.

# INVESTIGATION OF PULSATILE FLOW IN THE UPPER HUMAN AIRWAYS

G. EITEL, T. SOODT & W. SCHRÖDER

Institute of Aerodynamics, RWTH Aachen University, Wüllnerstrasse 5a, 52062 Aachen, Germany.

## ABSTRACT

The pulsatile flow field in the human lung is numerically and experimentally investigated. The realistic lung geometry of a human subject was acquired down to the sixth generation of bifurcation and used as a tracheobronchial model. The numerical analysis is based on a Lattice–Boltzmann method which is particularly suited for flows in extremely intricate geometries such as the upper human airways. The measurements are performed via the particle-image velocimetry method in a transparent cast generated from the original dataset. Experimental and numerical results are analyzed in a comparative way and a thorough discussion of the three-dimensional flow structures emphasizes the unsteady character of the flow field. It is evidenced that the asymmetric geometry of the human lung plays a significant role for the development of the flow field in the respiratory system. Secondary vortex structures and their temporal formation are analyzed and described in detail for two respiration frequencies. It is shown that the qualitative structure of the intricate flow field does not vary if a critical mass flux rate is exceeded. At inspiration, the primary flow shows separated flow regions and is highly influenced by secondary flow structures. By contrast, at expiration the primary flow distribution is far more homogeneous with a higher level of vorticity.

*Keywords:* counter-rotating vortices, human airways, Lattice–Boltzmann method, particle-image velocimetry, pulsatile flow, transparent lung cast.

## 1 INTRODUCTION

The human lung is a highly complex respiratory system consisting of a repeatedly bifurcating pipe network at progressively decreasing diameters. It fulfills multiple tasks in conjunction with the nasal cavity, *viz.*, the air transport and the exchange of carbon dioxide and oxygen in the pulmonary alveoli. Furthermore, at inspiration the air has to be heated up and moisturized and solid particles are removed from the flow. At expiration the loss of heat and humidity has to be limited. Thus, the requirements are challenging and several processes take place at the same time inside the respiratory tract.

The understanding of flow processes in the upper human airways is of great importance to develop aerosol drug delivery systems and to improve the efficiency and usability of artificial respiration systems. Numerous experimental and numerical investigations of lung flow have been conducted so far [1–4]. However, due to the high geometric intricacy of the human lung, there is still a considerable amount of uncertainty concerning the very complex flow field and fundamental results for realistic lung models are still rare. Many investigations are based on simplified models of the lung structure. The most popular of these models is the so-called Weibel model [5] which describes the bronchi as a symmetric tree structure of subsequent bifurcating pipes consisting of 23 generations. However, in most of the studies only the first three to five generations are considered and a planar representation is favored for simplicity. In Ref. [1] detailed experimental studies were performed for a planar Weibel model where fundamental flow phenomena like m-shaped velocity profiles and counter-rotating vortices were described. It was shown in numerical studies [2, 6], however, the flow field for the non-planar configuration differs significantly from the planar case. Studies considering asymmetric bifurcations [3], non-smooth surfaces [7] and CT-based models [4, 8, 9] show that the inspiration flow in the upper human airways is asymmetric and swirling. These results emphasize the importance of realistic airway models.

Generally, the aforementioned results show that an accurate lung geometry, i.e. CT data or a real human lung cast, is required to obtain physiologically relevant results. Grosse *et al.* [10, 11] experimentally investigated the steady and oscillating flow field in a silicon model of a human lung cast that covers the trachea and the bronchial tree down to the sixth generation. It was found that the flow structures mainly depend on the instantaneous Reynolds number and on the Womersley number. In the experiment only a parallel cutting plane could be taken into account, so the investigation of vortical structures was limited to a detailed qualitative analysis.

The present work focuses on the investigation of the unsteady three-dimensional flow for the lung model used by Grosse *et al.* [10] for a normal respiration at rest and for an increased rate of respiration. Numerical results are compared with experimental findings and flow structures are described in detail. The flow field is simulated via a Lattice-Boltzmann method (LBM) [12]. Unlike former numerical investigations, in which a simplified geometry was used, the present method can be efficiently applied to variable, realistic airway geometries. For instance the flow field downstream of the laryngeal region was recently investigated in Refs. [13, 14] by LBM. In combination with an automated grid generation [15] based on CT-data this method offers an efficient tool for biomedical flow problems. Since the numerical method is capable of reproducing small-scale features of the entire lung flow, the results support to fundamentally understand respiratory mechanisms. Thus, the numerical results allow an extended analysis of the three-dimensional flow structures observed in the experiment.

However, despite a long-term experience in the development and application of computational fluid dynamics methods to mechanical engineering problems, it is still a must to ensure the quality of the numerical solutions. In the present work, particle-image velocimetry measurements are used for the validation. The results mainly serve to fundamentally understand the three-dimensional flow structures and the time-dependent development within the upper bifurcations of the human lung under normal breathing conditions.

The structure of this paper is as follows. First, a concise description of the fundamental fluid mechanics is given. Then, the lung model, the experimental setup, and the numerical method are specified. Subsequently, numerical and experimental results are compared and discussed. Finally, the findings are summarized and some conclusions are drawn.

## 2 FUNDAMENTAL FLUID MECHANICS

In the following, the flow is assumed laminar and incompressible.

### 2.1 Steady flow in curved pipes

Since flows through bended pipes possess curved path-lines, centrifugal forces and pressure gradients normal to the axis of the pipe exist. This pressure gradient reads

$$\frac{\partial \rho}{\partial n} = -\rho \cdot \frac{u^2}{r_c}. \quad (1)$$

The expressions  $\partial \rho / \partial n$ ,  $\rho$ ,  $u$ , and  $r_c$  represent the pressure gradient normal to the streamwise direction, density, streamwise velocity component, and curvature radius, respectively. Higher axial velocities on the axis of the pipe cause higher centrifugal forces, i.e. the core flow is directed to the outer wall (O). The near-boundary fluid is displaced and moves near the pipe wall towards the inner part (I) (see Fig. 1). A secondary flow structure with velocities perpendicular to the pipe axis develops. The shift of the velocity maximum towards the outer wall enhances the pressure gradient

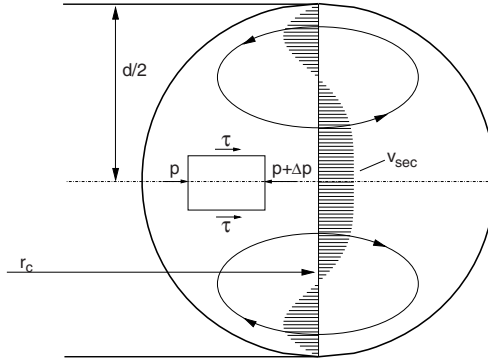


Figure 1: Illustration of the secondary velocity  $v_{sec}$  in a bended pipe with diameter  $d$  and curvature radius  $r_c$ . The shear stress  $\tau$ , and the pressure  $p$  are denoted for an evanescent volume on the plane of symmetry.

increasing the probability of flow separation [16]. For the steady flow case Dean [17, 18] has analytically described the development of two counter-rotating vortices. He proved that the flow can be characterized by the Dean number  $De = Re \cdot (d/r_c)^{1/2}$  where  $d$  represents the pipe diameter and  $Re$  is the Reynolds number  $Re = d\bar{u}/\nu$  based on the mean streamwise velocity and the kinematic viscosity  $\nu$ . Various publications (e.g. [19, 20]) intensively investigated this phenomenon and substantiated the fundamental understanding of bended pipe flows.

## 2.2 Pulsatile flows

In pulsatile flows the relationship between the applied pressure and the flow rate depends on the frequency. An exact theory for a time dependent flow in a long straight rigid and circular pipe under a periodic pressure gradient has been introduced by Womersley [21]. Regarding the oscillation frequency  $f$  a dimensionless number  $a = 0.5d\sqrt{2\pi f/\nu}$ , called Womersley number, can be derived. This number describes the development of velocity profiles in a viscous fluid with an alternating pressure gradient for different frequencies. For  $a > 1$  inertia effects arise which affect the velocity profile. First, the core flow becomes broader at increasing Womersley number, i.e. the velocity profile is flattened. Second, the near-wall flow is transiently reversed. This is illustrated by analytical results for different phase angles  $-\pi/2 < \phi < 0$  in Fig. 2a for  $a = 3.64$  and in Fig. 2b for  $a = 5.15$ . The distributions are calculated for a pipe with a hydraulic diameter of  $d_{hyd} = 4A/U = 18.3$  mm where  $A$  is the cross section area and  $U$  is the circumference of the pipe. The fluid properties are based on a water–glycerin mixture as used in the experiment. The temporal change of the pressure drop along the axis of the pipe is assumed to be sinusoidal. Due to inertia effects the mean flow lags the pressure gradient by about  $90^\circ$  at  $a > 10$ . Note that in bifurcating pipe systems at decreasing radius the local Womersley number decreases monotonically.

## 3 THE LUNG MODEL

The geometry for the numerical investigations is based on a radiological scan taken from a cast of a human lung including the larger part of the trachea down to the sixth generation of the bronchial tree. The digital geometry reconstruction encompasses the pre-processing, the segmentation, the surface generation, and the iterative surface smoothing. Based on the surface data a computational mesh is automatically generated by an in-house grid generator.

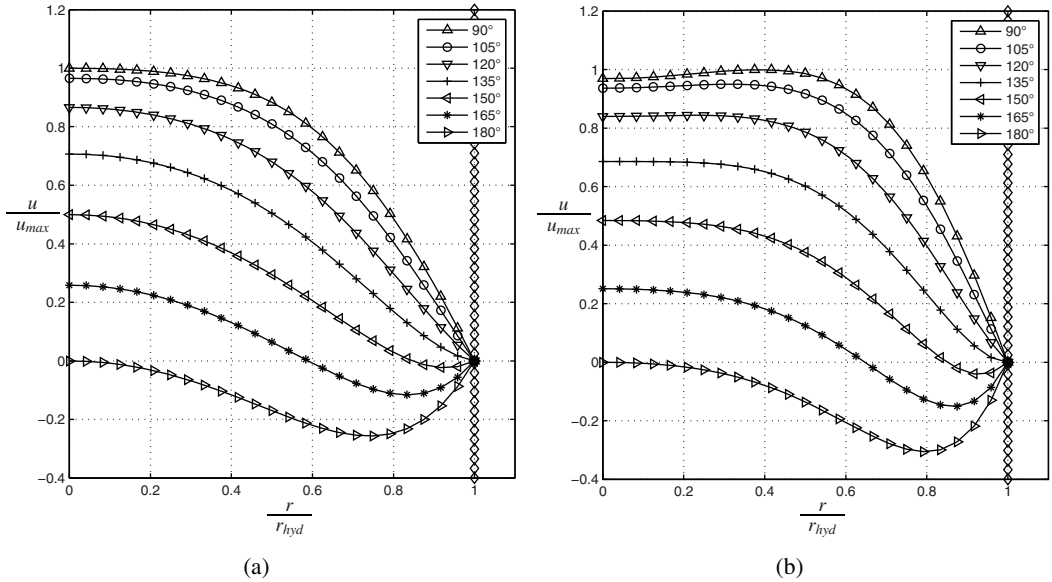


Figure 2: Temporal development of velocity profiles of circular pipe flow under a sinusoidal pressure gradient for (a)  $a = 3.64$  and (b)  $a = 5.15$ . The normalized velocity  $u/u_{\max}$  is plotted vs. the normalized radius  $r/r_{\text{hyd}}$ , where  $u_{\max}$  is the maximum streamwise velocity and  $r_{\text{hyd}}$  is the hydraulic radius. The symbols  $\triangle$ ,  $\circ$ ,  $\nabla$ ,  $+$ ,  $\triangleleft$ ,  $*$ ,  $\triangleright$  denote the phase angles from  $90^\circ$  to  $180^\circ$  and  $\diamond$  denotes the wall.

The same lung data was used to generate the silicon model for the PIV measurements in several manufacturing processes including corn starch rapid prototyping, surface coating, inlet insert attachment, transparent silicon (RTV815) casting, hot water wash-out, and manual channel drilling of the model's exits. These steps lead to models which allow flow field measurements within organic geometries and give the opportunity to understand *in vivo* flow phenomena.

The geometry is simplified in the sense that any elasticity of the configuration is not considered. However, the upper airways, as they are modeled here, are supported by chondral springs and can be assumed as the stiffest part of the lung. The physiological lung is an enclosed system with spatially varying tissue properties that lead to non-linear pressure–volume relations. The resulting spatial pressure distribution yields equilibrium processes which cannot be accounted in a model having open ends. At the tracheal cross section a fully developed laminar inflow is imposed by a Dirichlet boundary condition in the numerical analysis and by an extended trachea in the experiment.

Assuming a static geometry and neglecting any compliance influence of the lower lung parts, the present method delivers a fundamental insight into the lung flow, including the propagation of ventilation, frequency dependent spatial and temporal mass flow rates, shear stresses, dead water regions, and secondary flow structures. Fig. 3a shows the final experimental model from a dorsal point of view and in Fig. 3b the model of the numerical simulation is illustrated.

#### 4 EXPERIMENTAL SETUP

In the following the specifications of the experimental setup and the measuring parameters are discussed. The current study extends the investigation by Grosse *et al.* [10]. That is, in greater detail the

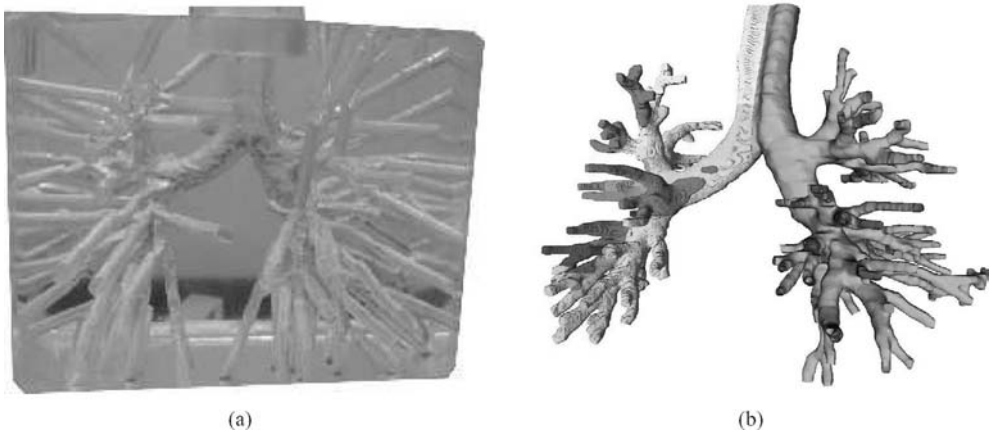


Figure 3: The employed lung model: (a) silicon model for PIV measurements and (b) surface data and computational grid.

three-dimensional flow structure and the pulsatile flow field are addressed. The ventilation is sinusoidal and represents human breathing at rest. The particle-image velocimetry (PIV) measurements of the human lung flow were performed in a 1:1 realistic lung cast based on computer tomography data.

The test rig schematically shown in Fig. 4a is designed as an open system containing a linearly actuated piston, a transparent container, an inflow pipe and equalizing tank. The pulsatile volume flux is generated by an assembly consisting of a motor prototype (MOOG Inc., Böblingen, Germany)

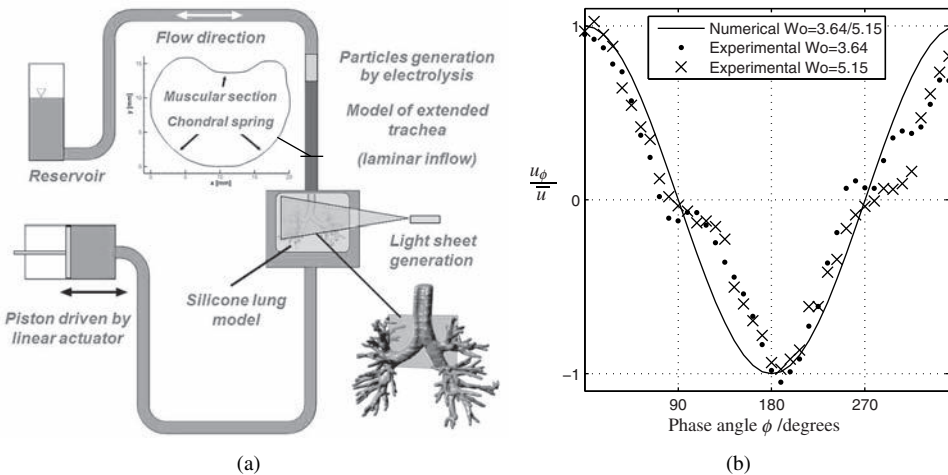


Figure 4: (a) Schematic of the experimental setup; (b) Normalized bulk velocities of the inflow for phase angles between  $0^\circ < \phi < 351^\circ$  and Womersley numbers of  $a_1 = 3.64$  (·) and  $a_2 = 5.15$  (×). The solid line denotes the ideal sinusoidal curvature used in the numerical analysis.

and a self-made piston. The amplitude  $A$  and the frequency  $f$  are adjusted in a range of  $A = 0\text{--}1.51/\text{s}$  and  $f = 0\text{--}3\text{ Hz}$ , respectively. The model is centered in the container at high distances to the PMMA (Plexiglas®) walls such that optical accessibility for the laser generated light sheet and the perpendicular mounted CCD camera (Sensicam QE, PCO, Kehlheim, Germany) is guaranteed and heterogeneous inflow conditions for the expiration phase can be neglected. The inflow pipe has a length of  $L = 500\text{ mm}$ , an anatomical inner contour matching the upper part of the shape of the trachea and a hydraulic diameter of approximately  $d_{\text{hyd}} = 18.3\text{ mm}$ . The length to diameter ratio of  $L/d_{\text{hyd}} = 27$  ensures a fully developed laminar velocity profile. The junction between the inlet pipe and the entry of the model can be assumed smooth such that no incipient flow separation occurs. The system is totally filled up by a fluid solution of water and glycerin. The glycerin fraction of the mixture is 60.7 mass percent to match the refraction index ( $n = 1.44$ ) of the model's silicon. This kind of adaption leads to an optical access without distortion.

At a measurement temperature of  $T = 25^\circ\text{C}$  the dynamic viscosity is  $\eta = 9.1 \times 10^{-3}\text{ Pa}\cdot\text{s}$ , the density is  $\rho = 1.153 \times 10^3\text{ kg/m}^3$ , and the kinematic viscosity is  $\nu = 7.89 \times 10^{-6}\text{ m}^2/\text{s}$ .

Due to the properties of the linear actuator the Reynolds number of  $Re_{\text{max}} = 1,600$  can be achieved at both Womersley numbers  $a_1 = 3.64$  and  $a_2 = 5.15$ . An electrolysis unit located between the model's inlet and the reservoir generates hydrogen bubbles in the size of  $d_b = 1\text{--}5\text{ }\mu\text{m}$  which are used as tracer particles. By changing the electrolysis voltage, the amount of saline addition, and the seeding time of the total amount of bubbles can be adjusted. The bubble lifetime ranges from 10 to 30 min which is large compared to the measuring time. The illumination of the tracers is done by an approximately 1 mm thick light sheet which is generated by a Nd:YAG-Laser (Minilite, Continuum, Inc., Darmstadt, Germany) with a nominal power of 25 mJ. The laser beam is widened by optical devices to cover the region of interest which is fully captured by a double shutter CCD camera (resolution:  $1,376 \times 1,040\text{ px}$ ). The calibration of the light sheet position was conducted by photometric comparison of the recorded images at different parallel positions with shifted slices of the numerical data set and by using a calibration target. The target also provides a gauge for the camera captured pixel distance. Normalized bulk velocities, measured at a distinct inflow section, are plotted in Fig. 4b for all recorded phase angles and both Womersley numbers. The deviations result from the non-optimal tracking between the motor's lift change and the fluid flux. Therefore, the arrangement of experimental and numerical data is based on the Reynolds similarity.

Images were captured every 9 degrees of one ventilation cycle with 200 records at each phase angle. This procedure was pursued for both Womersley numbers in three different measurement planes. Analyses including cross-correlating, filtering, adaptive cross-correlation, interpolation, and averaging were processed by the commercial software VidPIV (ILA GmbH, Jülich, Germany). The results contain velocity and vorticity distributions with a spatial resolution of  $R = 2.32\text{ vectors/mm}$  in both dimensions.

## 5 THE LATTICE-BOLTZMANN METHOD

Next, the Lattice-Boltzmann Method (LBM) is concisely described. The LBM is a solution algorithm for non-linear partial differential equations and it arose from Lattice Gas Cellular Automata (LGCA) which was introduced by Frisch *et al.* [22] in 1986. It was shown by the authors that a microscopic model describing molecular dynamics with collisions which conserve mass and momentum leads in the macroscopic limit to the Navier-Stokes equations if the underlying lattice possesses a sufficient symmetry. An extensive description of both methods, the LGCA and the LBM, is given in Refs. [12, 23, 24]. The most common variant of the LBM is based on the Boltzmann equation with a simplified collision operator proposed by Bhatnagar *et al.* [25] called BGK equation. The velocity

space is discretized into a set of  $n$  molecular velocities  $c_i$  with their associated distribution functions  $f_i(x, t)$ . The discrete BGK equation without external forcing reads

$$f_i(x + c_i \Delta t, t + \Delta t) - f_i(x, t) = \omega(f_i^{eq} - f_i), \quad (2)$$

where  $f^{eq}$  is the Maxwell equilibrium distribution function and  $\omega$  represents the collision frequency. The corresponding numerical method is referred to as LBM–BGK method. The left-hand side of eqn (2) contains the temporal change and the propagation term, whereas the right-hand side describes molecular collisions by a relaxation of the distribution functions towards thermodynamic equilibrium. Therefore, the algorithm of the flow solver is based on the iterative computation of propagation and collision processes for all cells of the computational grid. The macroscopic values of density  $\rho$  and momentum  $j$  are obtained as base moments of the distribution function which read

$$\rho(x, t) = \sum_{i=1}^n F_i(x, t) \quad (3)$$

$$j(x, t) = \rho(x, t) v(x, t) = \sum_{i=1}^n c_i F_i(x, t). \quad (4)$$

The LBM–BGK describes weakly compressible flows at moderate Reynolds numbers and it has been shown in the literature [26] that it yields indeed solutions to the Navier–Stokes equations. LBM models are characterized by the number of spatial dimensions  $m$  and the number of discrete velocities  $n$ . Therefore, the DmQn notation was introduced by Qian *et al.* [27]. Favored models in two and three dimensions are D2Q9, D3Q19, and D3Q27, since they offer sufficient lattice symmetry. The discrete velocity set for the D3Q19 model is shown in Fig. 5.

Since the LBM formulation is based on a uniform Cartesian mesh, it is highly adapted for parallel processing and it offers an efficient boundary treatment for fixed walls. The ability of reproducing variable organic geometries makes this method well suited for biomedical applications.

In this study the flow in the upper human airways was simulated by a D3Q19 LBM–BGK model with a modified equilibrium distribution function for incompressible flows as proposed by Zou *et al.* [28]. Solid wall nonslip boundary conditions were realized by an interpolated bounce-back rule [29]. A Dirichlet boundary condition imposing a fully developed laminar velocity profile was prescribed at the tracheal cross section, whereas a zero gradient condition was employed at the numerous

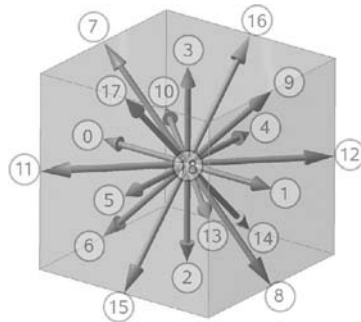


Figure 5: The discrete velocity set of the D3Q19 model.



outlets. The computational grid was automatically generated from surface data by an in-house grid generator [15] and consists of 2.5 million cells. It was shown, e.g. in Ref. [14] that the numerical method allows a detailed investigation of the three-dimensional flow field in the primary bronchi.

## 6 RESULTS

The time dependent inhalation and exhalation flow field has been investigated for a peak mass flux of 351 ml/s corresponding to a peak Reynolds number of  $Re_{\max} = 1,600$ . The value of the Reynolds number is based on the hydraulic diameter of the trachea  $d_{\text{hyd}} = 18.3$  mm. To investigate the unsteady behavior of the flow field during respiratory ventilation, simulations and measurements were performed for a normal respiration at rest at frequency  $f_1$  and for a higher respiration frequency  $f_2 = 2f_1$ . That is, the breathing periods are  $T_1 = 4$  s and  $T_1 = 2$  s which correspond to Womersley numbers  $\alpha_1 = 3.64$  and  $\alpha_1 = 5.15$ , respectively.

The temporal variation of the mass flux was prescribed by a sinusoidal curve as shown in Fig. 4b. The data were recorded after a transient time of one respiration cycle. In the following section numerical and experimental results are compared in a distinct cross section. Subsequently, the numerical data is further analyzed concerning the development of the three-dimensional flow structures.

### 6.1 Comparison of experimental and numerical data

In this section numerical and experimental data are compared in order to evidence the quality of the LBM solution. A brief comparison is presented for one plane of the first bifurcation which is defined in Fig. 6a. This region was chosen to globally evidence the mass flux into the lower bifurcations. Moreover, the phase angles at maximum inspiration and expiration can be compared with steady flow cases.

The comparison of the data at  $\alpha_1$  and  $\alpha_2$  shows no significant differences in the flow structures in this plane, which is why in the following only the solutions at  $\alpha_1 = 3.64$  are discussed. Figures 7 and 8 contain numerical and experimental results at different phase angles  $\phi$  of a sinusoidal ventilation cycle, where  $\phi = 0^\circ$  and  $\phi = 180^\circ$  represent maximum inspiration and expiration, respectively.

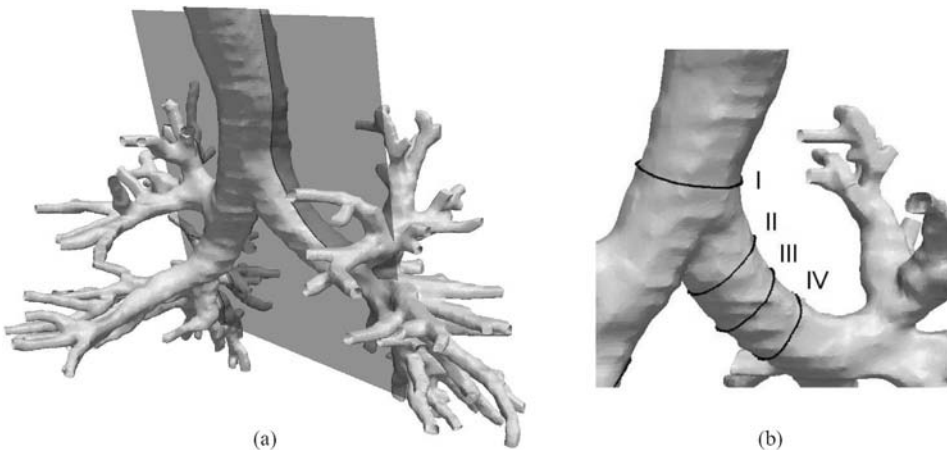


Figure 6: (a) Reference plane for the comparison of experimental and numerical data. (b) Cross sections for the investigation of secondary flow structures.

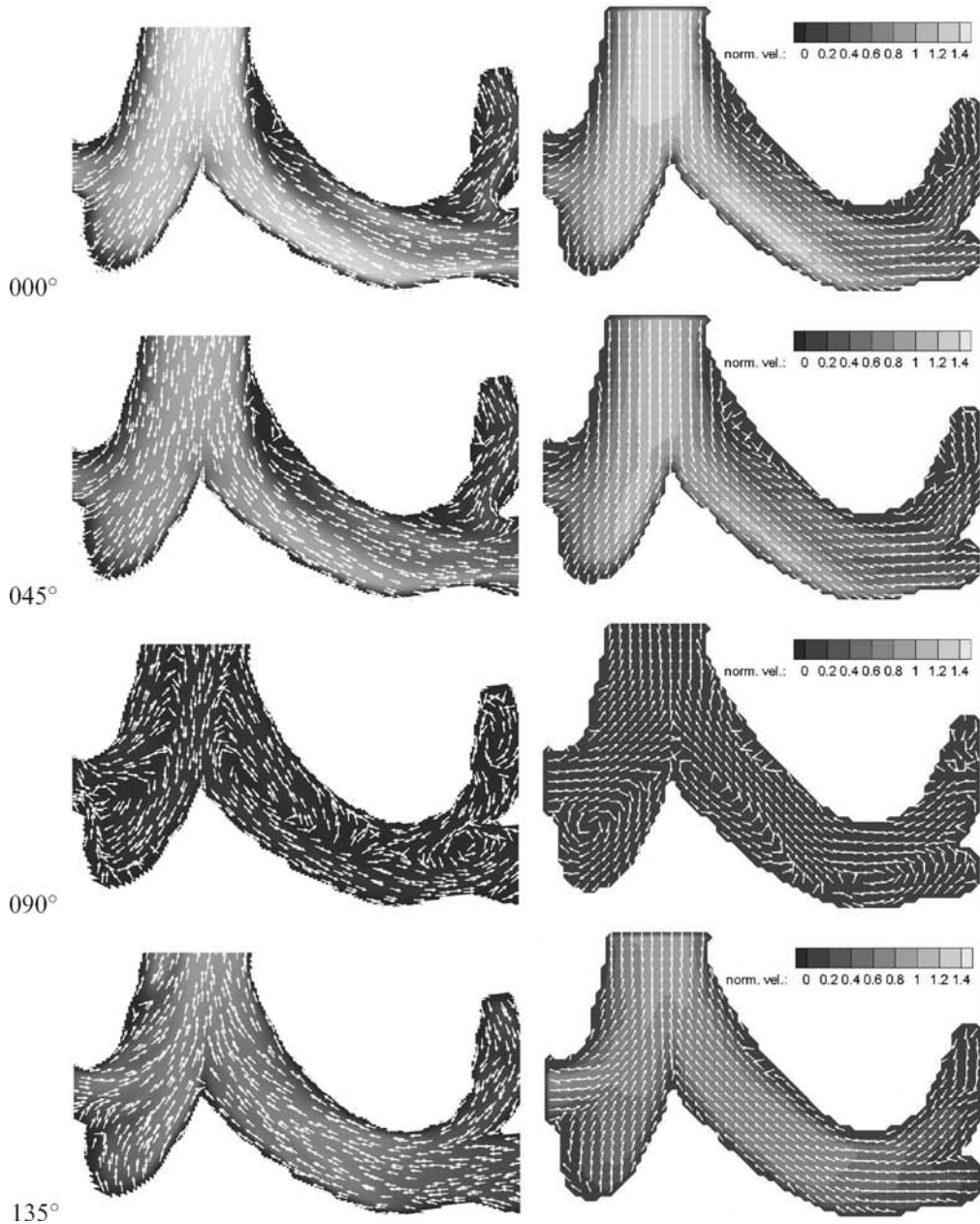


Figure 7: Time resolved data for the first half of a respiration cycle at rest, i.e.  $\phi = 0^\circ, 45^\circ, 90^\circ, 135^\circ$ ; LBM data (left), PIV data (right). The vectors have uniform length and indicate the flow direction. The gray scale values show the magnitude of the absolute velocity that is normalized by the bulk velocity at maximum inspiration for a defined tracheal section.

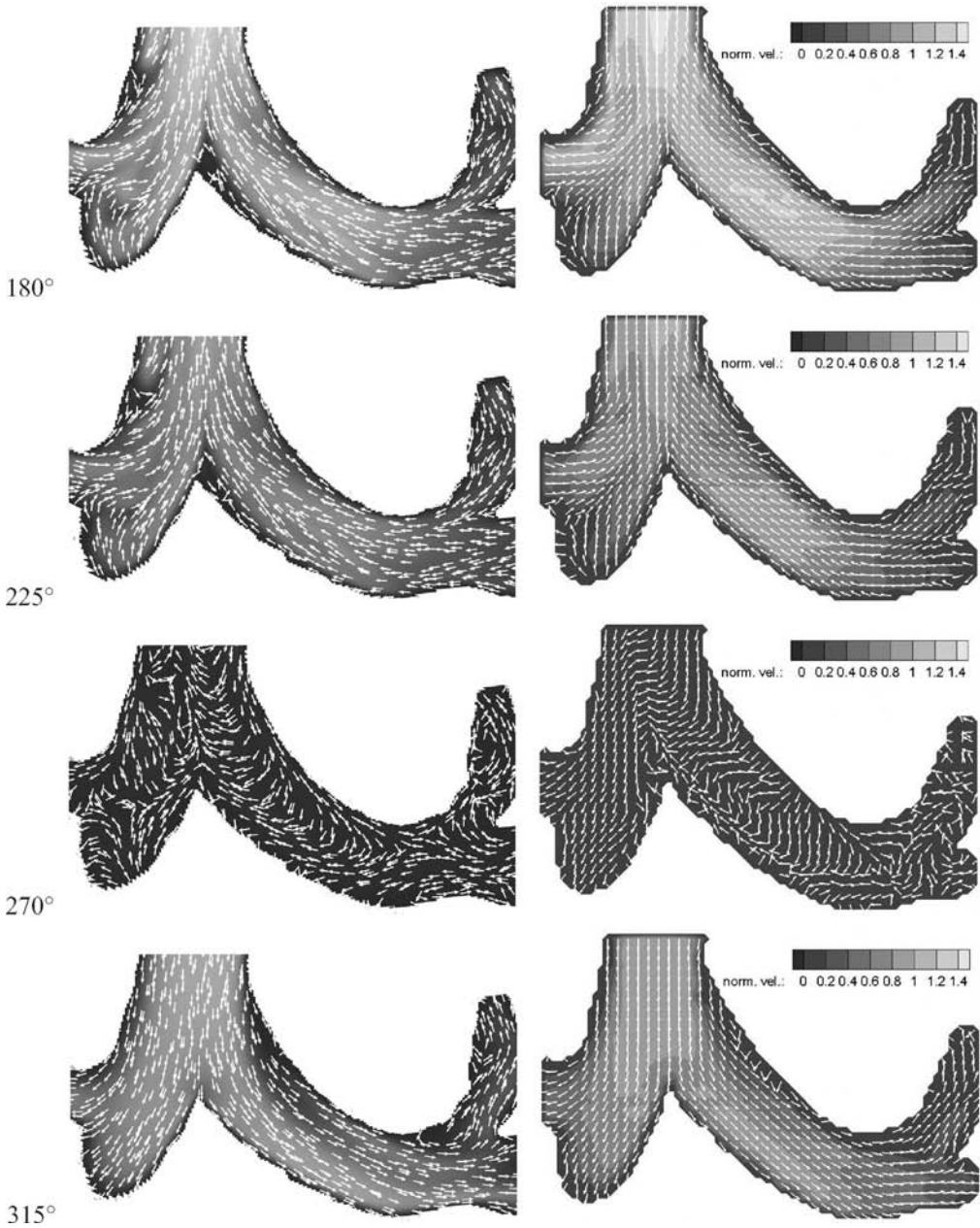


Figure 8: Time resolved data for the second half of a respiration cycle at rest, i.e.  $\phi = 180^\circ$ ,  $225^\circ$ ,  $270^\circ$ ,  $315^\circ$ ; LBM data (left), PIV data (right). The vectors have uniform length and indicate the flow direction. The gray scale values show the magnitude of the absolute velocity that is normalized by the bulk velocity at maximum inspiration for a defined tracheal section.

To emphasize the flow direction the vectors possess uniform length. The magnitude of the absolute velocity is normalized on the bulk velocity in cross section I in Fig. 6b at maximum inspiration. In the following, the terms *upper* and *lower* denote the upper and lower half of the main bronchi (bronchi principales), respectively. Note that there is a third sub-branch at the end of the posterior right main bronchus. The subsequent discussion of the numerical and experimental findings for various phase angles  $\phi = 0^\circ, 45^\circ, 90^\circ, 135^\circ, 180^\circ, 225^\circ, 270^\circ, 315^\circ$  shows the quality of the solutions of the Lattice–Boltzmann method under pulsatile flow conditions.

$\phi = 0^\circ$ : The flow field is almost identical with the steady case distribution which was extensively discussed in Ref. [14]. A distinct stagnation point occurs at the first bifurcation (carina tracheae). The LBM and PIV solutions possess a high-speed region near the lower wall which is very similar in extension and magnitude. A closer look indicates that the high-speed region reaches somewhat further into the next branch. Curvature induced separations at the upper wall near the main bronchial entry also do occur in the simulation and in the measurement. The structures of the sub-bronchial flow field are similar in both cases.

$\phi = 45^\circ$ : Compared to  $\phi = 0^\circ$  the velocity magnitude is globally reduced whereas the flow structures remain almost alike. The numerical solution possesses slightly higher peak values of velocity.

$\phi = 90^\circ$ : At this phase angle the inspiration ends and the expiration phase sets in. The high-speed region near the lower wall still exists, whereas the outflow is already established in the upper part of the bronchus. The resulting mixing layer is evident in the numerical and experimental findings. The illustrations show similar recirculation regions for the LBM and PIV data.

Nevertheless, there are some differences which occur especially in the tracheal flow pattern and in the extension of the high-speed region. This discrepancy is due to a phase shift, i.e. the simulation slightly lags the experiment. It is clear that during transition from inspiration to expiration the impact of a little difference in the numerical and experimental description is more pronounced. This is visualized in Fig. 7 at  $\phi = 90^\circ$ .

$\phi = 135^\circ$ : At this stage all inflow patterns have disappeared. A nearly homogeneous outflow from all sub-branches is observed such that is indicating an almost perfect wash-out.

$\phi = 180^\circ$ : At higher phase angles the outflow develops a more pronounced velocity distribution, i.e. the peak velocity and the bulk velocity differ clearly. This flow pattern is caused by the sub-branches since five high-speed streaks merge in the trachea. Only in the numerical solution a small recirculation region on the lower wall of the left bronchus is observed which interacts with the main-stream in the trachea. This discrepancy is likely to be due to slight deviations of the curvature of the lower wall in the final silicone model and the original lung data.

$\phi = 225^\circ$ : From  $\phi = 180^\circ$  to  $\phi = 225^\circ$  the overall flow structures do not change. Only the velocity magnitude is reduced.

$\phi = 270^\circ$ : The flow pattern characterizes the change from expiration to inspiration. It is clear that the simulation possesses a slight delay to the experiment. The simulation results evidence that inspiration first sets in near the upper walls of the primary bronchi.

$\phi = 315^\circ$ : The inspiration flow pattern is similar to the structure at  $\phi = 0^\circ$  although the separation regions are spatially reduced and the high-speed region is broader than at full inspiration ( $\phi = 0^\circ$ ).

In conclusion, the numerical and experimental data match satisfactorily. The slight differences of the LBM and PIV data are due to small deviations of the lung model and the original geometry data. Moreover, the discrepancies near the wall appear to be caused by a lack of seeding particles in the flow regimes resulting in a decreased resolution of the velocity distribution. Finally, the boundary conditions of the numerical and the experimental setup do not perfectly coincide, since the pipe extensions downstream of the sixth generation are not taken into account in the simulation and the

temporal change of the volume flux is not perfectly sinusoidal in the experiment. Keeping these facts in mind, the numerical–experimental agreement can be considered convincing.

## 6.2 Secondary flow structures

In order to obtain a deeper insight into the development of the flow pattern, the secondary flow structures are further analyzed in this section on the basis of the numerical solutions. The locations of the various cross sections denoted by I, II, III, and IV are defined in Fig. 6b. The flow field in the trachea is depicted for both Womersley numbers in Fig. 9 at maximum inspiration ( $\phi = 0^\circ$ ) and in Fig. 10 at maximum expiration ( $\phi = 180^\circ$ ). The black lines indicate the reference plane of the flow patterns which were discussed in the previous section.

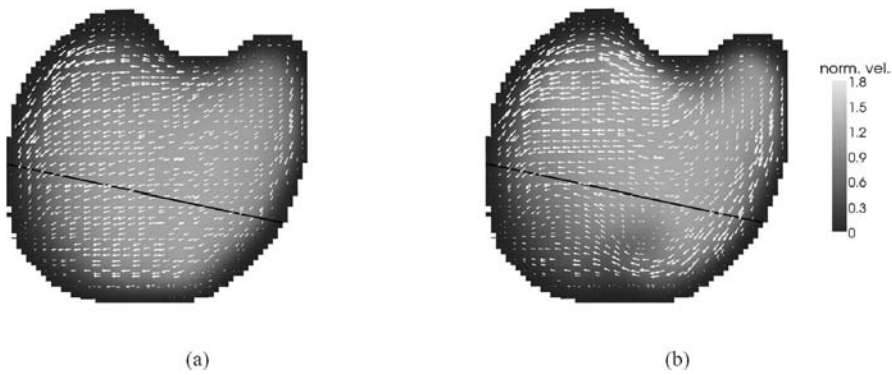


Figure 9: Flow field in the tracheal cross section I described in Fig. 6b at maximum inspiration; (a)  $a_1 = 3.64$  and (b)  $a_2 = 5.15$ . The levels of gray indicate the axial velocity magnitude and the arrows represent the in-plane velocity. The black lines indicate the reference plane described in the previous section.

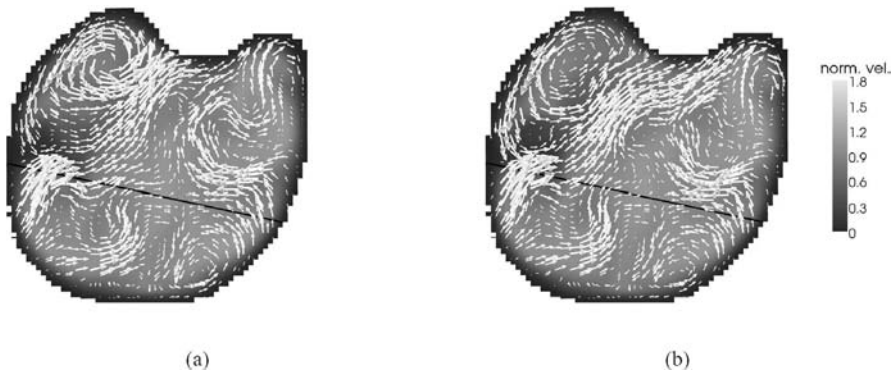


Figure 10: Flow field in the tracheal cross section I described in Fig. 6b at maximum expiration; (a)  $a_1 = 3.64$  and (b)  $a_2 = 5.15$ . The levels of gray indicate the axial velocity magnitude and the arrows represent the in-plane velocity. The black lines indicate the reference plane described in the previous section.

At maximum inspiration a well developed velocity profile is observed at  $a_1$  the shape of which is characterized by the geometry of the throat. At  $a_2$  the velocity distribution possesses clear deformations compared to the  $a_1$  profile. At maximum expiration strong vortical structures occur over the whole cross sections which are shown in Fig. 10. These structures are generated by the asymmetric merging of the air streams from the left and right principal bronchus. A stagnation point is observed near the right wall just above the reference plane. Note that unlike the inspiration structures the expiration structures show no significant dependence on the Womersley number.

In Fig. 11 the flow field at maximum inspiration and expiration at  $a_1 = 3.64$  is depicted in the cross sections II–IV. At inspiration the main mass flux is located near the lower wall. This corresponds to

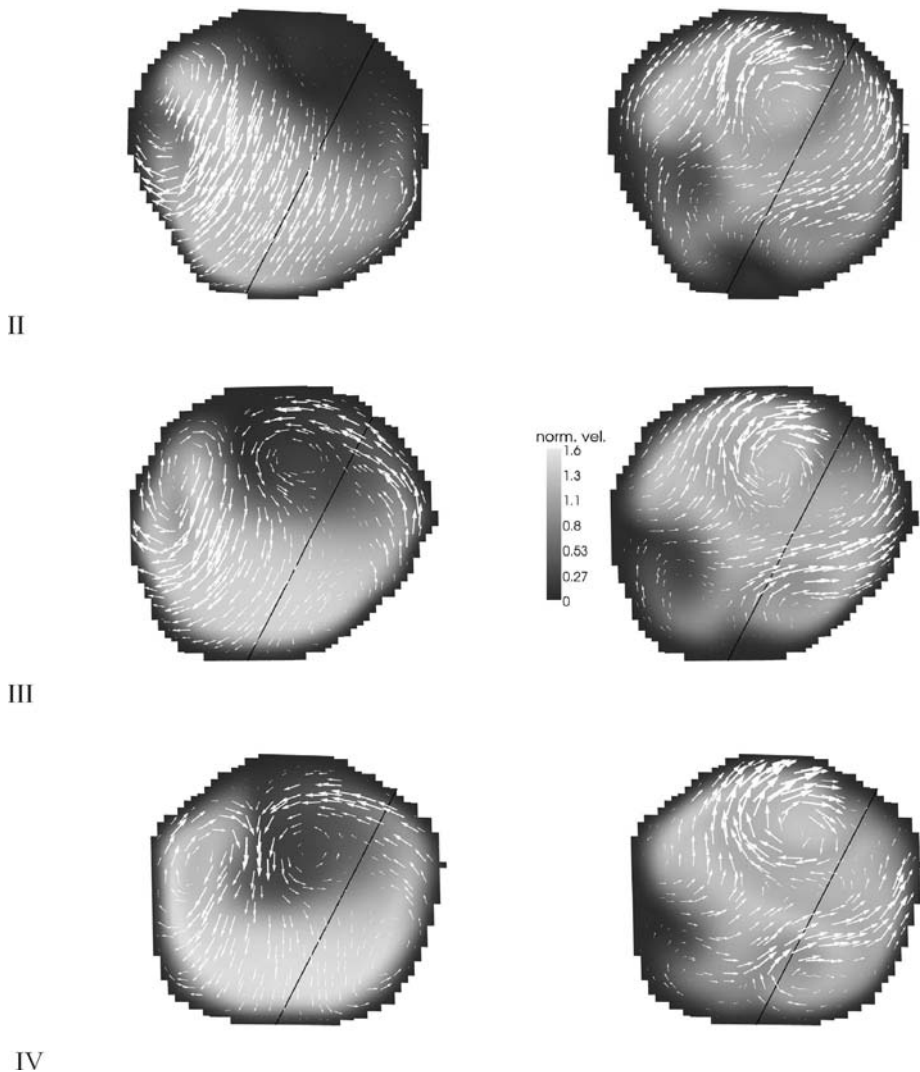


Figure 11: Flow field in the cross sections II–IV; inspiration (left), expiration (right). The axial velocity is shown by gray scale values and the arrows represent the in-plane velocity. The black lines indicate the reference plane described in the previous section.

the high velocity region shown in Fig. 7 at  $\phi = 0^\circ$ . Downstream of the first bifurcation a pair of counter-rotating vortices develops transporting fluid from the high-speed to the low-speed region along the outer walls. The right vortex has a center of rotation near the upper wall and covers most of the upper half of cross section IV. The left vortex is much smaller and it is located very close to the left wall. Such a vortex pair also was observed in the steady state simulations in Ref. [14]. The physics of its generation is related to the aforementioned Dean vortex. Once the next bifurcation is reached, the vortices do separate and each one enters a branch of the next higher bronchial generation.

At expiration the streamwise velocity is more evenly distributed than at inspiration. The mixing of streams coming from the higher generation bronchi generates a shear layer which yields a swirling region. Two stagnation regions are indicated in Fig.11. One is located at the lower wall and develops in the streamwise direction. The other stagnation region occurs at the left wall and vanishes when the trachea is approached. The in-plane velocity distribution evidences a strong clockwise rotating vortex near to the upper wall and more mass flux is coming from the ventral lung lobe.

In conclusion, the findings confirm pronounced secondary flow structures at inspiration and expiration. The numerical data emphasizes the strong asymmetry of the vortical structures. It is clear that the vortical flow structures are more intricate at expiration ensuring an almost perfect wash-out.

To show the temporal variation of the vortical structures the axial vorticity component in cross section IV was determined over a whole respiration cycle. The mean magnitude of the axial vorticity versus the phase angle  $\phi$  is shown in Fig. 12 for both Womersley numbers. The amount of vorticity clearly increased at higher Womersley number at inspiration. A slight phase shift is also evident

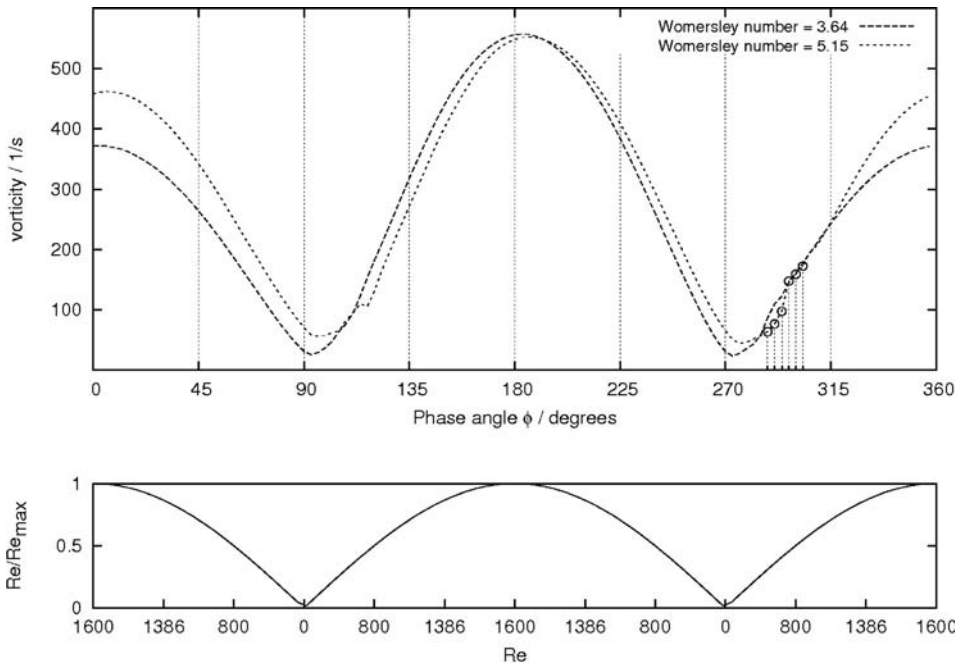


Figure 12: (Top) Mean in-plane vorticity magnitude plotted against the phase angle for the cross section IV in Fig. 6b. (Bottom)  $Re/Re_{max}$  as a function of the Reynolds number which varies with  $\phi$ .

between the two curves indicating that vortical structures appear at higher Reynolds number, if the Womersley number is increased. This is in agreement with pulsatile flow theory and was also observed by Grosse *et al.* [10] who found the critical Reynolds number  $Re_C$  for the creation of vortical structures to increase when the frequency of respiration is set to higher values. The level of vorticity in this distinct plane is higher at expiration than at inspiration which is in agreement with the observed intricate flow structures. At  $a_2$  the slope of the vorticity increases at a certain point during incremental inspiration which is highlighted in Fig. 12.

The temporal evolution of the flow field is analyzed in cross section IV at  $a_2$ . Figures 13 and 14 show the solutions for six phase angles at the very beginning of inhalation. The corresponding points

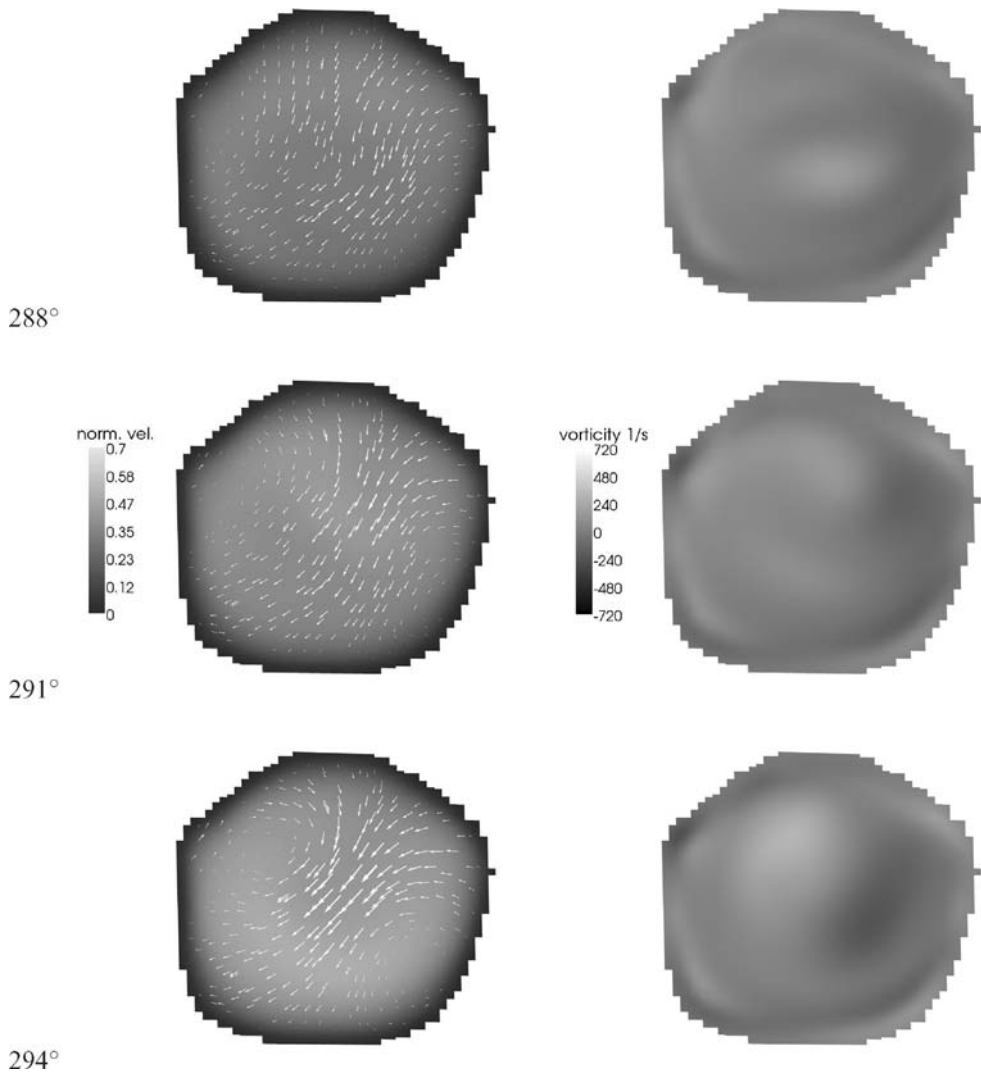


Figure 13: Distributions of velocity (left) and vorticity (right) in cross section IV in Fig. 6b at early inspiration for  $a_2 = 5.15$ . The arrows describe the in-plane velocity field and the levels of gray represent the magnitude of the axial velocity and the axial vorticity, respectively.



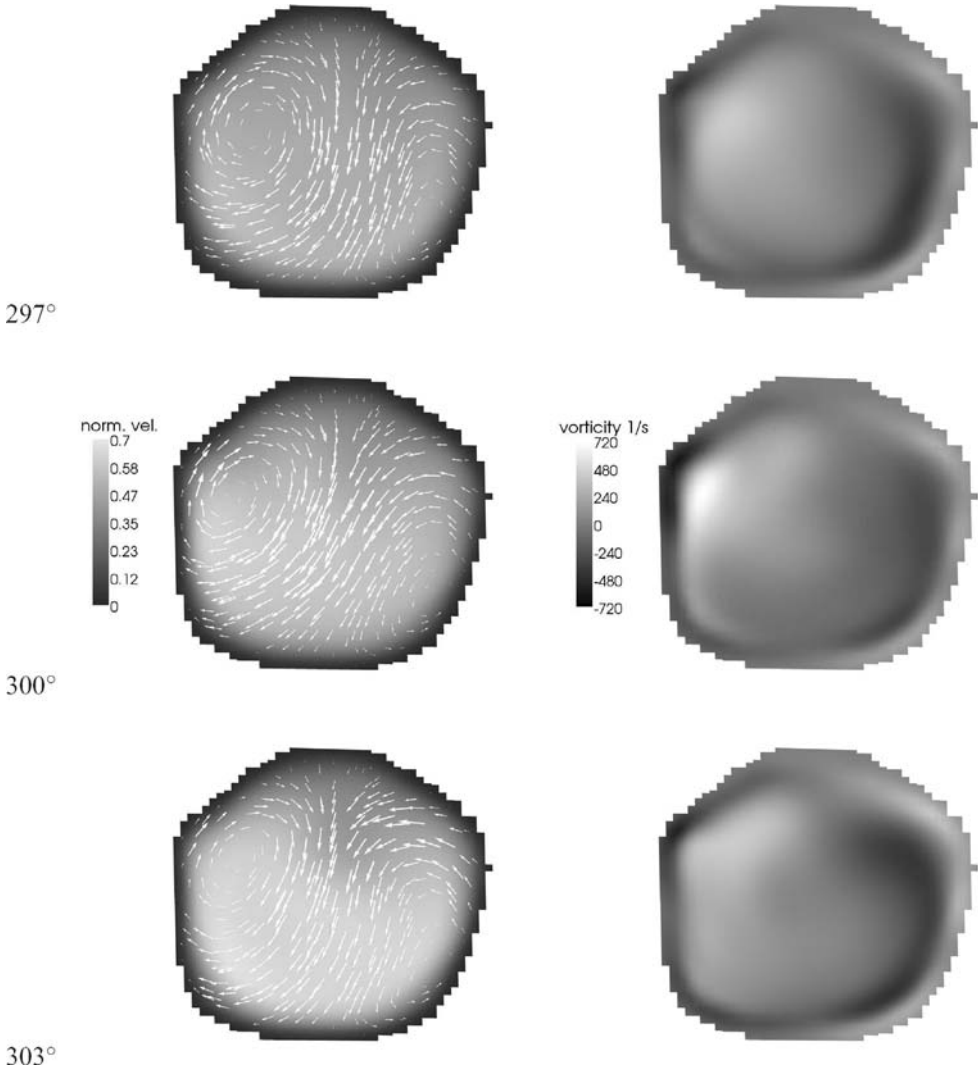


Figure 14: Distributions of velocity (left) and vorticity (right) in cross section IV in Fig. 6b at early inspiration for  $a_2 = 5.15$ . The arrows describe the in-plane velocity field and the gray scale values represent the magnitude of the axial velocity and the axial vorticity, respectively.

are highlighted in Fig. 12. The sequence starts 12.5 ms after the bulk velocity at the inlet cross section has reversed and covers 10.4 ms. At  $\phi = 288^\circ$  the distribution of the axial velocity shows a rather flat pattern and the vortical structures are still defined by those at maximum expiration, i.e. the clockwise rotating vortex is still there. At  $\phi = 297^\circ$  counter-rotating vortical structures form throughout the cross section and an incipient asymmetry of the axial velocity distribution is indicated, i.e. the location of the peak value occurs close to the lower wall. In the following time intervals the vorticity increases rapidly. Finally, the counter-rotating vortices and the axial velocity distribution at  $\phi = 303^\circ$  are already very similar to those observed at maximum inspiration. The increase of vorticity

at early inspiration is thus caused by the formation of the counter-rotating vortex pair. The same process also is detectable for  $a_1$ .

The numerical results show that the fundamental vortical structures and the high-speed region which have been observed at maximum inspiration are already encountered at  $Re_C(a_1) = 414$  and  $Re_C(a_2) = 651$ . This is in agreement with the experiment where the size of the counter-rotating vortices has been found to be independent of the Reynolds number as long as the Reynolds number is above a critical level.

## 7 SUMMARY AND CONCLUSIONS

The pulsatile flow field in a geometrically realistic model of the human lung was numerically and experimentally investigated for two Womersley numbers,  $a_1 = 3.64$  and  $a_2 = 5.15$ , and a maximum Reynolds number of  $Re_{\max} = 1,600$ . The Lattice–Boltzmann method proved to be an accurate tool to simulate flows through highly intricate geometries such as the upper human airways. The numerical findings were validated by particle-image velocimetry measurements. The overall flow structure at inspiration, which is characterized by local recirculation regions, and at expiration, which evidences a more homogeneous velocity distribution, was shown to be in convincing agreement. Secondary flow structures known from steady state simulations were clearly identified. A pair of counter-rotating vortices and a high-speed region were observed downstream of the first bifurcation in the left bronchus.

The growth of the vortical structures in the left branch of the first bifurcation was investigated in detail with respect to incipient inspiration. After reversal of the flow, the formation of secondary flow structures remains until the Reynolds number reaches a critical value. Above this value the overall flow structure remains qualitatively the same. The critical mass flux rate for the development of the characteristic flow structures was found to increase at higher Womersley numbers. At expiration the axial velocity distribution contains numerous secondary vortical flow structures being generated by merging streams of the higher generation bronchi. These vortical structures increase the kinetic energy near the wall and ensure an almost perfect cleaning stream at exhalation.

The results reflect the three-dimensional flow pattern inside the highly complex geometry of a real human lung. This knowledge is essential for the improvement of artificial respiration devices and for the development of aerosol drug delivery systems. In future investigations higher generations of the lung geometry and also the upper airways will be fully modeled including the nasal cavity and the laryngeal region.

## ACKNOWLEDGMENT

The support of the Deutsche Forschungsgemeinschaft (DFG) is gratefully acknowledged.

## REFERENCES

- [1] Zhao, Y. & Lieber, B.B., Steady expiratory flow in a model symmetric bifurcation. *Journal of Biomechanical Engineering*, **116**(3), pp. 318–323, 1994.
- [2] Comer, J.K., Kleinstreuer, C. & Kim, C.S., Flow structures and particle desposition patterns in double-bifurcation airway models. Part 1. Air flow fields. *Journal of Fluid Mechanisms*, **435**, pp. 25–54, 2001.
- [3] Liu, Y., So, R.M.C. & Zhang, C.H., Modelling the bifurcating flow in a human lung airway. *Journal of Biomechanics*, **35**(4), pp. 465–473, 2003.
- [4] van Ertbruggen, C., Hirsch, C. & Paiva, M., Anatomically based three-dimensional model of airways to simulate flow and particle transport using computational fluid dynamics. *Journal of applied physiology*, **98**, pp. 970–980, 2005.

- [5] Weibel, E., *Morphometry of the Human Lung*. Springer: Berlin, 1963.
- [6] Zhang, Z., Kleinstreuer, C. & Kim, C.S., Gas-solid two-phase flow in a triple bifurcation lung airway model. *International Journal of Multiphase Flow*, **28**(6), pp. 1021–1046, 2002.
- [7] Li, Z., Kleinstreuer, C. & Zhang, Z., Particle deposition in the human tracheobronchial airways due to transient inspiratory flow patterns. *Journal of Aerosol Science*, **38**(6), pp. 625–644, 2007.
- [8] Nowak, N., Kakade, P.P. & Annapragada, A.V., Computational fluid dynamics simulation of airfoil and aerosol deposition in human lungs. *Annals of Biomedical Engineering*, **31**, pp. 374–390, 2003.
- [9] Lin, C.L., Tawhai, M.H., McLennan, G. & Hoffman, E.A., Characteristics of the turbulent laryngeal jet and its effect on airflow in the human intra-thoracic airways. *Respiratory Physiology & Neurobiology*, **157**(2–36), pp. 295–309, 2007.
- [10] Große, S., Schröder, W., Klaas, M., Klöckner, A. & Roggenkamp, J., Time resolved analysis of steady and oscillating flow in the upper human airways. *Experiments in Fluids*, **42**, pp. 955–970, 2007.
- [11] Große, S., Schröder, W. & Klaas, M., Time-resolved PIV measurements of vortical structures in the upper human airways. *Particle Image Velocimetry*, volume 112/2008 of *Topics in Applied Physics*, Springer: Berlin/Heidelberg, pp. 35–53, 2008.
- [12] Succi, S., *The Lattice Boltzmann Equation for Fluid Dynamics and Beyond*. Oxford University Press: Oxford, 2001.
- [13] Ball, C.G., Uddin, M. & Pollard, A., Mean flow structures inside the human upper airway. *Flow, Turbulence and Combustion*, **81**, pp. 155–188, 2008.
- [14] Freitas, R.K. & Schröder, W., Numerical investigation of the three-dimensional flow in a human lung model. *Journal of Biomechanics*, **41**, pp. 2446–2457, 2008.
- [15] Hartmann, D., Meinke, M. & Schröder, W., An adaptive multilevel multigrid formulation for Cartesian hierarchical grid methods. *Computation Fluids*, **37**, pp. 1103–1125, 2008.
- [16] Truckenbrodt, E., *Fluidmechanik 1*. Springer-Verlag: Berlin, 1996.
- [17] Dean, W.R., Note on the motion of fluid in a curved pipe. *Philosophical Magazine*, **20**, pp. 208–23, 1927.
- [18] Dean, W.R., The streamline motion of fluid in a curved pipe. *Philosophical Magazine*, **30**, pp. 673–93, 1928.
- [19] Berger, S.A. & Talbot, L., Flow in curved pipes. *Annual Review of Fluid Mechanisms*, **15**, pp. 461–512, 1983.
- [20] Rütten, F., Schröder, W. & Meinke, M., Large-eddy simulation of low frequency oscillations of the Dean vortices in turbulent pipe bend flows. *Physics of Fluids*, **17**(035107), pp. 1–11, 2005.
- [21] Womersley, J.R., *An elastic tube theory of pulse transmission an oscillatory flow in mammalian arteries*. Technical report, Wright Air Development Center, 1957.
- [22] Frisch, U., Hasslacher, B. & Pomeau, Y., Lattice-gas automata for the Navier Stokes equation. *Physical Review Letters*, **56**(14), pp. 1505–1508, 1986.
- [23] Benzi, R., Succi, S. & Vergassola, M., The Lattice Boltzmann equation: theory and applications. *Physics Reports*, **222**(No. 3), pp. 145–197, 1992.
- [24] Chen, S. & Doolen, G.D., Lattice Boltzmann method for fluid flows. *Annual Review of Fluid Mechanisms*, **30**, pp. 329–364, 1998.
- [25] Bhatnagar, P.L., Gross, E.P. & Krook, M., A model for collision processes in gases. I. Small amplitude processes in charged and neutral one-component systems. *Physical Review*, **94**(3), pp. 511–525, 1954.

- [26] Hänel, D., *Molekulare Gasdynamik*, Springer: Berlin, 2004.
- [27] Qian, Y.H., D'Humieres, D. & Lallemand, P., Lattice BGK models for Navier–Stokes equations. *Europhysics Letters*, **17(6)**, pp. 479–484, 1992.
- [28] Zou, Q., Hou, S., Chen, S. & Doolen, G.D., An improved incompressible lattice Boltzmann model for time-independent flows. *Journal of Statistical Physics*, **81(1–2)**, pp. 35–48, 1995.
- [29] Bouzidi, M., Firdaouss, M. & Lallemand, P., Momentum transfer of a Boltzmann–Lattice fluid with boundaries. *Physics of Fluids*, **13(11)**, pp. 3452–3459, 2001.

*This page intentionally left blank*

# AN INNOVATIVE BRACE WITH PNEUMATIC THRUSTS FOR SCOLIOSIS TREATMENT

M.G. ANTONELLI<sup>1</sup>, P. BEOMONTE ZOBEL<sup>1</sup>, P. RAIMONDI<sup>1</sup>, T. RAPARELLI<sup>2</sup> & G. COSTANZO<sup>3</sup>

<sup>1</sup>Department of Mechanical Engineering, Energy and Management, University of L'Aquila, Italy.

<sup>2</sup>Department of Mechanics, Politecnico di Torino, Italy.

<sup>3</sup>Department of Orthopaedic Surgery, University of Rome "La Sapienza" Polo Pontino, Italy.

## ABSTRACT

Idiopathic scoliosis is the most common spinal deformity, and the brace treatment is the fundamental therapy. Brace works on the curve via the pressure they exert on the rib cage, usually on three points, to push against the progressive abnormal curvature of the spine and to reduce the local spasticity. Considering the possibility of the spine collapse, due to the six degrees of freedom of each vertebra with respect to the adjacent one, spine needs more thrusts relating to the curvature extension. This paper is focused on an innovative brace working by a three-dimensional thrusts system. The brace is internally covered by air pocket devices. Design and prototype of air pocket device is described. Air pockets apply the necessary corrective thrusts, at many levels of the spine, by compressed air at the specific pressure required in that area of the rib cage. Thrusts can be modified and checked. The design of the brace is presented together with a basic prototype, the design and the prototype of the air pocket device. First experimental tests on a simplified prototype of brace are also described. Finally, a pre-clinical test is performed by a healthy volunteer to validate the new brace concept.

*Keywords: brace design, FEM modelling, pneumatic pad, scoliosis brace.*

## 1 INTRODUCTION

Scoliosis is a spatial abnormal curvature of the spine: a lateral curvature on the frontal plane, a modification of the curves in the sagittal plane and a vertebral rotation in the horizontal plane [1]. The most common form is the idiopathic scoliosis. The incidence of it in the general population ranges from 0.2% to 0.3%, depending on the size of the curve, with a prevalence of 2–3% in school-aged children [2]. More is known about the natural history of curve progression in adolescent idiopathic scoliosis, which is dependent on the patient's skeletal maturity, the curve pattern and the curve magnitude [3]. On the contrary, the pathogenesis of it is still obscure. There are tentative aetiologies for idiopathic scoliosis, including, for example, differences in the growth rate of the anterior and posterior part of the spine. Recent evidences show that the disease has hereditary basis, supported by clinical manifestations as well as family studies that revealed the familiar tendency of idiopathic scoliosis [2]. The study of scoliosis has ancient origins. The deformity was firstly described by Hippocrates, around 400 BC; the diagnosis, the causes and, above all, the treatments have been the focus of a great deal of research. Hippocrates tried to reduce the scoliosis curvature using a table, to which the patient was tied, and a person who hopped on him pushing the spine. In the following centuries many scientists (Galeno, Parrè, Delpech and others) were engaged in finding a therapeutic method for scoliosis: the application of a mechanical pushing to convex parts of the spine, the extension of the spine by a traction force or by the weight of the patient. But only in the 1840 starts the activity of orthopaedic medical centres in France specifically devoted to the correction of the scoliosis. In the following decades the scientists move from the traction fixed devices to different ideas of brace. The brace of Shanz-Milwaukee (1945) and the optimised version of Blount and Schmidt (1958) are the most significant ones of that period. Towards the end of the 20th century there was a growing interest in research activities on scoliosis and on the improvement of braces. The brace is used to prevent and to slow the curve progression, but the results are difficult to predict. Braces work on the curve via the pressure they exert on the rib cage, usually on three points, to push against the

progressive abnormal curvature of the spine and to reduce the local spasticity. The brace applies direct thrusts, as primary correction effect, and reaction thrusts, at the contact area between brace and thorax.

In Fig. 1, three different curvature of the scoliotic spine are shown. The figure depicts the principal thrust, black arrow, and the reaction thrusts, the white ones, that the brace applies to the spine. The reaction thrusts apply in the pelvic shell and in the top part of the brace. The principal and the reaction thrusts don't succeed to apply the load to whole of the spine but just on the apex of the curvature and on the pelvic and on the neck regions. To increase the surface of the rib cage where the thrusts are applied, so that the correction pushing is applied to a greater part of the spine, some pads are used.

Brace treatment for idiopathic scoliosis has good support in published studies of Negrini *et al.* [1] and Labelle *et al.* [4]. It is non-invasive and preserves growth, motion and function of the spine [3]. Braces can be divided in two categories: fixed and removable. The choice of the category depends on the age, on the spine conditions and on the prognosis of scoliosis. The latter one is based on some clinical data (hump, Cobb angle, torsional angle, age, etc.) and on its localisation and curve pattern. After this step, the clinician specialised in spinal diseases, on the basis of his experience, will choose the specific brace, if necessary and useful.

For idiopathic scoliosis, removable brace treatment is a fundamental therapy, on condition that brace is light, patient compliance, constructed by an orthotist specialised in the construction of the prescribed brace system. The use of removable braces is recommended in scoliosis curvatures with the Cobb angle between  $20 \pm 5^\circ$  and  $40 \pm 5^\circ$  [1], depending on the authors. In this case the therapy is most effective with a physical rehabilitation. The therapeutic rehabilitation is addressed for Cobb angle less than  $15 \pm 5^\circ$ , whereas the fixed brace and the surgical treatment is the therapy for the Cobb angle greater than  $40 \pm 5^\circ$ .

Many removable brace systems have been proposed and developed in different countries and many different types are on the market, often specialised for a specific curvature and for a specific correction of the spine. The Lyon brace, designed in France, is indicated for lumbar and for thoracolumbar curves; the Cheneau brace, also designed in France, has three different versions: for single lumbar curves, for lumbar curves and for thoracic curve with an apex at L4/T10; La Padula brace, designed in Italy, is indicated for the lower lumbar and thoracolumbar curves; the Boston brace,

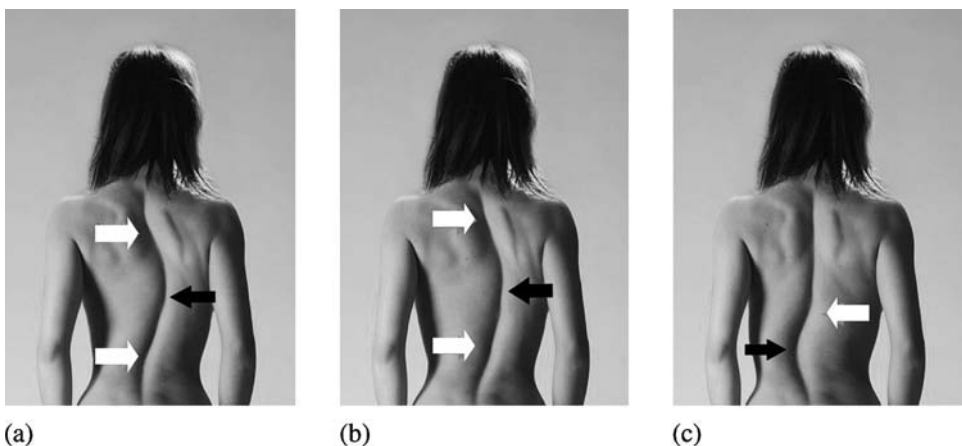


Figure 1: Example of thrusts application as some curvatures of the scoliotic spine: (a) thoracic, (b) thoracolumbar, and (c) lumbar.

designed in USA, is indicated for thoracolumbar curves. The Milwaukee brace, also designed in USA, is the most common one for the scoliosis treatment. It is used for thoracolumbar curves and for double curves. This brace uses two distinct principles: the three points thrust and the extension of the spine. The brace is linked to the pelvic region and has a top part to constraint the chin. The patient has to stay with the chin far from the constraint, and so a traction force is applied to the spine. To obtain this traction force, the Milwaukee brace has a pelvic shell modelled to reduce the lumbar lordosis. A lateral shell applies the main thrust.

This paper is focused on a new brace proposed for the scoliosis treatment. The presented brace is a suitable adapted Cheneau brace that relies on a three-dimensional thrusts system realised by air pocket devices, fixed inside it, to create an actuating shell around the entire rib cage. In each air pocket the air is inflated to a specific pressure value in order to apply the necessary corrective thrust in that specific area of the rib cage. The thrust can be modified and checked. In this way it is possible to apply different values of thrust at many levels of the spine so that the action on it can be more effective. The idea of the brace is presented together with a basic prototype, the design and the prototype of the air pocket device. Due to the behaviour of the material of the air pockets, a numerical model, implemented by a finite element code, was developed as a useful design tool for air pockets. The numerical model and its experimental validation are presented. First experimental tests on a simplified prototype of brace were performed. Finally, a pre-clinical test was performed by a healthy volunteer to validate the new brace concept.

## 2 NEW BRACE CONCEPT

The proposed brace is based on the ‘global thrust’, that is a three-dimensional thrusts system acting on the entire rib cage. The idea is to have thrusts at many levels of the spine, not only at three levels as with a traditional brace. This idea is supported by the consideration that the spine is formed by vertebrae and each of them has six degrees of freedom (dof) with respect to the adjacent one. These six dof have a limited movement range, but it exists the possibility of a collapse of the spine, where it has the maximum value of the instability, when the patient wears a brace with three thrusts, as shown in Fig. 2. It could happen because the spine is constrained only in correspondence of the thrusts point and in the lower and upper ends. The remaining unconstrained parts of the spine, due to the vertebrae dof, can be subdued to further uncontrolled curvature.

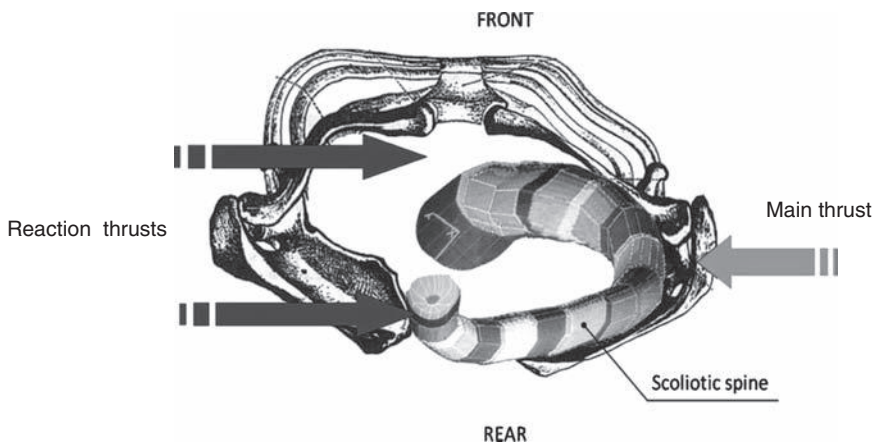


Figure 2: Scoliotic spine with main and reaction thrusts in a top view.



From the point of view of the authors, the spine can be considered as made by 24 cylindrical bodies: the vertebrae. The ends of each body articulate by pads of elastic or cartilaginous tissue with those of adjacent ones. This cylinder of 24 segments with a specific configuration, depending on the shape of the vertebrae, is linked to the rear part of the thorax, from the internal side, with a rotational joint, so that the spine can swing relative to the thorax, as represented in Fig. 3a. For this reason, the helical shape of the scoliotic spine has to be constrained inside a column of thrusts surrounding the entire spine. It means that the spine needs more thrusts relating to the extension of the curvature, as shown in Fig. 3b and c. This principle is as more true as more the extension of the curvature involves a high number of vertebrae: a scoliotic curvature extended for 10 vertebrae requires more thrusts than a curvature extended for only 5 vertebrae.

To provide the displacement, i.e. translation and rotation, of the spine in order to correct its curvature, the braces have to apply the thrusts on the rib cage. The greater is the surface where the thrust is applied the lesser is the possibility that the spine moves in unwanted directions. In the same time it has to be possible to control the intensity, the direction and the contact area of the thrusts. It is also important to consider that the intensity of the thrust has to be modified during the treatment, according to the modification of the spine curvature.

To satisfy the above mentioned requirements, the structural part of the new brace, the frame, could be as a traditional brace, except for the internal cover that is made by a shell of air pocket devices in compliant material, fixed on it and in contact with the whole rib cage. Each device is tuned individually, in order to obtain the wanted value of thrust, and each thrust has the possibility to be modified and checked.

The application of the brace should be as follows. At first the value of thrusts to be applied to the rib cage for reduction of the scoliotic curvature has to be settled; then the value of pressure necessary for each device, to obtain those thrusts system, has to be calculated for each point of the scoliotic curvature; finally each device has to be tuned at the specific value. In this way many thrusts are applied to the scoliotic curvature of the spine, one for each needing vertebra and composed by more radial components, except for the expanding part of the thorax.

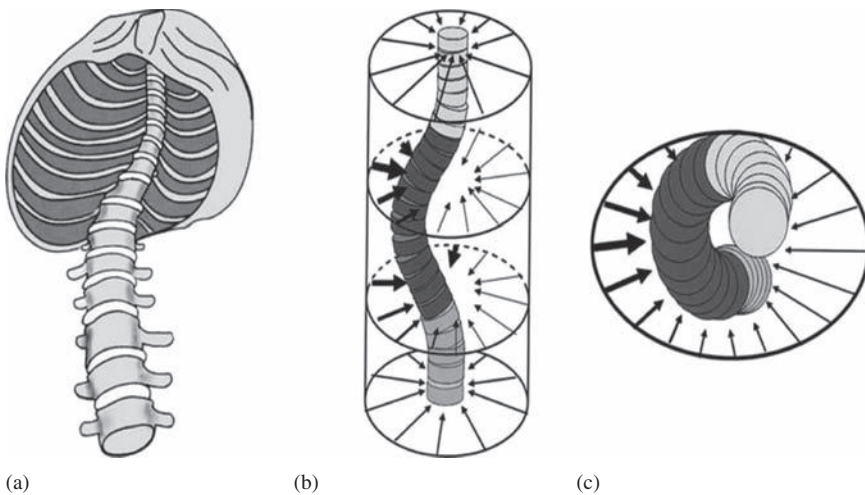


Figure 3: (a) Axonometric view of the scoliotic spine and the thorax; (b) axonometric view of the scoliotic spine model; (c) top view of the scoliotic spine model.

### 3 MATERIALS AND METHODS

The main objective of this research is the development of a suitable thrust device to put in practice the new brace concept. The measurement of thrusts in ordinary scoliotic braces is necessary as preliminary data. Based on these results, the technical specifications of the device were defined. Then it was possible to go on with the design and the prototyping. The design requires the development of a numerical model, implemented by a finite element code, also because the silicone and air compressed technology was used to construct the device. Finally the experimental tests were used to measure the performance of the thrust device, named 'air pocket device', as stand alone device and assembled in the new brace.

#### 3.1 Measurement of typical thrusts values

The knowledge of thrusts values in a scoliotic brace is necessary to design the air pocket device. For this goal some experimental tests have been scheduled with four scoliotic patients, selected from the clinician, to measure the contact pressure, and then the thrust, between the pad, normally used in Cheneau brace, and the rib cage. To know the thrusts value at the pad interface is useful for the idea of the new brace: air pocket device has to act as a classic pad, with the difference that it can be distributed all around the rib cage. All the patients selected have the same characteristic: a diagnosis of scoliosis and a therapy based on a three points Cheneau brace.

The measurement set up is made by a sensor matrix, a conditioning unit, all manufactured by Medizintechnik GmbH [5], a data acquisition board NIDAQ 6036E of National Instruments and a Personal Computer. The sensor matrix has a dimension of  $80 \times 85$  mm and a thickness of 2.3 mm. It is made by eight couples of pressure and temperature sensors, that are positioned in two rows, and each couple of pressure and temperature sensors are annealed in a gel cell to distribute the pressure on the sensor and to protect against the shock. Each couple of sensors appears as a single sensor and it has a dimension of  $11.5 \times 27.5$  mm. The maximum value of the pressure that each sensor can measure is 0.2 MPa with a maximum error of 5% (i.e.  $\pm 5$  kPa). Figure 4a shows the position of the eight sensors in the sensor matrix.

A simple protocol was defined to carry out these experimental tests. The protocol is as follows:

1. the clinician gives to the patient a complete information about the experimental test (goal, procedure, risk) and the patient accepts it signing a consensus agreement;
2. the patient wears the brace in the correct way;
3. the sensor is inserted in a disposable sterile small bag;
4. a data acquisition starts to check the sensor and to read the offset, i.e. the zero error of the instrument, before inserting the sensor;
5. the brace is removed from tension to insert the sensor between the thrust point and the rib cage. The positioning of the sensor is a delicate step because it is necessary to avoid the presence of wrinkles and the sensor has to remain finely in contact with the rib cage and the pad;
6. the brace is tensioned and the first data acquisition starts with the patient in erect position; a check on the acquired data is made, so that if something is wrong the test can be repeated;
7. a second acquisition starts with the patient in seated position; a check on the acquired data is made, so that if something is wrong the test can be repeated;
8. is it the first measurement point? If the answer is yes, go back to point 5 to go on with the second measurement point. If not, remove the brace from tension to recover the sensor: the test with the patient is completed.

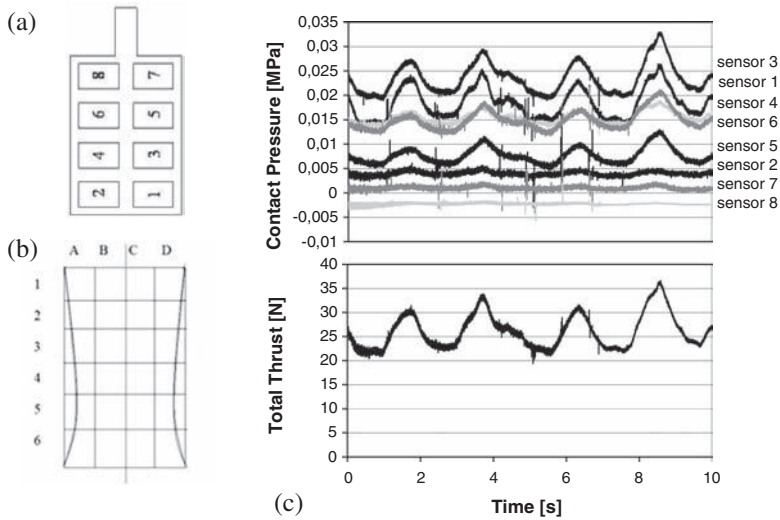


Figure 4: (a) Drawing of sensor matrix with sensors location; (b) grid of the back to locate the measurement points; (c) example of contact pressures measured by sensors and the respective total thrust.

All the signals are acquired at a sample frequency of 1 kHz for an amount of 10,000 acquired samples, i.e. 10 s as acquisition period. The total thrust  $F$  is calculated by eqn (1):

$$F = A \cdot \sum_{i=1}^8 p_i \quad (1)$$

where  $p_i$  is the pressure measured by the sensor  $i$  and  $A$  is the area ( $316 \text{ mm}^2 = 11.5 \times 27.5$ ) of each sensor. A grid of the back was used to locate the position of the measurement points for each patient, as shown in Fig. 4b. The measurement points of the patients, from 1 to 4, are respectively: 2C and 4B, 2C and 3B, 3C and 4A, 1B and 1C. In Fig. 4c, it is possible to see an example of the acquired pressure raw data, for each of the eight sensors, between the pad and the rib cage and the respective total thrust.

In Fig. 4c, data are oscillating because of the breathing: the change of the volume of the rib cage modifies the contact pressure and the thrusts. The maximum measured thrust value is 37 N (patient no. 1 in seated position, point 2C). In all the tests the maximum pressure value is measured in seated position. This is due to the kyphotic position of the upper back in many people when seated. Some measurements have shown very low level of pressure, less than 4 N. Probably in this cases a contact–no contact situation occurs at the interface pad rib cage.

### 3.2 Air pocket device

Following the measurement of the thrusts and considering the goal of the brace, the technical specifications of the air pocket device are defined. Specifically the device has:

- to exert a maximum level of force bigger than 40 N, on a area of about  $80 \times 80 \text{ mm}^2$ ;
- to be adjustable in order to modify the thrust force during the brace therapy;
- to use a suitable technology to fix the thrust at the desired value during the treatment period;

- to be provided with a suitable architecture in order to be integrated each other, so that a covering of devices inside the shell is possible, to apply the thrusts where they need;
- to produce a soft contact with the rib cage, for the maximum comfort of the brace.

To satisfy the technical specifications, a thrust device constructed in silicone material that can be inflated by air was conceived. A squared shape was chosen in order to integrate the air pocket devices inside the shell; silicon rubber (Silastic 3481 of Dow Corning) was chosen for its softness and its compatibility with the skin. The air pocket device was thought to be made by a chamber, constructed by two layers of silicon rubber linked each other on the edge, that can be pressurised. A hole has to be used to inlet and outlet the air from the pocket. Pressurising the air inside the pocket, the volume grows as a balloon, so that a thrust is obtained by the contact with the rib cage opposing to the volume of expansion. The air pocket device shows a strongly nonlinear behaviour by which output force depends on both the pressure inside the pocket and its volume. It is due to large strains to which it is subjected and to the constitutive material: silicon rubber, as all elastomeric materials, has a nonlinear  $\sigma$ - $\epsilon$  relationship. For this reason, before designing the air pocket device, it was useful to define a numerical model as a design tool able to predict the behaviour of air pockets. The principal aim was to study the relationship among the main design parameters of the air pocket and its performances: in particular, thrusts exerted by the air pocket as regards pressure values inside the chamber and chamber deformations.

The numerical model was implemented by a finite element model, developed by ANSYS code. It is a three-dimensional and parametric model. To reduce the number of nodes and then the computing time, the finite element model performs a quarter of air pocket, because of its geometry is twice symmetric. For the same reason, the lower layer of the air pocket was modelled with a rigid material, to study only the behaviour of the upper one.

Three different kinds of elements, chosen from ANSYS library [6], were used in the model: SOLID45 elements to model the rigid material inside the lower layer; LINK8 elements used as sensors to measure the exerted thrusts or as constrains of the maximum admitted displacement values; HYPER86 elements to model the silicone rubber. Due to the nonlinear behaviour of the silicone rubber, a nonlinear analysis by Newton–Raphson method was performed. The two coefficients Mooney–Rivlin formulation was applied to HYPER86 elements.

Two different models were implemented: one for the isometric test modelling and one for the isotonic test modelling. In the isometric test, consisting in constant deformation experiments, the force versus pressure inside the chamber is computed; in the isotonic test, consisting in constant force experiments, the displacement of the upper layer versus pressure is computed. In the isometric test modelling, input parameters, besides geometric ones, are pressure value and maximum admitted displacement value; in the isotonic test modelling, pressure value and force acting on the upper layer. Figure 5a and b show respectively the isotonic test model and the isometric one as an output of the calculation.

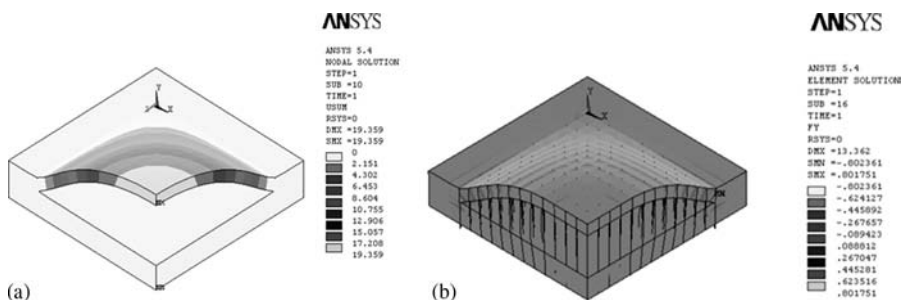


Figure 5: (a) Isotonic test model and (b) isometric test model.

An experimental prototype of the air pocket device was constructed with the same values of geometrical parameter of the numerical model to carry out an experimental validation.

The geometrical parameters are as follows:

- external edge dimension (squared shape): 120 mm;
- chamber edge dimension (squared shape): 96 mm;
- thickness of the lower layer (rigid material included): 7 mm;
- thickness of the upper layer: 4 mm.

In Fig. 6, the experimental prototype is shown. The manufacturing process was defined and tested and a simple technological set up was developed. The experimental validation of the numerical model was performed by means of isometric and isotonic tests of the experimental prototype. The design and the construction of a simple test bed were necessary to perform these tests. In isometric test, constrains are made by two simple metal plates. The deformation is fixed at different values by a simple screw–nut system that links the two plates. The deformation is measured by a measuring rod and a load cell on the screw is used for the traction force. A manometer measures the air pressure in the air pocket, modified by a pressure regulator, and a portable tensionmeter gives the tension value of the load cell to calculate the traction force. For isotonic test, the prototype is placed on two little plastic blocks. The constant load is obtained by a gravitational mass located on the upper layer of the prototype. In Fig. 7, isometric and isotonic test beds are shown.

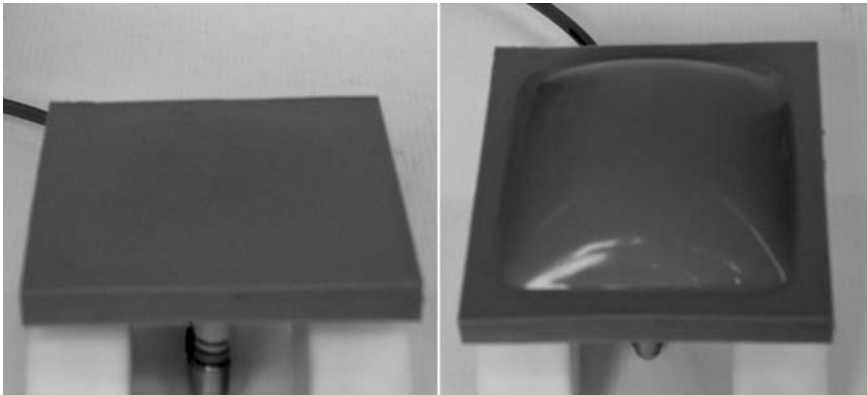


Figure 6: Experimental prototype for numerical model validation.

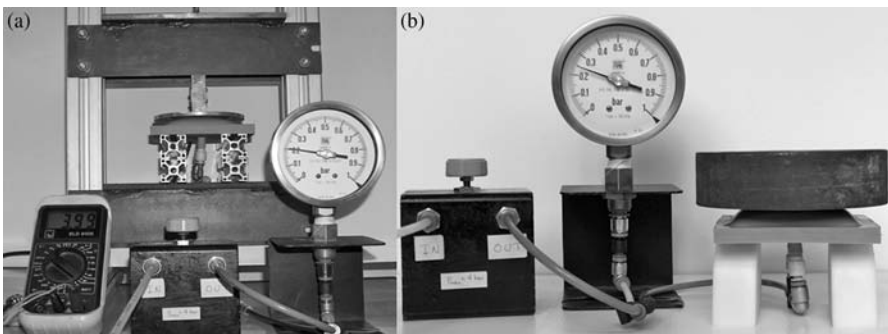


Figure 7: (a) Isometric test bed and (b) isotonic test bed.

Results obtained from the numerical model and the experimental prototype, in the same test conditions, are strictly correlated. The behaviour of the numerical model is close to the experimental prototype. From the comparison of the obtained results, as shown in Fig. 8, the maximum error registered in isometric test is about 10% and the maximum error in isotonic test is about 14%. During both these tests, the prototype showed a hysteretic behaviour: two separate curves are obtained increasing the pressure inside the pocket from zero to the target value and then decreasing to zero. This phenomenon is already described in literature for elastomeric materials [7], and the cause of hysteresis seems to be the viscoelastic phenomenon. Considering the limited error margin and the hysteretic behaviour, the numerical model is considered reliable.

Several simulations were performed by the numerical model in order to optimise the design of the air pocket device of the new brace. Finally the best set of geometrical parameters fitting the technical specifications was the following: external edge dimension (squared shape) = 100 mm, chamber edge dimension (squared shape) = 80 mm, thickness of the lower layer = 4 mm, thickness of the upper layer = 4 mm. Ten air pocket devices were manufactured to be used for the brace, using the same technological set up. A leak free valve was used for the inlet and the outlet of the air, so that the chosen value of pressure is used for the brace treatment. The leak free valve is also used to fasten the device to the brace by screwing a nut onto it. New experimental tests were scheduled with these prototypes.

A first set of experimental tests was performed to measure the maximum force applied by the air pocket device and the maximum test pressure. They were measured respectively as 100 N and 0.065 MPa. A second set of experimental tests was performed to check air leaks mainly at the interface between the air pocket and the valve. Two kinds of test were scheduled. In both, air pockets were inflated at 0.05 MPa checking the pressure for 48 h. A first simple test was performed putting the air pocket under water and checking the birth of air bubbles. A second test was performed loading each air pocket with a weight of 98.1 N. No air pocket devices showed air leak. A third set of experimental tests was performed to measure the burst pressure. Two kinds of test were scheduled. In both, air was inflated until burst occurred. A first test was performed at null deformation, constraining each air pocket between two rigid plates. The burst pressure was around 1 MPa. A second test was performed in free deformation condition. Some problems arose in doing this test, because of the nut for fixing the valve to the air pocket. When the volume of the air pocket device grows the fixing hole of the valve becomes larger. For this reason the valve was ejected at a pressure value of about 0.055 MPa. In the internal side of the brace the maximum deformation at design level is less than 10 mm. At this value the burst pressure is higher than 0.4 MPa, so that the maximum operative pressure is settled at 0.065 MPa. Finally isometric and isotonic tests were performed in order to obtain the control chart of the air pocket devices. The same previously described test beds were used. The isometric tests were performed by regulating the displacement from 0 to 40 mm.

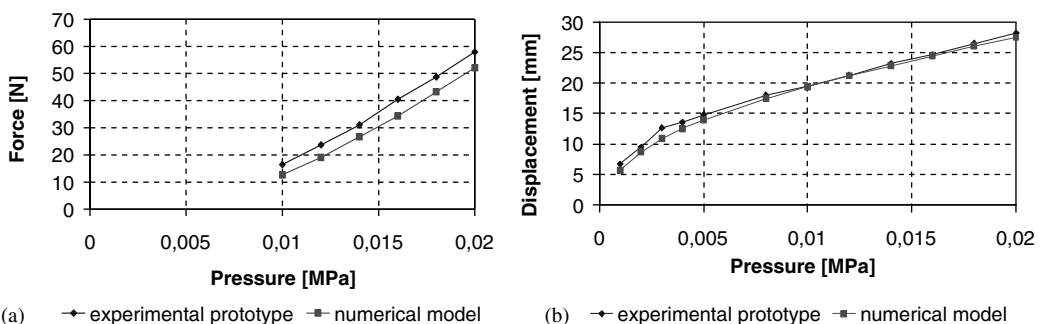


Figure 8: Comparison between experimental and numerical results in: (a) isometric tests and (b) isotonic tests.

The isotonic tests were performed until the pressure value of 0.6 bar is reached for five loads: from 9.8 N to 98 N. The hysteretic behaviour was neglected and the curves were constructed calculating the medium values. In Fig. 9, the results of isometric and isotonic tests are shown.

### 3.3 New brace prototype

A first prototype of the brace is manufactured in order to check the behaviour of the brace assembled with some air pocket devices. The construction of the shell was obtained by a traditional CAM (computer aided manufacturing) system normally used for the base frame of other braces, as Cheneau. The shell was modelled on the trunk of a healthy volunteer, inserting an offset, i.e. a backlash, of about 10 mm on the upper part. This offset was necessary because of the thickness of the air pocket (8 mm). A grid of holes was performed on the rear side of the shell, with a correct arrangement to assemble the air pocket devices by valve and nut from the internal side. Two air pocket prototypes were used for this first experimental test. Wearing the brace, made by the shell and the two air pockets, one close to the other, the impression was of too large size, with the devices in a contact–no contact condition with the thorax.

The measurement made by the sensors matrix confirmed this condition. For this reason a covering was necessary to have a uniform thickness in the internal side of the shell. This problem is due to the use of only two air pockets, but it will disappear with the construction of the complete prototype that needs something like 30 air pocket devices. A layer of material, similar to that used for the pad, with a thickness of about 5 mm was used. It was glued on the internal side of the shell, except where the two air pockets were assembled. After this modification the volunteer had good sensation wearing the brace, with a normal contact between thorax and brace (Fig. 10a). The measurements confirmed this good behaviour of the brace, giving values of the thrust less than 0.5 N. After this step the first experimental tests on the brace started to measure the thrusts due to a single air pocket. The test was carried out in two different position of the air pocket, approximately 3B and 4B, see Fig. 4b, increasing the pressure value from 0 to 0.065 MPa. The measured thrusts, by the sensors matrix, in the two different positions of the device versus the air pressure are very similar, with a maximum value of 25 N at 0.065 MPa. The graph that shows the thrust of one air pocket versus the air pressure is given in Fig. 10b.

The result shows that the maximum value of thrust doesn't meet the design value of 40 N, but it is important that the shape of the graph is not so far from a line. The deficit in the maximum value of the thrust that the device can apply means that a rectangle of four air pockets,  $200 \times 200 \text{ mm}^2$ , can apply a maximum thrust of 100 N, instead of 160 N. That's mean that this new brace could be really interesting considering that the complete brace has a covering of air pockets in the internal side.

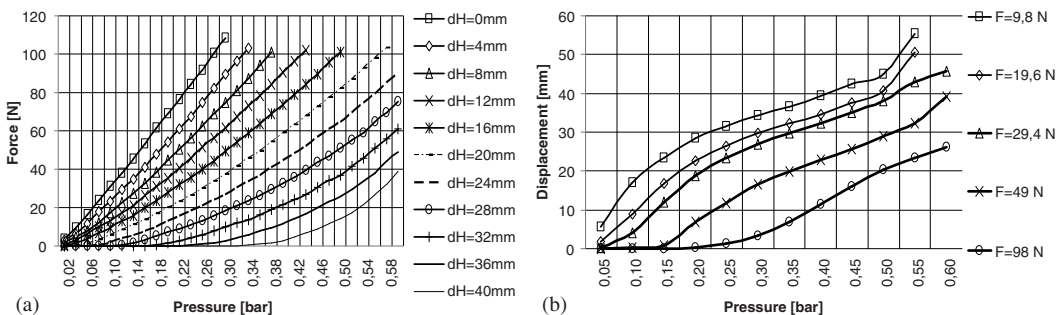


Figure 9: (a) Isometric tests and (b) isotonic tests for the air pocket device.

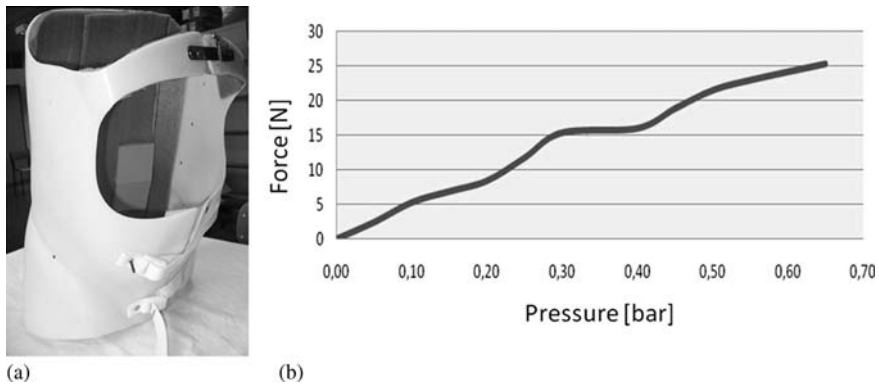


Figure 10: (a) First prototype of the brace and (b) thrust applied by one air pocket device.

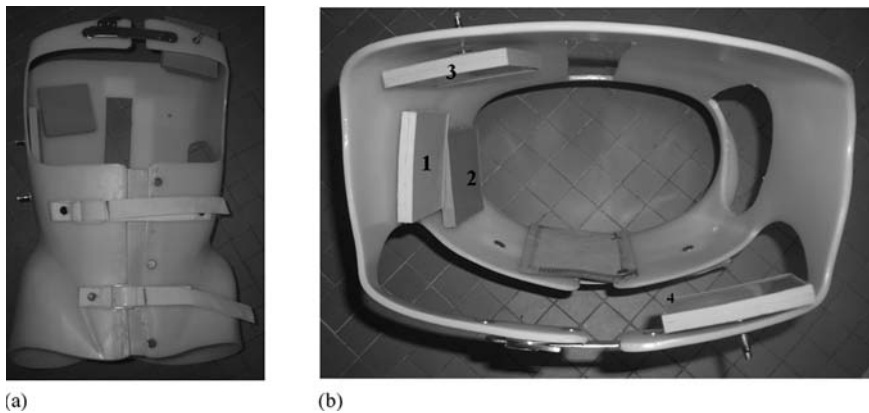


Figure 11: (a) Frontal view of the second prototype and (b) top view and locations of the air pocket devices.

#### 4 PRE-CLINICAL EVALUATION OF THE BRACE

The goal of these experimental tests was to validate the effectiveness of the new brace concept: the three-dimensional thrusts system, based on air pocket devices, is able to cause the curvature of the spine? To obtain an answer to these questions the experimental activity was settled to measure the curvature of the spine. The experimental activity was carried out on a female healthy volunteer, aged 26 years and with no history of spine disease, after signing an informed consent form.

A second brace prototype was used. It was modelled on the volunteer and it was manufactured in the same previously described manner. In order to provide an able to be seen spine curvature, thrusts were applied on the spine sector between vertebrae T5 and T12. The frame of the brace was modified as follows (Fig. 11). An opening was made in the back part to uncover the vertebrae from T6 to L3; a matrix of holes was made on the frame of the brace to allow the air pockets positioning; a triangular shape area of the frame was removed in the left side to allow the rib cage displacements in the opposite part of thrusts application area. Four air pockets were used. The thrusts system was obtained positioning the air pocket devices as shown in Fig. 11b: two air pockets, (1) and (2), in the



right side of the brace covering the spine sector between vertebrae T8 and T12; an air pocket (3) in the back side of the brace, at the level of T6; an air pocket (4) in the front side of the brace, at the level of T5.

To measure the curvature of the spine, a vision system, based on a good quality commercial digital camera with a resolution of 4 megapixels, was used. The photos are captured on the back side of the brace and optical markers are used to measure the spine displacement in both frontal and sagittal plane, as starting idea. The first kind of marker, used to measure displacements in the frontal plane, was made of a black disk with a diameter equal to 12 mm. The disks were directly placed on the spinous processes by glue. The second kind of marker, to be used for displacement measurement in the sagittal plane, was made of a black disk, with a diameter equal to 12 mm, a pin, 30 mm long, and a second white disk with a diameter equal to 9 mm. One end of the pin was linked to the centre of the first disk; the other was linked to the centre of the second one, so as to be perpendicular to both disks. First disk should be directly placed on the spinous processes by glue. Unfortunately the displacement of the spine caused instability of the second kind of markers, providing false and incongruous displacements of them. For this reason, the measurements were performed only in the frontal plane.

Three load conditions were subsequently applied to the rib cage: the first load condition (FLC) applies thrusts by air pocket 1 and 2 at the same time; the second load condition (SLC) is made of the previous one and of the thrust applied by air pocket 3; the third load condition (TLC) is made of the previous one and of the thrust applied by air pocket 4. The air pressure is the same for all the air pocket devices, 0.05 MPa. This pressure is very close to the maximum value, so that the effect on the spine is big and it is easier to detect the displacement.

Markers were placed on the spinous process of vertebrae from T6 to L3, for a total amount of 10 markers. For each load condition, besides rest condition (RC), a picture of the back of the brace was captured. The analysis of spine displacements was performed by means of an image analysis of markers positions in the different load conditions. A line was drawn between the centres of two consecutive markers, for a total amount of nine lines, as shown in Fig. 12. In each load condition, inclinations of lines were measured. A comparison among inclinations of each line was performed through load conditions in order to study the evolution of the spine curvature.

Hence, line's inclination, with respect to the vertical direction, at RC, at FLC, at SLC and at TLC were measured and also inclination between RC and FLC,  $\delta_1$ , between FLC and SLC,  $\delta_2$ , between

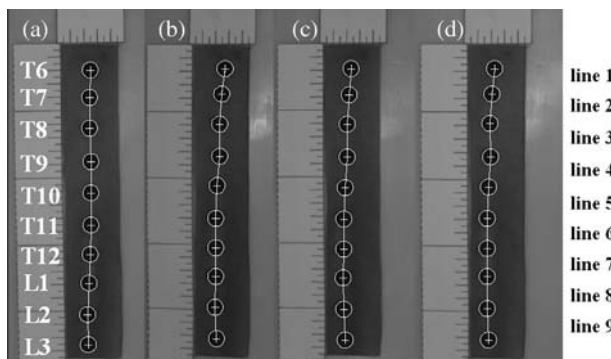


Figure 12: Marker positions at (a) rest condition, (b) first load condition, (c) second load condition, and (d) third load condition.

SLC and TLC,  $\delta_3$ , and between RC and TLC,  $\delta_{\text{tot}}$ , as reported in Table 1. Line's inclinations were measured according to the vertical line of the ruler fixed to the brace (Fig. 12). In order to reach the vertical position, positive angle value means a rotation of the line in clockwise direction; negative angle value means a rotation in anticlockwise direction. Positive angle value, between two lines, means a clockwise rotation of the 2<sup>nd</sup> line with respect to the 1<sup>st</sup> one; negative angle value means an anticlockwise rotation.

FLC produces a curvature in which the upper sector of the spine (from T11 to T6) has a positive rotation and the lower one (from T12 to L3) a negative rotation. Bigger rotations are registered at the ends of the interested sector of spine. This result is coherent with the thrust system applied. It can be compared to a distributed load on a double fixed beam whose effect is a displacement of the beam in the direction of the load. The same total behaviour is registered in TLC. The effects of SLC and TLC are less evident, probably because their actions involve displacements in the sagittal plane. Nevertheless, the almost absence of rotations in the sector between vertebrae T7 and L1 (from line 2 until line 7) suggests a torsion of the spine in the upper zone. In fact, the only significant rotations are registered in correspondence of line 1, both in SLC and in TLC, at the level of which thrusts were applied. FLC provided a maximum displacement of the spine, towards the left zone of the back window, equal to 5 mm; SLC equal to 7.5 mm; TLC equal to 9 mm. Taking into account the congruent correlation between thrusts and spine displacements, it follows that the applied thrusts system is able to produce a displacement of the spine.

## 5 CONCLUSIONS

This paper deals about an innovative brace for scoliosis treatment. The idea is to apply the thrust in more than three points, as is usual in many braces. The brace here proposed is based on the 'global thrust', that is a three-dimensional thrusts system acting on the entire rib cage at many levels of the spine.

The frame of the new brace is made with plastic shell and an internally fixed covering of air pocket devices. Each air pocket is made of silicon rubber and the internal air pressure can be regulated and checked. Starting from the measurement of typical thrust values in commercial braces, air pocket devices are designed and then manufactured. In order to optimise the air pocket device design and because of the constitutive law of the silicon rubber, a numerical model, implemented by a finite element code, is developed and then validated. Air pocket device is subjected to several tests to be

Table 1: Lines' inclination measured in the frontal plane.

Line no.	Slope at RC	Slope at FLC	Slope at SLC	Slope at TLC	$\delta_1$	$\delta_2$	$\delta_3$	$\delta_{\text{tot}}$
1	+1°	+8°	+4°	+6°	+7°	-4°	+2°	+5°
2	0°	+4°	+4°	+4°	+4°	0°	0°	+4°
3	-2°	0°	0°	-1°	+2°	0°	-1°	+1°
4	0°	+5°	+4°	+4°	+5°	-1°	0°	+4°
5	0°	+2°	+2°	+2°	+2°	0°	0°	+2°
6	+1°	0°	0°	0°	-1°	0°	0°	-1°
7	+3°	0°	+1°	0°	-3°	+1°	-1°	-3°
8	+2°	+1°	-1°	0°	-1°	-2°	+1°	-2°
9	+1°	-2°	-2°	-2°	-3°	0°	0°	-3°

characterised in terms of maximum output force, maximum operative air pressure, air leaks, and maximum burst pressure. Finally, isometric and isotonic tests are performed to define a control chart of air pocket devices based on the relationship of pressure, force and displacement values. The final experimental activity, on a healthy volunteer, shows that a thrusts system made by air pocket devices is able to obtain spine displacements. The encouraging results say that the new brace concept can be an alternative to the actual scoliosis braces. The work is in progress and the next step will be a clinical validation on ill subjects by a complete prototype.

#### ACKNOWLEDGEMENTS

The authors are thankful to Miss Silvia Sparvieri, as well as to Ortopedia Picena of Guiducci Quirino, Ascoli Piceno, Italy, for their kind support. A special thanks to Novatec Spinoff s.r.l. for its support to this research.

#### REFERENCES

- [1] Negrini, S., Aulisa, L., Ferraro, C., Fraschini, P., Masiero, S., Simonazzi, P., Tedeschi, C. & Venturin, A., Italian guidelines on rehabilitation treatment of adolescents with scoliosis or other spinal deformities. *Eura Medicophys*, **41**, pp. 183–201, 2005.
- [2] Shangguan, L., Fan, X. & Ming, L.I., Inherence involved in the pathogenesis of idiopathic scoliosis. *EXCLI Journal*, **7**, pp. 104–114, 2008.
- [3] Guille, J.T., D'Andrea, L.P. & Betz, R.R., Fusionless treatment of scoliosis. *Orthopedic Clinics of North America*, **38**, pp. 541–545, 2007.
- [4] Labelle, H., Dansereau, J., Bellefleur, C. & Poitras, B., Three-dimensional effect of the Boston brace on the thoracic spine and rib cage. *Spine*, **21(1)**, pp. 59–64, 1996.
- [5] Bignardi, C., Bondente, P.G. & Rosso, V., Non invasive measurement of body jacket pressures in scoliosis. *XIV International INTERBOR World Congress*, Boston, USA, July 14–17th, p. 31, 1999.
- [6] *ANSYS Theoretical Manual*, Swanson Analysis System Inc.: Houston, 1989.
- [7] Ferry, J.D., *Viscoelastic Properties of Polymers*, John Wiley & Sons, Inc.: New York, 1980.

# THE HUMAN LUMBAR VERTEBRAL BODY AS AN INTRINSIC, FUNCTIONALLY OPTIMAL STRUCTURE

D.N. GHISTA<sup>1</sup>, S.C. FAN<sup>2</sup>, K. RAMAKRISHNA<sup>3</sup> & I. SRIDHAR<sup>3</sup>

<sup>1</sup>School of Chemical and Biomedical Engineering, Nanyang Technological University, Singapore.

<sup>2</sup>School of Civil and Environmental Engineering, Nanyang Technological University, Singapore.

<sup>3</sup>School of Mechanical and Aerospace Engineering, Nanyang Technological University, Singapore.

## ABSTRACT

In the vertebral body (VB), the load carrying and transmitting function is primarily performed by the cortical VB. Hence, we have modelled the cortical VB as a hyperboloid shell whose geometry and composition are made up of its generators. This paper analyses the forces in the VB generators due to compression, bending and torsional loadings. The unique feature of the hyperboloid geometry is that all the loadings are transmitted as axial forces in the generators. This makes the VB a high-strength structure. Furthermore, because the cortical VB material is primarily made up of its generators (through which all the loadings are transmitted axially), it also makes the VB an intrinsically lightweight structure. We then analyse for the optimal hyperboloid shape and geometry by minimizing the sum of the forces in the hyperboloid VB generators with respect to the hyperboloid shape parameter (angle  $\beta$  between pairs of generators). The value of  $\beta$  is determined to be  $26.5^\circ$ , which closely matches with the *in vivo* geometry of the VB based on its magnetic resonance imaging scan. In other words, for the hyperboloid shape parameter  $\beta = 26.5^\circ$ , the VB generators' forces are minimal so as to enable it to bear maximal amounts of loadings. In this way, we have demonstrated that the VB is an intrinsically, functionally optimal structure.

*Keywords:* axial force, bending, torque, generators, hyperboloid, optimal structure, shape parameter, stress analysis, uniaxial compression, vertebral body.

## 1 INTRODUCTION

The skeletal system is important to the body both mechanically and metabolically. The bone is the main constituent of the skeletal system and differs from the connective tissues in rigidity and strength. The rigidity and strength of the bone enable the skeleton to maintain the shape of the body, to protect the soft tissues and organs, to supply the framework for the bone marrow, and to transmit the force of muscular contraction from one part of the body to another during movement. The mineral content of the bone serves as a reservoir for ions, particularly calcium, and also contributes to the regulation of extracellular fluid composition, particularly ionized calcium concentration. In addition, the bone is a self-repairing structural material that is able to adapt its mass, shape and properties to change in mechanical requirements and endures voluntary physical activity for life without breaking or causing pain.

As per the concept of optimal design in nature [1, 2], anatomical structures are also customized to be functionally optimal. If it is a load-bearing structure, then it is adroitly designed to be a lightweight and high-strength structure. For example, a long bone is modelled such that it can sustain maximum loading with least material. Consider the case of the femur. Its shape and material density correspond to its stress trajectories under its functional loading (see Fig. 1) as per Wolff's law [3]. In other words, there needs to be less density of bone where the stress trajectories are apart (such as in the trabecular bone) and more density of bone where the stress trajectories are closer (as in the cortical bone).

### 1.1 Optimal dimensions of the femur cortical bone

Now, let us examine the diaphysial part of a long bone (e.g. the femur) that carries most of the bending stress. Using the Euler–Bernoulli flexural equation, the normalized bending strength (BS)

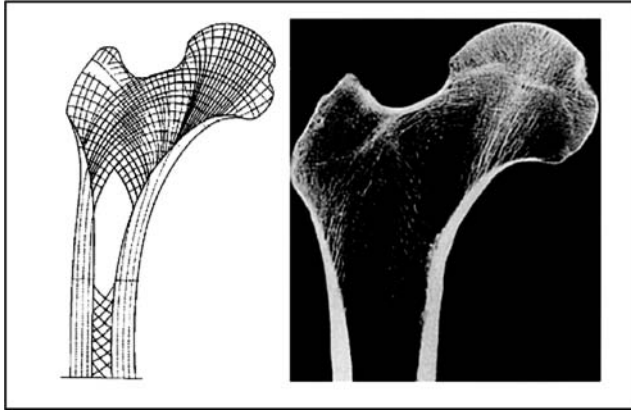


Figure 1: Wolff's drawing of the trabecular orientation in the proximal part of the femur and the cross section of the femur. It can be noted that the bone material distribution corresponds to the orientation of the stress trajectories [3].

can be defined as

$$BS \equiv \frac{4M}{\pi\sigma_b r_e^3} = 1 - \left(\frac{r_i}{r_e}\right)^4, \quad (1)$$

where  $M$  is the moment on the bone,  $\sigma_b$  is the maximum stress on the bone induced due to  $M$ ,  $r_e$  is the external radius of the bone and  $r_i$  is the internal radius of the bone (considering the long bone to be a hollow cylinder). Here, normalization is carried out with respect to the moment carrying capacity of a long bone.

Moreover, the normalized weight factor (WF, i.e. normalized weight per unit length) of a long bone can be represented as

$$WF \equiv \frac{\pi(r_e^2 - r_i^2)}{\pi r_e^2} = 1 - \left(\frac{r_i}{r_e}\right)^2. \quad (2)$$

Maximizing the function  $(BS - WF)$  with respect to  $r_i/r_e$ , the optimal  $r_i/r_e$  is found to be  $1/\sqrt{2}$  ( $\approx 0.707$ ), at which the long bone has minimum weight and maximum bending strength; the corresponding area ratio (inner to outer cross-sectional area) is 0.5. Based on our measurements of femur diaphysial cross-sections, this area ratio is in the range  $0.5 \pm 0.2$ . This analysis shows that at  $r_i/r_e = 0.707$ , bone has maximum bending stiffness, torsional strength and stiffness for minimal weight.

## 1.2 The spinal vertebral body as an optimal structure

Let us now consider the spine. It protects the spinal cord, while allowing for a full range of motion of the trunk of the body. Spinal biomechanical efficacy is to a large extent based on the optimal intrinsic designs of the spinal vertebral body (VB) and the disc for load bearing. This makes it possible for all types of loadings to be effectively sustained by the VB. In this paper, we first carry out a stress analysis of how effectively the cortical VB can bear uniaxial compression, bending and torsional loads.

Then the relationship between the dimensions of the VB (based on physiological loading conditions) that makes it to be a functionally optimal (lightweight and high-strength) structure is analysed.

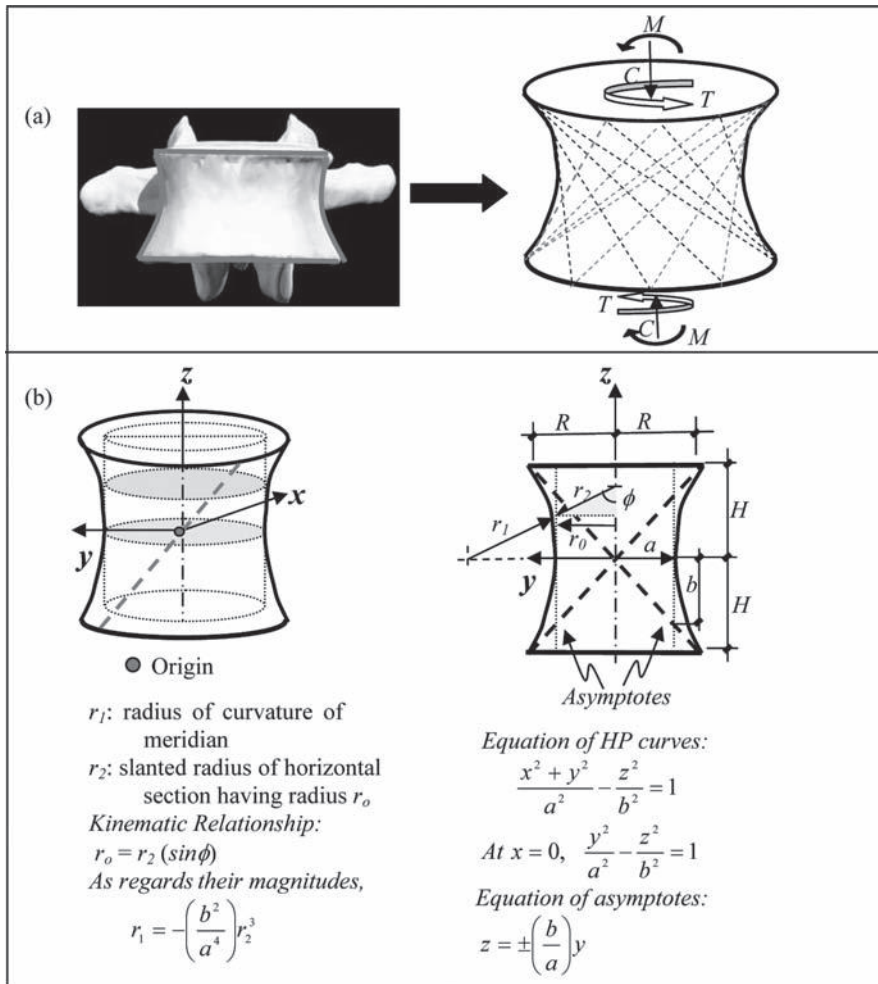


Figure 2: (a) The cortical VB is shaped as a hyperboloid (HP) shell formed of two sets of generators. The height of the HP can be expanded or reduced by the inclination of the generators. It also shows a typical VB. (b) The geometry of the HP shells [4, 5].

In other words, we will provide the relationship between the geometrical parameters of the VB that makes it an intrinsically optimal structure. Finally, the optimal design parameters obtained from the analysis are compared with published magnetic resonance imaging (MRI) scans of VBs.

## 2 VB SHAPE AND MEMBRANE STRESSES

### 2.1 Hyperboloid geometry of the VB

The hyperboloid geometry of the cortical VB is formed by two families of generators, as shown in Fig. 2a. Using shell membrane theory, we will analyse how this hyperboloid VB geometry

enables the VB to efficiently sustain: (i) compressive loading  $C$  on the VB, to cause axial compression in both sets of generators; (ii) bending moment  $M$ , to result in compressive forces in one set of generators (i.e. on the compression side of the neutral axis) and tensile forces in the other set of generators; (iii) torsional loading  $T$ , to result in compressive forces (per unit length) in one family of generators and tensile forces in the other family of generators oriented in the other direction.

Figure 2b illustrates the hyperboloid geometry of the spinal VB. If we intersect the hyperboloid shell surface with a vertical plane parallel to the  $yz$  plane but at  $x = -a$ , then the intersecting curves will be

$$\frac{a^2 + y^2}{a^2} - \frac{z^2}{b^2} = 1 \quad \text{or} \quad z = \pm \left( \frac{b}{a} \right) y, \quad (3)$$

which has the same slope as the asymptotes. Based on the hyperboloid geometry [4], the hyperboloid surface can be generated by a pair of intersecting lines inclined at an angle  $\beta = \tan^{-1}(a/b)$  in the vertical plane tangent to the waist circle ( $r_0 = a$ ).

The construction of the cortical VB hyperboloid by a set of generators [5] is illustrated in Fig. 3, wherein the end plate radius  $AN$  is  $R$ , the radius of the waist circle is  $a$  and the height of the VB is  $2H$ . Based on this, we define

$$\tan \beta = \frac{\sqrt{R^2 - a^2}}{H} = \frac{a}{b}. \quad (4)$$

The primary dimensional parameters of the VB hyperboloid are ( $R$ ,  $a$  and  $H$ ), and  $\tan \beta$  provides the relationship between them.

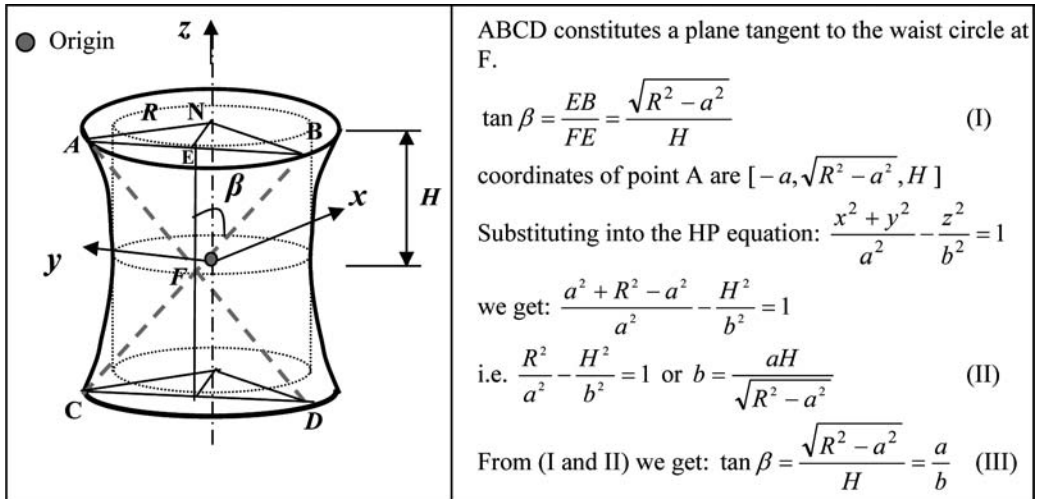


Figure 3: The geometry of hyperboloid generator: the generators AD and BC form the basis for the construction of the hyperboloid.

## 2.2 Membrane stresses in the VB cortex

We follow the membrane theory of shells to analyse the stresses in the cortical VB [6]. Membrane stresses  $\sigma_\phi$  (along the meridian) and  $\sigma_\theta$  (along the hoop) have a relationship with the normal pressure  $p_r$ , as depicted in Fig. 4. The equilibrium of forces in the radial ( $r$ ) direction gives

$$-2\sigma_\phi t(r_2 d\theta) \sin\left(\frac{d\phi}{2}\right) + 2\sigma_\theta t(r_1 d\phi) \sin\left(\frac{d\theta}{2}\right) + p_r \left[ 2r_1 \sin\left(\frac{d\phi}{2}\right) \cdot 2r_2 \sin\left(\frac{d\theta}{2}\right) \right] = 0, \quad (5)$$

wherein, in the case of a hyperboloid,  $r_2$  is considered to be positive and  $r_1$  is considered to be negative, and their magnitudes in terms of  $a$ ,  $b$  and  $\phi$  are

$$r_1 = \frac{a^2 b^2}{(a^2 \sin^2 \phi - b^2 \cos^2 \phi)^{3/2}}, \quad (6)$$

$$r_2 = \frac{a^2}{(a^2 \sin^2 \phi - b^2 \cos^2 \phi)^{1/2}}. \quad (7)$$

For small angles,  $\sin \theta \approx \theta$ , which leads eqn (5) to

$$-\sigma_\phi t r_2 (d\theta)(d\phi) + \sigma_\theta t r_1 (d\phi)(d\theta) = -p_r [r_1 (d\phi) \cdot r_2 (d\theta)]$$

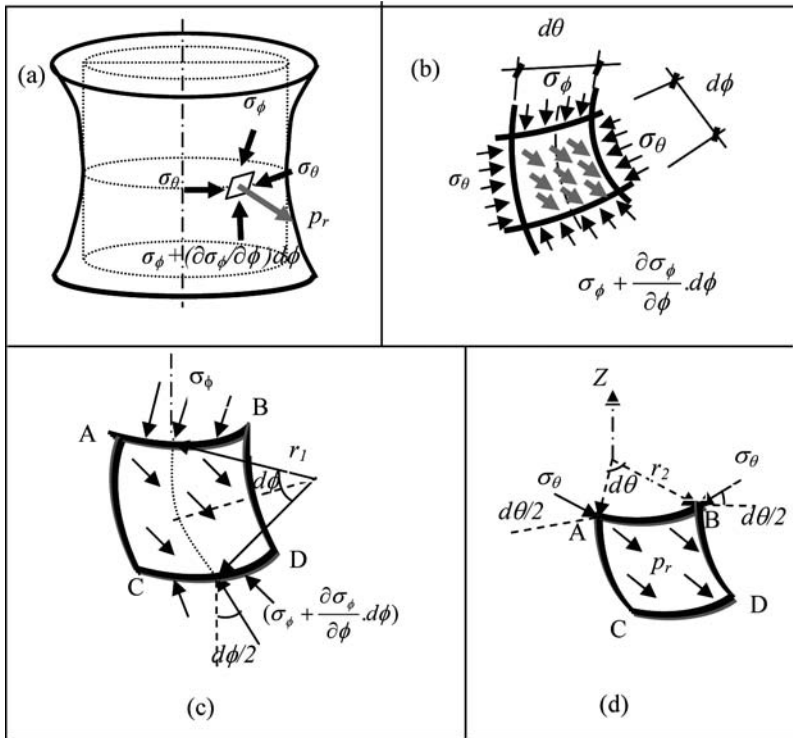


Figure 4: The stresses acting on an element of the hyperboloid shell.



or

$$\frac{\sigma_\phi t}{r_1} - \frac{\sigma_\theta t}{r_2} = p_r. \quad (8)$$

Denoting  $N_\phi = \sigma_\phi t$  and  $N_\theta = \sigma_\theta t$  as the stresses per unit wall thickness (or stress resultants), with  $t$  being the VB wall thickness, we obtain

$$\frac{N_\phi}{r_1} - \frac{N_\theta}{r_2} = p_r, \quad (9)$$

which is the *membrane equation* for the hyperboloid VB shell. This is because, for a hyperboloid shell,  $r_1$  is negative and  $r_2$  is positive. Now  $p_r$  is negligible due to the cancellous bone within the VB cortical shell. Hence, by substituting  $p_r = 0$  (i.e. for an internally non-pressurized cortical VB hyperboloid shell) in eqn (9), we obtain

$$N_\phi = \left( \frac{r_1}{r_2} \right) N_\theta. \quad (10)$$

Substituting  $r_1 = (b^2/a^4)r_2^3$  from Fig. 2 into eqn (10), we obtain

$$N_\phi = \left( \frac{b^2}{a^4} r_2^2 \right) N_\theta. \quad (11)$$

### 3 ANALYSIS OF FORCES IN THE VB GENERATORS UNDER DIFFERENT LOADINGS

#### 3.1 Stress analysis under axial compression

We will now analyse the stresses in the hyperboloid shell (generators) due to a uniaxial compressive force, as shown in Fig. 5. Assume that there are two sets of  $n$  number of straight bars, placed at an equal spacing of  $(2\pi a/n)$  measured at the waist circle, which constitute the hyperboloid surface as shown in Fig. 5b. Due to the axisymmetric nature of the vertical load, no shear stresses are incurred in the shell, i.e.  $\sigma_{\phi\theta} = 0$  as in Fig. 5a. We then delineate a segment of the hyperboloid shell and consider its force equilibrium (as illustrated in Fig. 5c). At any horizontal section, by force equilibrium

$$(2\pi r_0) N_\phi (\sin \phi) = C. \quad (12)$$

Now, consider the segment at the waist circle, where  $\phi = 90^\circ$  and  $r_2 = r_0 = a$  (throat radius),

$$(2\pi a) N_{\phi(\phi=90^\circ)} = C \quad \text{or} \quad N_{\phi(\phi=90^\circ)} = \frac{C}{2\pi a} \text{ (compressive)}. \quad (13)$$

At the waist circle where  $r_2 = a$ , eqn (11) yields

$$N_{\theta(\phi=90^\circ)} = \left( \frac{a^4}{b^2} \frac{1}{r_2^2} \right) N_{\phi(\phi=90^\circ)} = \left( \frac{a^2}{b^2} \right) N_{\phi(\phi=90^\circ)},$$

which on combining with eqn (13), leads to

$$N_{\theta(\phi=90^\circ)} = \left( \frac{a^2}{b^2} \right) \frac{C}{2\pi a} = \frac{C}{2\pi a} \tan^2 \beta, \quad (14)$$

which is compressive in nature.

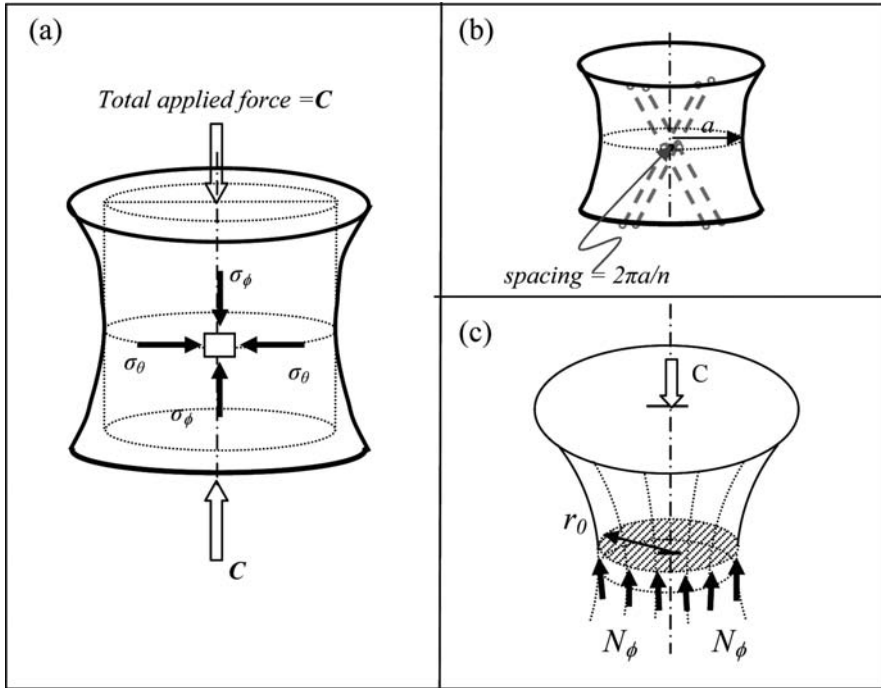


Figure 5: The stresses at the waist section of a hyperboloid shell. (a) Stress components; (b) equivalent straight bars (aligned with the generators) placed at equal spacing to take up the stresses; (c) equilibrium of forces on a shell segment.

From Fig. 6, the equivalent resultant compressive force  $F_c$  in a fibre (generator of the hyperboloid surface) is given by

$$F_c^2 = \left[ N_\phi \left( \frac{\pi a}{n} \right) \right]^2 + \left[ N_\theta \left( \frac{\pi b}{n} \right) \right]^2. \quad (15)$$

Substituting eqns (13) and (14) into eqn (15), we have

$$F_c = \frac{C}{2n \cos \beta} = \frac{C \sqrt{H^2 + R^2 - a^2}}{2nH}. \quad (16)$$

Thus the total axial loading is transmitted into the hyperboloid shell's straight generators as compressive forces.

### 3.2 VB stress analysis under bending moment

When the VB is subjected to a bending moment ( $M$ ), normal stresses ( $\sigma_y$ ) are developed at the waist circle ( $r_0 = a$ ) cross-section, as shown in Fig. 7. The bending moment sustained at the waist circle is given by

$$M = 2 \int_0^a \sigma_y \left[ 2 \frac{t}{\cos \alpha} dy \right] y, \quad (17)$$

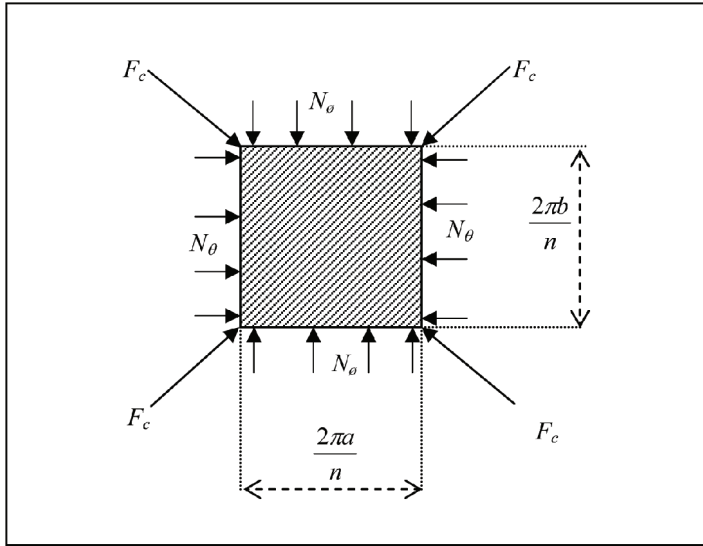


Figure 6: The equivalent diagonal forces in the intersecting bars to take up the stresses around a shell element.

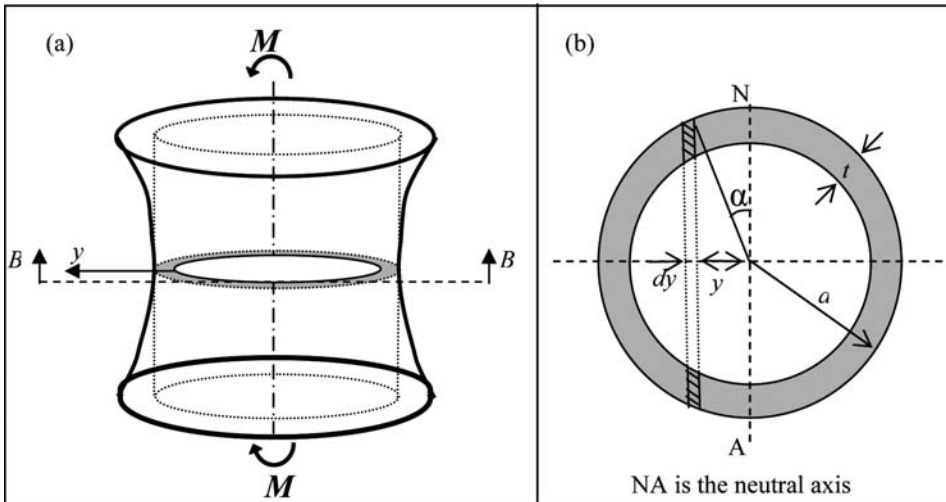


Figure 7: (a) The bending moment on the VB. (b) Plan view at the section BB (i.e. at the waist circle).

where  $\sigma_y$  is the compressive stress normal to the cross section (due to the bending moment  $M$ ) acting on the two rectangular elements of length  $2(t/\cos \alpha)$  and width  $dy$ . In addition,

$$\sigma_y = \frac{y}{a} \sigma_a, \quad (18)$$

where  $\sigma_a$  is the stress at  $y = a$ .

Combining eqns (17) and (18), we have

$$M = 4 \int_0^a \frac{y^2}{a} \sigma_a \frac{t}{\cos \alpha} dy$$

$$M = 4t\sigma_a \int_0^a \frac{y^2}{a \cos \alpha} dy. \quad (19)$$

Substituting for  $y = a \sin \alpha$  and  $dy = a \cos \alpha d\alpha$ , eqn (19) can be rewritten as

$$M = 4t\sigma_a \int_0^{\pi/2} \frac{a^2 \sin^2 \alpha}{a \cos \alpha} a \cos \alpha d\alpha. \quad (20)$$

Integrating eqn (20) gives

$$M = \pi a^2 t \sigma_a. \quad (21)$$

The normal stress at the waist circle in terms of the bending moment can be written as

$$\sigma_a = \frac{M}{\pi a^2 t}. \quad (22)$$

Then,  $N_\phi$ , on the waist-circle element at distance  $a$  from the neutral axis, is given by

$$(N_\phi)_a = \sigma_a t.$$

Thus from eqn (22),

$$(N_\phi)_a = \frac{M}{\pi a^2}. \quad (23)$$

According to Fig. 8c the force ( $F_m$ ) in the generator is given by

$$F_m^2 = \left[ \left( \frac{\pi a}{n} (N_\phi)_a \right)^2 + \left( \frac{\pi b}{n} (N_\theta)_a \right)^2 \right]. \quad (24)$$

Substituting the value of  $N_\theta$  from eqn (11), we get

$$F_m^2 = \left[ \left( \frac{\pi a}{n} (N_\phi)_a \right)^2 + \left( \frac{\pi b}{n} \left( \frac{a^2}{b^2} (N_\phi)_a \right) \right)^2 \right]. \quad (25)$$

Since  $\tan \beta = a/b$ , eqn (25) reduces to

$$F_m^2 = \left( \frac{M}{\pi a^2} \right)^2 \left( \frac{\pi a}{n} \right)^2 [1 + \tan^2 \beta]$$

or

$$F_m = \frac{M}{na \cos \beta}, \quad (26)$$

where  $F_m$  can be either compressive or tensile force based on the location of the generators relative to the plane about which the bending moment is applied.

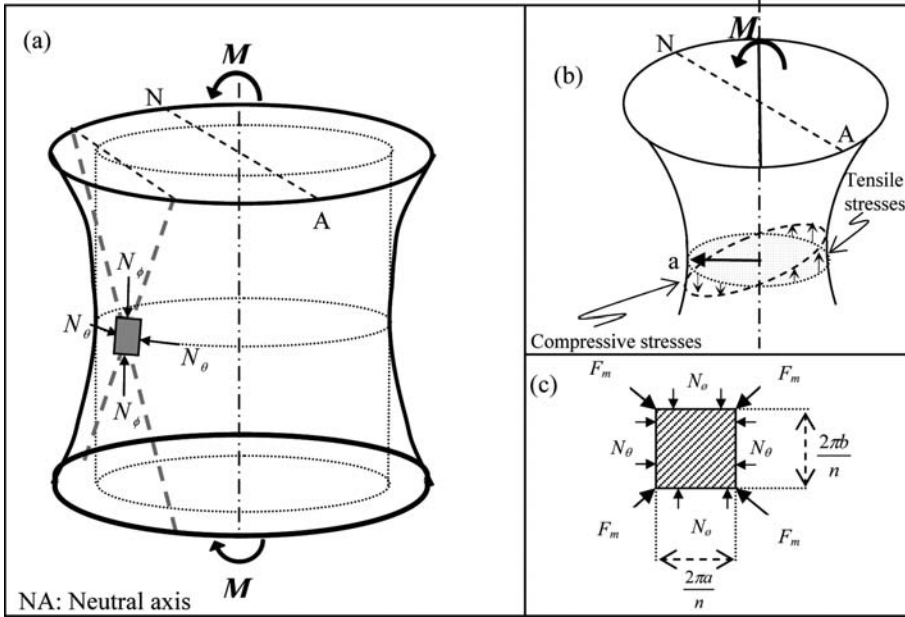


Figure 8: (a) Stress resultants at the waist section of the hyperboloid shell under bending. (b) Equilibrium of forces on a shell segment. (c) Equivalent diagonal forces in the intersecting bars to take up the stresses around a shell element on the compression side of the hyperboloid shell.

### 3.3 Stress analysis under torsional loading

Next, we analyse the compressive and tensile forces in the hyperboloid shell generators when the VB is subjected to pure torsion ( $T$ ). In this case (refer to Fig. 9a), the normal stress resultants are zero and only have shear resultants

$$N_\phi = N_\theta = 0 \quad \text{and} \quad N_{\phi\theta} = \tau t. \quad (27)$$

The equilibrium of a segment of the shell at a horizontal section (as in Fig. 9b) gives,

$$[(2\pi r_0)N_{\phi\theta}]r_0 = T \quad \text{or} \quad (2\pi r_0^2)N_{\phi\theta} = T. \quad (28)$$

At the waist circle,  $r_2 = r_0 = a$  (throat radius):

$$(2\pi a t \tau) a = T, \quad \text{i.e.} \quad N_{\phi\theta} = \frac{T}{2\pi a^2}. \quad (29)$$

Now, consider an element at the waist circle as shown in Fig. 9c. The equivalent compressive force ( $F_{cT}$ ) and tensile force ( $F_{tT}$ ), in the direction aligned to their respective set of shell generators, are given by

$$F_{cT}^2 = F_{tT}^2 = \left(N_{\phi\theta} \frac{\pi a}{n}\right)^2 + \left(N_{\phi\theta} \frac{\pi b}{n}\right)^2$$

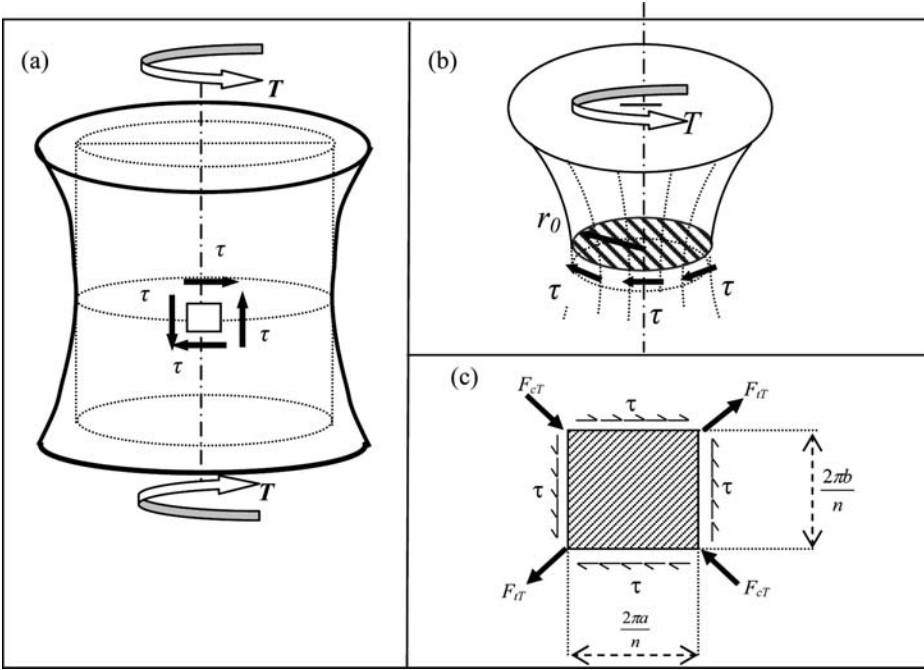


Figure 9: (a) Stress resultants in the hyperboloid shell element ( $N_\phi = N_\theta = 0$  and  $N_{\phi\theta} = \tau t$ ) due to torsion  $T$  acting on the VB. (b) Equilibrium of a shell segment under torsion ( $T$ ) and shear stresses ( $\tau$ ) (or shear stress resultant  $N_{\phi\theta}$ ). (c) Equivalent diagonal forces in the intersecting generators to take up the stresses around the shell element.

or

$$|F_{cT}| = |F_{tT}| = \frac{T}{2na \sin \beta}. \quad (30)$$

Thus, a torsional loading on the hyperboloid shell VB is taken up by one set of generators being in compression and the other set of generators being in tension.

#### 4 OPTIMAL DESIGN

##### 4.1 Structural analogy of the VB to the cane stool

The above analyses illustrate how the intrinsic hyperboloid shape design of the VB enables the loadings to be transmitted as axial (compressive/tensile) forces through the generators of the hyperboloid shell. In this regard, the VB can be compared to a hyperboloid cane stool (shown in Fig. 10a), which is an ideal high-strength and lightweight structure. This is because all the loading exerted on it (by a person sitting on it) is transmitted (to the ground) as axial forces in the cane generators. A material (such as cane) is strongest in compression provided its length is less than the buckling length. This makes the cane stool a high-strength and high load-bearing structure.

If the two sets of canes (at  $\pm\beta$ ) are encircled at the waist circle by a band, it increases the load-carrying capacity of the cane stool. If, additionally, these two sets of canes ( $\pm\beta$ ) are tied at all

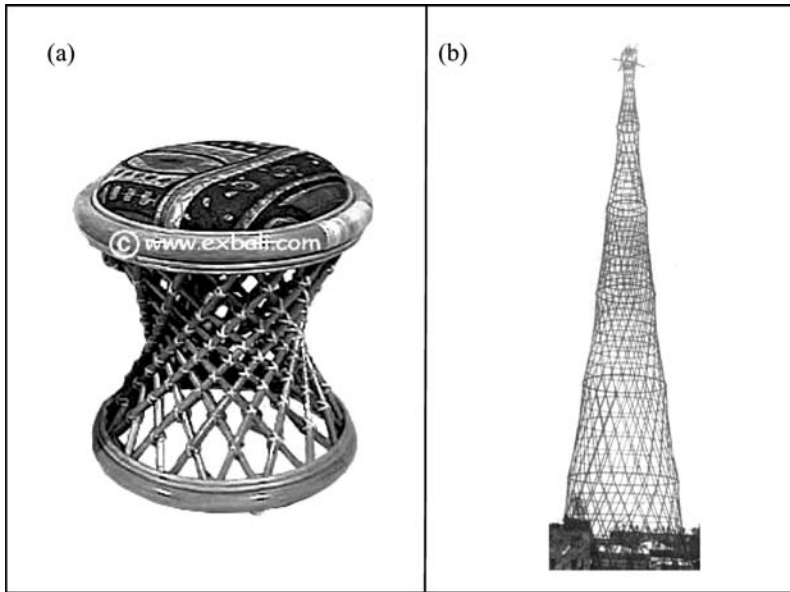


Figure 10: A couple of man-made hyperboloid structures: (a) the humble cane stool (reproduced with permission from [www.exbali.com](http://www.exbali.com)) weighing 2.5 kg but capable of bearing a load of 5000 N in compression; (b) the Shabolovka radio tower, Moscow, needed just 2200 tons of steel to build a 350 m high tower [7].

their intersecting points (as shown in Fig. 10a), their functional lengths are reduced, which further enhances the strength and load-carrying capacity of the cane stool. Furthermore, the cane stool is very light as it is just made up of discrete canes (as generators of the hyperboloid structure). This structural configuration makes the cane stool a very simple but effective load-bearing, high-strength and lightweight structure. Incidentally, such a cane stool of ( $R = 200$  mm,  $H = 175$  mm) has a nominal weight of 2.5 kg (or 25 N), but it can easily bear a load of at least 5000 N, which is 200 times its weight.

The spinal VB cortex has similar structural configuration and properties as the cane stool, which also make it an efficient load-bearing and load-transmitting, high-strength and lightweight structure. The VB wall can be considered to be primarily comprised of the two sets of generators. Just as in the case of the cane stool and the Shabolovka radio tower (Fig. 10), the VB wall transmits all the loading as axial forces through its generators. This is the basis for a high-strength and lightweight VB design.

#### 4.2 Optimization of the hyperboloid shape of the VB

The spinal VB has a definitive value range for the hyperboloid shape parameter  $\beta$  and hence for its hyperboloid shape. In order to determine the structural basis of this  $\beta$  value, we will calculate that value of  $\beta$  which makes the combined axial force in its generators to be minimum. In this case, the optimized VB structure will be able to sustain maximal loading, before the ultimate failure load of its generators is reached.

The VB is subjected to the combined compression, bending moment and torsional loadings. Under this combined loading, the forces in the generators given by eqns (16), (26) and (30) can be



Figure 11: MRI of lumbar vertebrae.  $H/R = 0.7$  (average of L2–L5) and  $a/R$  is 0.91 (average of L2–L5).

combined using the principle of linear superposition. For its optimal intrinsic design with respect to the hyperboloid shape parameter  $\beta$ , to sustain the combined loadings [i.e. compression from eqn (16), bending moment from eqn (26) and torsion from eqn (30)], we need to have

$$\frac{d}{d\beta} [\text{Combined forces in the generators}] = 0. \quad (31)$$

Hence from eqns (16), (26) and (30), we obtain

$$\frac{d}{d\beta} \left( \frac{C}{2n \cos \beta} + \frac{M}{na \cos \beta} + \frac{T}{2na \sin \beta} \right) = 0.$$

or

$$\left( \frac{\sqrt{R^2 - a^2}}{H} \right)^3 \left( \frac{C}{2} + \frac{M}{a} \right) = \frac{T}{2a}. \quad (32)$$

Equation (32) gives the relationship between the applied loading and the geometry of the VB. Interestingly, the value of  $a$  is not found in the literature [8, 9, 10]. However, for a specific set of values of  $R$  and  $H$  and functionally occurring ratios of the loading values ( $C$ ,  $M$ ,  $T$ ), the value of the hyperboloid shape parameter  $a$  can be calculated from eqn (32), for the intrinsic design of the VB. In eqn (32), considering the representative values of  $C = 1000$  N,  $M = T = 3$  Nm, along with



$R = 21.6$  mm and  $H = 14.75$  mm, based on Zhou *et al.* [10] and Guo *et al.* [11], we obtain  $a \approx 20.3$  mm; hence, from eqn (4),  $\beta = 26.5^\circ$ .

Hence, the optimal lightweight, high-strength spinal VB geometry is given by  $\beta = 26.5^\circ$  with  $a/R = 0.939$  (for  $H = 14.75$  mm). The  $a/R$  value of 0.91 measured from the lumbar vertebrae MRI scan shown in the Fig. 11 confirms our analysis. Thus, the intrinsic design of the VB hyperboloid geometry is such that it bears the combined loadings of compression, bending moment and torsion by minimizing the axial forces in the generators. In other words, it can sustain and transmit maximal values of the loadings with minimal amounts of material (because of all the loadings being transmitted as axial forces through the hyperboloid generators).

## 5 CONCLUSION

We have carried out an internal stress analysis of the hyperboloid VB under compression, bending moment and torsional loading. The analysis shows that all the loading states are transmitted by the VB generators as axial forces, thereby making it a high-strength structure with a high load-bearing capacity. Explicit expressions for these axial forces in the VB generators under compression, bending moment and torsional loading conditions are obtained (in terms of the VB geometrical parameters).

Minimization of the total axial force for the combined loadings gives the value of the hyperboloid shape parameter  $\beta = 26.5^\circ$ , for which  $a/R = 0.939$ , which closely matches the measured value of  $a/R = 0.91$  from the VB MRI. Therefore, for this value of  $\beta$ , the spinal VB can maximize its load-bearing capacity. Thus, we have demonstrated that the VB shape and material distribution are modelled by the loading to be an optimal high-strength and lightweight structure, in the same way as the femur's shape and material distribution are based on the stress trajectories (Fig. 1) due to the loading sustained by it.

## REFERENCES

- [1] Collins, M.W., Hunt, D.G. & Atherton, M.A., *Optimisation Mechanics in Nature*, WIT Press: Southampton, 2004.
- [2] Collins, M.W., Atherton, M.A. & Bryant, J.A., *Nature and Design*, WIT Press: Southampton, 2005.
- [3] Wolff, J., *Das Gesetz der Transformation der Knochen*, Hirschwald, 1892 (translated by P. Maquet & R. Furlong (1986) as *The Law of Bone Remodeling*, Springer: Berlin, 1986).
- [4] Harris, J.W. & Stocker, H., Hyperboloid of revolution. *Handbook of Mathematics and Computational Science*, Springer-Verlag: New York, p. 112, 1998.
- [5] Steinhaus, H., *Mathematical Snapshots*, Dover: New York, 1999.
- [6] Raamachandran, J., *Thin Shells: Theory & Problems*, Universities Press Limited: India, 1993.
- [7] Elizabeth, C.E., Vladimir Shukhov and the invention of hyperboloid structures. *Proc. of the 2005 Structures Congress and the 2005 Forensic Engineering Symposium*, 2005.
- [8] Nissan, M. & Gilad, I., Dimensions of human lumbar vertebrae in the sagittal plane. *Journal of Biomechanics*, **19(9)**, pp. 753–758, 1986.
- [9] Panjabi, M., Goel, V.K., Oxland, T., Takata, K., Duranceau, J., Krag, M. & Price, M., Human lumbar vertebrae: quantitative three-dimensional anatomy. *Spine*, **17**, pp. 298–306, 1992.
- [10] Zhou, S.H., McCarthy, I.D., McGregor, A.H., Coombs, R.R.H. & Hughes, S.P.F., Geometrical dimensions of the lower lumbar vertebrae—analysis of data from digitized CT images. *European Spine Journal*, **9**, pp. 242–248, 2000.
- [11] Guo, L.X., Teo, E.C. & Qiu, T.Z., Prediction of biomechanical characteristics of intact and injured lower thoracic spine segment under different loads. *Journal of Musculoskeletal Research*, **8(2&3)**, pp. 87–99, 2004.

# THE OPTIMAL STRUCTURAL DESIGN OF THE HUMAN SPINAL INTERVERTEBRAL DISC

D.N. GHISTA<sup>1</sup>, S.C. FAN<sup>2</sup>, I. SRIDHAR<sup>3</sup> & K. RAMAKRISHNA<sup>3</sup>

<sup>1</sup>University of New South Wales Asia, Singapore.

<sup>2</sup>School of Civil and Environmental Engineering, Nanyang Technological University, Singapore.

<sup>3</sup>School of Mechanical and Aerospace Engineering, Nanyang Technological University, Singapore.

## ABSTRACT

The intervertebral disc (IVD) acts as a shock-absorbing unit and effectively contains its lateral and axial deformations while providing the necessary flexibility to the spine. These attributes are due to the stress-stiffening material (elastic modulus) property of the annulus, caused by the pressure developed in the nucleus pulposus (NP). Hence, one of the biomechanical roles of the NP in the IVD is to stress the annulus while the IVD is loaded. In this paper, a closed-form solution of the IVD (with NP, i.e. a healthy IVD, and without NP, i.e. a nucleotomized IVD) under compressive loading is developed. Based on the analysis, it is observed that the deformations of the IVD do not increase in proportion to the load. Rather, the rate of increase in deformation decreases as the load increases. This is a key optimal feature because it means that deformations are contained and therefore stability is maintained. Further, it is shown that the nucleotomized IVD deforms more than the healthy IVD. This means that the nucleotomized IVD will have higher chances of collapse than the healthy IVD for the same level of loading. This result is a contra-indication for nucleotomy. Our proposal is to place a biocompatible gel-filled balloon to simulate the beneficial effects of the NP.

*Keywords: deformation, internal pressure, intervertebral disc, nucleotomy, nucleus pulposus, stress analysis, stress stiffening solid, thick-walled cylinder, uniaxial compression.*

## 1 CONCEPT OF THE INTERVERTEBRAL DISC AS AN OPTIMAL STRUCTURE

The human spine is made up of alternating vertebral body (VB) and intervertebral disc (IVD). In our earlier paper [1], we have shown how the VB is designed as an optimal lightweight structure because of its hyperboloid shape. An additional feature of the spine as a structure is its 'S' shaped configuration. This configuration has evolved to enable a human being to stand and move in an upright configuration while supporting the internal organs and providing rigidity for the functional role of sitting and squatting. However, the 'S' shaped configuration also acts as a shock absorber. In this function of the spine to act as a flexible shock-absorbing and protective structure, the IVD has an important role.

The IVD, as the principal component of the intervertebral joint (shown in Fig. 1a), sustains and transmits compressional, bending and torsional loadings. It is centrally pressurized by the nucleus pulposus (NP) and surrounded by the annulus (Fig. 1b). The annulus fibres are oriented helically, at almost 30°–50° [2, 3]. Even under torsion, the torsional shear stresses on a disc element will result in diagonally oriented tensile and compressive stresses. It is revealing that these tensile stresses due to torsion of the disc can thus be directly absorbed by these angled fibres of the annulus. Thus, the IVD is ideally designed for compression and bending as well as for torsion [4–12].

The IVD functions as the shock-absorbing component of the spinal unit, comprising two adjacent VBs on either side of the IVD. Additionally, the central portion of the VB end-plate functions as a diaphragm, through which (under compressive loading) NP fluid moves out of the disc into the VB, thereby helping to draw nutrition (as shown in Fig. 2a and b) into the disc upon removal of the loading. However, under rapidly applied loading, the VB end-plate offers resistance to the intrusion of fluid into the VB blood compartment, thereby lending a shock-absorbing property to the disc. Indeed, the IVD can be regarded as an effective viscoelastic shock-absorbing structure [13].

From a biomechanical viewpoint, the NP has another very important role, namely to contain the disc axial and radial deformations. The causative mechanism is that when the disc is loaded in axial

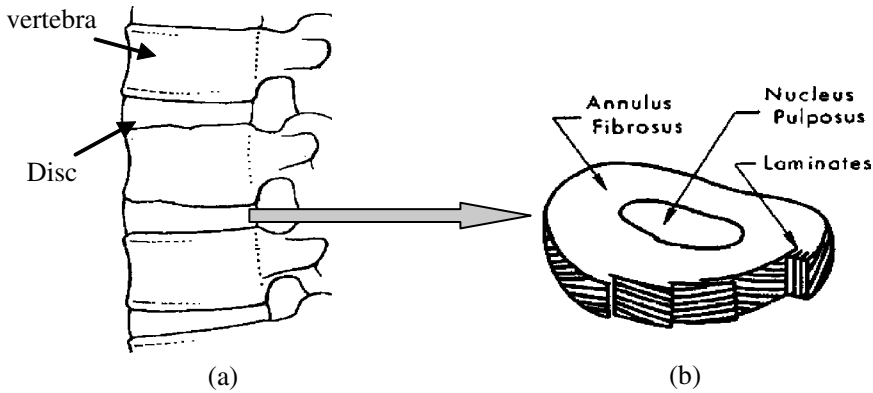


Figure 1: (a) The location of the IVD within the spinal column. (b) Schematic representation of the disc structure. The NP is surrounded by annulus fibrosus. This outer layer has a lamellar structure with highly ordered collagen fibres [4].

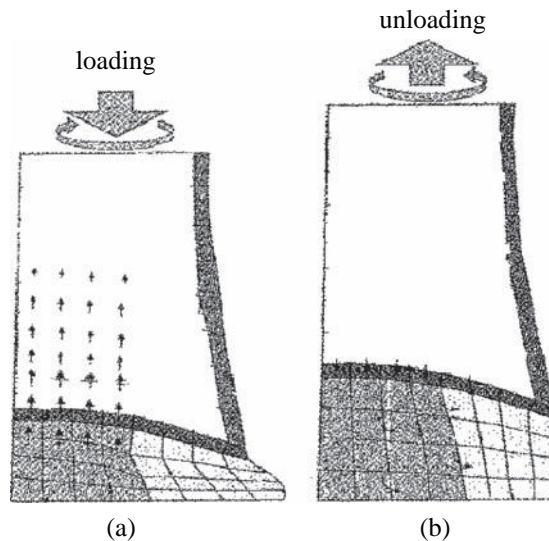


Figure 2: Nutrition mechanism of the disc (a) during loading, the NP enters the cancellous VB, and (b) during unloading, the NP draws nutrition into the disc [13].

compression (or bending or torsion), the NP fluid gets pressurized and stresses the surrounding annulus. The annulus is a stress-stiffening solid, such that its elastic modulus ( $E$ ) increases with the increase in stress (its stress-strain property is shown in Fig. 3b) [14, 15]. Hence, under increased loadings, its elastic modulus value also increases, so that the deformations are thereby contained.

The IVD's stress-deformation characteristics have been effectively analysed by finite element analysis [14]. Herein, an elasticity model of the disc as a closed thick-walled fluid-filled cylinder is employed to determine its stress and deformations under uniaxial compressive loading and demonstrates the role of the NP in containing the disc deformations. It is also demonstrated that

the nucleotomized disc will undergo larger deformations than the normal disc, for the same levels of loading, thereby drawing attention to the efficacy of nucleotomy to treat a ruptured disc and associated back pain.

The stress-dependent Young's modulus of the disc annulus can be represented as [14]

$$E = E_0 + 375.3 \sigma^{0.473}, \quad (1)$$

where  $E_0$  (the residual Young's modulus) = 4.2 MPa and the stress  $\sigma$  is expressed in MPa. This constitutive equation is employed to determine the  $E$  value for the uniaxially compressed disc. This constitution of the spinal disc, wherein the stress-dependent Young's modulus of its annulus encloses the NP, gives it a key self-reinforcing design property. The closest man-made self-reinforcing structure is a car tyre, which makes it lighter as well as lends it a shock-absorbing property.

The disc annulus is assumed to be isotropic, so that  $E_z = E_r = E_\theta = E$ . As the disc gets compressed (by increasing the applied compressive force  $F$ ), the annulus stresses ( $\sigma_z$ ,  $\sigma_r$  and  $\sigma_\theta$ ) keep increasing. For each updated value of  $E$  for the enhanced stress state (in response to increasing values of the compression force  $F$  on the disc),  $\sigma_z$  (in eqn (1)) is taken to be equal to the maximum value of the principal stress (which happens to be the axial stress  $\sigma_z$ ). For this relationship, as the disc is loaded, the annulus stress state  $\sigma = (\sigma_z)$  increases. Correspondingly, its  $E$  increases, to thereby contain the disc deformations.

In this paper, the mechanism of disc deformation containment for vertical loading is delineated. Compressive loading ( $F$ ) on the disc causes compressive axial stress ( $\sigma_z$ ) in the annulus and also pressurizes NP fluid, which then exerts hydrostatic pressure ( $p_i$ ) and hence compressive radial stress  $\sigma_r$  on the annulus. This radial pressure or stress ( $\sigma_r$ ) in turn causes circumferential tensile stress ( $\sigma_\theta$ ) in the annulus. These stresses in turn influence the strain state in the disc through the elastic modulus and, hence, the axial and radial deformations of the disc by virtue of eqn (1). Hence, the effect of the NP hydrostatic pressure is to stress the disc annulus and enhance the value of its  $E$ . This in turn stiffens the disc (according to eqn (1)) and enables it to bear heavy loads without large axial and lateral deformations.

## 2 ANALYSIS: DISC STRESSES, DISPLACEMENTS AND DEFORMED GEOMETRY

The disc is considered to be a thick-walled isotropic cylinder whose geometry and deformations are depicted in Fig. 3a. In this analysis, linear elasticity formulations of stress-strain constitutive relations have been employed. Under compressive loading of the order of 2000 N, the deformations are of the order of 1 mm. This result has been obtained by Fagan *et al.* [6, 16] and is shown in Fig. 3b. Hence, in order to compute the disc deformations under compressive loading, small incremental loadings are adopted so that the resulting strains are infinitesimal. Likewise, for each incremental load state, (1) the NP pressure is determined, (2) the incremental stresses and the total stress state are computed, (3) the disc material modulus value is revised as per eqn (1) and (4) the disc deformations are determined and its geometry is updated.

Stress equilibrium equations: Let  $u$  be the radial displacement and  $w$  be the axial displacement, as shown in Fig. 3. Because of the axial symmetry of the disc geometry and loading conditions, the shear stresses and the circumferential displacement are identically equal to zero. Thus, the stress-equilibrium equations are

$$\text{Radial direction} \quad \frac{d}{dr} \left( \frac{r}{r} \right) + \frac{r}{r} = 0 \quad (2)$$

$$\text{Axial direction} \quad \frac{d}{dz} \left( \frac{z}{z} \right) = 0. \quad (3)$$

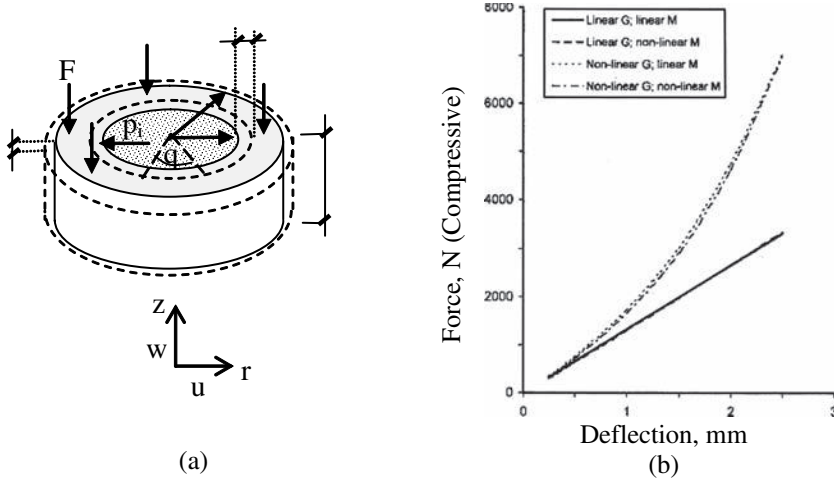


Figure 3: (a) Geometry and deformation variables of the spinal disc loaded in compressive force  $F$ . Note that  $u$  is depicted as expansive radial deformation while  $w$  is depicted as shortening axial deformation. (b) Comparison of the effects of including linear and non-linear material (M) and geometry (G) solution options on the compressive behaviour of the disc [6].

The strain-displacement relations are

$$\text{Radial strain} \quad r \quad \frac{r}{E} \quad \frac{(\quad + \quad z)}{E} \quad \frac{du}{dr}, \quad (4a)$$

$$\text{Circumferential strain} \quad = \quad \frac{(\quad z + \quad r)}{E} \quad \frac{u}{r} \quad (4b)$$

$$\text{Axial strain} \quad z \quad \frac{z}{E} \quad \frac{(\quad r + \quad )}{E} \quad \frac{dw}{dz}, \quad (4c)$$

wherein the annulus material modulus ( $E$ ) is adopted to be isotropic.

The disc material's constitutive stress-strain relations in terms of the disc material's Young's modulus ( $E$ ) and Poisson's ratio ( $\nu$ ) are hence given in the radial direction as

$$r \quad \frac{E}{1 + \quad} \quad \frac{(\quad + \quad z)}{(1 - 2 \quad)} \quad \frac{du}{dr} + \frac{u}{r} + \frac{dw}{dz} + \frac{du}{dr}, \quad (5a)$$

in the circumferential direction as

$$= \frac{E}{1 + \quad} \quad \frac{(\quad + \quad z)}{(1 - 2 \quad)} \quad \frac{du}{dr} + \frac{u}{r} + \frac{dw}{dz} + \frac{u}{r} \quad (5b)$$

and in the axial direction as

$$z \quad \frac{E}{1 + \quad} \quad \frac{(\quad + \quad z)}{(1 - 2 \quad)} \quad \frac{du}{dr} + \frac{u}{r} + \frac{dw}{dz} + \frac{dw}{dz}. \quad (5c)$$

Note that  $\quad$ ,  $r$ ,  $z$  are adopted to be positive for tensile stress.

Now, by substituting the constitutive relations in eqn (5a–c) into the equilibrium equations (2) and (3), two partial differential equations in displacements  $u$  and  $w$  are obtained, as follows

$$\frac{d}{dr} \left( \frac{1}{2} \frac{du}{dr} + \frac{u}{r} + \frac{dw}{dz} \right) + \frac{du}{dr} + \frac{1}{r} \frac{du}{dr} - \frac{u}{r} = 0, \quad (6a)$$

$$\frac{d}{dz} \left( \frac{1}{2} \frac{du}{dr} + \frac{u}{r} + \frac{dw}{dz} \right) + \frac{dw}{dz} = 0. \quad (6b)$$

The solutions of eqn (6a) and (6b) can be expressed as

$$u = \frac{A}{r} + Br, \quad (7)$$

$$w = Cz + D, \quad (8)$$

where, A, B, C and D are the constants of integrations. These constants can be determined by applying appropriate boundary conditions.

As the NP is incompressible [2], its volume after deformation is unchanged, so that

$$a^2 h = (a + u_a)^2 (h - w_h).$$

This can be simplified by neglecting higher-order terms ( $u_a w_h$  and  $u_a^2 w_h$ ), to yield

$$2 a h u_a - a^2 w_h = 0 \quad \text{or} \quad u_a = \frac{a}{2h} w_h, \quad (9)$$

It is to be noted that according to deformation as per Fig. 3a,  $w_h$  is the shortening deformation at  $z = h$ , while  $u_a$  is the radial expansion deformation at  $r = a$ .

The appropriate boundary conditions for solving eqns (7) and (8) are

$$u_r = 0 \quad \text{at} \quad r = a, \quad (10a)$$

$$r = 0 \quad \text{at} \quad r = b, \quad (10b)$$

$$w = 0 \quad \text{at} \quad z = 0, \quad (10c)$$

$$w = w_h \quad \text{at} \quad z = h. \quad (10d)$$

Using the boundary conditions from eqn (10) and utilizing eqns (5), (7) and (8), the constants in eqns (7) and (8) are obtained as

$$A = \frac{(1 - \frac{2}{a^2}) u_a a b^2}{b^2 + a^2 (1 - \frac{2}{a^2})}, \quad (11a)$$

$$B = u_a \frac{a^2 (1 - \frac{2}{a^2}) + 2 b^2}{a b^2 + a^3 (1 - \frac{2}{a^2})}, \quad (11b)$$

$$C = \frac{w_h}{h} - \frac{2u_a}{a}, \quad (11c)$$

$$D = 0. \quad (11d)$$

Using the constants  $A$ ,  $B$ ,  $C$  and  $D$ , the stresses in eqn (5) can be represented by

$$\begin{aligned} r &= \frac{E}{1 + \nu} \left[ \frac{(2B + C)}{(1 - \nu)} + B + \frac{A}{r^2} \right] \\ &= \frac{E}{1 + \nu} \left[ \frac{u_a a (1 - \nu)}{a^2 (1 - \nu) + b^2} + \frac{b^2}{r^2} + 1 \right], \end{aligned} \quad (12a)$$

$$\begin{aligned} &= \frac{E}{1 + \nu} \left[ \frac{(2B + C)}{(1 - \nu)} + B + \frac{A}{r^2} \right] \\ &= \frac{E}{1 + \nu} \left[ \frac{u_a a (1 - \nu)}{a^2 (1 - \nu) + b^2} + \frac{b^2}{r^2} + 1 \right], \end{aligned} \quad (12b)$$

$$\begin{aligned} z &= \frac{E}{(1 + \nu)} \left[ \frac{(2B + C)}{(1 - \nu)} + C - \frac{2u_a E}{a(1 + \nu)} \frac{a^2 (1 - \nu) + b^2 (1 + \nu)}{a^2 (1 - \nu) + b^2} \right] \\ &= \frac{w_h E}{(1 + \nu)} \frac{a^2 (1 - \nu) + b^2 (1 + \nu)}{a^2 (1 - \nu) + b^2}. \end{aligned} \quad (12c)$$

Then, from eqns (7), (11a) and (11b), the radial displacement is given by

$$u_r = \frac{A}{r} + Br - \frac{u_a}{ar} \frac{a^2 b^2 (1 - \nu) + r^2 [a^2 (1 - \nu) + 2b^2]}{a^2 (1 - \nu) + b^2} \quad (13a)$$

and hence  $u_b$  (at  $r = b$ ) is given by

$$u_b = \frac{2bu_a}{a} \frac{a^2 (1 - \nu) + b^2}{a^2 (1 - \nu) + b^2}. \quad (13b)$$

It is to be noted (from eqn (12c)) that  $z$  is uniform throughout the disc and the minus sign implies that  $z$  is compressive.

### 3 STRESS ANALYSIS OF THE HEALTHY DISC UNDER COMPRESSION

For an axially applied force  $F$  (as illustrated in Fig. 4), the equilibrium equation is

$$F = a^2 p_f - b^2 \sigma_z, \quad (14)$$

where  $p_f$  is the hydrostatic pressure in the fluid and  $\sigma_z$  is the axial stress in the annulus (as shown in Fig. 4). Its sign is taken to be negative in eqn (14), because positive  $\sigma_z$  is considered as tensile.

Because the disc height ( $h$ ) is small,  $p_f$  is approximately constant, and hence:

$$p_f = p_i \quad (r = a) \quad p_i \text{ (the pressure in the NP)}. \quad (15)$$

Based on eqns (15) and (12a),

$$p_i = \frac{E (1 - \nu)}{(1 + \nu)} \left[ \frac{u_a}{a} + \frac{b^2}{a^2 (1 - \nu) + b^2} \right]. \quad (16)$$

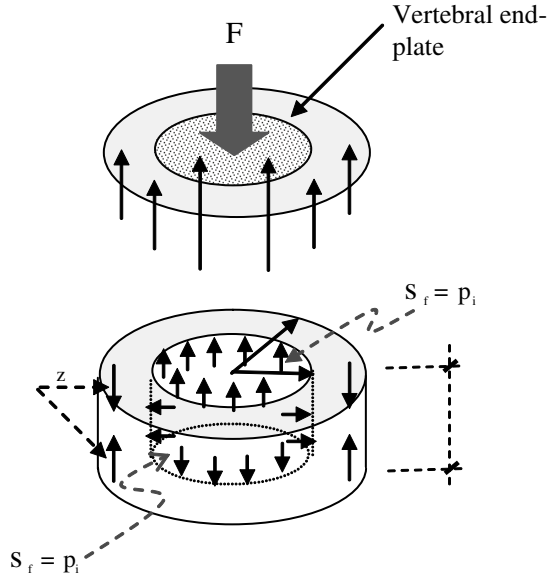


Figure 4: Normal stresses  $s_r$  and  $s_z$  under the applied compressive force  $F$ .

Then, substituting for  $u_a$  from eqn (16) into eqn (12c), we obtain

$$p_i = \frac{1}{2} \frac{F}{b^2} \frac{a^2}{a^2(1 - \frac{a^2}{b^2}) + b^2(1 + \frac{a^2}{b^2})} \quad (17)$$

The axial stress in the annulus is obtained by substituting the expression for  $p_i$  from eqn (17) into eqn (14) as

$$s_z = \frac{2}{b^2} \frac{F}{a^2} \frac{a^2(1 - \frac{a^2}{b^2}) + b^2(1 + \frac{a^2}{b^2})}{2b^2(1 + \frac{a^2}{b^2}) + a^2(3 - \frac{a^2}{b^2})} \quad (18)$$

Then, from eqns (17) and (18), the NP pressure is expressed in terms of the applied compressive force  $F$  as

$$p_i = \frac{1}{2} \frac{F}{3a^2(1 - \frac{a^2}{b^2}) + 2b^2(1 + \frac{a^2}{b^2})} \quad (19)$$

From eqns (18) and (12c), by equating the expressions for  $F$ , we get the radial deformation at the inner surface as

$$u_a = \frac{1}{E} \frac{1}{b^2} \frac{F}{a^2} \frac{a^3(1 - \frac{a^2}{b^2}) + ab^2}{2b^2(1 + \frac{a^2}{b^2}) + a^2(3 - \frac{a^2}{b^2})} \quad (20)$$

From eqns (20) and (9), we get the axial deformation as

$$w_h = \frac{2}{E} \frac{1}{b^2} \frac{F}{a^2} \frac{h}{2b^2(1 + \frac{a^2}{b^2}) + a^2(3 - \frac{a^2}{b^2})} \quad (21)$$



By substituting eqn (20) into eqn (13b), the expression for  $u_b$  (the radial deformation at the outer surface of the annulus) is obtained as

$$u_b = \frac{2}{E} \frac{1}{b^2} \frac{F}{a^2} - \frac{a^2 b (1 - \nu^2) + b^3}{2b^2 (1 + \nu) + a^2 (3 - 6\nu)} \quad (22)$$

Finally, from eqns (12a, b) and (20), we obtain the expressions for  $r$  and  $z$  in terms of applied load  $F$  as

$$r = \frac{1}{2} \frac{1 - \nu^2}{b^2 - a^2} \frac{F}{a^2} - \frac{a^2}{2b^2 (1 + \nu) + a^2 (3 - 6\nu)} + 1 - \frac{b^2}{r^2} \quad (23)$$

$$= \frac{1}{2} \frac{1 - \nu^2}{b^2 - a^2} \frac{F}{a^2} - \frac{a^2}{2b^2 (1 + \nu) + a^2 (3 - 6\nu)} + 1 + \frac{b^2}{r^2} \quad (24)$$

It is seen that as the disc gets loaded in compression (by the force  $F$ ), (1) both  $z$  and  $p_i$  increase, by virtue of eqns (18) and (19); (2) the increased  $p_i$  (which is a function of  $F$ , as per eqn (19)) causes  $r$ ,  $z$  and  $u_b$  to increase by virtue of eqns (22)–(24); (3) the axial (shortening) deformation  $w_h$  increases by the virtue of eqn (21). Finally, the stresses ( $r$ ,  $z$  and  $p_i$ ) are expressed in terms of  $F$  by eqns (18), (23) and (24), while the deformations ( $u_a$ ,  $u_b$  and  $w_h$ ) are expressed in terms of  $F$  by means of eqns (20)–(22).

#### 4 MECHANISM AND COMPUTATION OF DISC DEFORMATION

The NP gets pressurized when the load  $F$  acts on it, as per eqn (19). All the stresses increase with loading as per eqns (18), (23) and (24), and so does  $E$  according to eqn (1). Now  $E$  (the elastic modulus corresponding to the deformed state of the disc under load  $F$ ) will be greater than its value in the unloaded state of the disc, as per eqn (1). Hence, as per eqns (21) and (22), both the axial and the radial deformations will be contained.

This is attributed to the disc design, wherein the annulus contains the NP. This dependency of  $E$  on  $p_i$ , and hence on  $F$  and the disc annulus stress state represented by  $z$  was also reported by Shirazi-Adl [14] and Ranu [17, 18], based on the experimental and finite element analysis of the annulus. The following procedure is followed to determine the disc deformation in response to compressive load.

##### Step 1

Starting from the unloaded state,  $z_0 = 0$ , for which  $E = E_0$  as per eqn (1).

1. Now an incremental compressive force of  $F_1 = 1$  N is applied on the unstressed disc of dimensions ( $a_0$ ,  $b_0$  and  $h_0$ ), and the incremental stresses ( $r_1$ ,  $z_1$  and  $p_1$ ) are computed based on eqns (18), (23) and (24).
2. Next, the maximum value of these three stresses ( $z_1$ ,  $r_1$  and  $p_1$ ), which happens to be  $z_1$ , is noted. Then, based on  $z_1$ ,  $E = E_1$  is computed according to the relation (based on eqn (1)):  $E_1 = E_0 (= 4.2) + 373.3 z_1^{0.473}$ .
3. The disc deformations ( $w_{h1}$ ,  $u_{a1}$  and  $u_{b1}$ ), corresponding to the incremental stresses, are also computed from eqns (20)–(22), based on the above calculated value of  $E = E_1$ .
4. The disc geometry is now updated to  $h_1 = h_0 - w_{h1}$ ,  $a_1 = a_0 + u_{a1}$ ,  $b_1 = b_0 + u_{b1}$ .

##### Step 2

1. Again, an incremental  $F_2 = 1$  N is applied on the deformed geometry of the disc ( $a_1$ ,  $b_1$  and  $h_1$ ), and incremental stresses ( $r_2$ ,  $z_2$  and  $p_2$ ) are evaluated.
2. Next, the maximum value of these three stresses ( $z_2$ ,  $r_2$  and  $p_2$ ) is noted, which happens to be  $z_2$ .

3. The stress state is upgraded by adding  $\varepsilon_2$  to  $\varepsilon_1$ , and  $E_2$  is computed based on eqn (1) as:  
 $E_2 = E_0 (= 4.2) + 373.3 [\varepsilon_1 + \varepsilon_2]^{0.473}$ .
4. Then the incremental disc deformations ( $w_{h2}$ ,  $u_{a2}$  and  $u_{b2}$ ) are determined corresponding to ( $\varepsilon_2$ ,  $r_2$  and  $\varepsilon_2$ ), with  $E_2$  as the updated annulus modulus. The total disc deformation is now:  
 $w_{h1} + w_{h2}$ ,  $u_{a1} + u_{a2}$ ,  $u_{b1} + u_{b2}$ .
5. The deformed disc geometry is now updated to:  $h_2 = h_1 - (w_{h1} + w_{h2})$ ,  $a_2 = a_1 + (u_{a1} + u_{a2})$ ,  
 $b_2 = b_1 + (u_{b1} + u_{b2})$ .

### Step 3

Step 2 is repeated until the total compressive force reaches 2000 N in order to obtain the final deformed geometry at the desired applied load.

The resulting graphs of disc deformations  $w_h$ ,  $u_a$  and  $u_b$  vs. force ( $F$ ) are depicted in Fig. 5. The deformed geometry of the disc for  $F = 500$  N, 1000 N, 1500 N and 2000 N are shown in Fig. 6, so as to depict the ‘disc-hardening’ effect whereby the disc deformations do not increase linearly with  $F$ .

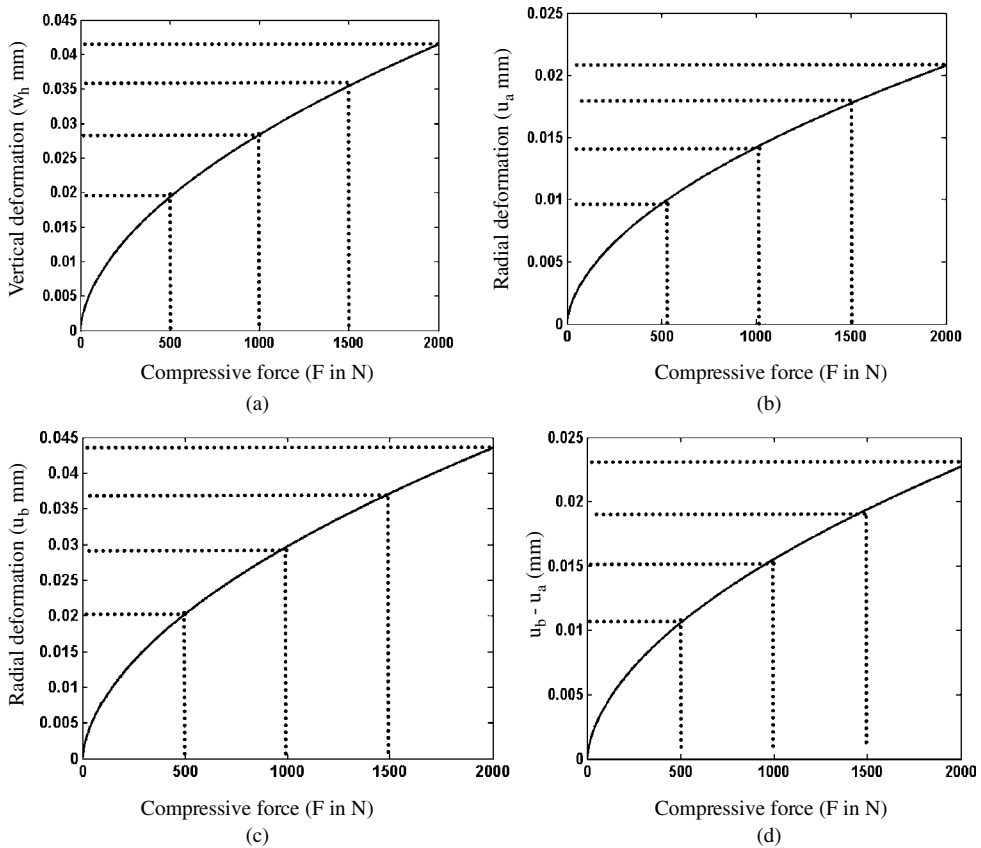


Figure 5: (a) Disc vertical deformation vs. compressive force on the annulus. (b) Radial bulge at  $r = a$  vs. compressive force on the annulus. (c) Disc radial bulge at  $r = b$  vs. compressive force. (d) Disc  $u_b - u_a$  vs.  $F$ . The initial disc geometrical parameters adopted are  $a = 11$  mm,  $b = 25$  mm and  $h = 11$  mm, and the annulus residual modulus  $E_0$  is taken to be 4.2 MPa.

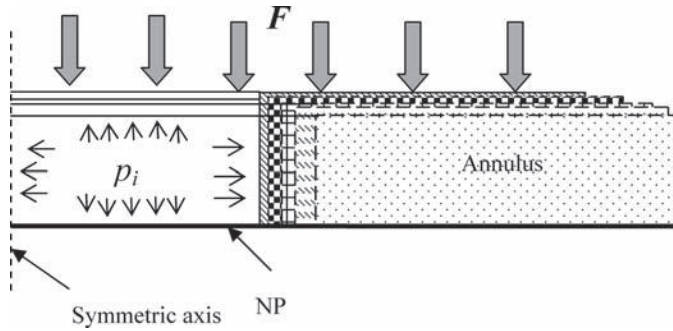

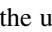
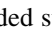
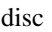



Figure 6: Graphical representation of disc deformation from the unloaded state until the compressive load of 2000 N is reached.  represents the unloaded state; disc geometry parameters are  $a = 11$  mm,  $b = 25$  mm,  $h = 11$  mm.  corresponds to the disc deformed state after 500 N; the deformed disc geometry parameters are  $a = 11.009$  mm,  $b = 25.02$  mm,  $h = 10.99$  mm.  corresponds to the deformed state after 1000 N; disc geometry parameters are  $a = 11.014$  mm,  $b = 25.029$  mm,  $h = 10.975$  mm.  represents the state after 1500 N; disc geometry parameters are  $a = 11.018$  mm,  $b = 25.037$  mm,  $h = 10.965$  mm.  represents the final disc deformed state when loaded by 2000 N; the corresponding final disc geometry parameters are  $a = 11.02$  mm,  $b = 25.044$  mm,  $h = 10.96$  mm.

## 5 DISC HERNIATION, BACK PAIN AND NUCLEOTOMY

If the load  $F$  becomes very large, it would exceed the sustainable value and cause the annulus to develop radial cracks. Then the NP breaks through the annulus. A herniated disc occurs most often in the lumbar region of the spine, especially at the L4–L5 ( $L =$  lumbar). This is because the lumbar spine carries most of the body's weight. People between the ages of 30 and 50 years appear to be more vulnerable because the elasticity and water content of the NP decreases with age. The pain resulting from herniation may be combined with radiculopathy (neurological deficit). The deficit may include numbness, weakness and reflex loss. These changes are caused by nerve compression, created by pressure from interior disc material. Percutaneous nucleotomy is carried out in order to remove the NP from the sequestered disc and thereby alleviate the back pain [19]. A probe is inserted into the centre of the herniated disc under fluoroscope monitoring and the NP is removed through the probe. The analysis for (1) volume aspiration of the NP fluid with respect to the time for different external suction pressures and (2) the pressure drop in the NP fluid with respect to the time was reported by Ghista *et al.* [13].

## 6 THE NUCLEOTOMIZED DISC: GEOMETRY, STRESSES AND DISPLACEMENTS

For the nucleotomized disc, only the axial equilibrium needs to be satisfied as there is no internal pressure, as given in eqn (3). Note that the radial and circumferential hoop stresses are identically equal to zero. Hence, the solution of eqn (3), with the boundary conditions  $w = w_{h,nu}$  at  $h = z$  and  $w = 0$  at  $h = 0$ , is given by

$$w - w_{nu} = w_{h,nu} \frac{z}{h}. \quad (25)$$

The circumferential strain is related to the axial strain (by the Poisson's ratio) as

$$= \frac{u_{nu}}{r} = -\nu \frac{dw_{nu}}{dz} = -\nu \frac{w_{h,nu}}{h}. \quad (26)$$

Hence, the radial displacements at  $r = a$  and  $r = b$  for the nucleotomized disc are given by

$$u_{a,nu} = \frac{w_{h,nu}}{h}a \quad \text{and} \quad u_{b,nu} = \frac{w_{h,nu}}{h}b. \quad (27)$$

### 6.1 Stress analysis for a vertical loading on the nucleotomised disc

For a vertically applied force  $F$ , the equilibrium of the disc is shown in Fig. 7; the minus sign is employed because the axial stress  $\sigma_{z,nu}$  (assumed to be tensile) acts on the vertebral end-plate and the axial stress  $\sigma_{z,nu}$  in the annulus is hence given by

$$\sigma_{z,nu} = -\frac{1}{b^2 - a^2} \frac{F}{2}. \quad (28)$$

Using Hooke's law, the axial deformation is related to  $\sigma_{z,nu}$  and hence to the applied force  $F$ , so that the decrease in disc height

$$w_{h,nu} = -\frac{1}{E} \frac{Fh}{b^2 - a^2}. \quad (29)$$

Then, from eqns (27) and (29), the radial expansion of the disc at  $r = a$ ,

$$u_{a,nu} = -\frac{1}{E} \frac{Fa}{b^2 - a^2}. \quad (30)$$

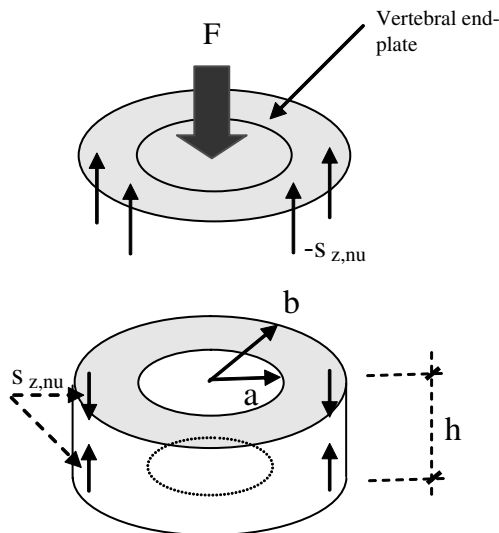


Figure 7: Normal stress  $\sigma_{z,nu}$  equilibrating the applied force  $F$  in a nucleotomized disc.

Similarly, the radial expansion of the disc at  $r = b$  is given by

$$u_{b,nu} = -\frac{1}{E} \frac{Fb}{b^2 - a^2} \quad \text{or} \quad u_{b,nu} = \frac{bu_{a,nu}}{a}. \quad (31)$$

## 7 MECHANISM OF DISC DEFORMATION IN THE NUCLEOTOMIZED DISC

The same procedure as outlined in Section 4 is used to determine the incremental and final deformations of the nucleotomized disc under a uniaxial compressive load of 2000 N. The resulting graphs of disc deformations  $w_{h,nu}$ ,  $u_{a,nu}$ ,  $u_{b,nu}$  vs.  $F$  and  $(u_{b,nu} - u_{a,nu})$  vs.  $F$  are plotted in Fig. 8 alongside the deformations of the normal disc in order to provide a comparison. Also shown in Fig. 9 are the deformed disc geometries for  $F = 0$ ,  $F = 500$  N,  $F = 1000$  N,  $F = 1500$  N and  $F = 2000$  N.

It is seen that the nucleotomized disc has considerably greater deformations than the normal disc. These deformations can result in compression of the nerve structures as well as the facet joints. Thus, the removal of the NP has adverse effects like disc collapse and excessive radial bulging. This trend is experimentally demonstrated by Meakin *et al.* [20] and Judith *et al.* [21].

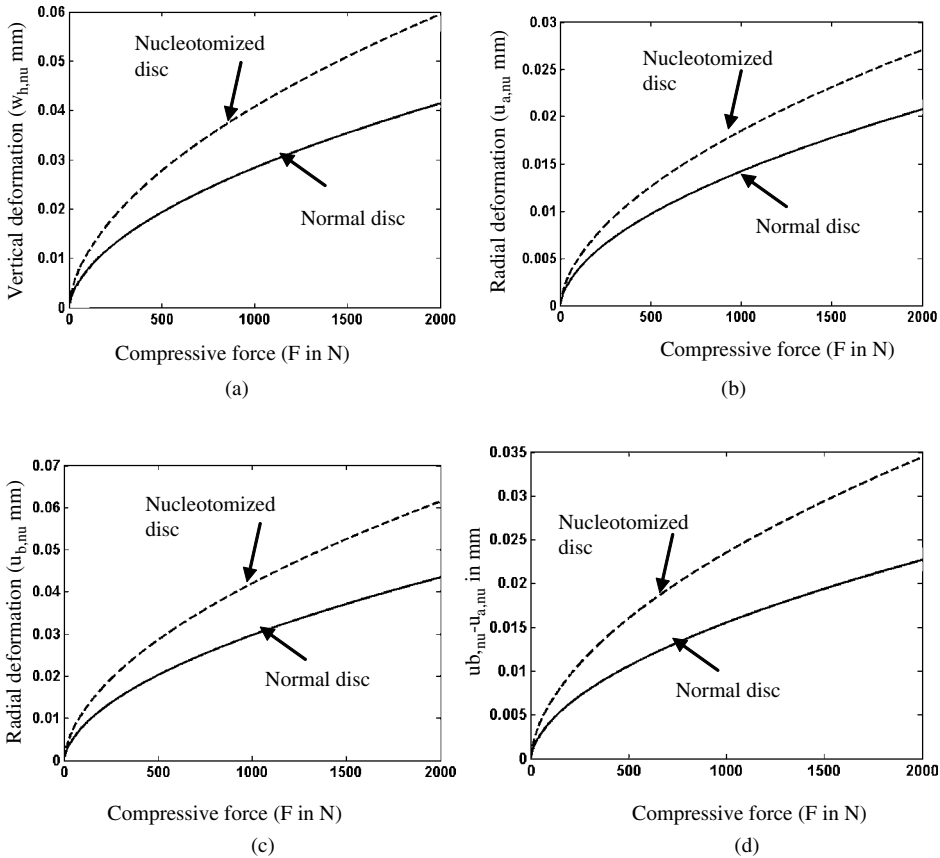


Figure 8: (a) Disc vertical deformation vs. compressive force on the annulus with and without NP. (b) Disc  $u_{a,nu}$  vs.  $F$  with and without NP. (c) Disc  $u_{b,nu}$  vs.  $F$  with and without NP. (d) Disc  $(u_{b,nu} - u_{a,nu})$  vs.  $F$  with and without NP. The initial disc geometric parameters adopted are  $a = 11$  mm,  $b = 25$  mm and  $h = 11$  mm and the residual modulus  $E_0$  is 4.2 MPa.

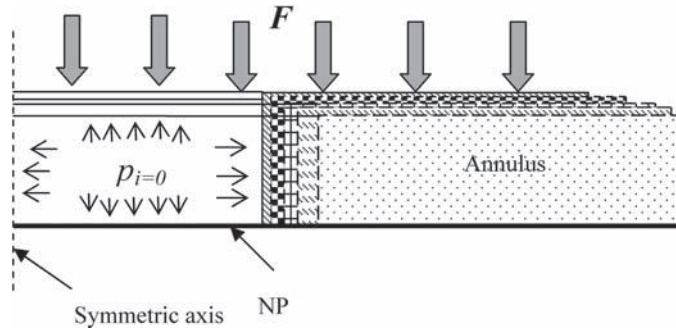

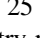
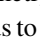
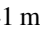
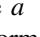


Figure 9: Graphical representation of the nucleotomized disc deformation from the unloaded state till the compressive load of 2000 N.  represents the unloaded state; disc geometry parameters are  $a = 11$  mm,  $b = 25$  mm,  $h = 11$  mm.  corresponds to the disc deformed state after 500 N; geometry parameters are  $a = 11.014$  mm,  $b = 25.029$  mm,  $h = 10.972$  mm.  corresponds to the deformed state after 1000 N; geometry parameters are  $a = 11.018$  mm,  $b = 25.041$  mm,  $h = 10.959$  mm.  represents the state after 1500 N; geometry parameters are  $a = 11.023$  mm,  $b = 25.051$  mm,  $h = 10.949$  mm.  represents the final disc deformed state when loaded by 2000 N; the corresponding final disc geometry parameters are  $a = 11.026$  mm,  $b = 25.061$  mm,  $h = 10.94$  mm.

## 8 CONCLUSION: THE IVD AS AN OPTIMAL STRUCTURE

Based on these results, in order to retain the stress-stiffening characteristic of the disc and mimic the normal disc load-deformation behaviour, it is not advisable to carry out nucleotomy on herniated discs. Instead, it is advisable to replace the NP with a gel-filled balloon [22] in the case of disc herniation.

This paper clearly illustrates the natural anatomical–physiological design of the IVD as an optimal load-bearing and deformation-containing structure. This is because of the composite design of the IVD, in which the NP is enclosed by the annulus. Thus, when the IVD is loaded, the NP gets pressurized, its annulus stress increases, the annulus (stress-dependent) modulus increases and, hence, the annulus deformation is contained. This is the salient feature of the IVD as an optimal structure, namely its ability to contain its axial and radial deformations under increased loading.

## NOMENCLATURE

$b$	outer radius of the annulus
$a$	inner radius of the annulus
$h$	height of the annulus
$p_i$	pressure of the NP
$F$	compressive load
$f$	induced fluid pressure
$z$	compressive stress induced in the annulus
	circumferential stress induced in the annulus
$r$	radial stress induced in the annulus,
	Poisson's ratio
$E$	Young's modulus
	strain

## REFERENCES

- [1] Ghista, D.N., Fan, S.C., Ramakrishna, K. & Sridhar, I., The human lumbar vertebral body as an intrinsic, functionally optimal structure. *International Journal of Design and Nature*, 1(1), pp. 34–47, 2007.
- [2] Humzah, M.D. & Soames, R.W., Human intervertebral disc: structure and function. *The Anatomical Record*, 220(4), pp. 337–356, 1988.
- [3] <http://www.spineuniverse.com/displayarticle.php/article1431.html> (accessed on 10th September 2005)
- [4] Shirazi-Adl, A., On the fibre composite material models of disc annulus-comparison of predicted stresses. *Journal of Biomechanics*, 22(4), pp. 357–365, 1989.
- [5] Shirazi-Adl, A., Finite-element simulation of changes in the fluid content of human lumbar discs: mechanical and clinical implications. *Spine*, 17(2), pp. 206–212, 1990.
- [6] Fagan, M.J., Julian, S., Siddall, D.J. & Mohsen, A.M., Patient-specific spine models. Part 1: Finite element analysis of the lumbar intervertebral disc – a material sensitivity study. *Proceedings of the Institution of Mechanical Engineers, Part H: Journal of Engineering in Medicine*, 216(5), pp. 299–314, 2002.
- [7] Lin, H.S., Liu, Y.K., Ray, G. & Nikravesh, P., Systems identification for material properties of the intervertebral joint. *Journal of Biomechanics*, 11(2), pp. 1–14, 1978.
- [8] Belytschko, T., Kulak, R.F., Schultz, A.B. & Galante, J.O., Finite element stress analysis of an intervertebral disc. *Journal of Biomechanics*, 7(3), pp. 277–285, 1974.
- [9] Wu, H.C. & Yao, R.F., Mechanical behavior of the human annulus fibrosus. *Journal of Biomechanics*, 9(1), pp. 1–7, 1976.
- [10] Kulak, R.F., Belytschko, T.B. & Schultz, A.B., Nonlinear behavior of human intervertebral disc under axial load. *Journal of Biomechanics*, 9(6), pp. 377–386, 1976.
- [11] Nick, D., Pope, M.H. & Krag, M.H., Mechanical model for the human intervertebral disc. *Journal of Biomechanics*, 20(9), pp. 839–850, 1987.
- [12] Martinez, J.B., Oloyede, V.O.A. & Broom, N.D., Biomechanics of load-bearing of the intervertebral disc: an experimental and finite element model. *Medical Engineering & Physics*, 19(2), pp. 145–156, 1997.
- [13] Ghista, D.N., Subbaraj, S., Mazumdar, J. & Rezaian, S.M., The biomechanics of back pain. *IEEE Engineering in Medicine and Biology Magazine*, 17(3), pp. 36–41, 1998.
- [14] Shirazi-Adl, A., Srivastava, S.C. & Ahmed, A.M., Stress analysis of the lumbar disc body unit in compression. *Spine*, 9, pp. 120–134, 1984.
- [15] Yamada, H., *Strength of Biological Materials*, Williams and Wilkins: Baltimore, MD, 1970.
- [16] Fagan, M.J., Julian, S. & Mohsen, A.M., Finite element analysis in spine research. *Proceedings of the Institution of Mechanical Engineers, Part H: Journal of Engineering in Medicine*, 216, pp. 281–298, 2002.
- [17] Ranu, H.S., Pressure-volume studies in human lumbar spinal discs. *Southern Biomedical Engineering Conference – Proceedings*, p. 263, 1995.
- [18] Ranu, H.S., Denton, R.A., & King, A.I., Pressure distribution under an intervertebral disc – an experimental study. *Journal of Biomechanics*, 12(10), pp. 807–812, 1979.
- [19] Amoretti, N., Huchot, F., Flory, P., Brunner, P., Chevallier, P. & Bruneton, J.N., Percutaneous nucleotomy: preliminary communication on a decompressor probe in percutaneous discectomy. Ten case reports. *Clinical Imaging*, 29, pp. 98–101, 2005.
- [20] Meakin, J.R. & Hukins, D.W.L., Effect of removing the nucleus pulposus on the deformation of the annulus fibrosus during compression of the intervertebral disc. *Journal of Biomechanics*, 33(5), pp. 575–580, 2000.

- [21] Judith, R.M., Thomas, W.R. & David, W.L.H., The effect of partial removal of the nucleus pulposus from the intervertebral disc on the response of the human annulus fibrosus to compression. *Clinical Biomechanics*, 16, pp.121–128, 2001.
- [22] Goel, V., Dooris, A.P., Dennis, M. & Rengachary, S., Biomechanics of artificial disc. *Advances in Spinal Fusion Molecular Science, Biomechanics, and Clinical Management*, eds. K. Lewandrowski, L.W. Donald, D.J. Trantolo, M.J. Yaszemski & A.A. White, Marcel Dekker: New York, 2004.